Dissertation

Schallquellenidentifikation bei der Reifen-Fahrbahn-Interaktion

ausgeführt zum Zwecke der Erlangung des akademischen Grades
eines Doktors der technischen Wissenschaften

eingereicht an der Technischen Universität Wien
Fakultät für Maschinenwesen und Betriebswissenschaften

von

Dipl.-Ing. Jonathan Jakob Nowak
Mat.Nr. 1027635

unter der Leitung von

Univ.Prof. Dipl.-Ing. Dr.techn. Manfred Kaltenbacher
Institut für Grundlagen und Theorie der Elektrotechnik
Technische Universität Graz
Inffeldgasse 18, 8010 Graz

begutachtet von

Ass. Prof. DI Dr. Franz Zotter

Institut für Elektronische Musik und Akustik
Universität für Musik und darstellende Kunst
Graz
Inffeldgasse 10/III, 8010 Graz

Privatdoz. DI Dr. techn. Christoph Reichl

Institut für Strömungsmechanik und
Wärmeübertragung
Technische Universität Wien
Getreidemarkt 9, 1060 Wien

Wien, August 2023

Kurzfassung

Verkehrslärm ist, angesichts der Tatsache, dass in Europa Millionen von Menschen dessen hohen Dauerlärmpegeln ausgesetzt sind, ein hochaktuelles Thema. Lärm aufgrund von Reifen-Fahrbahninteraktionen ist eine dominante Untergruppe des Verkehrslärms. In dieser Arbeit werden verschiedene frequenzbasierte Methoden der Schallquellenortung angewandt, die sich Mikrofonarraymessungen bedienen und die Identifikation der dominanten Schallquellen am Reifen zum Ziel haben. Für die Messungen wurde ein Fahrzeuganhänger verwendet, der mit einem Messreifen ausgestattet ist.

Es wird die Anwendung eines inversen Verfahrens präsentiert, mit dem Schallquellen in Amplitude und Phase identifiziert werden können. Diese Methode kombiniert Mikrofonarraymessungen und Simulationen mit der Finite-Elemente-Methode (FEM), um die dominanten Schallquellen aus den Schalldruckmessungen zu berechnen. Da bei dieser Methode numerische Simulationen verwendet werden, können die tatsächlich vorhandenen Randbedingungen der Messumgebung berücksichtigt werden.

Diese Arbeit beschreibt den Prozess, der nötig ist, um die korrekten Randbedingungen des Messanhängers zu bestimmen. Akustische Absorber, die innerhalb des Anhängers zur Schalldämmung aufgebracht sind, werden mit einem äquivalenten Fluid modelliert. Die Materialparameter wurden mit dem Johnson-Champoux-Allard-Lafarge-Modell berechnet, dessen Modellparameter mittels Impedanzrohrmessungen gefittet wurden. Die gefitteten Modellparameter wurden anschließend validiert, indem die mit der FEM simulierten Schalldrücke mit den Mikrofonarraymessungen verglichen wurden. Für die Messungen wurde der stationäre Messanhänger mit einem mit sinusförmigen Signalen angesteuerten Lautsprecher angeregt. Die Membranauslenkung wurde mit einem Laser-Scanning-Vibrometer bestimmt und konnte auf diese Weise als Neumann-Randbedingung im FE-Modell aufgeprägt werden.

Die vorliegende Arbeit vergleicht verschiedene Methoden zur Schallquellenortung miteinander, wobei zunächst virtuelle Schalldruckmessungen und die stationären Mikrofonmessungen für die Validierung verwendet werden. In weiterer Folge werden Schallquellen am rollenden Reifen identifiziert, wobei die inverse Methode und herkömmliche Verfahren verwendet werden. Letztere basieren auf der Beamforming-Methode. Hierfür wurden Messungen auf österreichischen Autobahnen bei unterschiedlichen Geschwindigkeiten und auf unterschiedlichen Fahrbahnbelägen durchgeführt. Nachdem die dominanten Schallquellen am Reifen identifiziert wurden, kann der Schalldruck innerhalb des Anhängers in einer Vorwärtssimulation rekonstruiert werden. Es konnte gezeigt werden, dass das inverse Verfahren eine sehr gute Übereinstimmung der simulierten mit den gemessenen Schalldrücken an den Mikrofonpositionen erzielen kann, und dass sie herkömmlichen, fortgeschrittenen beamforming-basierten Algorithmen – wie CLEAN-SC – überlegen ist. Daher ist es möglich, mit der inversen Methode das Schalldruckfeld an beliebigen Stellen innerhalb des Anhängers zu berechnen.

Eidesstattliche Erklärung

Ich erkläre an Eides statt, dass die vorliegende Arbeit nach den anerkannten Grundsätzen für wissenschaftliche Abhandlungen von mir selbstständig erstellt wurde. Alle verwendeten Hilfsmittel, insbesondere die zugrunde gelegte Literatur, sind in dieser Arbeit genannt und aufgelistet. Die aus den Quellen wörtlich entnommenen Stellen, sind als solche kenntlich gemacht.

Das Thema dieser Arbeit wurde von mir bisher weder im In- noch Ausland einer Beurteilerin/einem Beurteiler zur Begutachtung in irgendeiner Form als Prüfungsarbeit vorgelegt. Diese Arbeit stimmt mit der von den Begutachterinnen/Begutachtern beurteilten Arbeit überein.

Unterschrift

Ort, Datum

Dissertation

Sound Source Identification for Tire-Pavement Interaction

performed for the purpose of obtaining the academic degree
of Doctor of Technical Science

submitted to the Vienna University of Technology
Faculty of Mechanical and Industrial Engineering

by

Dipl.-Ing. Jonathan Jakob Nowak
Mat.Nr. 1027635

under the supervision of

Institute of Fundamentals and Theory in Electrical Engineering
Graz University of Technology
Inffeldgasse 18, 8010 Graz

reviewed by

Ass. Prof. DI Dr. Franz Zotter
Institute of Electronic Music and Acoustics
University of Music and Performing Arts
Inffeldgasse 10/III, 8010 Graz

Privatdoz. DI Dr. techn. Christoph Reichl
Institute of Fluid Mechanics and Heat Transfer
TU Wien, Vienna, Austria
Getreidemarkt 9, 1060 Vienna

Vienna, August 2023

Abstract

Environmental noise due to vehicle traffic is highly topical as it causes millions of people in Europe to be exposed to high long-term noise levels. Tire-pavement interactions are a dominant sub-source of vehicle traffic noise. This thesis demonstrates the application of different frequency-based sound source localization algorithms using microphone array measurements to identify the most dominant sound sources during the tire-pavement interaction. A vehicle trailer equipped with a test tire was used for the microphone array measurements.

The application of an inverse method for identifying sound sources in amplitude and phase is presented. This method uses microphone array measurements and Finite Element (FE) simulations to reconstruct the sound sources on the tire from sound pressure measurements. Due to the use of numerical simulations, the actual boundary conditions of the given measurement setup are fully considered.

This work illustrates the process of finding the measurement trailer's correct boundary conditions. Acoustic absorbers, which are mounted for sound insulation on the insides of the measurement trailer, are modeled as equivalent fluid in the FE model. Their material properties are obtained using the Johnson-Champoux-Allard-Lafarge model, whose parameters are fitted from impedance tube measurements. The fitted material properties were validated by comparing the acoustic pressure calculated with the FE method to microphone measurements. For the measurements, a loudspeaker inside the stationary trailer was excited with a sinusoidal signal, and its membrane deflection was measured using a laser scanning vibrometer. The thereby measured surface velocity was imposed as a Neumann boundary condition to the FE problem.

In the first step, the sound source localization algorithms are compared using virtual sound pressure measurements and the stationary microphone measurements from the validation setup. Subsequently, the sound sources on the running tire are identified using the inverse method and established beamforming-based methods. For this purpose, measurement runs were performed on Austrian highways with different speeds and on various pavements. With the primary sound sources identified, the sound pressure field within the trailer is reconstructed by forward FE simulations. It could be shown that the inverse method is capable of matching the simulated sound pressure at the microphone positions very well to the microphone measurements and that it outperforms commonly known advanced beamforming-based algorithms, such as CLEAN-SC. Thereby it is possible to reconstruct the sound pressure field at arbitrary positions within the measurement trailer via the inverse method.

Affidavit

I declare in lieu of oath, that I wrote this thesis and performed the associated research myself, using only literature cited in this volume. If text passages from sources are used literally, they are marked as such.

I confirm that this work is original and has not been submitted elsewhere for any examination, nor is it currently under consideration for a thesis elsewhere.

Signature

Place, Date

Symbols and Notation

a_n	Amplitude of nth source within Ω_{sc}
c	Speed of sound
c_p	Specific heat coefficient at constant pressure
c_v	Specific heat coefficient at constant volume
e	Euler's constant
f	Frequency
f_{S}	Sampling frequency
f_{l}	Lower frequency limit
f_{u}	Upper frequency limit
g	Green's function
h	Mesh size
j	Reduced functional
j	Imaginary unit
k	Wave number
k_0'	Static thermal permeability
m	Mass
p	Pressure
p_0	Ambient pressure
p_{a}	Acoustic pressure
$p_{\mathrm{a,sim}}$	Simulated acoustic pressure
r_{lm}	Distance between center point of loudspeaker's membrane and microphone
r_{tm}	Distance between center point of tire contact patch and microphone
$\underline{r}$	Reflection coefficient
$\underline{r}_{\mathrm{calc}}$	Calculated reflection coefficient
r_{E}	Power reflection coefficient
s	Entropy
$v_{\mathrm{a,n}}$	Normal component of acoustic particle velocity
v	Velocity
w	Test function
$z(t)$	Beamformer's output
$\underline{z}$	Adjoint state

He	Helmholtz number
J	Objective function (or cost function, fitness function)
$\underline{K}_{\mathrm{eff}}$	Effective compression modulus
L	Characteristic length
L_{dyn}	Dynamic range of source level
$L_{p_{\mathrm{a}}}$	Sound pressure level
L_{σ}	Sound source level
N_{m}	Number of microphones
N_{sc}	Number of sources within Ω_{sc}

N_{s}	Number of samples
P_{a}	Acoustic power
R	Specific gas constant
S	Sensitivity
T	Temperature
U	Voltage
V	Volume
W	Sobolev space
Z_0	Characteristic impedance
Z_{c}	Characteristic field impedance
Z_{S}	Specific impedance

$\mathcal{L}$	Lagrangian function

$\boldsymbol{f}$	External force density
$\boldsymbol{f}_{\mathrm{tot}}$	Total force
$\underline{\boldsymbol{g}}$	Steering vector
$\boldsymbol{n}$	Normal vector
$\underline{\boldsymbol{p}}_{\mathrm{a}}$	Vector of acoustic pressure signals at microphones
$\boldsymbol{v}$	Velocity vector
$\boldsymbol{v}_{\mathrm{a}}$	Acoustic particle velocity vector
$\boldsymbol{x}$	Observer position
$\boldsymbol{x}_{\mathrm{sc}}$	Source position within $\mathit{\Omega}_{\mathrm{sc}}$
$\boldsymbol{y}$	Source position
$\boldsymbol{y}_{\mathrm{f}}$	Assumed source position (focus point)

$\boldsymbol{\mathcal{F}}$	Source distribution
$\boldsymbol{\tau}$	Viscous stress tensor
$\underline{\boldsymbol{C}}$	Cross-spectral matrix
$\boldsymbol{I}_{\mathrm{a}}$	Acoustic intensity
$\underline{\boldsymbol{T}}$	Transfer matrix

α	Sound absorption coefficient
α_∞	High frequency limit of turtuosity
$\varepsilon_{\mathrm{rel,L2}}$	Relative L2-error of complex valued reconstructed and measured acoustic pressure
$\varepsilon_{\mathrm{abs,L2}}$	Relative L2-error of amplitudes of reconstructed and measured acoustic pressure
θ_{i}	Angle of incident
κ	Adiabatic exponent
λ	Wave length
λ_{th}	Thermal conductivity
μ	Dynamic viscosity
ν	Functional beamforming exponent
$\underline{\xi}_{\mathrm{S}}$	Specific impedance ratio

ρ_0	Density of air
$\underline{\rho}_{\mathrm{eff}}$	Effective density
σ	Monopole source strength
τ	Emission time, retarded time
ϕ	Porosity
φ_n	Phase of nth source within $\mathit{\Omega}_{\mathrm{sc}}$
ψ_{a}	Acoustic scalar potential
ω	Angular frequency

Γ	Surface
Λ	Viscous characteristic length
Λ'	Thermal characteristic length
$\mathit{\Xi}$	Flow resistivity
$\mathit{\Omega}$	Region, domain
$\mathit{\Omega}_{\mathrm{sc}}$	Source region

$\mathrm{D}/\mathrm{D}t$	Substantial derivative with respect to time
$\partial/\partial t$	Partial derivative with respect to time
$\mathcal{F}\{\Box\}$	Fourier transform of $\Box$
$\mathcal{F}^{-1}\{\Box\}$	Inverse Fourier transform of $\Box$
$\mathrm{Re}\{\Box\}$	Real part of $\Box$
$\mathrm{Im}\{\Box\}$	Imaginary part of $\Box$
$\lvert\Box\rvert$	Absolute value of $\Box$
$\lVert\Box\rVert$	Eucledian norm of $\Box$
$\lVert\Box\rVert_{\mathrm{F}}$	Frobenius norm of $\Box$
$\langle\cdot,\cdot\rangle$	Inner product
$\underline{\Box}$	Complex quantity
$\Box^{\mathrm{H}}$	Hermitian (conjugate complex) of $\Box$
$\breve{\Box}$	“Degraded” matrix (main diagonal removed)

Danksagung

An dieser Stelle möchte ich allen Personen meinen Dank aussprechen, die an der Entstehung dieser Arbeit direkt oder indirekt beteiligt waren. Zunächst danke ich Prof. Dr. techn. Dr. h.c. Manfred Kaltenbacher, der im Zuge meines Diplomstudiums mit seinen Vorlesungen mein Interesse an der Akustik geweckt hat und mich während der Erstellung dieser Dissertation fachlich und persönlich stets hervorragend unterstützt hat, obwohl sein Terminkalender immer gut gefüllt ist und er nach einiger Zeit den Wiener Stephansdom gegen den Grazer Uhrturm tauschte.

Zudem bedanke ich mich bei Ass. Prof. DI Dr. Franz Zotter und Privatdoz. DI Dr. techn. Christoph Reichl für ihr Interesse an meiner Arbeit und die Übernahme der Gutachten.

Weiters danke ich allen Mitgliedern der Akustikgruppe für den fachlichen Austausch und die freundschaftliche Stimmung am Institut und abseits davon. Hier möchte ich insbesondere Stefan Gombots, den Weisen des Südburgenlands, der meine Diplomarbeit betreute, Sebastian Floß, den zweitbesten Billardspieler der Stadt und wienerischsten Münchner, den ich kenne, Clemens Junger, durch den ich Linux und die Schwingungstechnik gelehrt bekam und Clemens Freidhager, zu dem ich lange Zeit unwissentlich verwandt war, erwähnen. Weiters gilt mein großer Dank Manfred Neumann, Reinhold Wagner und Christoph Keppel für die großartige und fachkundige Unterstützung bei den Messaufbauten sowie -fahrten. Außerdem danke ich Birgit Germ, Renate Mühlberger und Ruth Tscherne für die zuverlässige Erledigung von administrativen Angelegenheiten und bei Ruth zusätzlich für die hervorragende Zubereitung von zahlreichen Schnitzeln.

Zu guter Letzt danke ich meiner Familie. Meinen Eltern Rosa und Georg, die mich mein gesamtes bisheriges Leben und damit auch während meines Studiums stets so hervorragend unterstützt und mich in meinen akademischen Bestreben bestärkt haben, bin ich von Herzen dankbar. Ein riesiges Danke geht an meine Frau Birgit, die mich während der Entstehung meiner Dissertation nicht nur geheiratet hat, sondern mir vor allem in den vielen herausfordernden Phasen so viele Dinge abgenommen und mich damit ungemein unterstützt hat. Und *last*, aber wirklich nicht *least*, danke ich meinem Sohn Arthur, der so viel Verständnis für meine Tätigkeit aufgebracht hat, und der mir auf seine Art gezeigt hat, was die wirklich wichtigen Dinge im Leben sind.

Contents

CHAPTER 1

Introduction

1.1 Motivation

Noise from road traffic is a highly relevant topic since it is the most dominant source of environmental noise. It causes annoyance to humans, and it may as well impact people's health. According to the World Health Organization (WHO) it is estimated that in 2011 in Western Europe approximately one million deaths were caused by traffic-related noise [1]. According to [2], it is further estimated that in 2020 approximately 113 million people in Europe were exposed to long-term noise levels caused by road traffic of at least 55 dBA during the day-evening-night period inside urban areas. At least 20 % of the European population is exposed to high levels of road traffic noise during the day-evening-night-period and 15 % during the night-time period, respectively. These percentages may be even higher, as these numbers are based on data reported under the Environment Noise Directive (END), which only covers urbanized areas with a population of at least 100 000 inhabitants. Further, outside of urban areas, only major roads with more than 3 million passengers per year are considered.

Therefore, it is vital to focus topics of scientific research on reducing the noise levels to which humans are exposed. One part of this critical process is the development of suitable methods that enable us to identify the dominant sound sources during processes that generate noise. These methods can help understand noise generation mechanisms better and develop suitable noise mitigation strategies.

1.2 Vehicle Traffic Noise

Noise due to the tire-pavement interaction is stated in literature as the dominant sub-source of vehicle traffic noise at speeds above approximately 50 km/h for passenger cars and approximately 70 km/h for trucks [3, 4, 5, 6]. Other traffic noise sources are power train noise and aerodynamic noise. While tire-pavement noise is a function of tires and the pavement on which the vehicle is running, power train and aerodynamic sources depend solely on the vehicle. The term *power train noise* includes sources due to the engine, the induction system, the transmission and gears, the cooling fans, and the exhausts. Induction and exhaust system are sometimes considered as separate category. The trend of tire-pavement interactions being the primary sound source in vehicle noise is even more relevant when considering electric vehicles since their engine noise is significantly lower than that of comparable vehicles with a combustion engine. A comparison of controlled pass-by measurements (see Sec. 1.3.3) between different low-noise tires on electric vehicles can be found in [7].

Vehicle speed is the main influencing parameter for tire-pavement interaction and aerodynamically induced noise when considering A-weighted sound pressure levels during a passenger car's pass-by. Those two categories' dependency is typically stated to be proportional to $A \log(v/v_{\mathrm{ref}})$, where v is the vehicle speed, v_{ref} is a reference speed, and A is a suitable factor. Although this factor may be hard to determine and it varies significantly within different literature, it can be summarized that $A \approx 30$ for tire-pavement noise and $A \approx 60$ for aerodynamic sources. The dependency of the emitted noise level on vehicle speed is typically found via linear regression curves of the maximum A-weighted sound level. Additionally, tire-pavement noise increases with applied torque during acceleration.

Power train noise mainly depends on the engine speed and load, whereas according to literature [8, 9], torque only has a strong influence for engine speeds below 2000 rpm. Due to the dependency on the selected gear, there is no direct dependency on vehicle speed.

1.3 Sound Emission due to the Tire-Pavement Interaction

The sound-generating mechanisms during the tire pavement interaction are multifarious and challenging to determine independently. Therefore, no simple models and theoretical solutions exist. Determining the mechanisms involved is often based on experiments and measurements rather than analytic models or simulations and thus only allows empirical insight into the generation mechanisms. Results of a literature study on the existing tire-road models are presented in Sec. 1.3.2. Tire-road noise discussed in this thesis will be limited to exterior noise, i. e. noise perceived on the outside of the vehicle. The noise inside the vehicle, which affects the driver and passengers (*interior noise*), will not be considered.

A very well-known reference on tire and road noise is the *Tyre/Road Noise: Reference Book* by Sandberg and Ejsmont [3]. It covers – among many other related topics – an extensive investigation of different generating mechanisms during the tire-pavement interaction via measurements. A summary of the main findings in [3] and references to other studies will be given.

1.3.1 Tire-Pavement Interaction – Generating Mechanisms

According to literature, e. g. [3, 10], mechanisms generating sound during the tire-pavement interaction can be categorized into mechanic vibrations and aerodynamic phenomena. Additionally, amplification mechanisms occur.

Examples of **vibration effects** are

- radial and tangential vibrations of the tire due to tread and texture impact and running deflections
- adhesion mechanisms of the tread pattern (*stick-slip* and *stick-snap* effects).

Examples of **aerodynamic** generating mechanisms are

- air being displaced at the leading edge of the rolling tire and flowing to the trailing edge of the tire
- displacement of air in and out of cavities between the tread pattern and the road surface (*air-pumping*)
- turbulence around the tire due to the rotation of the tire
- vortex shedding.

Amplification mechanisms are

- Tread pattern functioning as Helmholtz resonators

- pipe resonances in channel-like tread pattern
- cavity resonances in the tire tube (torus cavity resonance)
- horn effect due to the curvature of the tire and the road surface forming a horn-like shape near the contact patch.

Vibration mechanisms that lead to noise generation are mainly determined by performing measurements and linking specific properties of the tire or the road to the measured sound. For example, a strong correlation could be shown between the frequency of tread blocks impinging on the road surface and the radiated sound. Further, studies using accelerometers, laser-Doppler-vibrometry, and coherence/correlation methods are presented in [10]. Vehicle speed is one of the main influences concerning the overall sound pressure and sound power level emitted by a rolling tire. Different simplified formulae of an estimate of the emitted sound pressure or sound power, respectively, are provided in [3, 10, 11, 12]. In [13], different studies are presented that investigate the influence of vehicle speed, tread design, road surface, tread wear, and effects of load and tire pressure on the emitted A-weighted sound pressure levels.

Aerodynamic sources due to flow over the tire or air turbulence caused by the rotation of the tire are considered to be insubstantial compared to noise due to the interaction of the tire with the pavement [13, 14, 15]. *Air-pumping* is a phenomenon that is often mentioned in literature when it comes to mechanisms that have a high impact on the generation of sound. The term air-pumping was mentioned in [16] by Hayden, describing the effect of air being displaced in cavities at the leading edge of the tire patch and cavity expansion at the trailing edge. Thus, the air is sucked in from one to the other side of the tire patch. Additionally, air can oscillate inside small cavities in the road surface due to the tire displacing air and air flowing back as soon as the tire leaves the surface. This effect is also called air-pumping in literature [17]. These oscillating flows are often modeled as monopole sources, see Sec. 2.1.3.

1.3.2 Models of a Tire

Because of the aforementioned complexity of the tire-pavement interactions' physics, all models that were found during a literature study focus on a specific aspect of the noise-generating process and additionally, certain simplifications are assumed in order to achieve solutions. In this section, theoretical and numerical models focusing on sound radiation are presented in contrast to the mainly measurement-driven approaches in [3]. Furthermore, there are hybrid methods to predict the pass-by noise due to tire-pavement interactions that combine analytical models with statistical models, e. g. the SPERoN model originally presented in [18] or the HyRoNE model. A comparison of the two methods can be found in [19, 20].

Aerodynamic Models

In [21], the sound emission due to air-pumping is investigated, modeling the process as a piston-like movement with a computational fluid dynamics (CFD) simulation. A Kirchhoff integral method is used to evaluate the far-field acoustic pressure. This model uses real tire geometries and is, therefore, a more practical model than previous studies [22, 23] that consider the fundamental effects of air-pumping without the application of tire geometries. A three-dimensional model of a tire that solves the Navier-Stokes equations via CFD and predicts the sound pressure in the far field, taking measured tire deformations into account, is presented in [24]. In [25] and [26, 27], the air-pumping mechanism of a slick tire rolling over a small cavity is investigated. Due to the tire patch penetrating, a volume variation of the cavity is caused, and the following pressure fluctuations are calculated via CFD.

Vibration Models

Although it is widely agreed that air-pumping is a main part of tire-road noise, there are also doubts about the importance of the aerodynamic sources described above. In [10], it is stated that tire vibrations can have a significant impact on tire-road noise if the vibrational (radial) modes are able to radiate sound efficiently. In general, tire vibrations do not radiate sound well because of the "hydrodynamic short-circuiting" effect, where air is flowing from regions of opposite phases of the tire but no sound propagation takes place. However, amplification mechanisms – i. e. the horn effect and Helmholtz and pipe resonances – and reflections can increase the efficiency of the tire vibrations' sound radiation.

The horn effect of a stationary tire was studied in detail in [28], where Boundary Element Method (BEM) calculations show a good agreement with measurements. The importance of low-order tire modes and their ability to radiate sound, even if the amplitudes of those modes are relatively low, is confirmed in [29]. In this paper, a tire-road noise model is presented using Wave Guide Finite Elements in connection with a contact model, which was further developed in [30]. The calculation of tire noise radiation via the Finite Element method with precomputed deformations of the tire, taking the excitation of an uneven road surface into account, and its eigenvalues is covered in [31].

In [32], a tire was excited on a shaker, and its surface acceleration was measured with a laser-Doppler-vibrometer. This data was used as input for a Finite Element computation. Subsequently, the radiated acoustic pressure was computed and compared to acoustic measurements with the tire being excited by a shaker or running inside a test drum. A good agreement could be shown up to a frequency of 600 Hz.

The speed dependency of noise induced by air-pumping and due to tire vibrations is investigated in [33]. In this paper, different speed exponents are investigated, with which the measured and simulated sound pressure of tire-road noise scales. Let v denote the vehicle speed. It could be shown that there are important contributions of tire vibrations to the emitted sound pressure that scale with v^4, as well as v^2, and v^6. However, the method presented did not prove suitable to separate noise created by tire vibrations from noise created by air-pumping.

1.3.3 Tire-Pavement Noise Measurement Methods

For the measurement of the tire-pavement interaction induced noise, several different standardized methods exist. The most important techniques will be presented in the following sections. The *Statistical Pass-By* and the *(Accelerated) Pass-By* method require stationary microphones placed at the side of the road. The *CPX* method measures the sound with microphones that move with the car and are mounted near the tire.

Statistical Pass-By (SPB) method

The statistical pass-by method is standardized in ISO 11819-1 and aims at determining how different pavements perform at absorbing the sound emitted due to tire-pavement interactions and the engines of passing vehicles at constant speeds of ≥ 50 km/h. Reference speeds are 50, 80 and 110 km/h.

The standard has the following main goals concerning the pavement under investigation: [34]

- Noise characterization and classification,
- assistance in auditing the production of pavements,
- evaluation of acoustic properties over the lifetime of road surfaces,
- investigation of the influence of various road surfaces on noise emissions,
- evaluation of the acoustic characteristics of road surfaces.

The method can be applied for passenger cars (Category P) and for twin- (Category H2) and multi-axle (Category H3) heavy vehicles. The minimum numbers of individually passing vehicles are 100 for Category P and 40 for Category H (sum of H2 and H3). The A-weighted sound pressure levels and the passing vehicles' speeds are measured and categorized according to P or H2/H3. For each vehicle category, maximum sound pressure levels are plotted in a regression diagram against the logarithmically scaled speeds. Further, the Statistical Pass-By Index (SPBI) can be calculated, which computes as the energy average of the maximum A-weighted sound pressure levels calculated for vehicle category P or H. The SPBI is used for the comparison of different road surfaces. The downside of this index is that it assumes a standardized proportion of trucks and passenger cars at each of the three reference speeds.

The microphone used for the sound pressure measurements has to be placed at the side of the road at a distance of 7.5 m from the center of the road under test. The road's test section has to extend at least 30 m on each side of the microphone. Further requirements concerning the conditions of the areas between the road and the microphone must apply, see [34].

The number of vehicles passing by can be significantly reduced if the goal of the measurements is a more detailed investigation of e. g. the influence of different sets of tires on the radiated maximum sound levels and, optionally, their frequency spectra. The vehicles pass at a constant speed with the engine running. The microphone is positioned in the same manner as the SPB method requires. This method is commonly called *Controlled Pass-By* (CPB) method.

Accelerated Pass-By method

This method is standardized in ISO 362-1 [35]. In contrast to the SPB method, here, only one vehicle passes two microphones on a standardized surface between two lines, where the speed of the passing vehicle increases from one line to the other. The pavement on which the vehicle is running is a reference surface, defined in ISO 10844. Since the road surface in this method is prescribed, the influence of the test vehicle, i. e. tire noise, engine noise and aerodynamic sources can be observed independently of the road surface.

The dimensions of the test area covered with the test road surface and microphone positions according to the norms can be seen in Fig. 1.1. A passenger vehicle has to approach line AA with a speed of 50 km/h and complete the distance between AA and BB under full acceleration. For heavy vehicles, the speeds are between 15 km/h and 50 km/h. The acceleration between lines AA and BB is approximated by the measured speeds of the vehicle at said lines. A target acceleration is defined whose value is computed via the total engine power of the test vehicle and its mass.

The result of a measurement according to ISO 362-1 is an A-weighted sound pressure level.

If the engine is switched off and the clutch is disengaged immediately before the vehicle reaches line AA, the method is called *Coast-By* method. In that case it is assumed that only tire-road noise is emitted.

Close-Proximity (CPX) Method

This method is standardized in ISO 11819-2. It has the same goals as the previously described SPB method and is applied for the following cases: [37]

- surveillance of the road surface's condition, e.g. wear and damage,
- testing of the homogeneity of a road section in the longitudinal and transverse directions,
- the development of low-noise road surfaces.

In contrast to the previously mentioned methods, here, the microphones are mounted on parts that are connected to the tire axle. Therefore, the microphones move with the vehicle and are not placed stationary along the road. Compared to the SPB method, the CPX method is faster and simpler to perform. However, the CPX method is only applicable in cases where the engine's noise is dominated

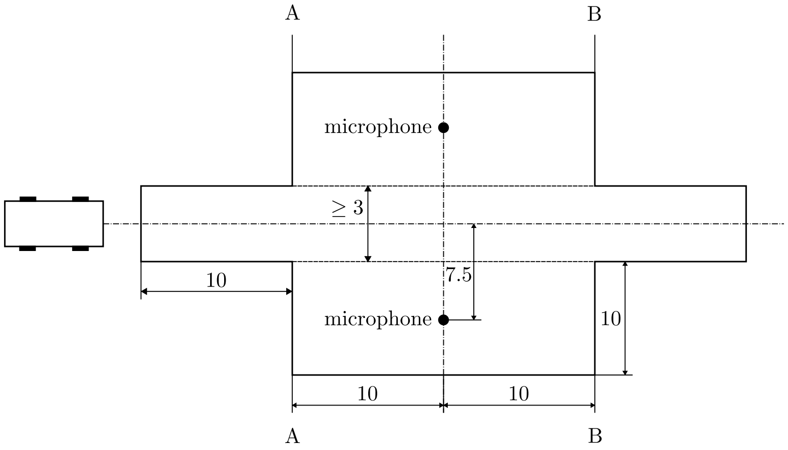

Figure 1.1: Dimensions in meters of the standardized test track; the area within the thick solid lines has to be covered with a surface complying with ISO 10844 [36]; sketch adapted from [35].

by noise due to the tire-pavement interactions. Often a protective vehicle trailer is used in order to reduce wind and engine noise.

The standard requires a minimum of two microphones facing the side wall of the tire near the contact patch at a 45° angle, see Fig. 1.2. Additional four microphone positions are optional.

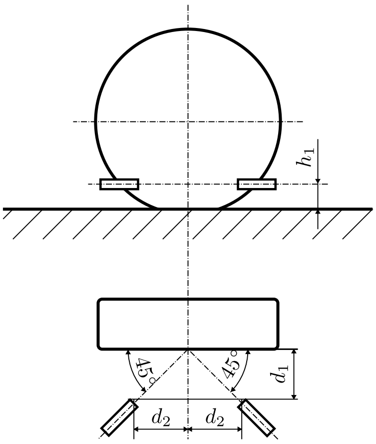

Figure 1.2: Mandatory microphone positions of CPX method, $h_1 = 0.1\,\mathrm{m}$, $d_1 = d_2 = 0.2\,\mathrm{m}$; sketch adapted from [37].

A measurement according to this standard requires the determination of a time-averaged A-weighted sound pressure level in the third-octave bands with band center frequencies from 315 Hz to 5000 Hz. The preferred reference speeds of the vehicle are 50 km/h, 80 km/h and 110 km/h. The standardized tires P1 (*Standard Reference Test Tyre*, SRTT) [38] or H1 (*Avon Supervan AV4*) [39] must be used.

The result of a measurement according to ISO 11819-2 is the third-octave band sound pressure level or an overall sound pressure level, which is averaged over the two microphone positions. Corrections are applied for temperature, rubber hardness, velocity, pavement condition, and other sound sources (e. g. wind noise). For details on the calculation see [37].

Due to measurements in the near field of the tire, results obtained with the CPX method have limited validity in the far field compared to the pass-by methods, which were mentioned in the previous section. However, the CPX method has the advantage that the sound pressure levels are averaged over longer road sections, whereas the results of the SPB method only cover a short road segment.

Some studies aim at linking the overall sound pressure levels of measurements according to the CPX standard with overall sound pressure levels obtained via SPB measurements. For example, the findings in [40], which analyzes measurement data mainly gathered during the EU-funded project ROSANNE suggest a linear relationship exists between the two overall sound pressure levels of CPX and SPB measurements, if the vehicle speeds are the same. Also, findings in [41] indicate a linear relationship between the results of the SPB and CPX method for vehicles of category P (passenger cars).

RVS

The RVS method [42] is an Austrian standardized measurement method that is similar to the CPX method described in Sec. 1.3.3. It also uses two mandatory microphone positions, with the main difference being that one microphone is placed behind the tire. Further, no optional positions are provided. The velocities during a measurement are 30 km/h, 50 km/h, and 80 km/h or 100 km/h. In contrast to the CPX method, the measurement tire used for the RVS method has no tread blocks. It is completely smooth and has four longitudinal grooves.

From the obtained sound pressures, two A-weighted continuous sound levels and A-weighted third-octave spectra with center frequencies between 250 Hz and 10 kHz are calculated. Corrections for temperature and velocity deviations are applied. The result of an RVS measurement is the LMA value, equaling the A-weighted sound pressure level's third-octave band of the rear microphone if this is higher than the corresponding value of the side microphone. Otherwise, the LMA value is the energy average third-octave spectrum of the two microphones. Because of the rear microphone position, the results from an RVS measurement are typically higher than those obtained via the CPX measurement [43].

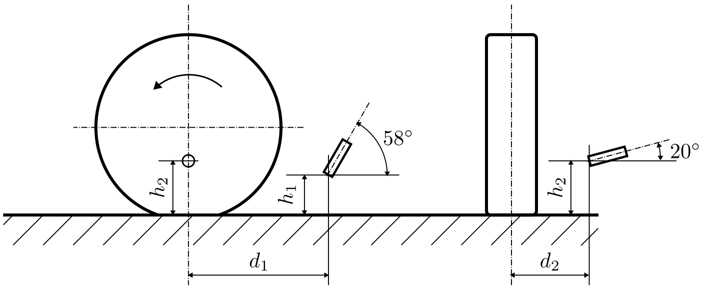

Figure 1.3: Microphone positions of RVS method, $h_1 = 0.1\,\text{m}$, $d_1 = 0.4\,\text{m}$, $h_2 = 0.15\,\text{m}$, $d_2 = 0.22\,\text{m}$; sketch adapted from [42].

Again, the validity of the results obtained by the RVS method is limited in the far field. Due to the use of a smooth measurement tire, the RVS method is assumed to overestimate road surfaces' effects on the emitted sound pressure level, since the tire lacks the typical interactions of the tire's tread blocks with the pavement [41]. Therefore, the RVS sound pressure levels show a higher value range than the CPX method when the same roads are evaluated.

Since the publication of the CPX method, which has become a European standard, the RVS is no longer considered state-of-the-art in Austria.

On-Board Sound Intensity (OBSI) Method

The On-Board Sound Intensity (OBSI) method uses a slightly different approach, standardized in [44]. Here, instead of the acoustic pressure – as in the previously mentioned methods – the sound intensity emitted by the rolling tire is measured. Determining the sound intensity is achieved using two sound intensity probes. As a sound intensity probe, two spaced microphones with a membrane diameter of 12.7 mm (= 0.5 in.) are used. It has to be noted that with this commonly used measurement method, an exact measurement of the sound intensity is not possible since this would require an accurate determination of the acoustic particle velocity, see (2.28). Here, the acoustic particle velocity is calculated via a finite differences approximation of (2.20); therefore, the acoustic pressure measurement with two microphones placed closely to each other is sufficient. The acoustic intensity is thereby only determined in the sensitivity axis of the intensity probe, i. e. the direction of the line connecting the two microphones.

In the OBSI method, the spacing between the centers of the microphone diaphragms must be 16 ± 1 mm and the sensitivity axis has to be parallel to the tire's rotation axis. A windscreen has to be mounted on each probe. The microphones are mounted closer to the tire and the pavement than in the CPX method: the normal distance between the midpoint between the two microphone membranes and the tire sidewall amounts to approx. 102 mm (4 in). The height of the microphones is approx. 76 mm (3 in), and the distance between the midpoints is approx. 210 mm (8.25 in).

The standard further requires using the Standard Reference Test Tyre (SRTT), and the preferred vehicle speed is 97 km/h (= 60 mph). The reported result of a measurement according to OBSI is an A-weighted sound intensity level in each third-octave band with center frequencies between 400 Hz and 5 kHz. Further, the pressure-intensity (PI) index is reported, which computes as the difference between the energy-averaged sound pressure and intensity level. The PI index has to lie within defined bounds in each third-octave band for the measurement to be valid.

The OBSI method is reported to be less prone to wind, exhaust, and engine noise than the CPX method, as the intensity probes have directional characteristics. Therefore, the probes are often mounted directly to the vehicle, and no trailers are used. Investigations in [45] of the correlation between the CPX and OBSI results show a strong linear relationship with low uncertainty between the two overall levels, although the microphone positions differ, and in case of the OBSI method, a sound intensity level is determined.

Laboratory Drum Method

This method is used in laboratories and uses either an outer or an inner drum in which the tire runs. To the drum, either replica pavement surfaces, which have similar properties as actual road surfaces, or smooth surfaces are mounted. The tire can be mounted such that the wheel load, slippage and steering angle are adjustable within bounds. The measurements performed with a drum show high accuracy and repeatability. Also truck tires can be mounted more easily than with the methods mentioned above. The sound pressure or intensity measurement positions are flexible and can e. g. be chosen according to the CPX or OBSI method. Alternatively, a microphone array can be used for sound source localization methods, see Chap. 3. Findings of studies presented in [3] state a strong correlation between sound pressure levels measured on real roads with trailers and with laboratory drums via the CPX method, given that the road surfaces used are almost identical in both methods.

On the downside, the curvature of the road surface leads to distorted sound radiation and noise due to bearings, the drum's drive, etc. will always be present in measurements. Moreover, usually, exchangeable cassettes are used as road surfaces. The discontinuities between the cassettes would not be present on a real road and may cause additional noise generation mechanisms.

An example of a large inner drum is located at the BASt (Federal Highway Research Institute) in Germany. It has a diameter of 5.5 m, a maximum speed of 280 km/h, a maximum wheel load of 6500 kg, and weighs approximately 32 000 kg [46].

1.4 Main Achievements

This thesis aims at identifying the dominant sound sources during the tire-pavement interaction. This identification shall be achieved via established methods and via an inverse method, called *Inverse Scheme*. The former approaches are based on beamforming, a technique using microphone arrays and simple analytic sound source and propagation models. Thereby, their performance is limited regarding their ability to identify the exact source positions in a real-world scenario, especially at low frequencies. The latter approach is a method that identifies the present sound source distribution in both amplitude and phase within a predefined region by minimizing the differences between microphone array measurements and Finite Element (FE) simulations of the acoustic pressure at the microphone positions. Thereby, the measurement setup's boundary conditions can be taken into account. In doing so, all materials – such as acoustic absorbers – present in the given measurement setup have to be characterized to incorporate them into the FE model.

In this thesis, a measurement trailer with a three-dimensional microphone array is used to record the sound pressure emitted by the rolling tire. The trailer is equipped with porous acoustic absorbers, whose sound absorption properties were measured with the impedance tube method. Its material properties were derived from those measurements, using the Johnson-Champoux-Allard-Lafarge (JCAL) material model. These material properties – the complex-valued compression modulus and complex-valued density – can subsequently be prescribed in the absorber region of the computational domain. In order to validate the FE model, the stationary trailer is excited with a loudspeaker, and the sound pressure is measured at various positions within the trailer. Using laser scanning vibrometer measurements of the loudspeaker's membrane, a suitable method was established to model the loudspeaker in the FE model. This allows for directly comparing the microphone measurements to the forward simulation of the acoustic pressure at the microphone positions.

Further, the performance of the Inverse Scheme is compared to commonly known sound source localization algorithms. In the first step, virtual measurements obtained via a forward FE simulation were used as input data. In the second step, actual microphone data from the stationary validation measurements served as input for the Inverse Scheme and the established sound source localization methods. It could be shown that the Inverse Scheme performed better at low acoustic frequencies than the other methods. However, the advanced beamforming-based method CLEAN-SC also performed well concerning the localization of the sound sources at higher frequencies.

In the final step, the dominant sound sources of the tire-pavement interactions were identified for different vehicle speeds, pavements, and frequencies within the frequency range of interest. For this purpose, the measurement trailer was equipped with 37 microphones distributed within the trailer to measure the sound emitted by the rolling tire. Additional sensors were used in order to determine the tire's rotational frequency and the trailer's running smoothness during the measurement runs. While the advanced algorithm CLEAN-SC can only localize the dominant sound source near the tire contact patch, it could be shown that the Inverse Scheme can identify additional weaker sources along the tire's circumference.

From the identified sources, the acoustic pressure at arbitrary locations of the computational domain may be obtained via a forward FE simulation. It has been demonstrated that the sound field of the forward simulation matches the actual sound field well if the sources identified via the inverse method are used in the forward computation. If the sources identified by the established method are applied in the forward simulation, the calculated sound pressures deviate significantly from the microphone measurements. Thereby, the superiority of the Inverse Scheme in a real-world application could be demonstrated. Additionally to the most dominant sound source, which was also localized by some of the beamforming-based algorithms, weaker sound sources could be identified by the Inverse Scheme. Further, if obtaining the sources' phases and calculating the resulting sound field is of interest, the inverse method is preferred.

The thesis is structured as follows: In Chap. 2, the fundamentals of acoustics and an overview of the used mathematical methods are provided. In Chap. 3, the basic principles of the mentioned established methods for the localization of sound sources using microphone arrays are given. Chap. 4 establishes an FE model of the measurement setup. Here, the focus is on modeling acoustic absorbers within the FE framework and validating the model with loudspeaker measurements. In Chap. 5 the mathematical fundamentals of the Inverse Scheme and its application to stationary measurements are presented. The application of the Inverse Scheme and beamforming-based methods to the rolling tire and the subsequent calculation of the resulting sound field can be found in Chap. 6. Chapter 7 summarizes this thesis and provides an outlook.

CHAPTER 2

Fundamentals

This chapter provides an overview of the mathematical and physical fundamentals which are required for the understanding of the following sections.

2.1 Acoustics

In this section, the derivation of the acoustic wave equation is established, and further fundamentals concerning acoustic, which will be referenced in the discussions of Chap. 4, 5 and 6, are provided.

2.1.1 Acoustic Wave Equation

When describing the propagation of sound in a compressible fluid, one has to consider conservation equations based on fluid dynamics: the conservation of mass, momentum, and energy. Additionally, due to the under-determination of the conservation equations, constitutive equations are needed to solve for e. g. the sound pressure p_a.

The conservation of mass states that the mass of this body is conserved over time. Therefore, the following condition must hold

$$\frac{\mathrm{D}m}{\mathrm{D}t} = \frac{\mathrm{D}}{\mathrm{D}t} \int\limits_{\Omega(t)} \rho(\boldsymbol{x},t)\,\mathrm{d}\boldsymbol{x} = 0\,. \tag{2.1}$$

Here, $\mathrm{D}/\mathrm{D}t$ denotes the substantial derivative, which is defined as

$$\frac{\mathrm{D}}{\mathrm{D}t} := \frac{\partial}{\partial t} + \boldsymbol{v}\cdot\nabla = \frac{\partial}{\partial t} + v_i \frac{\partial}{\partial x_i} \tag{2.2}$$

and represents the rate of change as measured by an observer moving with the fluid [47]. According to Reynold's transport theorem, which takes the time dependency of the domain $\Omega(t)$ into account, (2.1) results in

$$\frac{\mathrm{D}}{\mathrm{D}t} \int\limits_{\Omega(t)} \rho(\boldsymbol{x},t)\,\mathrm{d}\boldsymbol{x} = \int\limits_{\Omega(t)} \left(\frac{\partial\rho}{\partial t} + \nabla\cdot(\rho\boldsymbol{v})\right)\mathrm{d}\boldsymbol{x} = 0\,. \tag{2.3}$$

In (2.2), $\boldsymbol{v}$ denotes the velocity of the fluid. Since (2.3) must hold for an arbitrary domain Ω, the integral can be omitted. This leads to the mass conservation equation

$$\frac{\partial \rho}{\partial t} + \nabla \cdot (\rho \boldsymbol{v}) = 0 \,. \tag{2.4}$$

Conservation of momentum

The second conservation equation that is needed to derive the acoustic wave equation is the equation of momentum. Newton's second law of motion states that the momentum $\boldsymbol{p}_\mathrm{m}$ of a body is the product of its mass m and its velocity $\boldsymbol{v}$

$$\boldsymbol{p}_\mathrm{m} = m\boldsymbol{v} \,. \tag{2.5}$$

Deriving (2.5) with respect to time yields the total force $\boldsymbol{f}_\mathrm{tot}$ acting on the fluid. Applying Reynold's transport theorem again results in

$$\boldsymbol{f}_\mathrm{tot} = \frac{\mathrm{D}\boldsymbol{p}_\mathrm{m}}{\mathrm{D}t} = \frac{\mathrm{D}}{\mathrm{D}t}(m\boldsymbol{v}) = \frac{\partial}{\partial t}(m\boldsymbol{v}) + \nabla \cdot (m\boldsymbol{v} \otimes \boldsymbol{v}) \,, \tag{2.6}$$

where $\boldsymbol{v} \otimes \boldsymbol{v}$ denotes the dyadic product of the velocity with itself, which results in the tensor $v_i v_j$.

The forces $\boldsymbol{f}_\mathrm{tot}$ acting on the fluid can be split up into forces acting on the surface of the body, forces due to the momentum of the molecules, and external forces [48, 49]. Exploiting the fact that $m = \rho V$, with the volume V of the fluid, we arrive at the (specific) momentum equation

$$\frac{\partial}{\partial t}(\rho \boldsymbol{v}) + \nabla \cdot (\rho \boldsymbol{v} \otimes \boldsymbol{v}) = -\nabla p + \nabla \cdot \boldsymbol{\tau} + \boldsymbol{f} . \tag{2.7}$$

In (2.7), p denotes the pressure, $\boldsymbol{\tau}$ the viscous stress tensor, and $\boldsymbol{f}$ any external forces. With the use of vector identities and incorporation of the mass conservation (2.4), the momentum equation may be rewritten by

$$\rho \frac{\partial \boldsymbol{v}}{\partial t} + \rho \boldsymbol{v} \cdot \nabla \boldsymbol{v} = -\nabla p + \nabla \cdot \boldsymbol{\tau} + \boldsymbol{f} \,. \tag{2.8}$$

Constitutive equations

Since sound is defined as isentropic pressure-density perturbations, the isentropic speed of sound c is defined by

$$c^2 = \left(\frac{\partial p}{\partial \rho} \right)_s \,, \tag{2.9}$$

where the entropy s is held constant at its value in the undisturbed fluid. From this follows that the propagation of sound is adiabatic, i. e. losses due to heat transfer are neglected [50]. In engineering applications, the medium in which sound is traveling is often air at ambient conditions. Therefore, the equation of state for ideal gases is applicable

$$\frac{p}{\rho} = RT \tag{2.10}$$

with the specific gas constant R and the temperature T. The specific gas constant for an ideal gas computes as

$$R = c_p - c_V \,. \tag{2.11}$$

In (2.11), c_p and c_V denote the specific heat coefficients at constant pressure and volume, respectively. With the use of the adiabatic exponent $\kappa = c_p/c_V$, (2.9) may be rewritten as

$$c^2 = \kappa \frac{p}{\rho} = \kappa R T \,, \tag{2.12}$$

which shows that the speed of sound, in this case, is only dependent on the temperature but not on pressure or density. For air the adiabatic exponent is $\kappa \approx 1.402$.

The general pressure-density relation for an isentropic state reads as

$$\frac{\mathrm{D}p}{\mathrm{D}t} = c^2 \frac{\mathrm{D}\rho}{\mathrm{D}t} \,. \tag{2.13}$$

2.1.2 Linearized Acoustic Wave Equation

Assuming a non-viscous fluid and neglecting all external forces, we can set $\boldsymbol{\tau}$ and $\boldsymbol{f}$ in (2.7) to zero. Further, a perturbation ansatz is chosen for the field quantities pressure p, density ρ, and velocity $\boldsymbol{v}$

$$\begin{aligned} p &= p_0 + p_\mathrm{a} \,, \\ \rho &= \rho_0 + \rho_\mathrm{a} \,, \\ \boldsymbol{v} &= \boldsymbol{v}_0 + \boldsymbol{v}_\mathrm{a} = \boldsymbol{v}_\mathrm{a} \,. \end{aligned} \tag{2.14}$$

Note that no background flow is assumed, hence $\boldsymbol{v}_0 = \mathbf{0}$. In (2.14), p_a is called the acoustic pressure, ρ_a the acoustic density and $\boldsymbol{v}_\mathrm{a}$ the acoustic particle velocity.

By assuming

$$|p_\mathrm{a}| \ll |p_0|; \quad |\rho_\mathrm{a}| \ll |\rho_0| \,, \tag{2.15}$$

neglecting all quadratic and bilinear terms of perturbation quantities $\square_\mathrm{a}$, assuming no source terms and constant mean pressure p_0, we arrive at the linearized versions of mass, momentum and constitutive equations

$$\frac{\partial \rho_\mathrm{a}}{\partial t} + \nabla \cdot (\rho_0 \boldsymbol{v}_\mathrm{a}) = 0 \,, \tag{2.16}$$

$$\rho_0 \frac{\partial \boldsymbol{v}_\mathrm{a}}{\partial t} + \nabla p_\mathrm{a} = \mathbf{0} \,, \tag{2.17}$$

$$\frac{\partial p_\mathrm{a}}{\partial t} = c^2 \left(\frac{\partial \rho_\mathrm{a}}{\partial t} + \boldsymbol{v}_\mathrm{a} \cdot \nabla \rho_0 \right) . \tag{2.18}$$

Now, we apply the chain rule to (2.16) and substitute it into (2.18) and yield the final two equations for linear acoustics

$$\frac{1}{\rho_0 c^2} \frac{\partial p_\mathrm{a}}{\partial t} + \nabla \cdot \boldsymbol{v}_\mathrm{a} = 0 \,, \tag{2.19}$$

$$\frac{\partial \boldsymbol{v}_\mathrm{a}}{\partial t} + \frac{1}{\rho_0} \nabla p_\mathrm{a} = \mathbf{0} \,. \tag{2.20}$$

Note that in (2.19) the medium may be inhomogenous, i. e. $\nabla \rho_0 \neq \mathbf{0}$. The linearized acoustic wave equation for an inhomogeneous medium can be obtained from these two equations. Applying the partial time derivative $\frac{\partial}{\partial t}$ to (2.19) and the divergence operator $\nabla\cdot$ to (2.20) and subtracting the resulting equations yields

$$\frac{1}{\rho_0 c^2} \frac{\partial^2 p_\mathrm{a}}{\partial t^2} - \nabla \cdot \frac{1}{\rho_0} \nabla p_\mathrm{a} = 0 \,. \tag{2.21}$$

If a homogeneous medium is considered, the mean density ρ_0 is not dependent on space ($\nabla \rho_0 \equiv \mathbf{0}$), and (2.21) results in the well-known homogeneous linear acoustic wave equation

$$\frac{1}{c^2} \frac{\partial^2 p_\mathrm{a}}{\partial t^2} - \nabla \cdot \nabla p_\mathrm{a} = 0 \,. \tag{2.22}$$

In the homogeneous case, where $\rho_0 = \text{const.}$, the constitutive equation (2.18) reads as

$$p_{\mathrm{a}}^2 = c^2 \rho_{\mathrm{a}} \,. \tag{2.23}$$

Applying the curl-operator $\nabla\times$ to (2.20) results in

$$\nabla \times \left(\frac{\partial \boldsymbol{v}_{\mathrm{a}}}{\partial t} + \frac{1}{\rho_0} \nabla p_{\mathrm{a}} \right) = \nabla \times \frac{\partial \boldsymbol{v}_{\mathrm{a}}}{\partial t} = \mathbf{0} \,. \tag{2.24}$$

The second term is zero per definition, as every conservative field is rotation free. For the same reason, from (2.24) can be concluded that for the acoustic particle velocity $\boldsymbol{v}_{\mathrm{a}}$, there exists a scalar acoustic potential which satisfies

$$\boldsymbol{v}_{\mathrm{a}} = -\nabla \psi_{\mathrm{a}} \,. \tag{2.25}$$

Inserting (2.25) into (2.20) yields the relation between acoustic pressure and scalar velocity potential

$$\nabla \left(p_{\mathrm{a}} - \rho_0 \frac{\partial \psi_{\mathrm{a}}}{\partial t} \right) = \mathbf{0} \,.$$

Omitting the gradient yields

$$p_{\mathrm{a}} = \rho_0 \frac{\partial \psi_{\mathrm{a}}}{\partial t} \,. \tag{2.26}$$

Substituting (2.26) into (2.19) and using (2.25) shows the existence of the linear wave equation for the acoustic scalar potential

$$\frac{1}{c^2} \frac{\partial^2 \psi_{\mathrm{a}}}{\partial t^2} - \nabla \cdot \nabla \psi_{\mathrm{a}} = 0 \,. \tag{2.27}$$

Another important acoustic quantity is the acoustic intensity $\boldsymbol{I}_{\mathrm{a}}$. It is defined as the product of acoustic pressure and particle velocity

$$\boldsymbol{I}_{\mathrm{a}} = p_{\mathrm{a}} \boldsymbol{v}_{\mathrm{a}} \,. \tag{2.28}$$

With this, the acoustic power P_{a} can be computed via integration over a closed surface $\mathit{\Gamma}$ with normal vector $\boldsymbol{n}$

$$P_{\mathrm{a}} = \oint_{\mathit{\Gamma}} \boldsymbol{I}_{\mathrm{a}} \cdot \mathrm{d}\boldsymbol{s} = \oint_{\mathit{\Gamma}} p_{\mathrm{a}} \boldsymbol{v}_{\mathrm{a}} \cdot \boldsymbol{n} \, \mathrm{d}s = \oint_{\mathit{\Gamma}} p_{\mathrm{a}} v_{\mathrm{a,n}} \, \mathrm{d}s \,. \tag{2.29}$$

2.1.3 Modeling of Acoustic Sources

In this section the inhomogeneous wave equation and the modeling of sound sources will be discussed.

Impulsive Point Sources

A unit impulse point source at the position $\boldsymbol{x} = \mathbf{0}$ produces a sound field that is defined by

$$\frac{1}{c^2} \frac{\partial^2 \psi_{\mathrm{a}}}{\partial t^2} - \nabla \cdot \nabla \psi_{\mathrm{a}} = \delta(\boldsymbol{x}) \delta(t) \,, \tag{2.30}$$

with the delta distribution δ. Here, the impulse point source ansatz is chosen for the potential formulation of the acoustic wave equation. The ansatz could also be made for the pressure formulation (2.21) and (2.22), respectively. Due to the basic property of the delta distribution

$$\delta(a) = \begin{cases} +\infty & \text{for } a = 0 \\ 0 & \text{for } a \neq 0 \end{cases} \tag{2.31}$$

the source only exists at $t = 0$ at $\boldsymbol{x} = \mathbf{0}$ and is zero everywhere else. The general solution of (2.30) is given by [50, 51]

$$\psi_\mathrm{a} = \frac{f_1\left(t - \frac{r}{c}\right)}{r} + \frac{f_2\left(t + \frac{r}{c}\right)}{r}\,, \tag{2.32}$$

with $r = |\boldsymbol{x}| > 0$.

The first summand in (2.32) represents a spherically symmetric wave propagating in the direction of increasing values for r. The latter represents an incoming wave traveling to $\boldsymbol{x} = \mathbf{0}$. Physically, f_2 must be set to zero, since sound produced by a source must radiate away from the source. This is, of course, only valid for infinite open spaces without reflecting boundaries. The mentioned condition is called *causality* or *Sommerfeld radiation* condition.

The solution of (2.30) is given by [50]

$$\psi_\mathrm{a}(\boldsymbol{x}, t) = \frac{1}{4\pi r}\,\delta\left(t - \frac{r}{c}\right)\,, \tag{2.33}$$

with $r = |\boldsymbol{x}|$.

From (2.33) immediately follows the free-field Green's function $g(\boldsymbol{x}, \boldsymbol{y}, t, \tau)$ of the wave equation (2.27)

$$g(\boldsymbol{x}, \boldsymbol{y}, t, \tau) = \frac{1}{4\pi|\boldsymbol{x} - \boldsymbol{y}|}\,\delta\left(t - \tau - \frac{|\boldsymbol{x} - \boldsymbol{y}|}{c}\right) \tag{2.34}$$

which gives the causal solution due to an impulse point source $\delta(\boldsymbol{x} - \boldsymbol{y})\delta(t - \tau)$ located at the point $\boldsymbol{x} = \boldsymbol{y}$ emitted at time $t = \tau$ of

$$\frac{1}{c^2}\frac{\partial^2 g}{\partial t^2} - \nabla \cdot \nabla g = \delta(\boldsymbol{x} - \boldsymbol{y})\delta(t - \tau), \quad \text{where } g = 0 \ \text{ for } \ t < \tau\,. \tag{2.35}$$

This represents an impulsive spherically symmetric wave that is radiated from source point $\boldsymbol{y}$ at the speed of sound c. The amplitude of this wave is inversely proportional to the distance $r = |\boldsymbol{x} - \boldsymbol{y}|$.

This is a significant solution since it is possible to use Green's function for calculating the solutions of the linearized wave equation (2.22) with generalized source distributions $\boldsymbol{\mathcal{F}}(\boldsymbol{x}, t)$ as right-hand side

$$\frac{1}{c^2}\frac{\partial^2 p_\mathrm{a}}{\partial t^2} - \nabla \cdot \nabla p_\mathrm{a} = \boldsymbol{\mathcal{F}}(\boldsymbol{x}, t)\,. \tag{2.36}$$

The overall source distribution $\boldsymbol{\mathcal{F}}(\boldsymbol{x}, t)$ is regarded as a distribution of individual impulsive point sources

$$\begin{aligned} \boldsymbol{\mathcal{F}}(\boldsymbol{x}, t) &= \int\limits_0^T \int\limits_{-\infty}^{\infty} \boldsymbol{\mathcal{F}}(\boldsymbol{y}, \tau)\,\delta(\boldsymbol{x} - \boldsymbol{y})\delta(t - \tau)\ \mathrm{d}\boldsymbol{y}\,\mathrm{d}\tau \\ &= \int\limits_0^T \int\limits_{\Omega_\mathrm{sc}} \boldsymbol{\mathcal{F}}(\boldsymbol{y}, \tau)\,\delta(\boldsymbol{x} - \boldsymbol{y})\delta(t - \tau)\ \mathrm{d}\boldsymbol{y}\,\mathrm{d}\tau\,. \end{aligned} \tag{2.37}$$

The latter equality holds for finite source regions Ω_sc, which will be assumed in the following.

The solution for each individual source strength

$$\boldsymbol{\mathcal{F}}(\boldsymbol{y}, \tau)\,\delta(\boldsymbol{x} - \boldsymbol{y})\delta(t - \tau)\ \mathrm{d}\boldsymbol{y}\,\mathrm{d}\tau$$

is given by

$$\boldsymbol{\mathcal{F}}(\boldsymbol{y}, \tau)\,g(\boldsymbol{x}, \boldsymbol{y}, t - \tau)\ \mathrm{d}\boldsymbol{y}\,\mathrm{d}\tau\,.$$

The overall solution of (2.36) for the sound pressure p_a can be calculated by adding all individual point source contributions, i. e. integrating over the source domain, and all times τ

$$\begin{aligned} p_\mathrm{a}(\boldsymbol{x},t) &= \int\limits_0^T \int\limits_{\Omega_\mathrm{sc}} \boldsymbol{\mathcal{F}}(\boldsymbol{y},\tau)\, g(\boldsymbol{x},\boldsymbol{y},t-\tau)\ \mathrm{d}\boldsymbol{y}\,\mathrm{d}\tau \\ &= \frac{1}{4\pi} \int\limits_0^T \int\limits_{\Omega_\mathrm{sc}} \frac{\boldsymbol{\mathcal{F}}(\boldsymbol{y},\tau)}{|\boldsymbol{x}-\boldsymbol{y}|}\, \delta\left(t-\tau-\frac{|\boldsymbol{x}-\boldsymbol{y}|}{c}\right)\ \mathrm{d}\boldsymbol{y}\,\mathrm{d}\tau \\ &= \frac{1}{4\pi} \int\limits_{\Omega_\mathrm{sc}} \frac{\boldsymbol{\mathcal{F}}\left(\boldsymbol{y},t-\frac{|\boldsymbol{x}-\boldsymbol{y}|}{c}\right)}{|\boldsymbol{x}-\boldsymbol{y}|}\ \mathrm{d}\boldsymbol{y}\,. \end{aligned} \tag{2.38}$$

The last equality follows from the sifting property of the delta distribution, see e. g. [52]. (2.38) represents the acoustic pressure p_a as an integral equation at an arbitrary observer point $\boldsymbol{x}$ at time t by superimposing sources at source points $\boldsymbol{y}$, which radiated sound at earlier times $t-\frac{|\boldsymbol{x}-\boldsymbol{y}|}{c}$. In literature this is often called *retarded* or *emission time*. Therefore, (2.38) is also called the retarded formula. Again, it has to be stressed that this equation uses the *free-field* Green's function and therefore is only applicable to an open domain problem without any obstacles or partially absorbing boundary conditions. In case of scatterers or non-open domains, which is usually the case in real-world scenarios, one has to find a suitable tailored Green's Function which can be very challenging [53].

Monopoles, Dipoles and Quadrupoles

In this section, more specific source models are presented that can be used to model different types sound sources.

First, we consider a pulsating sphere (volume point source) with a time-dependent amplitude $\sigma(t)$. In this case, the source distribution becomes

$$\boldsymbol{\mathcal{F}}(\boldsymbol{x},t) = -\sigma(t)\delta(\boldsymbol{x})\,.$$

The corresponding differential equation for the acoustic potential ψ_a reads as

$$\frac{1}{c^2}\frac{\partial^2 \psi_\mathrm{a}}{\partial t^2} - \nabla\cdot\nabla\psi_\mathrm{a} = -\sigma(t)\delta(\boldsymbol{x})\,. \tag{2.39}$$

The solution for the potential due to this source distribution can be calculated analogously with (2.38), only we are solving for ψ_a instead of p_a. Hence, we arrive at

$$\psi_\mathrm{a}(\boldsymbol{x},t) = \frac{-\sigma(t-\frac{|\boldsymbol{x}|}{c})}{4\pi|\boldsymbol{x}|}\,. \tag{2.40}$$

The solution for the acoustic pressure due to a potential as in (2.40) can be subsequently derived with (2.26)

$$p_\mathrm{a} = \rho_0\frac{\partial\psi_\mathrm{a}}{\partial t} = -\frac{\rho_0}{4\pi r}\frac{\partial}{\partial t}\left[\sigma\left(t-\frac{r}{c}\right)\right]\,. \tag{2.41}$$

In a similar manner, integral equations for dipoles and quadrupoles can be deduced. Here, the pressure formulation of the acoustic wave equation is chosen. A dipole can be interpreted as two monopoles with equal amplitude but opposite phases. For the dipole, the source distribution in (2.36) reads as

$$\boldsymbol{\mathcal{F}}(\boldsymbol{x},t) = \nabla\cdot\boldsymbol{f}(\boldsymbol{x},t)\,, \tag{2.42}$$

with an arbitrary vector $\boldsymbol{f}(\boldsymbol{x}, t)$.

A quadrupole source consists of two dipoles with opposite phases [54, 55]. The source distribution in case of the quadrupole in (2.36) is characterized by a second space derivative of a tensor T_{ij}

$$\boldsymbol{\mathcal{F}}(\boldsymbol{x}, t) = \frac{\partial^2 T_{ij}}{\partial x_i \partial x_j}(\boldsymbol{x}, t)\,, \tag{2.43}$$

The formulae for dipole and quadrupole are provided without derivation. A detailed derivation can be found in [50]. The acoustic pressure p_a due to a dipole source in free-field computes as

$$p_\mathrm{a}(\boldsymbol{x}, t) = \frac{1}{4\pi} \frac{\partial}{\partial x_j} \int\limits_{\Omega_\mathrm{sc}} \frac{f_j\left(\boldsymbol{y}, t - \frac{|\boldsymbol{x}-\boldsymbol{y}|}{c}\right)}{|\boldsymbol{x}-\boldsymbol{y}|}\, \mathrm{d}\boldsymbol{y} \tag{2.44}$$

and due to a quadrupole reads as

$$p_\mathrm{a}(\boldsymbol{x}, t) = \frac{1}{4\pi} \frac{\partial^2}{\partial x_i \partial x_j} \int\limits_{\Omega_\mathrm{sc}} \frac{T_{ij}\left(\boldsymbol{y}, t - \frac{|\boldsymbol{x}-\boldsymbol{y}|}{c}\right)}{|\boldsymbol{x}-\boldsymbol{y}|}\, \mathrm{d}\boldsymbol{y}\,. \tag{2.45}$$

Interface Conditions

Consider an oscillating body inside a fluid domain with a velocity denoted by $\boldsymbol{v}_\mathrm{mech}$. Due to kinematic continuity, the normal components of the mechanic velocity $\boldsymbol{v}_\mathrm{mech}$ and the acoustic particle velocity $\boldsymbol{v}_\mathrm{a}$ must be equal at the interface Γ_i. Thus, the relation

$$\boldsymbol{n} \cdot (\boldsymbol{v}_\mathrm{mech} - \boldsymbol{v}_\mathrm{a}) = 0 \tag{2.46}$$

must hold. Further, the continuity of forces is provided by

$$\boldsymbol{\sigma}_n = -\boldsymbol{n} p_\mathrm{a} = -\boldsymbol{n} \rho_0 \frac{\partial \psi_\mathrm{a}}{\partial t}\,, \tag{2.47}$$

where $\boldsymbol{\sigma}_n$ denotes the mechanical stress acting on the surface of the solid body due to the pressure p_a.

2.1.4 Wave Equation in the Frequency Domain

The homogeneous wave equation (2.22) and the inhomogeneous wave equation (2.36) can be transformed into the frequency domain by performing a Fourier transform.

The forward Fourier transform $\underline{x}(\omega)$ of a continuous time signal $x(t)$ is defined as [56, 57, 58]

$$\underline{x}(\omega) = \mathcal{F}\{x(t)\} = \int\limits_{-\infty}^{\infty} x(t)\, \mathrm{e}^{-\mathrm{j}\omega t}\, \mathrm{d}t\,, \tag{2.48}$$

with the imaginary unit $\mathrm{j} = \sqrt{-1}$ and the radial frequency $\omega = 2\pi f$. The inverse transform corresponding to (2.48) is

$$x(t) = \mathcal{F}^{-1}\{x(t)\} = \frac{1}{2\pi} \int\limits_{-\infty}^{\infty} \underline{x}(\omega)\, \mathrm{e}^{\mathrm{j}\omega t}\, \mathrm{d}\omega\,. \tag{2.49}$$

The choice of the sign in the exponent as well as the factor before the integral in (2.48) and (2.49) may vary in the literature. The factor $\frac{1}{2\pi}$ may be shifted to the forward Fourier transform or symmetrically applied as $\frac{1}{\sqrt{2\pi}}$ to (2.48) and (2.49). Independent of the convention the relation

$$\mathcal{F}^{-1}\{\mathcal{F}\{x(t)\}\} \equiv x(t) \tag{2.50}$$

must hold.

According to (2.48), the Fourier transform of the time derivative $\frac{\partial}{\partial t}$ is

$$\mathcal{F}\left\{\frac{\partial x(t)}{\partial t}\right\} = -\mathrm{j}\omega \underline{x}(\omega)\,. \tag{2.51}$$

Therefore the inhomogeneous wave equation in the frequency domain, which is commonly known as the inhomogeneous Helmholtz equation, reads as

$$\nabla \cdot \nabla \underline{p}_{\mathrm{a}}(\boldsymbol{x},\omega) + k^2 \underline{p}_{\mathrm{a}}(\boldsymbol{x},\omega) = \underline{\boldsymbol{\mathcal{F}}}(\boldsymbol{x},\omega)\,. \tag{2.52}$$

In (2.52), $k = \omega/c$ denotes the wave number and $\underline{\boldsymbol{\mathcal{F}}}(\boldsymbol{x},\omega)$ represents one frequency component of the source term $\boldsymbol{\mathcal{F}}(\boldsymbol{x},t)$ in (2.36) s.t. [50]

$$\boldsymbol{\mathcal{F}}(\boldsymbol{x},t) = \frac{1}{2\pi}\int\limits_{-\infty}^{\infty} \underline{\boldsymbol{\mathcal{F}}}(\boldsymbol{x},\omega)\,\mathrm{e}^{\mathrm{j}\omega t}\,\mathrm{d}\omega\,. \tag{2.53}$$

The free-field Green's function $g(\boldsymbol{x},\boldsymbol{y},t-\tau)$ in (2.34) can be transformed to the frequency domain. $\underline{g}(\boldsymbol{x},\boldsymbol{y},\omega)$ is given by solving the differential equation (2.52) with $\underline{\boldsymbol{\mathcal{F}}} = \delta(\boldsymbol{x}-\boldsymbol{y})$

$$\nabla \cdot \nabla \underline{g}(\boldsymbol{x},\omega) + k^2 \underline{g}(\boldsymbol{x},\omega) = \delta(\boldsymbol{x}-\boldsymbol{y})$$

or by applying the Fourier transform to (2.34)

$$\begin{aligned}
\underline{g}(\boldsymbol{x},\boldsymbol{y},\omega) &= \int\limits_{-\infty}^{\infty} g(\boldsymbol{x},\boldsymbol{y},t-\tau)\,\mathrm{e}^{-\mathrm{j}\omega(t-\tau)}\,\mathrm{d}(t-\tau) \\
&= \int\limits_{-\infty}^{\infty} \frac{1}{4\pi|\boldsymbol{x}-\boldsymbol{y}|}\,\delta\left(t-\tau-\frac{|\boldsymbol{x}-\boldsymbol{y}|}{c}\right)\mathrm{e}^{-\mathrm{j}\omega(t-\tau)}\,\mathrm{d}(t-\tau) \\
\underline{g}(\boldsymbol{x},\boldsymbol{y},\omega) &= \frac{1}{4\pi|\boldsymbol{x}-\boldsymbol{y}|}\,\mathrm{e}^{\mathrm{j}k|\boldsymbol{x}-\boldsymbol{y}|}\,.
\end{aligned} \tag{2.54}$$

The sound pressure $\underline{p}_{\mathrm{a}}(\boldsymbol{x},\omega)$ generated by a source distribution $\underline{\boldsymbol{\mathcal{F}}}(\boldsymbol{y},\omega)$ can be calculated in the frequency domain analogously to (2.38) via

$$\begin{aligned}
p_{\mathrm{a}}(\boldsymbol{x},\omega) &= \int\limits_{\Omega_{\mathrm{sc}}} \underline{\boldsymbol{\mathcal{F}}}(\boldsymbol{y},\omega)\,\underline{g}(\boldsymbol{x},\boldsymbol{y},\omega)\,\mathrm{d}\boldsymbol{y} \\
&= \frac{1}{4\pi}\int\limits_{\Omega_{\mathrm{sc}}} \underline{\boldsymbol{\mathcal{F}}}(\boldsymbol{y},\omega)\frac{\mathrm{e}^{\mathrm{j}k|\boldsymbol{x}-\boldsymbol{y}|}}{|\boldsymbol{x}-\boldsymbol{y}|}\,\mathrm{d}\boldsymbol{y}\,.
\end{aligned} \tag{2.55}$$

In case of a single monopole source $\underline{\sigma}(\omega)$ located at the point $\boldsymbol{y}_{\mathrm{s}}$ this equation reduces to

$$\underline{p}_{\mathrm{a}}(\boldsymbol{x},\omega) = \underline{\sigma}(\omega)\,\underline{g}(\boldsymbol{x},\boldsymbol{y}_{\mathrm{s}},\omega)\,. \tag{2.56}$$

2.1.5 Near and Far Field

The terms *near field* and *far field* are often used to approximate the solution of a sound field when the observer is near the source or far away. In order to distinguish between these two fields, a pulsating sphere (*breathing sphere*) is considered [47, 59, 60]. This is a spherical source that consists of a solid sphere with radius a, which varies sinusoidally with a small amplitude. Due to the sound pressure being proportional to the reciprocal distance r to the source (cf. (2.32)) and the assumption that the sound wave can expand freely radially, the ansatz for the sound pressure p_a due to the radiating sphere is

$$\underline{p}_\mathrm{a}(r,k) = \frac{\underline{A}(k)}{r}\mathrm{e}^{-\mathrm{j}kr}\,. \tag{2.57}$$

In (2.57), $k = \omega/c$ denotes the wave number, and $\underline{A}(k)$ a not-yet determined amplitude. This amplitude can be calculated via (2.17), which reads in the frequency domain as

$$\mathrm{j}\omega\underline{v}_\mathrm{a} = -\frac{1}{\rho}\nabla p_\mathrm{a}\,. \tag{2.58}$$

In case of the pulsating sphere (2.58) becomes

$$\begin{aligned} \underline{v}_\mathrm{a,n} = \frac{\mathrm{j}}{\omega\rho}\frac{\partial p_\mathrm{a}}{\partial r} &= \frac{\underline{A}}{\rho c}\left(1 - \frac{\mathrm{j}}{kr}\right)\frac{\mathrm{e}^{-\mathrm{j}kr}}{r} \\ &= \frac{\underline{p}_\mathrm{a}}{\rho c}\left(1 - \frac{\mathrm{j}}{kr}\right)\,, \end{aligned} \tag{2.59}$$

and defines the relation between acoustic pressure and particle velocity. The phase relation β between these two properties calculates via

$$\tan\beta = \frac{1}{kr}\,. \tag{2.60}$$

In the near field the following relation holds

$$kr \ll 1, \quad \beta \to \frac{\pi}{2} \tag{2.61}$$

and in the far field

$$kr \gg 1, \quad \beta \to 0\,. \tag{2.62}$$

For $kr \gg 1$, (2.59) results in the plane wave relation between p_a and $\boldsymbol{v}_\mathrm{a}$, see (2.76), where sound pressure and particle velocity are in phase.

With a given normal velocity $\underline{v}_\mathrm{a,n}(a) = \underline{v}_a$ at the surface of the sphere, the amplitude $\underline{A}$ computes to

$$\underline{A} = \frac{\rho c \underline{v}_a a}{1 - \frac{\mathrm{j}}{ka}}\mathrm{e}^{\mathrm{j}ka}\,. \tag{2.63}$$

2.1.6 Compactness of Sources

The wavelength λ of sound emitted by a source distribution at an acoustic frequency f is computed via

$$\lambda = \frac{c}{f} \tag{2.64}$$

with the speed of sound c.

Consider a source distribution for which $\underline{\boldsymbol{\mathcal{F}}}(\boldsymbol{x},\omega) \neq 0$ only within a finite source domain Ω_sc with a characteristic length L. With the dimensionless Helmholtz number

$$He = kL = \frac{L\omega}{c} = \frac{2\pi L}{\lambda} \tag{2.65}$$

the source is called *compact* if

$$He \ll 1\,. \tag{2.66}$$

With the change of variables

$$\bar{x}_i = \frac{x_i}{L} \quad \text{and} \quad \bar{t} = \omega t\,, \tag{2.67}$$

and therefore

$$\frac{\partial}{\partial x_i} = \frac{1}{L}\frac{\partial}{\partial \bar{x}_i} \quad \text{and} \quad \frac{\partial}{\partial t} = \omega \frac{\partial}{\partial \bar{t}}\,,$$

the homogeneous acoustic wave equation (2.22) becomes dimensionless [53]

$$He^2 \frac{\partial^2 p_\mathrm{a}}{\partial \bar{t}^2} - \nabla_{\bar{x}} \cdot \nabla_{\bar{x}} p_\mathrm{a} = 0\,, \tag{2.68}$$

with

$$\nabla_{\bar{x}} = \begin{bmatrix} \partial/\partial \bar{x}_1 \\ \partial/\partial \bar{x}_2 \\ \partial/\partial \bar{x}_3 \end{bmatrix}.$$

If – due to the values of ω and L – the spacial and time derivatives $\nabla_{\bar{x}}^2$ and $\frac{\partial^2 p_\mathrm{a}}{\partial \bar{t}^2}$ are in the same order of magnitude, the character of the wave propagation can be described by the Helmholtz number. In compact regions, the time derivative may be neglected due to the multiplication with $He \ll 1$, and the dimensionless wave equation can be approximated with Laplace's equation

$$\nabla^2 p_\mathrm{a} = 0\,. \tag{2.69}$$

If the pulsating sphere described in Sec. 2.1.5 can be considered as compact, i. e. $He = ka \ll 1$, in (2.63) 1 can be neglected compared to $\frac{\mathrm{j}}{ka}$ in the denominator, and the amplitude is approximately given by

$$\underline{A}_\mathrm{c} \approx \mathrm{j}\omega\rho\underline{v}_a a^2 \mathrm{e}^{\mathrm{j}ka}\,. \tag{2.70}$$

Inserting (2.70) into (2.59) yields in case of a compact sphere

$$\underline{p}_{\mathrm{a,c}}(r,k) = \mathrm{j}\omega v_a \rho a^2 \frac{\mathrm{e}^{-\mathrm{j}k(r-a)}}{r}\,. \tag{2.71}$$

If the sphere is non-compact, the amplitude is

$$\underline{A}_\mathrm{nc} \approx \underline{v}_a \rho c a \mathrm{e}^{\mathrm{j}ka} \tag{2.72}$$

and the sound pressure becomes [51]

$$\underline{p}_{\mathrm{a,nc}}(r,k) = \underline{v}_a \rho c a \frac{\mathrm{e}^{-\mathrm{j}k(r-a)}}{r}\,. \tag{2.73}$$

Comparing (2.71) and (2.73) shows that the pressure emitted by a compact sphere is smaller by a factor of $\omega a/c$ – with $\omega a/c \ll 1$ in the compact case – compared to the non-compact case. Moreover, the sound radiated by a compact source increases with increasing frequencies which is a behavior that is not shown by non-compact spheres.

2.1.7 Sound Propagation

Up to now, all equations calculating the sound pressure assumed free-field radiation. This section will discuss sound propagation with phenomena such as reflection and attenuation.

Plane waves

Tho homogeneous one-dimensional wave equation reads as [50, 51, 59, 60]

$$\frac{1}{c^2}\frac{\partial^2 p_\mathrm{a}}{\partial t^2} - \frac{\partial^2 p_\mathrm{a}}{\partial x^2} = 0\,. \tag{2.74}$$

Solutions of (2.74) are of the form

$$p_\mathrm{a}(x,t) = f_1(t - x/c) + f_2(t + x/c) = f_3(x - ct) + f_4(x + ct)\,, \tag{2.75}$$

where f_i denote functions that must fulfill boundary and initial conditions but are arbitrary otherwise. Comparing (2.75) to the general solution of the three-dimensional wave equation, one can see that – in contrast to (2.32) – there is no change in amplitude with increasing or decreasing values for x. It has to be mentioned that plane waves only occur in limited cases, e. g. in ducts with sound-hard ($\boldsymbol{v}_\mathrm{a} \cdot \boldsymbol{n} = 0$) walls and when the wavelength is large compared to the duct diameter [47, 50]. Further, in regions without obstacles, a spherical wave can be locally approximated by a plane wave in the far field, see (2.59) for $kr \gg 1$. With (2.17), the acoustic particle velocity in case of a plane wave is given by

$$v_\mathrm{a} = \frac{1}{\rho c} p_\mathrm{a}\,. \tag{2.76}$$

The factor

$$Z_0 = \rho c \tag{2.77}$$

is called *characteristic impedance*, which is real-valued and constant in case of plane waves.

Impedance

In general, the specific impedance $\underline{Z}_\mathrm{s}$ is defined as the complex-valued ratio between the acoustic pressure and the normal component of the acoustic particle velocity in frequency domain

$$\underline{Z}_\mathrm{s}(\boldsymbol{x},\omega) = \frac{\underline{p}_\mathrm{a}(\boldsymbol{x},\omega)}{\underline{\boldsymbol{v}}_\mathrm{a}(\boldsymbol{x},\omega)\cdot\boldsymbol{n}(\boldsymbol{x})}\,, \tag{2.78}$$

defined at a point $\boldsymbol{x}$ on a surface with normal vector $\boldsymbol{n}$. $\mathrm{Re}\{\underline{Z}_\mathrm{s}\}$ is called *resistance* and $\mathrm{Im}\{\underline{Z}_\mathrm{s}\}$ is called *reactance*.

In general, the acoustic impedance $\underline{Z}_\mathrm{s}$ is not a property of the surface alone since it also depends on the acoustic field. If this is not the case, i. e. the surface's response to an excitation is linear and pointwise, the surface is called *locally reacting* [53]. In this particular case, the impedance is solely a property of the surface.

Transmission

In the one-dimensional case of a plane wave impinging at a partially reflecting surface with complex-valued impedance $\underline{Z}_\mathrm{s}$ at an arbitrary angle θ_i, see Fig. 2.1, the acoustic pressure can be described according to (2.75), where the total acoustic pressure consists of the incident and reflected plane waves. The incident and reflected wavefronts have normal vectors $\boldsymbol{n}_\mathrm{i}$ and $\boldsymbol{n}_\mathrm{r}$, respectively. The total sound pressure can be written as [47, 60]

$$\underline{p}_\mathrm{a} = \underline{f}_1 \mathrm{e}^{-\mathrm{j}k_x x}\left(\mathrm{e}^{-\mathrm{j}k_y y} + \underline{r}(\theta_\mathrm{i},\omega)\,\mathrm{e}^{\mathrm{j}k_y y}\right)\,, \tag{2.79}$$

with

$$k_x = \frac{\omega}{c}\sin\theta_\mathrm{i}\,, \qquad k_y = \frac{\omega}{c}\cos\theta_\mathrm{i} \tag{2.80}$$

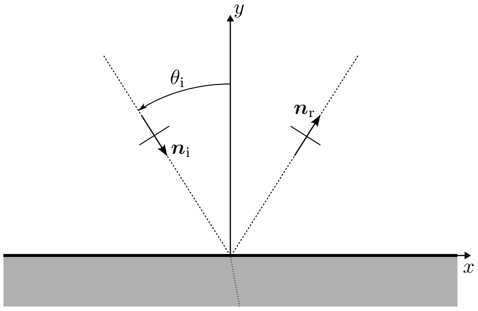

Figure 2.1: Plane wave impinging at an angle θ_i at a partially reflecting surface with impedance $\underline{Z}_\mathrm{s}$.

and the reflection coefficient

$$\underline{r}(\theta_\mathrm{i}, \omega) = \frac{\underline{f}_2}{\underline{f}_1}\,. \tag{2.81}$$

From (2.58) multiplied with the unit vector $\boldsymbol{e}_y$ in y-direction and (2.80) follows

$$\underline{v}_y = \frac{\cos\theta_\mathrm{i}}{\rho c}\underline{f}_1 \mathrm{e}^{-\mathrm{j}k_x x}\left(-\mathrm{e}^{-\mathrm{j}k_y y} + \underline{r}(\theta_\mathrm{i}, \omega)\,\mathrm{e}^{\mathrm{j}k_y y}\right)\,. \tag{2.82}$$

Dividing (2.79) by (2.82) yields together with (2.78), evaluated at $y = 0$, the expression for the reflection coefficient

$$\underline{r}(\theta_\mathrm{i}, \omega) = \frac{\underline{Z}_\mathrm{s}\cos\theta_\mathrm{i} - Z_0}{\underline{Z}_\mathrm{s}\cos\theta_\mathrm{i} + Z_0} = \frac{\underline{\zeta}_\mathrm{s}\cos\theta_\mathrm{i} - 1}{\underline{\zeta}_\mathrm{s}\cos\theta_\mathrm{i} + 1}\,. \tag{2.83}$$

In (2.83), $\underline{\zeta}_\mathrm{s}$ denotes the ratio of specific acoustic impedance and characteristic impedance

$$\underline{\zeta}_\mathrm{s}(\omega) = \frac{\underline{Z}_\mathrm{s}(\omega)}{Z_0}\,. \tag{2.84}$$

The magnitude of $\underline{r}$ is

$$|\underline{r}| < 1 \quad \text{for} \quad \mathrm{Re}\{\underline{Z}_\mathrm{s}\} > 0\,.$$

For the time-averaged acoustic energy $E_\mathrm{i,avg}$ of the incident wave the following applies

$$\begin{aligned} E_\mathrm{i,avg} &= \frac{1}{2}\mathrm{Re}\{-\underline{p}\bar{\underline{v}}_y\} \\ &= E_\mathrm{r,avg} + E_\mathrm{a,avg}\,, \end{aligned} \tag{2.85}$$

where $E_\mathrm{r,avg}$ and $E_\mathrm{a,avg}$ denote the reflected and absorbed time-averaged acoustic energy, respectively. Therefore, the absorption coefficient α is defined as

$$\alpha = 1 - |\underline{r}|^2 = 1 - r_\mathrm{E} \tag{2.86}$$

and is equivalent to the fraction of the incident acoustic energy that is absorbed.

Dependent on the characteristics of the surface, the following can be concluded at $y = 0$

- Fully reflecting (*rigid* or *sound-hard*) surface: $\underline{Z}_\mathrm{s} \to \infty,\ \underline{r} = 1,\ \alpha = 0,\ v_{\mathrm{a},y} = 0$
- Fully absorbing surface: $\underline{Z}_\mathrm{s}\cos\theta_\mathrm{i} = Z_0,\ \underline{r} = 0,\ \alpha = 1$
- Pressure-release surface: $\underline{Z}_\mathrm{s} \to 0,\ \underline{r} = -1,\ \alpha = 0,\ p_\mathrm{a} = 0$

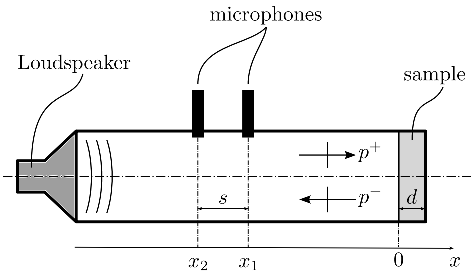

Figure 2.2: Sketch of an impedance tube with two microphones; adapted from [67].

2.1.8 Standing Wave Impedance Tube

Tubes with cylindrical or rectangular cross-sections can be used to determine a sample's acoustic impedance and other related acoustic properties, see Fig. 2.2. The sample of width d is placed inside a tube with rigid walls and a sound-hard termination at $x = d$. Standardized methods use two or four microphones [61, 62, 63, 64]. Further, a method for a similar setup using a single axially movable microphone can be found in [65]. The tube is usually excited with a loudspeaker. In order to restrict the sound field inside the tube to plane waves, an upper frequency limit f_u exists. For circular tubes, this limit is defined as [47, 61, 66]

$$f_\mathrm{u} < \frac{1.841}{\pi}\frac{c}{d_\mathrm{t}}\,, \tag{2.87}$$

with the inner impedance tube diameter d_t, and for rectangular tubes, it is

$$f_\mathrm{u} < \frac{1}{2}\frac{c}{l_\mathrm{max}}\,, \tag{2.88}$$

where l_max denotes the maximum length of the rectangular cross-section.

Since the two-microphone method is used in this thesis, the fundamentals will only deal with this method. The two-microphone method works for transient, harmonic, and stationary-random excitation signals. Due to efficiency, usually, a broadband random signal such as white noise is used.

According to (2.79), with $\theta = 0$ due to (2.87), the pressure along the axis of the duct may be written as

$$\underline{p}_\mathrm{a}(x,\omega) = \underline{p}^+\left(\mathrm{e}^{-\mathrm{j}kx} + \underline{r}\,\mathrm{e}^{\mathrm{j}kx}\right)\,, \qquad \underline{r} = \frac{\underline{p}^-}{\underline{p}^+}\,, \tag{2.89}$$

where $\underline{p}^+$ denotes the incident and $\underline{p}^-$ the reflected wave's amplitude. Therefore, the acoustic pressure at the microphones 1 and 2 is given by

$$\underline{p}_{\mathrm{a},1}(k) = \underline{p}^+\left(\mathrm{e}^{-\mathrm{j}kx_1} + \underline{r}\,\mathrm{e}^{\mathrm{j}kx_1}\right) \tag{2.90}$$

$$\underline{p}_{\mathrm{a},2}(k) = \underline{p}^+\left(\mathrm{e}^{-\mathrm{j}k(x_1+s)} + \underline{r}\,\mathrm{e}^{\mathrm{j}k(x_1+s)}\right)\,. \tag{2.91}$$

Dividing (2.91) by (2.90) and solving for $\underline{r}$ yields

$$\underline{r}(k) = \mathrm{e}^{-\mathrm{j}kx_1}\frac{\mathrm{e}^{-\mathrm{j}ks} - \underline{H}_{21}}{\underline{H}_{21} - \mathrm{e}^{\mathrm{j}ks}}\,, \tag{2.92}$$

where $\underline{H}_{21} = \frac{\underline{p}_2}{\underline{p}_1}$ is the complex-valued transfer function between the Fourier transforms of the microphone signals.

The distance s between the two microphones must fulfill [64]

$$s < 0.45\frac{c}{f_{\mathrm{u}}} \tag{2.93}$$

$$s > 0.05\frac{c}{f_{\mathrm{l}}}\,. \tag{2.94}$$

(2.93) must hold in order for (2.90) being linearly independent of (2.91) [68]. Combining (2.87) and (2.93) yields

$$s < 0.85 d_{\mathrm{t}}\,. \tag{2.95}$$

From (2.89) and (2.17), the two-port network equations can be derived [55]. With this set of equations the acoustic pressure $\underline{p}_{\mathrm{a},x_1}$ and normal particle velocity $\underline{v}_{\mathrm{a},x_1}$ at an arbitrary position $x_2 = x_1 + h$ in simple ducts under plane wave conditions can be calculated from the given values at the position x_1 via

$$\begin{bmatrix} \underline{p}_{\mathrm{a},x_2} \\ \underline{v}_{\mathrm{a},x_2} \end{bmatrix} = \boldsymbol{T} \begin{bmatrix} \underline{p}_{\mathrm{a},x_1} \\ \underline{v}_{\mathrm{a},x_1} \end{bmatrix} \tag{2.96}$$

with the transfer matrix $\boldsymbol{T}$

$$\boldsymbol{T} = \begin{bmatrix} \cos kh & \mathrm{j}\omega\frac{\varrho}{k}\sin kh \\ \mathrm{j}\frac{k}{\omega\varrho}\sin kh & \cos kh \end{bmatrix}\,. \tag{2.97}$$

2.1.9 Weak Formulation

The weak formulation of the Helmholtz equation (2.52) is derived by multiplying with a suitable, complex-valued test function $\underline{w} \in W$, with an appropriate function space W, and integrating over the computational domain Ω

$$\int\limits_{\Omega} \left(\overline{\underline{w}} \nabla \cdot \nabla \underline{p}_{\mathrm{a}} + k^2 \overline{\underline{w}}\,\underline{p}_{\mathrm{a}} \right) \mathrm{d}\boldsymbol{x} = \int\limits_{\Omega} \underline{\boldsymbol{\mathcal{F}}}\,\overline{\underline{w}}\,\mathrm{d}\boldsymbol{x}\,, \tag{2.98}$$

with $\overline{\underline{w}} = w_{\mathrm{Re}} - \mathrm{j}w_{\mathrm{Im}}$ denoting the conjugate complex of the test function. Applying Green's first integration theorem, which states that

$$\int\limits_{\Omega} \left(U_1 \nabla \cdot \nabla U_2 + \nabla U_1 \cdot \nabla U_2 \right) \mathrm{d}\boldsymbol{x} = \int\limits_{\partial\Omega} U_1 \nabla U_2 \cdot \mathrm{d}\boldsymbol{s}\,, \tag{2.99}$$

where U_1 and U_2 are scalar field functions, yields

$$\int\limits_{\Omega} \left(\overline{\underline{w}} k^2 \underline{p}_{\mathrm{a}} - \nabla \underline{p}_{\mathrm{a}} \cdot \nabla \overline{\underline{w}} \right) \mathrm{d}\boldsymbol{x} = \int\limits_{\Omega} \overline{\underline{w}}\,\underline{\boldsymbol{\mathcal{F}}}\,\mathrm{d}\boldsymbol{x} - \int\limits_{\partial\Omega} \overline{\underline{w}} \nabla \underline{p}_{\mathrm{a}} \cdot \mathrm{d}\boldsymbol{s} \qquad \forall \underline{w} \in W. \tag{2.100}$$

An oscillating surface with given amplitude $\underline{v}_{\mathrm{mech},n}$ in normal direction can be very efficiently modeled with the framework of the weak formulation. Due to (2.46) and (2.20), the surface term in (2.100) can be expressed as

$$-\int\limits_{\partial\Omega} \overline{\underline{w}} \nabla \underline{p}_{\mathrm{a}} \cdot \boldsymbol{n}\,\mathrm{d}s = \int\limits_{\partial\Omega} \overline{\underline{w}}\,\mathrm{j}\omega\rho_0 \underline{v}_{\mathrm{a},n}\,\mathrm{d}s\,. \tag{2.101}$$

2.2 Inverse Problems

Inverse problems are usually defined as being the inverse of a *direct* or *forward* problem [69, 70]. This section covers the mathematical basics of inverse problems and possibilities of their regularization.

2.2.1 Basics

Generally speaking, forward problems determine the effects w of given causes u and a well-defined mathematical model A. The effects w are then defined as $A(u) = w$. An inverse problem, however, usually aims to determine the causes u with given effects w. Another type of inverse problem is the model identification, where u and w are given and A is to be determined. Regarding the acoustic wave equation, the forward problem is to solve for the acoustic pressure or velocity potential with a given source distribution, and the inverse problem is to identify the source distribution for a given sound pressure field.

Inverse problems are often not well-posed in the sense of Hadamard [71, 72].

Definition 2.2.1:
$A : \mathbb{U} \subseteq X \to \mathbb{W} \subseteq Y$ is a mapping between the vector spaces X and Y. The inverse problem of solving the equation

$$A(u) = w, \quad u \in \mathbb{U}, \quad w \in \mathbb{W}, \tag{2.102}$$

with respect to u for given w is called well-posed *or* properly posed *if*

(a) a solution $u \in \mathbb{U}$ exists for all $w \in \mathbb{W}$;

(b) the solution is unique;

(c) the inverse function $T^{-1} : \mathbb{W} \to \mathbb{U}$ is continuous.

Otherwise, the inverse problem is considered ill-posed.

The first of Hadamard's criteria, (a), is usually satisfied for parameter identification problems. The second criterion is crucial, as it the given data w must be sufficient for identifying the searched-for parameters u uniquely. This, however, is often difficult to prove, especially for large unstructured ODE models [73]. If the second condition is not met, additional information (*a priori* information) is required. The last requirement of well-posedness according to Hadamard is often not provided in inverse problems, as they are often not stable. Small perturbations in the given data can lead to significant deviations in the result. Thus, the inverse operator is not continuous. Therefore, inverse problems usually require regularization. Illustrative examples of how small perturbations can have substantial impacts on the quality of the solutions of inverse problems can be found e. g. in [58, 70].

If any of Hadamard's conditions are not fulfilled, the problem is considered *ill-posed.*

2.2.2 Regularization

To overcome the restrictions of ill-posed problems, inverse problems are often regularized. The regularization used for the inverse scheme for sound source localization presented in this thesis is the Tikhonov regularization.

Parameter identification problems can most often be formulated as an operator equation according to (2.102), with the continuous operator $A : \mathcal{D}(A) \subset \mathbb{U} \to \mathbb{W}$ with domain $\mathcal{D}(A) \subset \mathbb{U}$, $\mathbb{U}$ and $\mathbb{W}$ being real Hilbert spaces. Since w is often given as measurements, which are usually noisy, the noisy data w^δ is assumed to be given as

$$\|w^\delta - w\| \leq \delta \,. \tag{2.103}$$

Tikhonov regularization of (2.102) leads to the minimization problem

$$\min_{u \in \mathcal{D}(A)} \|A(u) - w^\delta\|^2 + \alpha_\mathrm{r} \|u - u_0\|^2 \,, \tag{2.104}$$

with a penalty factor α_r and an initial guess u_0 for the exact solution $u^\dagger$. In a general non-linear case (2.104) is not guaranteed to have a solution and, therefore, additional assumptions on the operator A may be required. Additionally, even if (2.104) has a unique solution for $\alpha = 0$ there may be more than one global minimizer for $\alpha > 0$. In some cases, such as the inverse scheme for sound source localization presented in Chap. 5, it might be useful to use different penalty terms. [73]

2.3 Optimization

A comprehensible introduction to optimization and its numerical methods can be found in [74] and [75], on which this section is based. Optimization seeks to minimize an *objective function* (or *cost function*, *fitness function*) $J(\boldsymbol{x})$

$$\min_{\boldsymbol{x}\in\mathbb{R}^n} J(\boldsymbol{x})\,, \tag{2.105}$$

where $J : \mathbb{R}^n \to \mathbb{R}$ is a smooth function. While (2.105) is an unconstrained problem, the constrained problem reads as

$$\min_{\boldsymbol{x}\in\mathbb{R}^n} J(\boldsymbol{x}) \quad \text{s. t.} \tag{2.106a}$$

$$c_i(\boldsymbol{x}) = 0, \quad i = 1, \ldots, N_\mathrm{e}; \tag{2.106b}$$

$$c_j(\boldsymbol{x}) \geq 0, \quad j = 1, \ldots, N_\mathrm{i}\,, \tag{2.106c}$$

with N_e equality constraints c_i and N_i inequality constraints c_j. The domain $\mathcal{S}$, which contains all points that satisfy all equality and inequality constraints, is called the *feasible domain*. It is defined via

$$\mathcal{S} = \{\boldsymbol{x} \mid c_i(\boldsymbol{x}) = 0,\, i = 1, \ldots, N_\mathrm{e};\; c_j(\boldsymbol{x}) \geq 0,\, j = 1, \ldots, N_\mathrm{i}\}\,. \tag{2.107}$$

Therefore, we can rewrite (2.106) as

$$\min_{\boldsymbol{x}\in\mathcal{S}} J(\boldsymbol{x})\,. \tag{2.108}$$

A global minimizer $\boldsymbol{x}^*$ of the unconstrained problem (2.105) satisfies

$$J(\boldsymbol{x}^*) \leq J(\boldsymbol{x}) \;\forall\; x \in \mathbb{R}^n\,. \tag{2.109}$$

The point $\boldsymbol{x}^*$ is called a *weak* local minimizer if there is an open set $\mathcal{N}$ that contains $\boldsymbol{x}^*$ s. t.

$$J(\boldsymbol{x}^*) \leq J(\boldsymbol{x}) \;\forall\; x \in \mathcal{N} \tag{2.110}$$

and a *strict* or *strong* minimizer if

$$J(\boldsymbol{x}^*) < J(\boldsymbol{x}) \;\forall\; x \in \mathcal{N}\,. \tag{2.111}$$

In case of an unconstrained problem and if $J(\boldsymbol{x})$ is twice continuously differentiable, the necessary conditions for a local minimizer are

$$\begin{aligned} \nabla J(\boldsymbol{x}^*) &= 0 \\ \nabla^2 J(\boldsymbol{x}^*) &\text{ is positive semidefinite.} \end{aligned} \tag{2.112}$$

Sufficient conditions for a strong local minimizer in the unconstrained case are

$$\begin{aligned} \nabla J(\boldsymbol{x}^*) &= 0 \\ \nabla^2 J(\boldsymbol{x}^*) &\text{ is positive definite.} \end{aligned} \tag{2.113}$$

In the constrained case, we define the Lagrangian function $\mathcal{L}(\boldsymbol{x}, \boldsymbol{\lambda})$, with the Lagrange multiplier vector $\boldsymbol{\lambda}$, for the general problem (2.106) as

$$\mathcal{L}(\boldsymbol{x}, \boldsymbol{\lambda}) = J(\boldsymbol{x}) - \sum_{k=1}^{N^\mathrm{e}+N^\mathrm{i}} \lambda_k c_k(\boldsymbol{x})\,. \tag{2.114}$$

The first-order necessary conditions, also known as *Karush-Kuhn-Tucker* conditions, state that

$$
\begin{aligned}
\nabla \mathcal{L}(\boldsymbol{x}^*, \boldsymbol{\lambda}^*) &= 0 && (2.115a)\\
c_i(\boldsymbol{x}^*) &= 0, \quad i = 1, \ldots, N_\mathrm{e} && (2.115b)\\
c_j(\boldsymbol{x}^*) &\geq 0, \quad j = 1, \ldots, N_\mathrm{i} && (2.115c)\\
\lambda_j^* &\geq 0, \quad j = 1, \ldots, N_\mathrm{i} && (2.115d)\\
\lambda_k^* c_k(\boldsymbol{x}^*) &= 0, \quad k = 1, \ldots, N_\mathrm{e} + N_\mathrm{i}\,. && (2.115e)
\end{aligned}
$$

In (2.115), $\boldsymbol{x}^*$ is a local solution of (2.106), J and c_i are continuously differentiable and the linear independence constraint qualification [74] holds. Any $(\boldsymbol{x}^*, \boldsymbol{\lambda}^*)$ fulfilling (2.115) is called a *Karush-Kuhn-Tucker* point [76].

2.3.1 Gradient Based Optimization

All algorithms for minimization problems require an estimate $\boldsymbol{x}_0$ of the minimizer. From this starting point, the algorithms iteratively search for better solutions $\boldsymbol{x}_k$ in the direction of descent of the cost function from the previous solution. The iteration is terminated when either the value of the cost function does not improve sufficiently or the first condition in (2.112) is sufficiently met.

One important category of algorithms is the line search strategy, which searches for the new iterate $\boldsymbol{x}_i$ along a direction $\boldsymbol{p}_i$ with a certain step length t_i

$$\boldsymbol{x}_i = \boldsymbol{x}_{i-1} + t_i \boldsymbol{p}_i\,. \tag{2.116}$$

For the choice of the direction, there exist several methods, e. g. the *steepest descent method* where

$$\boldsymbol{p}_i = -\nabla J_i \tag{2.117}$$

and, therefore, no calculation of second-order derivatives are required. Another well-known method is *Newton's Method* where

$$\boldsymbol{p}_i = -(\nabla^2 J_i)^{-1} \nabla J_i\,. \tag{2.118}$$

The optimal value of the step size can be found by solving

$$\min_{t>0} J(x_i + t\boldsymbol{p}_i)\,, \tag{2.119}$$

although finding the exact solution of (2.119) may be expensive. Therefore, a different approach is often used such as *Armijo Rule*, which is a modification to the successive step size reduction and eliminates its possible convergence difficulties. Armijo's rule introduces fixed scalars ξ and β_l with $0 < \xi < 1$ and $0 < \beta_\mathrm{l} < 1$. The step size is set $t_i = \beta_\mathrm{l}^{m_i} t$, where m_i is the first nonnegative integer for which the following inequality applies [74, 77]

$$J(x_i) - J(x_i + \beta_\mathrm{l}^m t \boldsymbol{p}_i) \geq -\xi \beta_\mathrm{l}^m t \, \nabla J(x_i)^\mathsf{T} \boldsymbol{p}_i\,. \tag{2.120}$$

The factor ξ is typically chosen close to zero, e. g. $10^{-5} \leq \xi \leq 10^{-1}$, and the reduction factor $0.1 \leq \beta_\mathrm{l} \leq 0.5$. Other step size selection methods are the *Goldstein rule*, *constant step size*, *diminishing step size*, *Wolfe conditions* and *strong Wolfe conditions* [74, 77].

The general structure of the line search method is shown in Fig. 2.3.

Since the derivatives are not always available, other methods approximate the gradient. Two of the most common methods are *Finite Differencing* and *Automatic Differentiation*, see e. g. [74]. The Inverse Scheme for sound localization presented in Chap. 5 uses the adjoint method for calculation of the gradient.

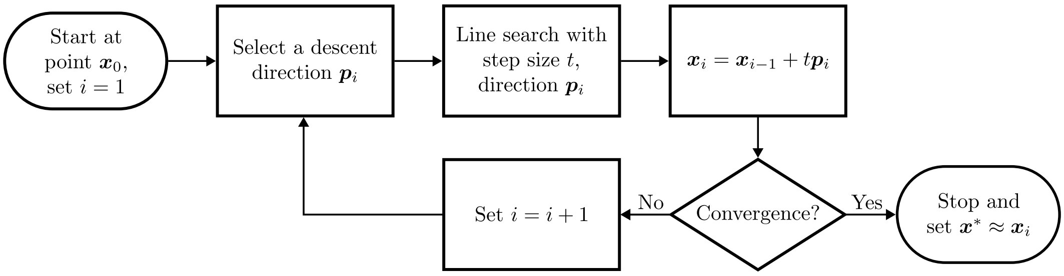

Figure 2.3: General structure of a line search method, adapted from [75].

2.3.2 Gradient Free Optimization

If the computation or approximation of the gradient is not feasible, another approach for solving the minimization problem is derivative-free optimization (DFO) algorithms. DFO methods can easily handle simple constraints such as bounds. An overview of general constraints can be found in [78]. The genetic-based optimization algorithm is a DFO method and is categorized as a meta-heuristic algorithm. It was used in this thesis in Sec. 4.1.4 and shall therefore be considered in more detail.

According to [79] genetic algorithms (GAs) have the following in common: they start with a randomly chosen set (*population*) of parameters (*chromosomes*), that represent a possible solution of the optimization problem. A new generation is obtained via genetics-inspired operators of selection, crossover and mutation. This process is repeated until a suitable solution to the optimization problem is found.

The typical steps of a GA are as follows [79]

1. Select a random population of n chromosomes. This step is similar to selecting an estimate $\boldsymbol{x}_0$ described in Sec. 2.3.1.
2. Calculate the fitness of each chromosome, i. e. evaluation of the objective function $J(\boldsymbol{x})$. If convergence is reached, the iteration is stopped.
3. Create n children from the current population with the following steps
   a *Selection* of a pair (or sometimes also a group) of parent chromosomes from current population where the probability of selection is a function of fitness. There are several approaches concerning the selection, e. g. *truncation selection*, *tournament selection* or *fitness proportionate selection*, see [80].
   b *Crossover*: The parent chromosomes are combined to form two children. The crossover can be a *single-point crossover*, a *two-point crossover* or a *uniform crossover*, see Fig. 2.4
   c *Mutation*: The two children's chromosomes are modified to find solutions that were not present in either of the parents. Usually, these modifications only represent minor changes to the chromosomes in order to find results in the neighborhood of
4. Repeat step 2 with the new population.

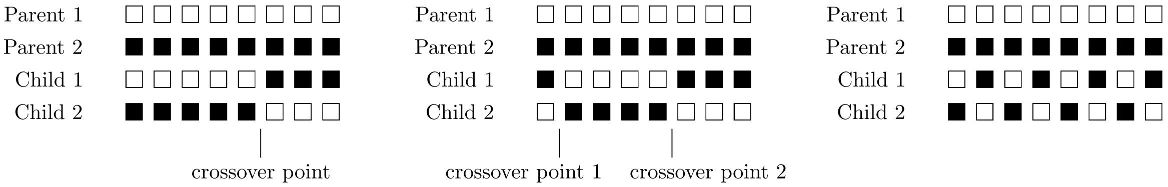

(a) Single-point crossover.

(b) Two-point crossover.

(c) Uniform crossover.

Figure 2.4: Visualization of different crossover schemes in genetic algorithms; adapted from [80].

CHAPTER 3

Established Methods for Sound Source Localization

3.1 Beamforming

Acoustic beamforming is a technique used to localize sound sources within a predefined search area using microphone array measurements. The microphone positions and all points within the search area have to be known. Moreover, the microphone signals have to be recorded simultaneously. Beamforming may be used in the time domain, where it is commonly called *Delay-and-Sum* (DAS), as well as in the frequency domain. The fundamentals of the beamforming method is easiest understood in the time domain.

3.1.1 Delay-and-Sum

Consider an acoustic source $\sigma(t)$ located at $\boldsymbol{y}^0$. M distributed microphones measure the sound emitted by $\sigma(t)$. The signal $y_m(t)$ measured by the mth microphone at location $\boldsymbol{x}_m$ is then delayed by $\Delta_{m\mathrm{f}}$ and summed. Therefore, the beamformer's output $z(t)$ is given by [81, 82]

$$z(t) = \sum_{m=1}^{M} w_m y_m(t - \Delta_{m\mathrm{f}}), \tag{3.1}$$

where w_m is the weight of the mth microphone and may be used to reduce the sidelobe's level. The delays $\Delta_{m\mathrm{f}}$ can be adjusted to focus the "beam" of the array to the source's position. The search area is denoted by Ω_f.

Beamforming for Spherical Waves

The sound pressure at microphone position $\boldsymbol{x}_m$ due to an acoustic monopole with amplitude $\sigma(t)$ located at $\boldsymbol{y}^0$ is given by (see (2.40))

$$p_\mathrm{a}(\boldsymbol{x}_m, \boldsymbol{y}^0, t) = \frac{\sigma(t - r_m^0/c)}{4\pi r_m^0}, \quad r_m^0 = |\boldsymbol{x}_m - \boldsymbol{y}^0|\,. \tag{3.2}$$

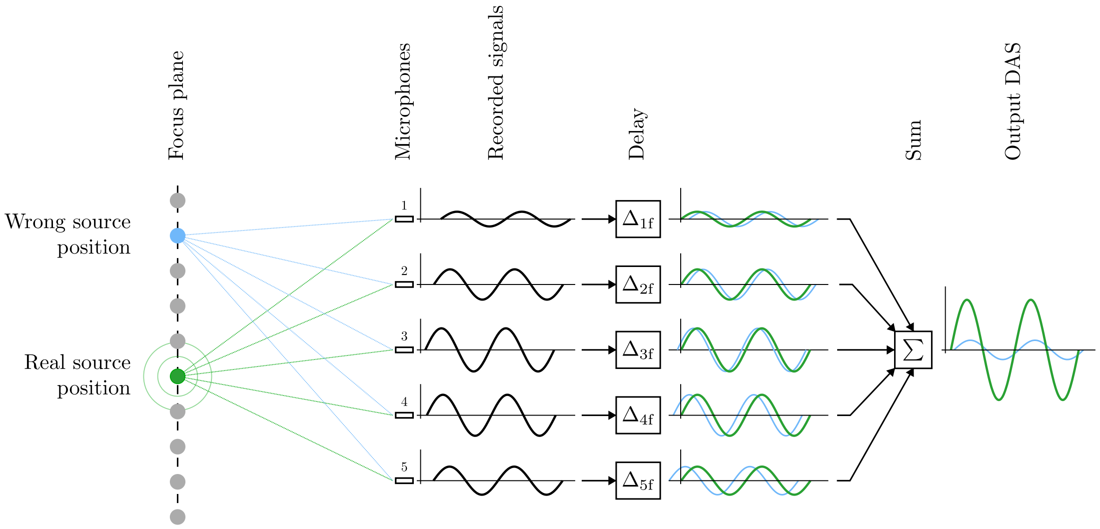

Figure 3.1: Schematic explanation of Delay-and-Sum beamforming in time domain, adapted from [81, 83].

The so-called phase center $\boldsymbol{\xi}^0$ is defined by $\boldsymbol{\xi}^0 = \sum_{m=1}^{M} \boldsymbol{x}_m$ and is chosen to coincide with the origin of the coordinate system. Due to (3.2) the delay is chosen

$$\Delta_{m\mathrm{f}} = \frac{r_\mathrm{f} - r_{m\mathrm{f}}}{c} \,, \tag{3.3}$$

where $r_{m\mathrm{f}} = |\boldsymbol{x}_m - \boldsymbol{y}_\mathrm{f}|$ denotes the distance between an assumed source position within Ω_f and the mth microphone and $r_\mathrm{f} = |\boldsymbol{y}_\mathrm{f}|$. The beamformer's output, in the general case, computes to

$$z(t) = \frac{1}{4\pi} \sum_{m=1}^{M} \frac{w_m}{r_m^0} \sigma \left(t - \frac{r_\mathrm{f} - (r_m^0 - r_{m\mathrm{f}})}{c} \right) . \tag{3.4}$$

In the special case of $\boldsymbol{y}_\mathrm{f} = \boldsymbol{y}^0$, the output $z(t)$ reaches a maximum since assumed and measured delays match

$$z(t) = \frac{1}{4\pi} \sigma \left(t - \frac{r^0}{c} \right) \sum_{m=1}^{M} \frac{w_m}{r_m^0} . \tag{3.5}$$

The DAS algorithms can be visualized in a simple 2D example, see Fig. 3.1. The actual source position is depicted in green. The sound emitted by this source is recorded with the five microphones arranged in a line array. Microphones that are farther away receive the signal at a later point in time and with a lower amplitude than the microphones near the source. The received signals are delayed and scaled in amplitude for each point on the focus grid, depicted in grey. The delay and scaling are adjusted for each focus point as if the source was at the assumed point. After applying the delay, the signals are summed. If the assumed and actual source positions coincide (green), a maximum value of the DAS output is reached. If the assumed source position is wrong (blue), the value of the DAS output is lower. A similar approach, involving the filtering of the microphone signals in order to focus the sound source localization to a certain frequency band, to reduce unwanted noise and to avoid aliasing, is called *Filter-and-Sum* Beamforming [81].

3.1.2 Frequency Domain Beamforming

The previously described DAS Beamforming in the time domain can be carried out in the frequency domain. This is commonly called *Conventional Beamforming* (ConvBF or CBF) or *Frequency Domain Beamforming* (FDBF). It can either be derived by summing the short-time frequency spectra of (3.4) or by minimizing a functional comparing an acoustic source model in the frequency domain with the measured and Fourier-transformed microphone signals. The latter derivation shall be summarized here.

Each microphone signal $p_{\mathrm{a},m}(t)$ is transformed to the frequency domain, noted by $\underline{p}_{\mathrm{a},m}(\omega)$. Subsequently, the cross-spectral matrix (CSM) $\underline{\boldsymbol{C}}(\omega)$ of measured pressures can be computed by

$$\underline{\boldsymbol{C}}(\omega) = \underline{\boldsymbol{p}}_{\mathrm{a}}\underline{\boldsymbol{p}}_{\mathrm{a}}^{\mathrm{H}}, \quad \underline{\boldsymbol{p}}_{\mathrm{a}}(\omega) = \begin{bmatrix} \underline{p}_{\mathrm{a},1}(\omega) \\ \vdots \\ \underline{p}_{\mathrm{a},m}(\omega) \\ \vdots \\ \underline{p}_{\mathrm{a},M}(\omega) \end{bmatrix}, \tag{3.6}$$

where $(\underline{\boldsymbol{A}}_{i,j})^{\mathrm{H}} = \bar{\underline{\boldsymbol{A}}}_{j,i}$ denotes the Hermitian (conjugate transpose). Thus, the CSM contains the cross-correlation of the microphone pressures, which becomes the auto-correlation in the main diagonal. Since the auto-correlations do not provide information about the phase differences between two microphone positions but may contain noise from measurements, in practice, the main diagonal of the CSM is commonly set to zero [84]. The CSM is usually estimated from measurements using Welch's method [85], where the measured microphone signals are split into N equal blocks that are multiplied with a suitable window function, and a Fast Fourier transform (FFT) is applied. The blocks are subsequently averaged, and the estimation for the CSM reads as

$$\mathbb{E}\left[\underline{\boldsymbol{C}}(\omega)\right] = \frac{1}{N}\sum_{i=1}^{N} \underline{\boldsymbol{p}}_{\mathrm{a},i}\underline{\boldsymbol{p}}_{\mathrm{a},i}^{\mathrm{H}}. \tag{3.7}$$

As an acoustic source model, again, the acoustic monopole is used. Therefore, the acoustic pressure due to a single monopole source at an assumed source position $\boldsymbol{y}_{\mathrm{f}}$ can be computed with Green's function $\underline{g}(\omega)$ via (2.56). Subsequently, a cross-spectral matrix calculated with the source model is defined by

$$\underline{\boldsymbol{C}}_g(\omega) = a_{\mathrm{s}}\underline{\boldsymbol{g}}\underline{\boldsymbol{g}}^{\mathrm{H}}, \tag{3.8}$$

$$\underline{\boldsymbol{g}} = \begin{bmatrix} \underline{g}(\boldsymbol{x}_1, \boldsymbol{y}_{\mathrm{f}}, \omega) \\ \vdots \\ \underline{g}(\boldsymbol{x}_m, \boldsymbol{y}_{\mathrm{f}}, \omega) \\ \vdots \\ \underline{g}(\boldsymbol{x}_M, \boldsymbol{y}_{\mathrm{f}}, \omega) \end{bmatrix}, \tag{3.9}$$

with $a_{\mathrm{s}} = |\underline{\sigma}|^2$. The vector $\underline{\boldsymbol{g}}$ is called *steering vector*. Throughout this thesis, the free field Green's function of an acoustic monopole is used to calculate the steering vector. The influence of other steering vectors on the obtained source map is studied in [86]. It was found that the choice of the steering vector is a trade-off between determining the correct source position and finding the correct source amplitude. In [87], first-order reflections are taken into account for calculating the steering vectors using either numerical calculations or experimental measurements to account for mirror sources.

Further, the steering vectors may be calculated using numerical methods, which allows to account

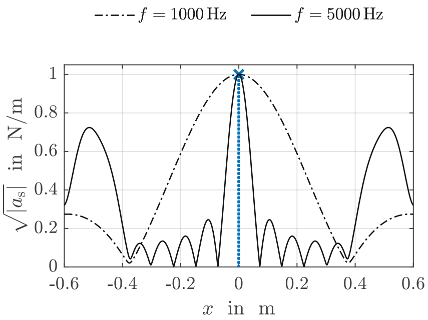

Figure 3.2: Array response function (Point Spread Function, PSF) of a line array to a point source (depicted in blue), calculated for two different frequencies.

for the actual measurement setup's environment where e. g. partially reflecting obstacles are present. A scheme exploiting the reciprocity of microphone and source positions is presented in [83].

Let J denote a functional, defined by [88]

$$J(a_\mathrm{s}) = \|\underline{\boldsymbol{C}} - \underline{\boldsymbol{C}}_g\|_\mathrm{F}^2\,, \tag{3.10}$$

with the Frobenius norm $\|\boldsymbol{A}\|_\mathrm{F}^2 = \sum\limits_i \sum\limits_j |a_{i,j}|^2$.

Minimizing the functional (3.10) yields the searched for source strength at each assumed source position $\boldsymbol{y}_\mathrm{f}$, called source map, at a discrete frequency ω

$$a_\mathrm{s}(\boldsymbol{y}_\mathrm{f}, \omega) = \underline{\boldsymbol{w}}^\mathrm{H}\underline{\boldsymbol{C}}\underline{\boldsymbol{w}}\,, \quad \underline{\boldsymbol{w}} = \frac{\underline{\boldsymbol{g}}}{\underline{\boldsymbol{g}}^\mathrm{H}\underline{\boldsymbol{g}}}\,. \tag{3.11}$$

The Conventional Beamforming method is well-known, robust, and fast in computation. However, its main downside is that the source map is a convolution of the real source distribution and the Point Spread Function (PSF) [84]. The PSF can be interpreted as the array response to a monopole source. It depends on the microphone array geometry, source position, and frequency. The presence of the PSF in the source map may lead to the masking of weaker sources or sources close to one another being identified as one source. The PSF of a microphone array is determined in frequency domain via

$$\sigma(\boldsymbol{x}_m, \boldsymbol{y}_0, \omega) = \sqrt{\boldsymbol{w}^\mathrm{H}\boldsymbol{C}_0\boldsymbol{w}}, \quad \boldsymbol{C}_0 = \boldsymbol{g}(\boldsymbol{y}_0)\boldsymbol{g}^\mathrm{H}(\boldsymbol{y}_0)\,, \tag{3.12}$$

with a monopole source $|\underline{\sigma}_0| = 1$ located at $\boldsymbol{y}_0$.

Exemplarily, the PSF of a line array consisting of 7 microphones shall be calculated: The microphones are spaced equally along the x-axis between $[-0.45, 0.45]\,\mathrm{m}$, and the point source is located at $\boldsymbol{y} = [0, 0, 1]\,\mathrm{m}$. The frequency of the point source is chosen $f = 1\,\mathrm{kHz}$, and $f = 5\,\mathrm{kHz}$, respectively. The PSF is evaluated at $z = 1\,\mathrm{m}$, see Fig. 3.2.

While there is a distinctive main lobe at the actual source position with the correct amplitude, several side lobes with smaller amplitude are also present. Additionally, two mirror sources occur at the higher frequency. Therefore, sources of smaller amplitude may be masked by the wide main lobe or side lobes and mirror sources. The latter is caused by spatial aliasing. Analog to the time domain, where a continuous signal must be sampled according to Nyquist theorem with a sampling rate $f_\mathrm{S} > 2f_\mathrm{max}$, where f_max is the maximum frequency occurring in the signal. In order to avoid spatial aliasing, the following condition concerning the microphone spacing Δx_m must be met [89]

$$x_\mathrm{m} < \frac{\lambda}{2}\,. \tag{3.13}$$

Since fulfilling (3.13) would require a very large number of needed microphones at higher frequencies, in practice, often irregular arrays are used as they are not as prone to mirror sources as regular arrays.

Due to the above reasons, ConvBF is limited regarding its resolution and dynamic range. The resolution determines the minimum distance two separate sources may have in order to be identified as individual sources. The minimum distance is defined by the Rayleigh [81] and Sparrow [90, 91] limit. The dynamic range is defined as the difference between the amplitudes of the main and first side lobes. A useful collection of practical design aspects concerning microphone arrays can be found in [83, 89]. To overcome the limitations of ConvBF, several advanced beamforming algorithms were developed.

3.2 Advanced Beamforming Algorithms

The main drawback concerning Conventional Beamforming is that the source map is a convolution of the actual source distribution and the microphone array's Point Spread Function (PSF), see Sec. 3.1.2. Therefore, weaker sources may be hidden by side lobes and the resolution is limited, especially at lower frequencies, see Fig. 3.2. Therefore, several advanced beamforming algorithms have been developed to overcome these drawbacks. One important category of advanced beamforming algorithms uses deconvolution. Another method described in [92] is based on an eigenvalue decomposition of the CSM and performing beamforming for each component to determine the sound sources' positions and amplitudes.

In the following sections two of these advanced algorithms will be explained in detail as they were applied in the result section of this thesis.

3.2.1 Functional Beamforming

One method aiming at reducing amplitudes of the side lobes is called *Functional Beamforming* (FuncBF) [93, 94]. A small modification is made to the ConvBF algorithm defined in (3.11)

$$a_{\mathrm{s}}(\boldsymbol{y}_{\mathrm{f}}, \omega) = \left[\underline{\boldsymbol{w}}^{\mathrm{H}} \underline{\boldsymbol{C}}^{\frac{1}{\nu}} \underline{\boldsymbol{w}} \right]^{\nu} , \tag{3.14}$$

with the exponent $\nu \geq 1$. For $\nu = 1$ (3.14) reduces to the equation for ConvBF. The calculation of $\underline{\boldsymbol{C}}^{\frac{1}{\nu}}$ is performed via spectral decomposition of the CSM

$$\underline{\boldsymbol{C}}^{\frac{1}{\nu}} = \boldsymbol{U} \mathrm{diag} \left[\lambda_1^{\frac{1}{\nu}}, \ldots, \lambda_M^{\frac{1}{\nu}} \right] \boldsymbol{U} , \tag{3.15}$$

where λ_i denotes the ith eigenvalue of the matrix $\underline{\boldsymbol{C}}$ and $\boldsymbol{U}$ is a unitary matrix whose columns are the eigenvectors of $\underline{\boldsymbol{C}}$. Figure 3.3 shows the PSF calculated with three values for $\nu \geq 1$, where $\nu = 1$ corresponds to ConvBF. It can be seen, that for $\nu > 1$ the side lobe level is decreased by applying $\square^{\nu}$ to the beamforming result, and the main peak width is decreased simultaneously. In case of a simulated single source, the side lobe level is reduced by a factor ν. Theoretically, the beamforming result will improve with increasing exponent values. However, an upper bound $\nu_{\max}$ exists for real measurement data, where the steering vectors, i. e. the source model, may not be calculated exactly. In this case, if $\nu > \nu_{\max}$, the value of the beamforming result at an actual source position will be decreased as well when ν is increased [94].

Another important category of advanced algorithms uses deconvolution to reduce the influence of the PSF in the source map. The most common algorithms will be presented in the following section, where the algorithms CLEAN-SC will be explained in more detail as it is used in the result section of this thesis.

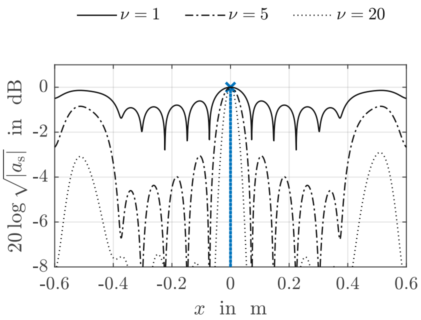

Figure 3.3: PSF of a line array to a point source (depicted in blue), calculated at 5000 Hz with Functional Beamforming using different exponents.

3.2.2 Deconvolution Methods

Most deconvolution methods require a beamforming result acquired e. g. by ConvBF (3.11), called the *dirty map*, as starting values for the deconvoluted result. A good comparison of the performance of conventional and deconvolution algorithms can be found in [95, 96, 97, 98].

It is usually assumed that the dirty map is generated solely by uncorrelated point sources. In principle, it is also possible to take correlated sources into account, which was done in [99] and [100], but this increases the complexity of the formulation of the deconvolution process.

The process of deconvolution can be denoted in matrix notation as

$$\boldsymbol{\Sigma} \boldsymbol{a}_\mathrm{dc} = \boldsymbol{a}_0 \tag{3.16}$$

$$\text{w.r.t.} \quad a_{\mathrm{dc},i} \geq 0 \,, \tag{3.17}$$

where $\boldsymbol{a}_0$ denotes the dirty map in each scanning point, $\boldsymbol{\Sigma}$ the known PSF matrix for each scanning point and $\boldsymbol{a}_\mathrm{dc}$ the searched for deconvoluted source distribution. The vectors $\boldsymbol{a}_0$ and $\boldsymbol{a}_\mathrm{dc}$ have the dimension $N_{xy} = N_x N_y$, with the numbers of possible source points N_x and N_y within the source map, in x- and y-direction. The PSF matrix is of dimension $N_{xy} \times N_{xy}$. In many applications $\boldsymbol{\Sigma}$ is singular, which leads to an infinite number of solutions for $\boldsymbol{a}_\mathrm{dc}$ if $\boldsymbol{a}_0$ is in the range of $\boldsymbol{\Sigma}$. There exists no solution if $\boldsymbol{a}_0$ is in not the range of $\boldsymbol{\Sigma}$ or all possible $\boldsymbol{a}_{\mathrm{dc},i}$ violate the constraint (3.17).

The deconvolution technique DAMAS (Deconvolution Approach for the Mapping of Acoustic Sources) was first presented in [101, 102]. It solves the linear set of equations (3.16) iteratively using a Gauss-Seidl-type relaxation and by ensuring that (3.17) is fulfilled in each iteration step for all $a_{\mathrm{dc},i}$. As the initial solution, often $\boldsymbol{a}_\mathrm{dc} = \boldsymbol{0}$ is assumed. Since the nonnegativity of the solution is enforced, convergence to the exact solution is not guaranteed, even if it exists [95].

Additionally, no regularization is used, as it is the case in other algorithms. DAMAS reduces the sidelobe level significantly, but the iterative method requires high computational effort. The algorithm DAMAS2 reduces the computational costs by assuming the PSF to be shift invariant [103]. Another improvement of DAMAS is called DAMAS-C and uses spatial coherence of sources [99].

In [104], a sparsity constrained version of DAMAS is presented, called SC-DAMAS. Further, a covariance matrix fitting (CMF) method is proposed, where a synthetic covariance matrix is fitted to measurements. CMF does not require a dirty map calculated from the DAS algorithm.

Alternatively, (3.16) can be solved via nonnegative least-squares (NNLS) algorithms by minimizing the functional J defined by

$$J = \frac{1}{2} \| \boldsymbol{\Sigma} \boldsymbol{a}_\mathrm{dc} - \boldsymbol{a}_0 \|_\mathrm{L2}^2 \,. \tag{3.18}$$

CLEAN-SC

A different approach for deconvolution is chosen by the CLEAN-SC method [105], which is based on the CLEAN method used in astronomy [106]. Its idea is to remove the PSF in the dirty map only for sources with the highest amplitude. The CLEAN algorithm calculates the deconvoluted source map $\boldsymbol{a}_{\mathrm{dc}}$ from the dirty source map $\boldsymbol{a}_0$ iteratively with the following steps

1. Initialization
   (a) "Degraded" beamforming source map $\boldsymbol{b}^{(0)} = \boldsymbol{a}_0$
   (b) "Degraded" Cross-Spectral Matrix $\underline{\boldsymbol{D}}^{(0)} = \breve{\underline{\boldsymbol{C}}}$,
   where $\breve{\underline{\boldsymbol{C}}}$ denotes that the main diagonal of the CSM is set to zero, also called "trimmed" CSM

2. Search for maximum value $b_{\max}^{(i)}$ in the degraded source map $\boldsymbol{b}^{(i)}$ at location $\boldsymbol{y}_{\mathrm{S,max}}^{(i)}$

3. Calculate a clean map $\boldsymbol{Q}^{(i)}$ consisting of an appropriately scaled clean beam $\Psi \leq 1$ at $\boldsymbol{y}_{\mathrm{S,max}}^{(i)}$ with a defined width

$$Q_j^{(i)} = \vartheta b_{\max}^{(i-1)} \Psi(\boldsymbol{y}_{\mathrm{S},j} - \boldsymbol{y}_{\mathrm{S,max}}^{(i)}) \,, \tag{3.19}$$

   with a safety factor $0 < \vartheta \leq 1$, called "loop gain".

4. Calculate the degraded CSM $\underline{\boldsymbol{D}}^{(i)}$

$$\underline{\boldsymbol{D}}^{(i)} = \underline{\boldsymbol{D}}^{(i-1)} - \vartheta \underline{\boldsymbol{G}}^{(i)} \,, \tag{3.20}$$

   where $\underline{\boldsymbol{G}}^{(i)}$ is calculated according to

$$\underline{\boldsymbol{G}}^{(i)} = b_{\max}^{(i-1)} \underline{\boldsymbol{g}}_{\max}^{(i)} \underline{\boldsymbol{g}}_{\max}^{\mathrm{H}(i)}, \qquad \underline{\boldsymbol{g}}_{\max}^{(i)} = \underline{\boldsymbol{g}}(\boldsymbol{y}_{\mathrm{S,max}}^{(i)}) \,. \tag{3.21}$$

5. Analogously to (3.11), the degraded beamforming map can be calculated with the degraded CSM

$$b_j^{(i)} = \underline{\boldsymbol{w}}_j^{\mathrm{H}} \breve{\underline{\boldsymbol{D}}}^{(i)} \underline{\boldsymbol{w}}_j \,. \tag{3.22}$$

   This is equivalent to subtracting the scaled PSF associated with the source located at $\boldsymbol{y}_{\mathrm{S,max}}^{(i)}$ from the degraded beamforming map

$$b_j^{(i)} = b_j^{(i-1)} - \vartheta \underline{\boldsymbol{w}}_j^{\mathrm{H}} \breve{\underline{\boldsymbol{G}}}^{(i)} \underline{\boldsymbol{w}}_j \,. \tag{3.23}$$

6. Resume with step 2 until a stopping criterion is met, e. g. $\|\underline{\boldsymbol{D}}^{(i+1)}\| \geq \|\underline{\boldsymbol{D}}^{(i)}\|$. This is the case if the degraded CSM contains more "information" than in the previous iteration step.

After the iteration process is finished ($i = N_{\mathrm{i}}$), the deconvoluted source map is calculated as the sum of clean beams and the remaining dirty map

$$a_{\mathrm{dc},j} = \sum_{i=1}^{N_{\mathrm{i}}} Q_j^{(i)} + b_j^{(N_{\mathrm{i}})} \,. \tag{3.24}$$

The CLEAN-PSF algorithm assumes that the sound field consists of a finite number of monopole sources, causing a combination of PSFs in the source map. From this, the assumption of no loss of coherence follows. To overcome these limitations, the algorithm CLEAN-SC was proposed in [105].

CLEAN-SC ("CLEAN based on spacial Source Coherence") exploits that the side lobes are coherent with the main lobe. The algorithm is similar to CLEAN-PSF, as the degraded beamforming map is calculated via (3.23) but a different choice for the matrix $\underline{\boldsymbol{G}}^{(i)}$ is made

$$\underline{\boldsymbol{G}}^{(i)} = b_{\mathrm{max}}^{(i-1)} \breve{\left[\underline{\boldsymbol{h}}^{(i)} \underline{\boldsymbol{h}}^{(i)\mathrm{H}}\right]} \,, \tag{3.25}$$

where $\breve{\square}$ again denotes that the matrix's main diagonal is set to zero. (3.25) assumes, that $\underline{\boldsymbol{G}}^{(i)}$ is due to a single coherent source component $\underline{\boldsymbol{h}}^{(i)}$. The conditional equation for $\underline{\boldsymbol{h}}^{(i)}$ reads as

$$\underline{\boldsymbol{h}}^{(i)} = \frac{1}{\left(1 + \underline{\boldsymbol{w}}_{\mathrm{max}}^{\mathrm{H}(i)} \underline{\boldsymbol{H}}^{(i)} \underline{\boldsymbol{w}}_{\mathrm{max}}^{(i)}\right)^{1/2}} \left(\frac{\underline{\breve{\boldsymbol{D}}}^{(i-1)} \underline{\boldsymbol{w}}_{\mathrm{max}}}{b_{\mathrm{max}}^{(i-1)}} + \underline{\boldsymbol{H}}^{(i)} \underline{\boldsymbol{w}}_{\mathrm{max}}^{(i)} \right) . \tag{3.26}$$

In (3.26) $\underline{\boldsymbol{H}}^{(i)}$ denotes the main diagonal of $\underline{\boldsymbol{h}}^{(i)} \underline{\boldsymbol{h}}^{\mathrm{H}(i)}$

$$\breve{\left[\underline{\boldsymbol{h}}^{(i)} \underline{\boldsymbol{h}}^{\mathrm{H}(i)}\right]} = \underline{\boldsymbol{h}}^{(i)} \underline{\boldsymbol{h}}^{\mathrm{H}(i)} - \underline{\boldsymbol{H}}^{(i)} \,.$$

Therefore, (3.26) has to be solved iteratively with starting value $\underline{\boldsymbol{h}}_0^{(i)} = \underline{\boldsymbol{g}}_{\mathrm{max}}^{(i)}$. The iteration is stopped when the CSM is degraded enough. Hence, the stopping criterion is e. g. $\|\underline{\breve{\boldsymbol{D}}}^{(N_{\mathrm{i}})}\| \ll \|\underline{\breve{\boldsymbol{C}}}\|$.

3.3 Sound Source Localization at the Tire

The sound field near the rolling tire has been studied with a view to identifying the positions and strengths of the dominant sound sources, whereas various approaches were used. The measurement quantity is the sound pressure or the sound intensity field near the rolling tire. Usually, a microphone grid with several spatially distributed microphones is used, where some methods allow for sequential measurements, resulting in a reduced number of required microphones.

Another distinction between the types of measurement methods can be made concerning the relative velocity between the tire and sensors: the sensors are either stationary or moving with the tire. In the first case, where a vehicle is passing the microphone array similar to the CPB method (see Sec. 1.3.3), the Doppler effect due to the speed difference between the tire and the microphones has to be accounted for during the localization process. In the second case, there is no relative motion between the microphones, apart from the rotation of the tire, which is usually neglected since the contribution of the air turbulence due to the tire's rotation to the overall noise is considered insubstantial. Another possibility is to use the laboratory drum method with stationary sensors.

The first attempts to localize regions with strong contributions to the overall noise due to the tire-pavement interactions were measurements of the sound intensity field, performed in the 1980s and 1990s, see [107, 108, 109, 110]. The measurements were either carried out in a wind tunnel or with a pp-probe, consisting of two spaced microphones mounted to a moving truck tire. The findings of these publications show frequency-dependent contour plots of the sound intensity in a plane parallel to the tire's sidewall, which exhibits regions of higher sound intensity levels near the tire contact patch and at the leading and trailing edge of the tire.

Other publications used Near-Field Acoustic Holography (NAH), an inverse method with which the sound pressure and acoustic particle velocity distribution can be calculated in a source plane from microphone array measurements. The microphones are arranged, usually in a regular microphone grid, in a plane parallel to the source plane in a small distance from the sound sources. NAH can be applied in the time as well as in the frequency domain. The fundamentals of this method are covered in [58]. Several advanced algorithms based on NAH were developed over time, e. g. Statistically Optimal NAH (SONAH) [111] or Helmholtz equation least-squares (HELS) [112, 113]. In [15], a trailer equipped with a regular microphone array was used to identify the dominant sound sources at the rolling tire. Due to the design of the trailer, which was an open construction, the mean airflow velocity was accounted for by modifying the NAH algorithm with a convective wave equation. In [114, 115], NAH was applied using a tire running on laboratory drums with a stationary microphone array, and in [116], a microphone array was mounted to a moving car.

Another method for the localization of the various sound sources emitted by a moving car uses stationary microphone arrays at the roadside with the vehicle passing by. Thereby, not only the sources due to the tire-pavement interactions are localized but also sound sources emitted by the combustion engine or – at higher speeds – aerodynamic sources. The methods presented in Sec. 3.1 and Sec. 3.2 may be used with adaptions for the localization of moving sound sources. Due to the vehicle passing the microphones, the distances between scan points and the microphone positions become a function of time. The relative motion between the source and the microphones leads to a frequency shift perceived at the observer positions, known as the Doppler effect. It has to be considered by the beamforming algorithm. Beamforming methods applied to sources moving along an arbitrary trajectory can be found in [117, 118]. In [119, 120], the sound sources emitted by different vehicles passing in a setup similar to one defined in the Pass-By method [35], see Sec. 1.3.3, are identified via Beamforming using de-dopplerization of the recorded signals. NAH with a stationary microphone line array, identifying the sound sources of a passing car is presented in [121, 122].

Further works and a good overview of different sound source localization methods applied to moving cars and rolling tires can be found in [123, 124]. A general overview of the application of different sound source localization methods is provided in [125].

CHAPTER 4

The Forward Problem

This chapter will address the process of creating a Finite Element model of the vehicle trailer. This FE model will be used for forward acoustic simulations, i. e. prescribing acoustic sources and calculating the acoustic pressure, and subsequently for the sound source identification with the Inverse Scheme, see Chap. 5. Apart from constructing a CAD model of the trailer – or at least the acoustically essential parts of it – creating the FE model involves mainly finding suitable boundary conditions for the regions where acoustic absorbers are mounted. Further, a method for validation via microphone measurements will be established.

In Sec. 4.1, material models for characterization of the acoustic properties of acoustic absorbers will be presented. Subsequently, two different material models will be applied to the used absorber, which requires fitting the model parameters via impedance tube measurements. Thereafter, in Sec. 4.2 the forward model will be validated with in-situ microphone measurements.

4.1 Modeling of Sound Absorbing Materials

Porous materials play a significant role in many applications. They are widely used in room acoustics and technical applications where sound has to be attenuated. Therefore, developing mathematical and physical models to describe their absorbing behavior has been of great interest. The fundamental idea of the models for poroelastic materials is that they consist of an elastic frame and a fluid surrounding the frame. Acoustic absorption of sound energy within poroelastic materials is mainly caused by dissipative effects within the fluid and by the deformation of the frame. Biot's theory is the basis for describing the poroelastic material's motion. It states that the average displacement of the fluid and the frame take place separately but are coupled. In [126, 127], a system of coupled displacement equations for the frame and the saturating fluid is proposed.

4.1.1 Equivalent Fluid

The acoustic properties of a porous material can be described in some simple cases on a microscopic scale, e. g., by assuming pores with cylindrical cross-sections. However, the properties of actual acoustic absorbers are usually challenging to determine because of the complex geometries of the frame. Therefore, a homogenization approach is chosen, and the microscopic properties are averaged to a macroscopic scale. Further, the absorbing material is assumed to be isotropic and homogeneous with a finite thickness. Assuming isotropy is a valid approach if the dimensions of the pores are small compared to the smallest acoustic wavelength of interest and the surrounding fluid is incompressible at a microscopic scale [128].

Generally, the motion inside the poroelastic material consists of three types of waves: a longitudinal (compressional) wave in the fluid part, a longitudinal wave in the solid part and a transversal (shear) wave in the solid part. In cases where there is no visco-inertial coupling between the frame and the fluid, the frame can be considered as motionless, i. e. rigid. This is a valid assumption for frequencies above the decoupling frequency f_{dc}, which is given by [128]

$$f_{\mathrm{dc}} = \frac{\Xi \phi^2}{2\pi \rho_{\mathrm{f}}}\,. \tag{4.1}$$

In (4.1) ρ_{f} denotes the density of the frame. The flow resistivity Ξ and the porosity ϕ are material properties will be defined in the following section.

In case of a motionless frame, only the longitudinal wave within the fluid phase is considered, and therefore, the sound propagation within the porous absorber can be described by an equivalent fluid wave equation, analogous to (2.52), which reads in the homogeneous case, i. e. without any sources present, as

$$\nabla \cdot \underline{\rho}_{\mathrm{eff}} \nabla \underline{p}_{\mathrm{a}}(\boldsymbol{x},\omega) + \frac{\omega^2}{\underline{K}_{\mathrm{eff}}} \underline{p}_{\mathrm{a}}(\boldsymbol{x},\omega) = 0\,. \tag{4.2}$$

An effective, complex-valued density $\underline{\rho}_{\mathrm{eff}}(\omega)$ and compression modulus $\underline{K}_{\mathrm{eff}}(\omega)$ are introduced to account for visco-inertial effects and thermal dissipative effects within the absorber [129]. Also, the characteristic field impedance becomes complex-valued and a function of frequency $Z_{\mathrm{c}} = \underline{Z}_{\mathrm{c}}(\omega)$. The characteristic field impedance and the wave number can be expressed in terms of the effective density and compression modulus via

$$\begin{aligned} \underline{Z}_{\mathrm{c}}(\omega) &= \sqrt{\underline{\rho}_{\mathrm{eff}} \underline{K}_{\mathrm{eff}}} \\ \underline{k}(\omega) &= \omega \sqrt{\frac{\underline{\rho}_{\mathrm{eff}}}{\underline{K}_{\mathrm{eff}}}}\,. \end{aligned} \tag{4.3}$$

The speed of sound within the poroelastic medium also becomes complex-valued and frequency-dependent – in contrast to air where c is not dependent on the excitation frequency. It can be calculated via

$$\underline{c}(\omega) = \sqrt{\frac{\underline{K}_{\mathrm{eff}}}{\underline{\rho}_{\mathrm{eff}}}}\,. \tag{4.4}$$

The attenuation effect of a complex-valued wave number within an acoustic absorber can be illustrated by inserting $\underline{k}(\omega)$ into the solution for the one-dimensional wave equation, see (2.89). For a purely propagating wave, this reads as

$$\underline{p}_{\mathrm{a}}(x,\omega) = \hat{\underline{p}}_{\mathrm{a}} \mathrm{e}^{-\mathrm{j}\underline{k}x} = \hat{\underline{p}}_{\mathrm{a}} \mathrm{e}^{-\mathrm{j}k_{\mathrm{Re}}x} \mathrm{e}^{k_{\mathrm{Im}}x}\,, \qquad \underline{k} = k_{\mathrm{Re}} + \mathrm{j}k_{\mathrm{Im}}\,. \tag{4.5}$$

The term $\mathrm{e}^{k_{\mathrm{Im}}x}$ leads to an attenuation for increasing values of x if $k_{\mathrm{Im}} < 0$.

Besides the particular case of a rigid frame, under some conditions, one can assume a limp frame, i. e. a negligible frame stiffness. The limp model may be used when the absorbing material's density is very low, e. g. light fiberglass, or due to the mounting or the excitation of the absorber [128]. Models for materials with a limp frame are given in e. g. [130, 131, 132, 133] but will not be covered here.

4.1.2 Material Models

Over time, a large number of material models were developed, with which the effective density and compression modulus can be calculated. This chapter is restricted to models, which assume a rigid frame. Material models can be divided into phenomenological models, based solely on measurements of different types of absorbers, analytical models, which are typically only valid for absorbers of simple geometries, e. g. with pores with cylindrical cross-sections and the combination of the two types, the semi-empirical models. The latter models are therefore a combination of empirical and analytical models. An overview of existing models can be found in [128, 134, 135].

Material model parameters

In the following, important material parameters, which are parameters of models used in this thesis, will be explained on basis of [128, 134, 136]. In this thesis the fluid surrounding the frame is always assumed as air, since this will be the case in the applications.

The porosity ϕ is the ratio of the air volume V_a and the total volume of the absorber V_t, which is the sum of the air and the frame's volume $V_\mathrm{t} = V_\mathrm{a} + V_\mathrm{f}$

$$\phi = \frac{V_\mathrm{a}}{V_\mathrm{t}} \,. \tag{4.6}$$

High porosity is linked to sizeable viscothermal dissipation and, therefore, high values for the absorption coefficient. Measurement methods of ϕ can be found in [137, 138].

The flow resistivity $\varXi$ is defined as the ratio of the pressure differential Δp across the thickness h of a material sample to the mean normal flow velocity $\overline{v}$ through the sample

$$\varXi = \frac{\Delta p}{\overline{v} h} \,. \tag{4.7}$$

The method for determining $\varXi$ is standardized in [139].

The high frequency limit of tortuosity α_∞ describes how much the trajectory of the fluid particles is deviated due to the frame from the normal direction. The dynamic tortuosity $\alpha'(\omega)$ is defined as the ratio of the dynamic density due to drag effects ρ_dyn and the equilibrium fluid density ρ_0. Therefore, α_∞ can be interpreted as a correction term for ρ_dyn at high frequencies. It can be measured by electrical measurements or by using superfluid ^{4}He as surrounding fluid [140, 141].

The viscous characteristic length Λ is defined as [140]

$$\Lambda = 2 \frac{\int\limits_V |\boldsymbol{v}(\boldsymbol{r})|^2 \,\mathrm{d}V}{\int\limits_A |\boldsymbol{v}(\boldsymbol{r}_\mathrm{w})|^2 \,\mathrm{d}A} \,, \tag{4.8}$$

where V denotes the volume of the pores, A the surface of the pore walls, and $\boldsymbol{v}(\boldsymbol{r})$ and $\boldsymbol{v}(\boldsymbol{r}_\mathrm{w})$ denote the microscopic velocity of the fluid in the pores and at the surface of the walls, respectively. In other words, Λ is a velocity-weighted surface-to-pore ratio.

The fibers can be modeled as infinitely long cylindrical channels in fibrous materials such as fiberglass. If the direction of sound propagation is perpendicular to the cylinders and the porosity is close to 1, Λ is given by [128]

$$\Lambda = \frac{1}{2\pi l_\mathrm{f} r_\mathrm{f}} \,, \tag{4.9}$$

where l_f is the total length of fibers per unit volume and r_f the radius of the cylinder's cross-section.

The thermal characteristic length Λ' is defined as the surface-to-pore ratio without the velocity weighting

$$\Lambda = 2\frac{\int\limits_V \mathrm{d}V}{\int\limits_A \mathrm{d}A} = \frac{2V}{A}\,. \tag{4.10}$$

In case of fibrous materials with the assumed properties, as stated in the paragraph above, the thermal characteristic length is given by

$$\Lambda' = 2\Lambda\,. \tag{4.11}$$

The static thermal permeability k'_0 is the value of the thermal permeability $k'(\omega)$ at low-frequencies. $k'(\omega)$ provides a description of the thermal exchanges between the rigid frame and the fluid.

Delany-Bazely-Miki (DBM) Model

The DBM model, sometimes referred to as *Miki model* in literature, was proposed in [142] which is an extension to the original model presented by Delany and Bazely in [143], a purely empirical model. Further improvements have been published in [144]. It is a popular model for highly porous materials since it only requires one parameter, the flow resistivity. In the original work, the acoustic properties of various fibrous acoustic absorbers were determined in an impedance tube under plane wave conditions. The acoustic absorbers under test covered a wide range of flow resistivity values. With this data, a regression analysis was performed. The influence of the frequency divided by the flow resistivity f/Ξ on the normalized characteristic impedance $\underline{Z}_\mathrm{c}/(\rho_0 c)$ and the normalized wave number $\underline{k}/(\omega/c)$ was investigated. The functions are assumed as

$$\underline{Z}_\mathrm{c}(f/\Xi) = \rho_0 c \left[1 + a_Z\left(\frac{f}{\Xi}\right)^{p_Z} + \mathrm{j} b_Z\left(\frac{f}{\Xi}\right)^{q_Z}\right] \tag{4.12}$$

$$\underline{k}(f/\Xi) = \frac{\omega}{c}\left[a_k\left(\frac{f}{\Xi}\right)^{p_k} + \mathrm{j}\left(1 + b_k\left(\frac{f}{\Xi}\right)^{q_k}\right)\right]. \tag{4.13}$$

In Miki's modified version, a positive-real condition of the impedance function and an additional restriction on the wave number are introduced. These conditions are derived from an electro-acoustic analogy of a cylindrical tube and lead to a linear dependency of the coefficients and exponents in (4.12) and (4.13). The original model did not consider these conditions. Hence, the coefficients of the Delany-Bazely (DB) model are not physically realizable and may lead to significant errors, especially in the lower range of f/Ξ. The structure of the Miki model's equations remains the same as for the DB model, see (4.12) and (4.13).

The bounds of f/Ξ in the original model are given by

$$0.01 \leq f/\Xi \leq 1\,. \tag{4.14}$$

The authors of the DBM model claim the validity of their model even outside of this range.

The coefficients and exponents of the DB and the DBM model are shown in Tab. 4.1 [142, 143, 144]. Note that the original paper assumes a centimeter–gram–second (CGS) system of units; therefore, the numeric values of coefficients provided differ from the original publication.

The downside of the DBM model is that it provides realistic values only for absorbers with porosity and tortuosity close to unity since the measurements by Delany and Bazely were carried out with highly porous foams and fibrous materials. Improvements could be achieved by replacing the flow resistivity Ξ with an effective flow resistivity $\Xi_\mathrm{e} = \Xi\phi$ in [145].

	DB model	DBM model
a_Z	0.050	0.070
b_Z	−0.076	−0.107
p_Z	−0.754	−0.632
q_Z	−0.732	−0.632
a_k	0.169	0.160
b_k	0.086	0.109
p_k	−0.595	−0.618
q_k	−0.700	−0.618

Table 4.1: Coefficients and exponents of the original DB model and the DBM model.

Johnson-Champoux-Allard-Lafarge (JCAL) Model

The JCAL model [146] is a semi-empirical model that extends to the Johnson-Champoux-Allard model [140, 141]. In [141], an expression for the frequency-dependent tortuosity in porous materials was found to predict the high frequency asymptotic behavior. From the tortuosity $\underline{\alpha}'(\omega)$, the dynamic density can easily be calculated via

$$\underline{\rho}_{\mathrm{dyn}} = \underline{\alpha}' \rho_0 \,. \tag{4.15}$$

In [140], the model by Johnson is extended to a phenomenological frequency-depended model of the effective bulk modulus $K_{\mathrm{eff}}(\omega)$ of a fluid saturating a rigid frame. The characteristic lengths Λ and Λ' are used to approximate the asymptotic behavior of ρ_{dyn} and K_{eff} in the high frequency regime. The effective density $\underline{\rho}_{\mathrm{eff}}$ and the dynamic density are related by

$$\underline{\rho}_{\mathrm{eff}} = \frac{\underline{\rho}_{\mathrm{dyn}}}{\phi} \,. \tag{4.16}$$

The expressions of effective density and compression modulus are given by [128, 134]

$$\underline{\rho}_{\mathrm{eff}}(\omega) = \frac{\alpha_\infty \rho_0}{\phi} \left[1 + \frac{\Xi \phi}{\mathrm{j}\omega \rho_0 \alpha_\infty} \sqrt{1 + \mathrm{j} \frac{4\alpha_\infty^2 \mu \rho_0 \omega}{\Xi^2 \Lambda^2 \phi^2}} \right] , \tag{4.17}$$

$$\underline{K}_{\mathrm{eff}}(\omega) = \frac{\kappa p_0 / \phi}{\kappa - (\kappa - 1) \left[1 - \mathrm{j} \dfrac{\phi \lambda_{\mathrm{th}}}{k_0' c_p \rho_0 \omega} \sqrt{1 + \mathrm{j} \dfrac{4 {k_0'}^2 c_p \rho_0 \omega}{\lambda_{\mathrm{th}} {\Lambda'}^2 \phi^2}} \right]^{-1}} \,. \tag{4.18}$$

In (4.17), the following constants related to the saturating fluid are introduced: the dynamic viscosity μ and the thermal conductivity λ_{th}.

Additional work on the JCAL model was done in [147] and refined in [146], resulting in the JCAPL model. In this version of the model, possible constrictions between the pores can be modeled. The JCAL model can be interpreted as a special case of the more general JCAPL model.

Another material model which aims at matching the material's middle-frequency behavior is presented in [148]. Since neither model is used in this thesis, they will not be discussed in detail.

4.1.3 Integration of Material Models within the Finite Element Framework

In this thesis, the material models are applied in order to integrate regions with acoustic absorbers in an acoustic FE simulation. In other words, they model the boundary conditions of a given measurement setup. The frame of the poroelastic medium is considered as rigid. Therefore, the sound propagation within the absorber can be described by an equivalent fluid equation, see (4.2).

A more general version of the Helmholtz equation shall be considered, allowing for a space-dependent density, i. e. an inhomogeneous medium. Applying the Fourier transform to an inhomogeneous version of (2.21) yields

$$\nabla \cdot \frac{1}{\rho(\boldsymbol{x})} \nabla \underline{p}_{\mathrm{a}} + \frac{\omega^2}{K(\boldsymbol{x})} \underline{p}_{\mathrm{a}} = \underline{\boldsymbol{\mathcal{F}}}(\boldsymbol{x}) \,. \tag{4.19}$$

The FE model considered in Sec. 4.2 includes regions with air, denoted by Ω_{air}, and regions with an acoustic absorber, denoted by Ω_{damp}, see Fig. 4.1. The computational domain, therefore, consists of two different piecewise homogeneous media. In this case, the general density $\rho(\boldsymbol{x})$ and compression modulus $K(\boldsymbol{x})$ in (4.19) are defined as

$$\rho(\boldsymbol{x}) = \begin{cases} \underline{\rho}_{\mathrm{eff}} & \text{if } \boldsymbol{x} \in \Omega_{\mathrm{damp}} \\ \rho_0 & \text{if } \boldsymbol{x} \in \Omega_{\mathrm{air}} \end{cases} , \qquad K(\boldsymbol{x}) = \begin{cases} \underline{K}_{\mathrm{eff}} & \text{if } \boldsymbol{x} \in \Omega_{\mathrm{damp}} \\ K_0 = \rho_0 c^2 & \text{if } \boldsymbol{x} \in \Omega_{\mathrm{air}} \end{cases} . \tag{4.20}$$

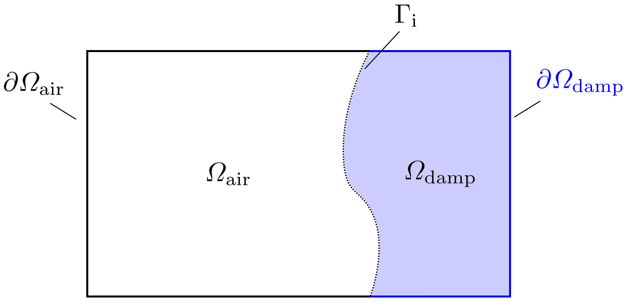

Figure 4.1: Computational domain with two piecewise homogeneous media, denoted by Ω_{air} and Ω_{damp}.

The acoustic absorbers are therefore modeled as separate regions with their actual physical dimensions. The computational domain Ω therefore is $\Omega = \Omega_{\mathrm{air}} \bigcup \Omega_{\mathrm{damp}}$. The material properties $\rho(\boldsymbol{x})$ and $K(\boldsymbol{x})$ are calculated with a suitable material model, e. g. the JCAL model. The material parameters can be fitted with impedance tube measurements, see Sec. 4.1.4. Additionally, boundary conditions on the outer boundaries $\partial\Omega_{\mathrm{air}}$ and $\partial\Omega_{\mathrm{damp}}$ can be incorporated, e. g. the sound-hard boundary condition $\nabla p_{\mathrm{a}} \cdot \boldsymbol{n} = 0$ which leads to full reflection.

A different approach excludes the absorber regions from the computational domain, i. e. $\Omega = \Omega_{\mathrm{air}}$, and prescribes the impedance at the interface Γ_{i}. This can be achieved in the Finite Element framework by inserting (2.78) into the weak formulation of the Helmholtz equation (2.100). Neglecting any source terms within $\Omega \setminus \partial\Omega$ yields, under consideration of (2.101),

$$\int\limits_{\Omega} \left(\overline{w} k^2 \underline{p}_{\mathrm{a}} - \nabla \underline{p}_{\mathrm{a}} \cdot \nabla \overline{w} \right) \mathrm{d}\boldsymbol{x} = \mathrm{j}\omega\rho_0 \int\limits_{\partial\Omega} \overline{w} \frac{\underline{p}_{\mathrm{a}}}{\underline{Z}_{\mathrm{s}}} \, \mathrm{d}s \,. \tag{4.21}$$

Because of the structure of the wave equation, the impedance boundary condition can only consider normal components of the acoustic particle velocity without any tangential components. Therefore, this particular boundary condition only yields valid results for planar surfaces and plane waves at normal incidence or locally reacting absorbers, where there is no sound propagation in the lateral direction, cf. Sec. 2.1.7.

4.1.4 Fitting of Material Model Parameters via Impedance Tube Measurements

In this section, the characterization process of an acoustic absorber material using the two-microphone method will be considered. The absorption and reflection coefficient can be inferred from these plane wave measurements, among other material properties. The measurement of the reflection coefficient was used to identify the material model parameters of the absorber material attached to the inner surfaces of the measurement trailer. This trailer was deployed for gathering the microphone measurements to identify the sound sources in the real-world application. For a detailed description of the trailer, see Chap. 6.

Determining the material model parameters of the material sample via impedance tube measurements is a parameter identification problem. The cost function to solve this minimization problem is given by

$$J_r = \sum_{i=1}^{N_\mathrm{f}} |\underline{r}_\mathrm{meas}(\omega_i) - \underline{r}_\mathrm{calc}(\omega_i)|^2 \,. \tag{4.22}$$

In (4.22), $\underline{r}_\mathrm{meas}(\omega)$ denotes the measured reflection coefficient and $\underline{r}_\mathrm{calc}(\omega)$ the calculated reflection coefficient, where the material properties are calculated with the JCAL model, see (4.24). Since the reflection coefficient is a function of frequency ω, the summation in (4.22) is carried out over N_f discrete frequencies within a defined frequency band $\omega_\mathrm{l} \leq \omega_i \leq \omega_\mathrm{u}$.

For the calculation of $\underline{r}_\mathrm{calc}(\omega)$ we consider the analytic solution of the sound transmission of plane waves through an acoustic absorber, which is given by (2.96), where $\rho = \underline{\rho}_\mathrm{eff}$ and $k = \underline{k}_\mathrm{eff}$. Due to the sound-hard termination at the end of the impedance tube in the two-microphone setup – see Fig. 2.2 – in (2.96), for the velocity the relation $\underline{v}_{\mathrm{a},x_1} = \underline{v}_\mathrm{a}(x = d) = 0$ holds. Here, the arbitrary positions x_1 and x_2 in (2.96) are chosen at the two surfaces of the absorber: $x_1 = d$ and $x_2 = 0$.

Therefore, the specific impedance of an absorber is given by

$$\begin{aligned} \underline{Z}_\mathrm{s,eff} = \underline{Z}_\mathrm{s}(x=0) &= \frac{\underline{p}_{\mathrm{a},x_2}}{\underline{\boldsymbol{v}}_{\mathrm{a},x_2} \cdot \boldsymbol{n}} = \frac{T_{11}}{T_{21}} \\ &= \frac{\cos \underline{k}_\mathrm{eff} h}{\mathrm{j} \frac{\underline{k}_\mathrm{eff}}{\omega \underline{\rho}_\mathrm{eff}} \sin \underline{k}_\mathrm{eff} h} = -\mathrm{j} \underline{Z}_\mathrm{c} \cot \underline{k}_\mathrm{eff} h \,, \end{aligned} \tag{4.23}$$

with the thickness h of the sample, the elements T_{11} and T_{21} of the transfer matrix defined in (2.97) and the (effective) characteristic field impedance $\underline{Z}_\mathrm{c} = \underline{\rho}_\mathrm{eff} \underline{c}_\mathrm{eff}$. With (4.23), (2.83) and with $\theta_\mathrm{i} = 0$, the reflection coefficient $\underline{r}_\mathrm{calc}$ is calculated via

$$\underline{r}_\mathrm{calc} = \frac{\underline{Z}_\mathrm{s,eff}(\zeta_{\mathrm{J},i}) - Z_0}{\underline{Z}_\mathrm{s,eff}(\zeta_{\mathrm{J},i}) + Z_0} \,, \tag{4.24}$$

where $\zeta_{\mathrm{J},i}$ denotes the six material parameters of the JCAL model ϕ, k_0', Λ, Λ', $\mathit{\Xi}$ and α_∞.

To yield the material parameters of the JCAL model from which the material properties $\underline{\rho}_\mathrm{eff}$ and $\underline{K}_\mathrm{eff}$ of the absorber can be calculated, the unconstrained minimization problem

$$\min_{\zeta_{\mathrm{J},i}} J_r \tag{4.25}$$

has to be solved.

Results of the Material Parameter Fitting

This subsection describes the process of determining the correct material properties of the acoustic absorbers mounted inside the used measurement trailer.

A circular impedance tube manufactured by Brüel & Kjær, with an inner diameter of 100 mm was used. For measurements in the higher frequency regime, a different configuration of the impedance tube with an inner diameter of 29 mm has to be used. For the larger tube, an upper frequency limit of $f_\mathrm{u} = 1600\,\mathrm{Hz}$ results from the restrictions concerning the frequency limits mentioned in (2.87). Since the dominant sound sources of the main mechanisms during the tire-pavement interactions are below this frequency limit, only measurements with the larger impedance tube were carried out.

The signal generation and data acquisition was performed using the software PULSE Acoustic Material Testing in a Tube, a data acquisition interface including an analog-to-digital converter and an amplifier produced by Brüel & Kjær. Cylindrical samples of the acoustic absorber were cut out and placed in the impedance tube with no distance to the sound-hard termination. The reflection coefficient was measured with the two-microphone method. Since cutting the absorbers is done by hand, a variation of the measured material properties has to be expected. Therefore, five samples were cut, and the measured reflection coefficient was averaged.

The acoustic absorbing material under test is an open-cell acoustic foam with a thickness of 50 mm and a coating on the front for protection against moisture and oil. Its density is given by $30\,\mathrm{kg/m^3}$ [149]. Because of the absorber's high density, the assumption of a poroelastic material with a rigid (motionless) frame is justified, see (4.1).

The minimization of (4.25) was performed via a genetic optimization algorithm implemented in the Optimization Toolbox of MATLAB. The fundamentals of the genetic algorithm are covered in Sec. 2.3.2 and [150]. The following options were set:

- Number of chromosomes in a population: 70
- Number of maximum generations (number of maximum iterations): 100
- Number of individuals that are guaranteed to be selected for the next generation (Elitism): 4

In the first step, the simple DBM model was used, and later results of a fitting using the JCAL model will be presented. The material parameters of the DBM and JCAL model are assumed to be a property of the material itself and are not frequency dependent. However, the fitting is performed for three different frequency bands, namely for

- FB 1: $200 \leq f/\mathrm{Hz} \leq 500$
- FB 2: $500 < f/\mathrm{Hz} \leq 1000$ ans
- FB 3: $1000 < f/\mathrm{Hz} \leq 1600$

in order to achieve better fitting results.

While the optimization is an unconstrained problem, for each optimization parameter, a lower bound and upper bound is defined. The optimization results of the DBM parameter and the JCAL parameters for each frequency band and the predefined parameter bounds can be seen in Tab. 4.2 and Tab. 4.3, respectively. The bounds for the DBM model have to be chosen frequency dependent in order to fulfill the model constraint (4.14). Therefore, for each frequency band, the bounds for Ξ are determined according to

$$\Xi_\mathrm{min} = f_\mathrm{max}(1+p) \tag{4.26}$$
$$\Xi_\mathrm{max} = 100 f_\mathrm{min}(1-p)\,, \tag{4.27}$$

with a factor $0 \leq p < 1$ that allows Ξ taking values outside the boundaries in (4.14). For the results presented below, a value of $p = 0.2$ was chosen. However, also setting its value as high as $p = 0.8$ did not significantly improve the fitness value.

The bounds in case of the JCAL model remained the same for each frequency band and are therefore only stated once in Tab. 4.3.

Frequency	Bounds		
band	lower	upper	Ξ_{opt}
FB 1	400	24000	24000
FB 2	800	60000	33406
FB 3	1280	120000	32543

Table 4.2: DBM model parameter bounds and optimization results for each frequency band.

Para-	Bounds		Optimal values		
meter	lower	upper	FB 1	FB 2	FB 3
ϕ	0.38	1	0.94	0.87	0.54
Ξ	1.20 E4	3.60 E4	3.32 E4	2.49 E4	1.63 E4
α_∞	1.25	3.76	3.76	3.11	1.91
Λ	4.50 E−5	1.35 E−4	1.17 E−4	1.35 E−4	1.21 E−4
Λ'	4.50 E−5	1.35 E−4	7.86 E−5	1.35 E−4	1.35 E−4
k_0'	5.70 E−10	3.42 E−9	3.42 E−9	3.42 E−9	1.08 E−9

Table 4.3: JCAL model parameter bounds and optimization results for each frequency band. FB 1: $200 \leq f/\text{Hz} < 500$, FB 2: $500 \leq f/\text{Hz} < 1000$, FB 3: $1000 \leq f/\text{Hz} < 1600$.

Figure 4.2 shows the visualization of the JCAL model parameters' optimization results relative to their individual bounds. The three frequency ranges FB $1-3$ are depicted separately. As a reference, the optimization results are also provided for the case that the optimization is carried out over the whole frequency range $200 \leq f/\text{Hz} < 1600$ (FB 4). The optimization results of FB 4 are close to the ones of the middle frequency band FB 2, as can be seen in Fig. 4.2. The optimal JCAL model parameters Λ, Λ' and k_0' in FB 2 and FB 4 are very close to their corresponding upper bounds, whereas they do not show this behavior in other frequency bands.

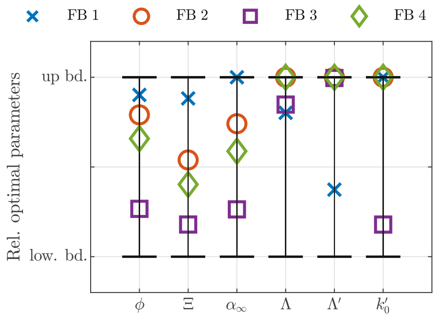

Figure 4.2: Optimal parameters of the JCAL model in each frequency band after the genetic optimization, visualized relative to their bounds.
FB 1: $200 \leq f/\text{Hz} < 500$, FB 2: $500 \leq f/\text{Hz} < 1000$, FB 3: $1000 \leq f/\text{Hz} < 1600$.

In order to determine which model achieves the best description of the used acoustic absorber, the reflection coefficient $\underline{r}$ calculated with the optimal DBM and JCAL model parameters, via (4.24), in comparison to the impedance tube measurement is shown in Fig. 4.3. In Figs. 4.3a and 4.3c, the calculation of the reflection coefficient is performed for each frequency band FB 1 to FB 3 separately with the corresponding model parameters listed in Tab. 4.3. Therefore, the graph of the reflection coefficient – depicted as a thick blue line – is not continuous. Additionally, there are semi-transparent lines plotted in the graph, which correspond to $\underline{r}$-values within frequency ranges outside of the fitted frequency bands. This shows the deviation of the calculated reflection coefficient from the measurement outside those frequency bands, where the optimization was performed.

Suppose the optimization is carried out over the whole frequency range of the measurement, i. e. in the interval $[200, 1600]$ Hz. In that case, the calculated reflection coefficient matches the measurement in no frequency band as well as in the case where the fitting is performed separately, see Figs. 4.3b and 4.3d.

From Fig. 4.3, it becomes clear that the DBM model is not able to approximate the frequency behavior of the used acoustic absorber as well as the JCAL model. Therefore, all further investigations will focus on the material properties inferred via the JCAL model.

Comparing the performance of the JCAL model when all frequencies are fitted (FB 4), one can see that especially the calculated value of the reflection coefficient's imaginary part $\mathrm{Im}\{\underline{r}\}$ deviates more from the measurement in Fig. 4.3d than in Fig. 4.3c. However, it can be concluded that the absorption behavior of the tested material sample can be very well approximated with the JCAL model. Therefore, the hereby identified complex-valued density and compression modulus can be validated in a forward simulation.

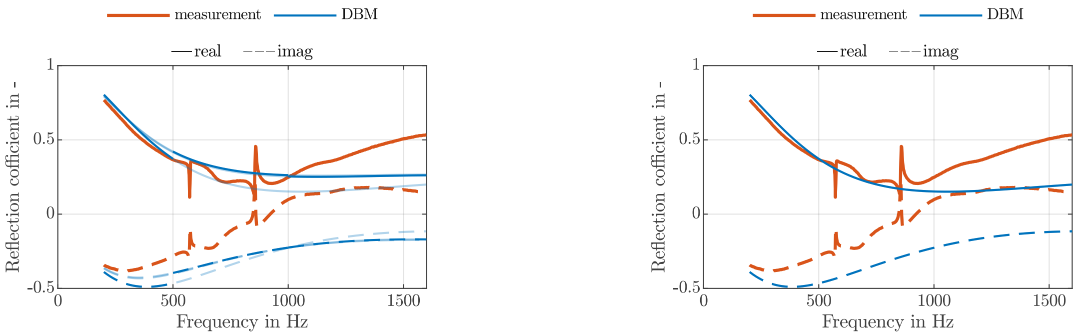

(a) DBM: Optimization performed in separate frequency bands. Calculated values outside of these bands are shown as semi-transparent.

(b) DBM: Optimization performed in the whole frequency range of measurement.

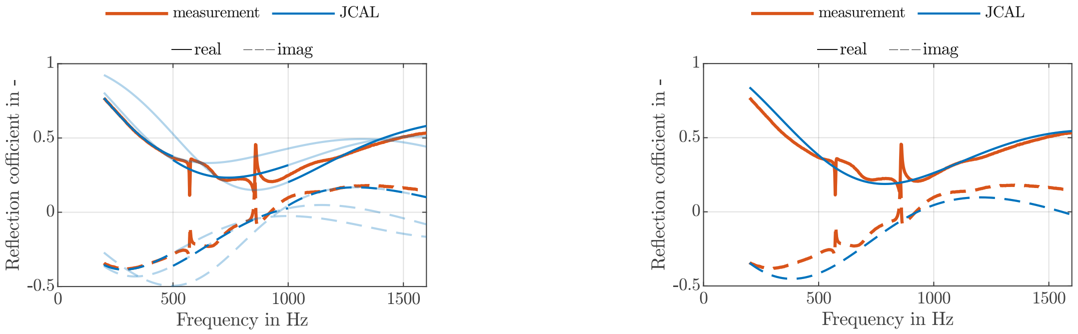

(c) JCAL: Optimization performed in separate frequency bands. Calculated values outside of these bands are shown as semi-transparent.

(d) JCAL: Optimization performed in the whole frequency range of measurement.

Figure 4.3: Calculated reflection coefficient of the material sample with optimal DBM and JCAL material parameters and measured values.

4.2 Validation of the Forward Model

In this section, the material properties $\underline{\rho}_{\text{eff}}$ and $\underline{K}_{\text{eff}}$, which were inferred via the JCAL model and a genetic optimization – described in the section before – are used in a forward acoustic simulation of the measurement trailer. In the following subsections, the Finite Element (FE) model of the used measurement trailer and its validation are presented.

4.2.1 FEM Model of the Used Trailer

In order to simulate the acoustic pressure within the measurement trailer via the Finite Element Method, a three-dimensional model of the trailer has to be generated. First, a CAD model of the trailer, including all acoustically relevant geometries and scatterers, has to be established.

In Fig. 4.4, the trailer is depicted. The enclosure of the measurement trailer is made out of sheet steel, which is assumed to be a sound-hard boundary, i. e. $v_{\text{a,n}} = 0$ at the surfaces of the sheet metal. On the inner surfaces of the enclosure, one layer of an acoustic absorber material is mounted for sound insulation and to absorb the radiated sound from the rolling tires. The thickness of the absorbers is $h = 50\,\text{mm}$. The regions of the absorbers are modeled as separate region in the FE model. Within this absorber region, the density and compression modulus are assumed complex-valued and therefore model the absorbing behavior of the poroelastic material. Details on the modeling of the absorbers can be found in the previous sections.

The trailer's interior consists of two mirror-symmetric chambers with one measurement tire each. The chambers are separated with a double layer of thick sheet metal and absorbers are mounted on each side. The chambers are closed on all sides and the top but completely open at the bottom. The pavement on which the trailer stands is modeled as sound-hard.

(a) Outside of the measurements trailer. ©AIT – Johannes Zinner

(b) Inside of one chamber of the measurements trailer with mounted microphones and loudspeaker in the back.

Figure 4.4: Measurement trailer.

Strut bars, the wheel suspension, microphone mounts, etc., are acoustic obstacles within the trailer where the sound is (partially) reflected, scattered, and diffracted. In order to reduce the effort of meshing, some of the mentioned obstacles are neglected. Whether neglecting an acoustic obstacle is justified, a measure is the acoustic wavelength, which is calculated via (2.64). Since the maximum frequency of interest is 1600 Hz, the minimum wavelength at ambient conditions of 20 °C is $\lambda_{\min} \approx \frac{343\,\text{m/s}}{1600\,\text{Hz}} = 214\,\text{mm}$. Therefore, e. g. thin bars for mounting the microphones with a $20\,\text{mm} \times 40\,\text{mm}$ cross-section are neglected, i. e. modeled as air. Further, all microphone cables, the microphones themselves, bolts and screws etc., are not included in the model. All other scatterers with characteristic dimensions $> 40\,\text{mm}$ are considered and modeled as sound-hard boundaries. Nevertheless, some parts were geometrically simplified. For example, the enclosure is assumed to be a perfect rectangular prism, where, in fact, it is built of folded and reinforced sheet metal, including two doors on each side.

The trailer is variable in height, so the gap between the lateral walls of the enclosure and the pavement is adjustable. For the validation measurements with a loudspeaker and the measurements on the road, the minimum slit size of approximately 80 mm was chosen. This slit represents an impedance jump that causes partial reflections and therefore has to be considered in the FE model. To model the sound propagation to the outside, an air volume around the gap is added. Free sound propagation is assumed outside of the trailer, which means no reflections from the outside back to the interior are considered.

The regions of the forward problem's computational domain Ω are shown in Fig. 4.5. The FE model is clipped such that the interior is visible. In the left chamber (light blue), a loudspeaker is placed for validation measurements, which will be explained in detail later. In the right chamber (dark blue), a cylindrical cavity with sound-hard boundaries represents the measurement tire. The acoustic absorber region with material properties $\underline{\rho}_{\mathrm{eff}}$ and $\underline{K}_{\mathrm{eff}}$ is depicted in pink. On the floor and the absorber's outer boundaries, a sound-hard boundary ($v_{\mathrm{a,n}} = 0$) condition is imposed, where the latter models the trailer's metal sheet enclosure.

The gap around the lower edge of the lateral wall can be seen in the image's lower left and lower right corners. The air volume around the trailer is depicted in light green. In dark green, one can see the computational domain called Perfectly Matched Layer (PML), which models free field radiation outside of the trailer. A detailed explanation of this technique follows later.

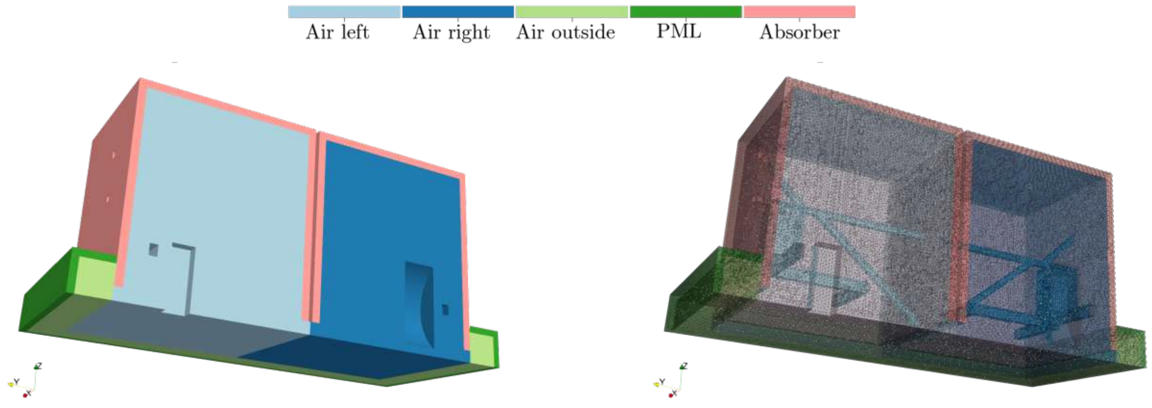

Figure 4.5: Computational domain of the forward problem, clipped to show cavities with sound-hard surfaces to model the loudspeaker in the left chamber and the tire in the right chamber; other sound scatterers and the mesh are visible in the semi-transparent visualization on the right side.

The simplified geometry of the measurement trailer was meshed using tetrahedrons with linear ansatz functions. The mesh size was chosen according to the rule of thumb, which states that at least 10 to 20 linear elements have to be used per wavelength in order to resolve the sound field sufficiently [151]

$$h_{\mathrm{min}} = \frac{\lambda_{\mathrm{min}}}{10} = \frac{1}{10}\frac{c}{f_{\mathrm{max}}} \,. \tag{4.28}$$

This yields a minimum mesh size of $h_{\mathrm{min}} \approx 21$ mm at the highest frequency of interest $f_{\mathrm{max}} = 1600$ Hz. Since the later described Inverse Scheme is computationally demanding, three meshes with different mesh sizes were used to reduce the number of degrees of freedom and therefore the computation time at lower frequencies. The meshes with the lower resolution have a mesh size of $h_{500} = 68$ mm and $h_{1000} = 34\,\mathrm{mm}$, which correspond to 10 linear elements per wavelength at 500 Hz and 1000 Hz, respectively. The resulting number of nodes of the computational mesh can be taken from Tab. 4.4.

f_max in Hz	h in mm	No. nodes
500	68	24.1 E3
1000	34	169.5 E3
1600	21	661.0 E3

Table 4.4: Mesh sizes h for different maximum frequencies f_max and the resulting number of nodes.

A PML (Perfectly Matched Layer) is added to the air volume around the gap to model the free field radiation outside of the trailer. The PML is a damping region within the computational domain, whose specific impedance is matched to the specific impedance of the propagating domain – in this case, the air domain surrounding the gap. Therefore, sound waves can enter the PML region at any arbitrary angle without being reflected. Within the PML region, the sound pressure's amplitude is attenuated such that the amplitude of the sound wave, which is reflected from the sound-hard termination of the PML region back into the air region, is negligible.

The PML technique leads to a modified Helmholtz equation within the PML region, which reads as [151]

$$\underline{\eta}_{x_2}\underline{\eta}_{x_3}\frac{\partial}{\partial x_1}\left(\frac{1}{\underline{\eta}_{x_1}}\frac{\partial \underline{p}_\mathrm{a}}{\partial x_1}\right) + \underline{\eta}_{x_1}\underline{\eta}_{x_3}\frac{\partial}{\partial x_2}\left(\frac{1}{\underline{\eta}_{x_2}}\frac{\partial \underline{p}_\mathrm{a}}{\partial x_2}\right) + \underline{\eta}_{x_1}\underline{\eta}_{x_2}\frac{\partial}{\partial x_3}\left(\frac{1}{\underline{\eta}_{x_3}}\frac{\partial \underline{p}_\mathrm{a}}{\partial x_3}\right) \\ + \underline{\eta}_{x_1}\underline{\eta}_{x_2}\underline{\eta}_{x_3}k^2\underline{p}_\mathrm{a} = 0\,. \tag{4.29}$$

or written in matrix notation, since $\underline{\eta}_{\bar{x}_i} = \underline{\eta}_{\bar{x}_i}(\bar{x}_i)$,

$$\nabla\cdot\left(\underline{\boldsymbol{D}}\,\nabla\underline{p}_\mathrm{a}\right) + \underline{b}k^2\underline{p}_\mathrm{a} = 0\,, \tag{4.30}$$

where

$$\underline{\boldsymbol{D}}(x_i) = \mathrm{diag}\left(\frac{\underline{\eta}_{x_2}\underline{\eta}_{x_3}}{\underline{\eta}_{x_1}},\ \frac{\underline{\eta}_{x_1}\underline{\eta}_{x_3}}{\underline{\eta}_{x_2}},\ \frac{\underline{\eta}_{x_1}\underline{\eta}_{x_2}}{\underline{\eta}_{x_3}}\right)$$

$$\underline{b}(x_i) = \underline{\eta}_{x_1}\underline{\eta}_{x_2}\underline{\eta}_{x_3}\,.$$

In (4.29), the functions $\underline{\eta}_{x_i}$ compute as follows

$$\underline{\eta}_{x_i}(x_i) = 1 + \frac{\sigma_{x_i}(x_i)}{\mathrm{j}\omega}\,, \tag{4.31}$$

where σ_{x_i} is an appropriate damping function and x_i are e. g. the cartesian coordinates x, y, z. For the damping functions σ_{x_i}, different choices are possible. For $\sigma_{x_i} = 0$, it follows that $\underline{\eta}_{x_i}(x_i) = 1$ and (4.29) becomes the standard homogeneous Helmholtz equation (2.52) which means that $\underline{\boldsymbol{D}} = b = 1$ in (4.30).

In this concrete application, the Inverse Distance approach was chosen. In doing so, the damping functions are defined as

$$\sigma_{x_i}(x_i) = \frac{c}{L_\mathrm{PML} - |x_i|}\,, \tag{4.32}$$

where L_PML denotes the thickness of the PML and x_i is zero at the interface between PML and air.

This choice is called *unbounded PML* since

$$\int_0^\infty \sigma_{x_i}\, \mathrm{d}x_i = \infty\,.$$

It was shown that the Inverse Distance damping is optimal for the Helmholtz equation [151, 152]. Within the PML region, the same discretization as in the air domain and a minimum amount of two finite elements along the thickness of the PML was used.

Alternatives to the PML technique are absorbing boundary conditions (ABC) [153] or infinite elements [154]. Further details on the treatment of open domain problems can be found in [151].

The final FE model now needs to be validated. This was achieved by placing a loudspeaker inside the stationary trailer. Thereby, a known acoustic excitation of the trailer is accomplished and a forward simulation of the acoustic pressure can be compared to microphone measurements. In order to model the loudspeaker's moving membrane as an appropriate boundary condition, the membrane velocity was measured with a laser-Doppler-vibrometer (LDV) and subsequently prescribed at the membrane in the FE model.

4.2.2 Modeling of Loudspeaker

The basic idea of modeling a loudspeaker within the acoustic FE simulation is to cut its membrane and housing from the computational mesh. A picture of the used loudspeaker model and the housing is shown in Fig. 4.6a. The loudspeaker is manufactured by Visaton, model FR10 with an impedance of 4 Ω and a membrane diameter of 100 mm [155]. The housing has a quadratic cross-section with an outer dimension of 140 mm and a height of 380 mm. It is made out of aluminum with a thickness of 10 mm and therefore is assumed to be sound-hard.

(a) Photo of loudspeaker.

(b) Surfaces of computational mesh.

Figure 4.6: Used loudspeaker for validation measurements: Visaton FR10 4 Ω, and its aluminum housing.

In the FE model, the normal velocity of the surface is prescribed. This can readily be achieved in the FE framework via the surface term in (2.101). In order to determine the surface velocity $\underline{v}_{\mathrm{a},n}$ as a function of frequency, the loudspeaker was excited with an exponential sweep and the normal component of the mechanic velocity at discrete points of the membrane was measured with an LDV.

The measurement grid is a circular grid with 13 concentric circles with 21 measurement points along each circumference.

The LDV measurements showed that the membrane moves as a rigid body up to a frequency of approximately 1200 Hz. Above this frequency, the rigid body movement is superimposed by a higher-order mode of the membrane. In Fig. 4.7, values of the membrane deflection for the discrete frequencies $f = 200, 800, 1200, 1600\,\text{Hz}$ are shown. The relative displacement z_{rel} is plotted, which computes as

$$z_{\text{rel}}(x, y, f) = \frac{z(x, y, f)}{z_{\text{mid}}(f)}\,, \tag{4.33}$$

where $z_{\text{mid}}(f) = z(x = 0, y = 0, f)$ denotes the midpoint deflection. Note that the outermost circles of measurement points, where $r > 40\,\text{mm}$, are not shown, as the amplitude of the membrane's displacement decreases towards the outer radius due to the mounting of the membrane.

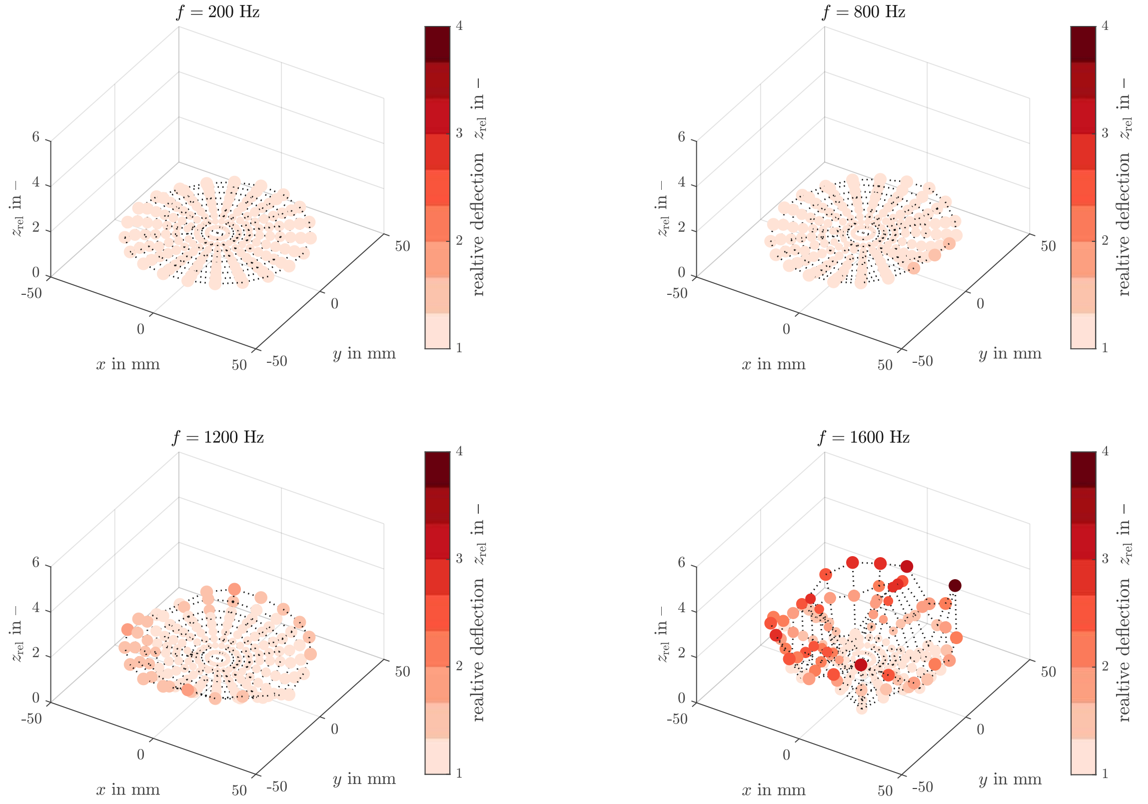

Figure 4.7: Measurements with an LDV of the membrane's ($\mathit{\Gamma}_{\text{mem}}$) deflection relative to the center point measurements of the membrane at 200, 800, 1200, 1600 Hz. Measurement points in a circular grid, only points with $r \leq 40\,\text{mm}$ shown.

Although the assumption of the rigid body movement is not entirely valid for frequencies above 1200 Hz, the boundary condition in the simulation for those frequencies was chosen the same as for $f \leq 1200\,\text{Hz}$: a constant normal surface velocity on a circular surface is prescribed $\underline{v}_{\text{a},n}(\boldsymbol{x}, \omega) = \underline{\hat{v}}(\omega)$. This membrane surface is depicted in red in Fig. 4.6b ($\mathit{\Gamma}_{\text{mem}}$).

A blending function is introduced to take the decreased velocity amplitude near the edge of the membrane into account. The blending function is defined via

$$f_{\text{blend}}(r) = \begin{cases} 1 & \text{for } r < R_{\text{co}} \\ \frac{1}{2}\left[\cos\left(\pi \frac{r-R_{\text{co}}}{R-R_{\text{co}}}\right)+1\right] & \text{for } r \geq R_{\text{co}}\,, \end{cases} \tag{4.34}$$

with the empirically chosen crossover radius $R_{\text{co}} = 29\,\text{mm}$ and the membrane radius $R = 50\,\text{mm}$. A plot of the appropriately scaled blending function can be seen in Fig. 4.8. This figure shows the maximum and minimum membrane displacement, $z_{\min}$ and $z_{\max}$, respectively, as a function of the radial direction $r = \sqrt{x^2+y^2}$. Exemplary, the frequency $f = 500\,\text{Hz}$ is shown. The function $\max\{z_{\text{mem}}\}\, f_{\text{blend}}(r)$ approximates the membrane displacement very well.

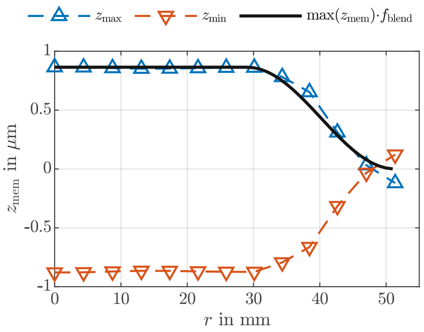

Figure 4.8: Membrane displacement as a function of the radial direction r at top and bottom dead center, $z_{\max}$ and $z_{\min}$, respectively, and appropriately scaled blending function.

Since LDV measurements of the membrane synchronous to microphone measurements are not feasible in a closed measurement trailer, characteristic curves of the membrane's velocity at its center point and the current through the loudspeaker at discrete frequencies $200, 300, \ldots 1600\,\text{Hz}$ were recorded. Different amplifier gains were used. The characteristic curves in amplitude and phase are shown exemplarily for five frequencies in Fig. 4.9. It can be seen that there is a linear relationship between the current I through the loudspeaker and the normal velocity's amplitude in the ranges of interest $I < 1\,\text{A}$ and $f \leq 1600\,\text{Hz}$. From these results, it is possible to calculate the slopes of the characteristic curves and the phase offsets between current and normal velocity at each frequency. Therefore, it is sufficient to measure the current through the loudspeaker synchronously with the microphone data to determine via linear interpolation the correct excitation for the FE simulation – i. e. amplitude and phase of the membrane's normal surface velocity.

As shown in the left graph of Fig. 4.9, the slopes of the characteristic curves vary over the frequency. The slopes can be interpreted as the sensitivity $|\underline{E}_v|$ of the velocity of the membrane's midpoint to the current excitation, whose unit is $\frac{\text{m/s}}{\text{A}}$. In other words, this is the amplitude of the membrane's velocity at its center point at a current of 1 A through the loudspeaker. The phase offsets in the right graph of Fig. 4.9 can be interpreted as the phase φ_{E_v} of the sensitivity $\underline{E}_v$. Plotting the amplitudes and phases of the sensitivity $\underline{E}_v$ over the frequency results in the graphs depicted in Fig. 4.10. It can be observed that, in general, the sensitivity's amplitude is lower at higher frequencies. The phase of the sensitivity has values just above $-\pi/2$, with smaller peaks at $f = 500,\ 900$ and $1300\,\text{Hz}$.

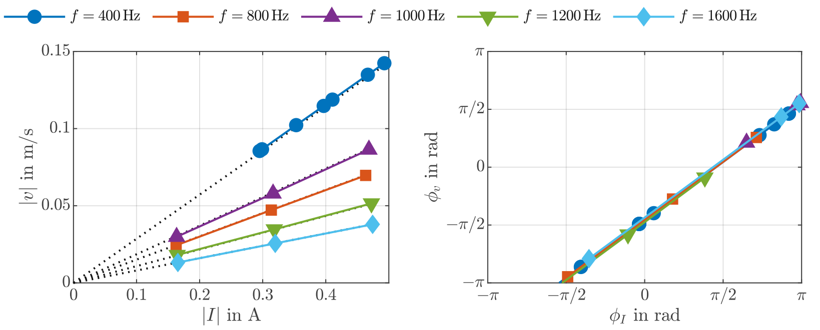

Figure 4.9: Characteristic curves of current I through the loudspeaker and amplitudes and phases of the normal velocity of the membrane's center point; evaluated at discrete frequencies.

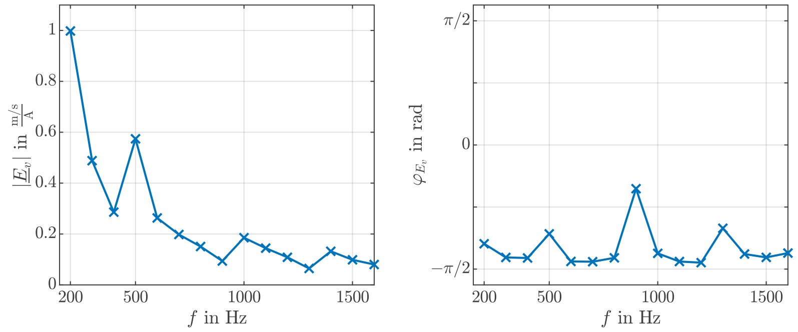

Figure 4.10: Sensitivities of the membrane velocity in amplitude and phase.

4.2.3 Comparison of Simulated and Measured Sound Pressure

With the geometry including all relevant sound-hard scatterers, appropriate model parameters of the acoustic absorbers, and a suitable method to calculate the amplitude of the loudspeaker membrane at discrete frequencies, the forward FE model can be validated with microphone measurements. The loudspeaker with its housing is placed inside the stationary trailer and is excited with a sinusoidal signal at discrete frequencies $f = 200, 300, \ldots 1600\,\mathrm{Hz}$. The current through the loudspeaker is recorded simultaneously with the microphone signals. Inside the trailer, a three-dimensional microphone array consisting of 33 microphones is mounted on mounting bars, see Figs. 4.4b and 4.11. In Fig. 4.11, the outlines of the trailer's left chamber with the loudspeaker, including its housing and the microphone positions, are depicted. The microphones surround the loudspeaker at randomly chosen positions with varying distances to the loudspeaker membrane. Of course, the chosen positions had to be feasible with the mounting bars depicted in Fig. 4.4b. An irregular 3D array surrounding the sound sources is favored over a (regular) 2D array, since it achieves better sound source localization results, even with conventional beamforming-based methods, cf. Sec. 3.1.2.

Subsequently, the Fourier transform of each microphone signal is compared to the simulated acoustic pressure at the microphone positions. Again, it has to be stressed that absolute values of the sound pressures and their phases can be compared as no amplitude scaling or phase offset is necessary since the correct excitation values can be inferred from the electrical current measurements.

The first simulation results with the material properties from the fitting of the calculated reflection coefficient to impedance tube measurements showed an overall good agreement between measured and simulated acoustic pressures. While the qualitative course of the simulated sound pressure amplitudes and phases matches the measurements well, there are larger deviations at some microphones.

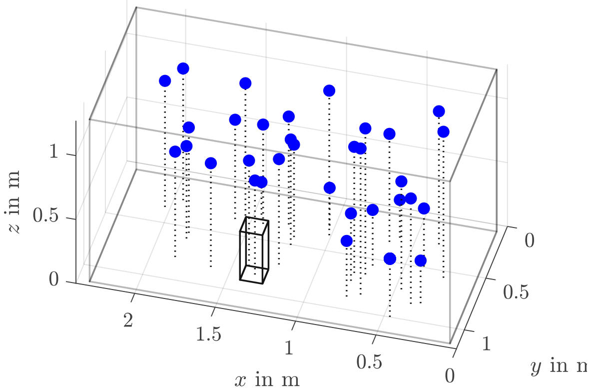

Figure 4.11: Positions at which the sound pressure is measured with microphones and the acoustic pressure is evaluated in the FE simulation; the outlines of the trailer's chamber and the loudspeaker are depicted.

Therefore, an additional, direct fitting of the material parameters was introduced.

Fitting of Material Properties via Microphone Measurements

While in the first fitting of the material properties, the cost function consisted of the measured and calculated reflection coefficient, now the cost function is adjusted to

$$J_p = \sum_{i=1}^{N_\mathrm{m}} \left| \underline{p}_{\mathrm{a,sim}}(\boldsymbol{x}_{\mathrm{m},i}, \underline{K}, \underline{\rho}, \omega) - \underline{p}_{\mathrm{a,meas}}(\boldsymbol{x}_{\mathrm{m},i}, \omega) \right|^2 , \tag{4.35}$$

where $\underline{K}(\omega)$ denotes the complex-valued compression modulus, $\underline{\rho}(\omega)$ the complex density of the porous material and $\boldsymbol{x}_{\mathrm{m},i}$ the microphone positions. In contrast to the cost function (4.22) in the previous fitting, where the summation was carried out over all frequencies within a defined frequency band, it is now carried out over all microphone positions $\boldsymbol{x}_{\mathrm{m},i}$.

The optimization problem for the second fitting reads as

$$\min_{K_\mathrm{Re}, K_\mathrm{Im}, \rho_\mathrm{Re}, \rho_\mathrm{Im}} J_p \,, \tag{4.36}$$

which is again solved with a genetic algorithm. The optimization is performed separately for each frequency of interest. This second optimization requires an FE simulation for each chromosome in each generation. Therefore, the computational demand is significantly higher than in the first optimization, which only required the evaluation of the JCAL model equations for each chromosome. Further, the evaluation of the simulated sound pressures with openCFS has to be included in the genetic optimization workflow of Matlab, which requires customizing internal Matlab functions.

The optimization parameters are the real and imaginary parts of $\underline{K}$ and $\underline{\rho}$. Their bounds $[b_{\square,\mathrm{low}}, b_{\square,\mathrm{up}}]$

are determined as follows

$$\begin{aligned}
b_{K_{\mathrm{Re}},\mathrm{low}} &= 0.5\mathrm{Re}\{\underline{K}_{\mathrm{opt}}\}\,, & b_{K_{\mathrm{Re}},\mathrm{up}} &= 1.5\mathrm{Re}\{\underline{K}_{\mathrm{opt}}\}\\
b_{K_{\mathrm{Im}},\mathrm{low}} &= 0.5\mathrm{Im}\{\underline{K}_{\mathrm{opt}}\}\,, & b_{K_{\mathrm{Im}},\mathrm{up}} &= 1.5\mathrm{Im}\{\underline{K}_{\mathrm{opt}}\}\\
b_{\rho_{\mathrm{Re}},\mathrm{low}} &= 0.5\mathrm{Re}\left\{\underline{\rho}_{\mathrm{opt}}\right\}, & b_{\rho_{\mathrm{Re}},\mathrm{up}} &= 1.5\mathrm{Re}\left\{\underline{\rho}_{\mathrm{opt}}\right\}\\
b_{\rho_{\mathrm{Im}},\mathrm{low}} &= 0.5\mathrm{Im}\left\{\underline{\rho}_{\mathrm{opt}}\right\}, & b_{\rho_{\mathrm{Im}},\mathrm{up}} &= 1.5\mathrm{Im}\left\{\underline{\rho}_{\mathrm{opt}}\right\}\,.
\end{aligned} \tag{4.37}$$

The nominal values $\underline{K}_{\mathrm{opt}}$ and $\underline{\rho}_{\mathrm{opt}}$ in (4.37) are the optimal values from the first optimization of the JCAL model parameters, see Tab. 4.3. Since in this second optimization, the values of $\underline{K}$ and $\underline{\rho}$ are optimized directly without any material model, the optimization result is not guaranteed to provide material parameters of a physically feasible acoustic absorber. However, some effects of the limitations of the FE model mentioned in Sec. 4.2 can be included in the complex fluid domain to improve the match of the simulated sound pressures at the microphone positions to the measurements.

To gauge how well the simulated sound pressure $\underline{p}_{\mathrm{a,sim}}$ matches the measured sound pressure $\underline{p}_{\mathrm{a,meas}}$ at the microphone positions, two relative errors are calculated:

$$\varepsilon_{\mathrm{rel,L2}} = \frac{\left\|\underline{\boldsymbol{p}}_{\mathrm{a,sim}} - \underline{\boldsymbol{p}}_{\mathrm{a,meas}}\right\|_{\mathrm{L2}}}{\left\|\underline{\boldsymbol{p}}_{\mathrm{a,meas}}\right\|_{\mathrm{L2}}} \tag{4.38}$$

$$\varepsilon_{\mathrm{abs,L2}} = \frac{\left\||\underline{\boldsymbol{p}}_{\mathrm{a,sim}}| - |\underline{\boldsymbol{p}}_{\mathrm{a,meas}}|\right\|_{\mathrm{L2}}}{\left\|\underline{\boldsymbol{p}}_{\mathrm{a,meas}}\right\|_{\mathrm{L2}}}\,, \tag{4.39}$$

where $\underline{\boldsymbol{p}}_{\mathrm{a},\square}$ denotes $[N_{\mathrm{m}} \times 1]$ the vector of sound pressures at each of the N_{m} microphone positions. The L2-norm is calculated via

$$\|\underline{\boldsymbol{p}}_{\mathrm{a}}\|_{\mathrm{L2}} = \sqrt{\sum_{i_{\mathrm{m}}=1}^{N_{\mathrm{m}}} |\underline{p}_{\mathrm{a},i_{\mathrm{m}}}|^2}\,. \tag{4.40}$$

While (4.38) takes the complex values and, therefore, the phase differences between simulated and measured sound pressures into account, (4.39) calculates a relative L2-error of the sound pressure amplitudes.

The plots of the calculated relative errors of the acoustic pressures are shown in Fig. 4.12 as a function of frequency. The calculation is carried out for the acoustic pressures of the simulation with complex material parameters calculated with optimal JCAL model parameters (first optimization, orange lines in Fig. 4.12) and with optimal complex material parameters from the second optimization (purple lines Fig. 4.12). As can be seen, both relative errors, $\varepsilon_{\mathrm{rel,L2}}$ and $\varepsilon_{\mathrm{abs,L2}}$, are lower in case of using the material parameters of the second optimization. In general, the relative error $\varepsilon_{\mathrm{rel,L2}}$ is much higher than the relative error value of the pressure amplitudes, $\varepsilon_{\mathrm{abs,L2}}$. Especially the high peaks at 200, 500 and 900 Hz in the curve of the relative error $\varepsilon_{\mathrm{rel,L2}}$ in Fig. 4.12a are not present in $\varepsilon_{\mathrm{abs,L2}}$ in Fig. 4.12b. This fact leads to the assumption that the phase mismatch at these frequencies dominates the error values.

Note that at 900 Hz, the relative error of acoustic pressure amplitudes is higher for the simulation using the material parameters from the second optimization than in case of values from the first optimization, see Fig. 4.12b. While this fact might be surprising at first, it can easily be explained since the cost function of the second optimization, J_p, calculates the difference between the *complex* values of simulated and measured sound pressures. Indeed, the relative error of complex sound pressures decreases for the second optimization at 900 Hz, see Fig. 4.12a.

In order to take a deeper look into the validity of the forward model, the simulated sound pressure's

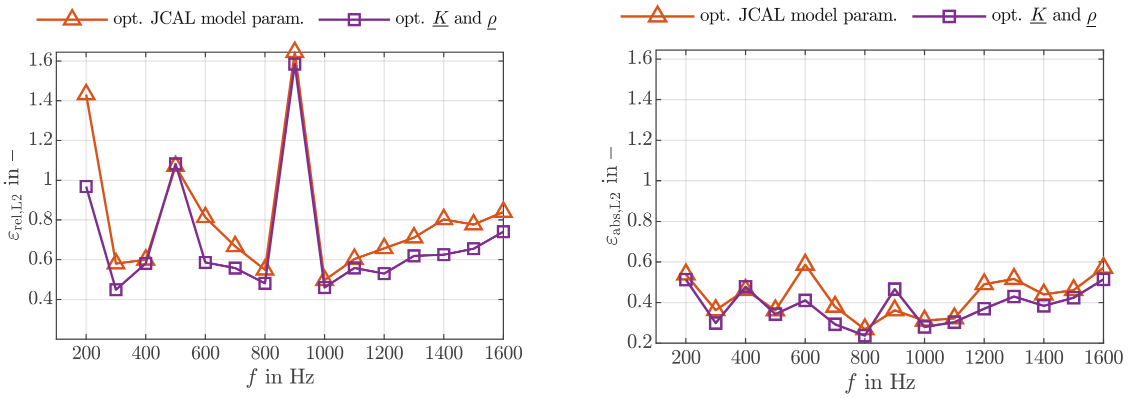

(a) Relative errors of complex-valued sound pressures.

(b) Relative errors of amplitude values of sound pressures.

Figure 4.12: Relative L2 errors between simulated sound pressures and measurements at microphone positions inside the measurement trailer with loudspeaker excitation. The simulation is performed with material parameters from the first (orange lines) and second optimization (purple lines).

amplitude and phase at each microphone are compared to the microphone measurements. In Fig. 4.13 and Fig. 4.14, this is done for characteristic frequencies: frequencies with the highest and lowest relative errors. The simulated and measured sound pressures are plotted as a function of the distance r_{lm} between the microphone points and the center point of the loudspeaker's membrane. Additionally, the distance scaled with the wavelength λ at the corresponding frequency for each microphone point is calculated according to

$$r_{\mathrm{lm,rel}} = \frac{r_{\mathrm{lm}}}{\lambda} \,. \tag{4.41}$$

Again, the plots of the individual acoustic pressures prove that the simulations with material properties obtained via the second optimization, (4.36), is superior to the one where the material properties are fitted with the first optimization (4.25).

Figure 4.13 and Fig. 4.14 show that the overall qualitative course of the sound pressure's amplitude and phase match the measurements well at most microphone positions. This is also the case for frequencies with higher relative errors, e. g. at 500 Hz. At this frequency, single microphone points, such as microphones with $r_{\mathrm{lm}} = 0.71\,\mathrm{m}$ and $r_{\mathrm{lm}} = 1.01\,\mathrm{m}$, show more significant errors in amplitude than other microphones. Additionally, there is a constant phase offset between simulation and measurement. The constant phase offset can also be observed at 900 Hz. These two factors lead to high relative overall errors.

Other reasons for the deviations between simulation and measurement may be the simplifications of the CAD model concerning its geometry and the assumption of the membrane's rigid body movement, which is not entirely true for higher frequencies – this may explain the rise of the L2 errors for frequencies $f > 1000\,\mathrm{Hz}$. Further, the used current sensor module for measuring the current through the loudspeaker may cause phase errors, which could explain the significant phase offset between measured and simulated sound pressures at specific frequencies. Since at frequencies of 500 and 900 Hz the phase offset between measurement and simulation is high, and at those frequencies also the peaks in the phase offset between current and membrane velocity occur – see right graph in Fig. 4.10 – the assumption of an error in the current measurement module seems plausible.

All microphones are calibrated using a Brüel & KjærSound Calibrator, Type 4231 [156], which operates at 1 kHz. Other frequencies are not calibrated; therefore, some microphones may show deviations in phase and amplitude from the real values. Another uncertainty is the microphone

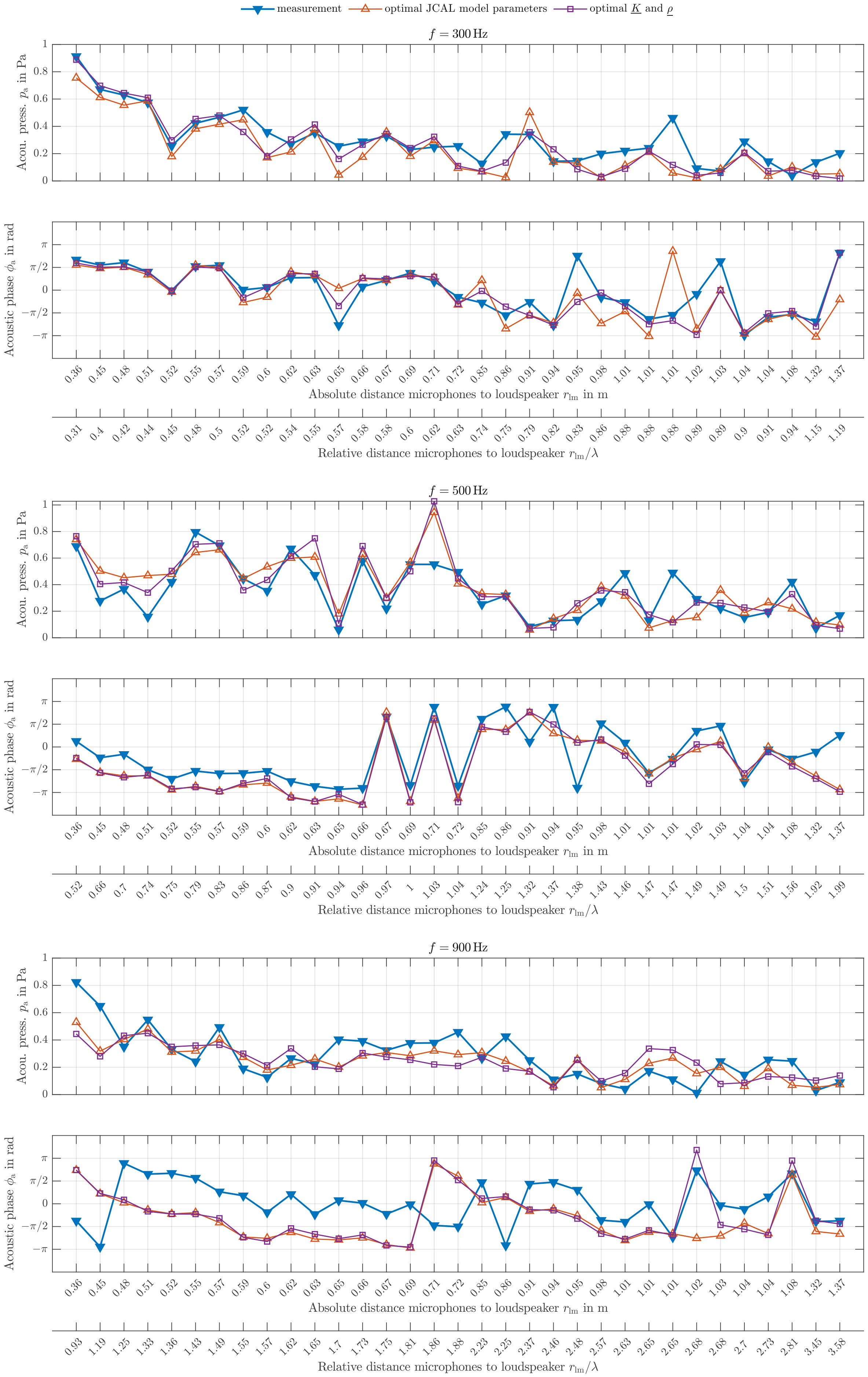

Figure 4.13: Comparison of simulated sound pressures at microphone positions with measurements at 300 Hz, 500 Hz and 900 Hz; material parameters obtained with different optimizations.

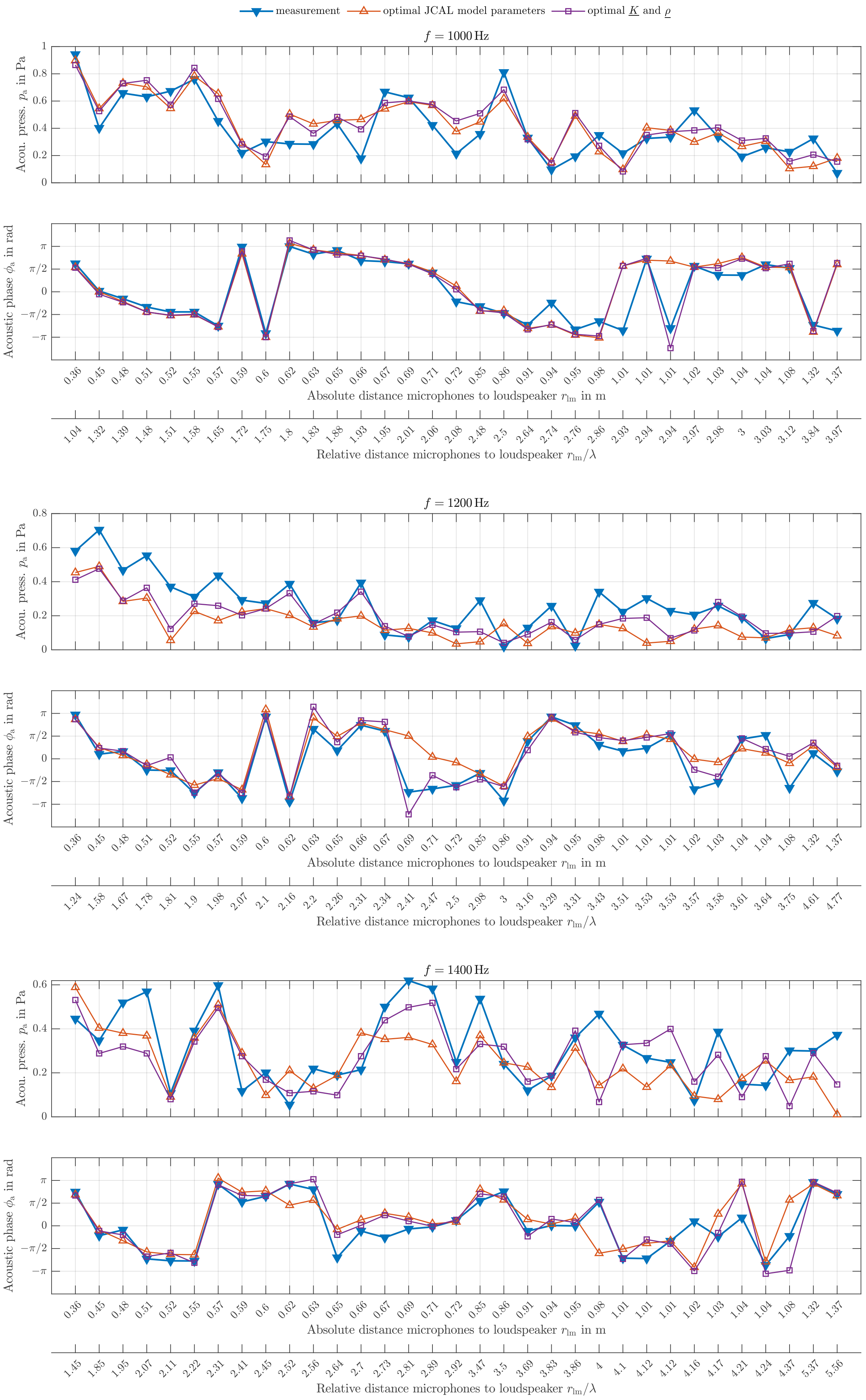

Figure 4.14: Comparison of simulated sound pressures at microphone positions with measurements at 1000 Hz, 1200 Hz and 1400 Hz; material parameters obtained with different optimizations.

positions, since they are measured manually. The maximum positioning error is estimated to be 5–10 mm.

However, the overall validation result is satisfying, and it can be concluded that the forward model of the trailer is suitable for the sound source localization calculations with the Inverse Scheme. Although there are significant deviations at some frequencies and microphone positions, one has to bear in mind that the comparison is done in Pascal (Pa). The commonly used value in acoustics, however, is the sound pressure level, L_{p_a}, which is defined by

$$L_{p_\mathrm{a}} = 20 \log_{10} \left(\frac{p_\mathrm{a,rms}}{p_0} \right) , \tag{4.42}$$

with

$$p_\mathrm{a,rms} = \sqrt{\frac{1}{T} \int\limits_0^T p_\mathrm{a}(t)} \,, \quad p_0 = 20\,\mathrm{\mu Pa} \,.$$

The absolute deviation of simulated and measured sound pressure level, averaged over all N_f frequencies and N_m microphone, is

$$L_\mathrm{err} = \frac{1}{N_\mathrm{f}} \sum_{i_\mathrm{f}=1}^{N_\mathrm{f}} L_{i_\mathrm{f},\mathrm{err}} = \begin{cases} 6.43\,\mathrm{dB} & \text{First optimization} \\ 5.59\,\mathrm{dB} & \text{Second optimization} \end{cases} , \tag{4.43}$$

where

$$L_{i_\mathrm{f},\mathrm{err}} = \sqrt{\frac{1}{N_\mathrm{m}} \sum_{i_\mathrm{m}=1}^{N_\mathrm{m}} |L_{i_\mathrm{m},\mathrm{meas}} - L_{i_\mathrm{m},\mathrm{sim}}|^2} \,. \tag{4.44}$$

CHAPTER 5

The Inverse Problem

The Inverse Scheme for sound source localization was first presented by Kaltenbacher et al. in [157].

The acoustic forward problem is defined by the Helmholtz equation (2.52), which is the wave equation in the frequency domain. This partial differential equation solves for the acoustic pressure $\underline{p}_\mathrm{a}(\boldsymbol{x},\omega)$ with a given source distribution $\underline{\boldsymbol{\mathcal{F}}}(\boldsymbol{x},\omega)$. The considered inverse problem is to reconstruct the source distribution $\underline{\boldsymbol{\mathcal{F}}}(\boldsymbol{x},\omega)$ within a finite region $\boldsymbol{x} \in \mathit{\Omega}_\mathrm{sc}$ from microphone measurements $\underline{p}_i^\mathrm{ms}$ at the microphone positions $\boldsymbol{x}_{\mathrm{m},i} \in \mathit{\Omega} \setminus \mathit{\Omega}_\mathrm{sc}$ via minimizing the difference $\sum_i |\underline{p}_\mathrm{a}(\boldsymbol{x}_{\mathrm{m},i}) - \underline{p}_i^\mathrm{ms}|^2$ between the microphone measurements $\underline{p}_i^\mathrm{ms}$ and FE simulations $\underline{p}_\mathrm{a}(\boldsymbol{x}_{\mathrm{m},i})$. Since the inverse problem is ill-posed in the sense of Hadamard, see definition 2.2.1, a regularization is required.

The following sections describe the mathematical and physical model and address the optimization problem and its regularization. These sections are based on [157]. Further, sound source identification results using virtual measurements and microphone measurements of the stationary setup, described in the chapter before, will be presented.

5.1 Mathematical Formulation

The governing equation is the weak form of the Helmholtz equation (2.100), which can be expanded without any restrictions to the more general Helmholtz equation for an inhomogeneous medium (4.19). Since the relation

$$\begin{aligned}\int\limits_{\mathit{\Omega}} \nabla \frac{1}{\rho(\boldsymbol{x})} \cdot \nabla \underline{p}_\mathrm{a} \underline{\overline{w}} \,\mathrm{d}\boldsymbol{x} &= \int\limits_{\mathit{\Omega}} \nabla \cdot \left(\frac{1}{\rho(\boldsymbol{x})} \nabla \underline{p}_\mathrm{a} \underline{\overline{w}} \right) \mathrm{d}\boldsymbol{x} - \int\limits_{\mathit{\Omega}} \frac{1}{\rho(\boldsymbol{x})} \nabla \underline{p}_\mathrm{a} \cdot \nabla \underline{\overline{w}} \,\mathrm{d}\boldsymbol{x} \\ &= \int\limits_{\partial\mathit{\Omega}} \frac{1}{\rho(\boldsymbol{x})} \nabla \underline{p}_\mathrm{a} \underline{\overline{w}} \cdot \mathrm{d}\boldsymbol{s} - \int\limits_{\mathit{\Omega}} \frac{1}{\rho(\boldsymbol{x})} \nabla \underline{p}_\mathrm{a} \cdot \nabla \underline{\overline{w}} \,\mathrm{d}\boldsymbol{x}\end{aligned} \tag{5.1}$$

holds, the weak form of (4.19) is equal to (2.100). We will use this to include acoustic absorbers in the computational domain.

In order to include also monopole sources that are described via the delta distribution, the weak form of the inhomogeneous Helmholtz equation is rewritten as

$$\int_{\Omega} \left(\nabla \underline{p}_{\mathrm{a}} \cdot \nabla \overline{\underline{w}} + k^2 \underline{p}_{\mathrm{a}}\, \overline{\underline{w}}\right) \mathrm{d}\boldsymbol{x} = -\left\langle \underline{\boldsymbol{\mathcal{F}}}^{\mathrm{in}} + \underline{\boldsymbol{\mathcal{F}}}^{\mathrm{bd}}, \overline{\underline{w}} \right\rangle_{W^*,W} \qquad \forall \underline{w} \in W\,. \tag{5.2}$$

In (5.2), $\underline{\boldsymbol{\mathcal{F}}}^{\mathrm{in}}$ denotes sources located at positions $\boldsymbol{x}_{\mathrm{sc},n} \in \Omega_{\mathrm{sc}}$ within the source domain Ω_{sc} and $\underline{\boldsymbol{\mathcal{F}}}^{\mathrm{bd}} = \nabla \underline{p}_{\mathrm{a}} \cdot \boldsymbol{n}$ denotes sources at the boundaries $\partial\Omega_{\mathrm{sc}}$. W is a real Hilbert space with the inner product

$$(\underline{v}, \underline{w}) = \mathrm{Re}\left\{ \int_{\Omega} \left(\nabla \underline{v} \cdot \nabla \overline{\underline{w}} + \underline{v}\, \overline{\underline{w}}\right) \mathrm{d}\boldsymbol{x} \right\}$$

and W^* its dual.

We split the acoustic pressure $\underline{p}_{\mathrm{a}}$ and the test function $\underline{w}$ in the variational problem (5.2) into real and imaginary parts

$$\underline{p}_{\mathrm{a}} = p_{\mathrm{a,Re}} + \mathrm{j} p_{\mathrm{a,Im}} \tag{5.3}$$

$$\overline{\underline{w}} = w_{\mathrm{Re}} - \mathrm{j} w_{\mathrm{Im}}\,. \tag{5.4}$$

Since it can readily be proven that the imaginary part of (5.2) is redundant, only the real part will be considered. Rewriting the weak form of the Helmholtz equation in terms of real values amounts to

$$\begin{aligned} \mathrm{Re}\left\{ \int_{\Omega} \left(\nabla \underline{p}_{\mathrm{a}} \cdot \nabla \overline{\underline{w}} + k^2 \underline{p}_{\mathrm{a}}\, \overline{\underline{w}}\right) \mathrm{d}\boldsymbol{x} \right\} &= \\ \int_{\Omega} \left(\nabla p_{\mathrm{a,Re}} \cdot \nabla w_{\mathrm{Re}} + \nabla p_{\mathrm{a,Im}} \cdot \nabla w_{\mathrm{Im}} - k^2 (p_{\mathrm{a,Re}} w_{\mathrm{Re}} + p_{\mathrm{a,Im}} w_{\mathrm{Im}})\right) \mathrm{d}\boldsymbol{x} &= \\ -\mathrm{Re}\left\{ \left\langle \underline{\boldsymbol{\mathcal{F}}}^{\mathrm{in}} + \underline{\boldsymbol{\mathcal{F}}}^{\mathrm{bd}}, \underline{w} \right\rangle_{W^*,W} \right\}&. \end{aligned} \tag{5.5}$$

The same considerations hold for a PML region, where the Helmholtz equation is extended to (4.30), see [157]. The left-hand side of (5.5) is defined as $A(\underline{p}_{\mathrm{a}}, \underline{w})$. Since we divide it into real and imaginary parts, it also becomes clear that

$$\begin{aligned} A(\underline{p}_{\mathrm{a}}, \underline{w}) &= \mathrm{Re}\left\{ \int_{\Omega} \left(\nabla \underline{p}_{\mathrm{a}} \cdot \nabla \overline{\underline{w}} + k^2 \underline{p}_{\mathrm{a}}\, \overline{\underline{w}}\right) \mathrm{d}\boldsymbol{x} \right\} \\ &= A(\overline{\underline{p}}_{\mathrm{a}}, \overline{\underline{w}}) \end{aligned} \tag{5.6}$$

defines a nonsymmetric bilinear form on W. Since we can consider the model, which will later be included as a constraint in our inverse problem, as a linear equation of $p_{\mathrm{a,Re}}$ and $p_{\mathrm{a,Im}}$ in real function spaces, we can conclude that while the squared complex value $\underline{w} \mapsto |\underline{w}|^2$ is not complex Gâteaux differentiable, the expression $w_{\mathrm{Re}}, w_{\mathrm{Im}} \mapsto w_{\mathrm{Re}}^2 + w_{\mathrm{Im}}^2$ is real differentiable with respect to w_{Re} and w_{Im}.

In this thesis, sound sources are modeled as delta distributions, i. e. monopole sources. This leads to the ansatz

$$\underline{\boldsymbol{\mathcal{F}}}^{\mathrm{in}} + \underline{\boldsymbol{\mathcal{F}}}^{\mathrm{bd}} = \sum_{n=1}^{N_{\mathrm{sc}}} a_n \mathrm{e}^{\mathrm{j}\varphi_n} \delta(\boldsymbol{x}_{\mathrm{sc},n})\,, \tag{5.7}$$

with the total number of sources $N_{\mathrm{sc}} = N_{\mathrm{in}} + N_{\mathrm{bd}}$, where N_{in} is the number of sources within the volume Ω_{sc} and N_{bd} is the number of sources on the boundary $\partial\Omega_{\mathrm{sc}}$. The amplitudes and phases of the nth source are denoted by a_n and φ_n, respectively. Due to the properties of the delta distribution, the inner product in (5.2) becomes

$$\left\langle \underline{\boldsymbol{\mathcal{F}}}^{\mathrm{in}} + \underline{\boldsymbol{\mathcal{F}}}^{\mathrm{bd}}, \overline{\underline{w}} \right\rangle_{W^*,W} = \sum_{n=1}^{N_{\mathrm{sc}}} a_n \mathrm{e}^{\mathrm{j}\varphi_n} \overline{\underline{w}}(\boldsymbol{x}_{\mathrm{sc},n})\,, \tag{5.8}$$

if the test functions $\underline{w} \in W$ are continuous at $\boldsymbol{x}_{\mathrm{sc},n}$. This is provided by using the Sobolev space $W = W^{1,r}$, with $r > d$, where $\varOmega \in \mathbb{R}^d,\ d \in [2, 3]$.

More general cases, where the sources are modeled as sums of smooth functions, e. g. Gaussian functions and with the use of the finite element ansatz functions, or as the normal component $\underline{v}_{\mathrm{a,n}}$ of the acoustic particle velocity $\underline{v}_{\mathrm{a}}$ on $\partial\varOmega_{\mathrm{sc}}$, are covered in [157] and [158], respectively.

The unknown amplitudes and phases of the sound sources are the parameters of the underlying parameter identification problem. It is ill-posed in the sense of Hadamard, and, therefore a regularization – in this case by means of Tikhonov – is needed.

Solving for the unknown parameters amounts to the following constrained optimization problem

$$\begin{aligned} &\min_{\underline{p}_{\mathrm{a}} \in U,\, \underline{a} \in \mathbb{R}^{N_{\mathrm{sc}}},\, \varphi \in [-\pi/2, \pi/2]^{N_{\mathrm{sc}}}} J(\underline{p}_{\mathrm{a}}, a, \varphi) \\ &\text{s.t.} \quad A(\underline{p}_{\mathrm{a}}, \underline{w}) = -\mathrm{Re}\left\{ \left\langle \underline{\boldsymbol{\mathcal{F}}}^{\mathrm{in}} + \underline{\boldsymbol{\mathcal{F}}}^{\mathrm{bd}}, \overline{\underline{w}} \right\rangle_{W^*,W} \right\} \qquad \forall \underline{w} \in W\,. \end{aligned} \tag{5.9}$$

Note, that the source phases φ_n are subject to a box constraint $-\pi/2 \leq \varphi_n \leq \pi/2$. Therefore, the source's amplitudes can also take negative values to cover the whole complex plane.

Since the Inverse Scheme is defined in the frequency domain, any dependency on the angular frequency $\omega = 2\pi f$ will be omitted in further notations. In (5.9), J is a functional, defined as the difference of microphone measurements $\underline{p}_i^{\mathrm{ms}}$ and simulated acoustic pressures $\underline{p}_{\mathrm{a}}$ at the same microphone positions $\boldsymbol{x}_{\mathrm{m},i}$ and a Tikhonov regularization. The definition of the functional reads as

$$\begin{aligned} J(\underline{p}_{\mathrm{a}}, a, \varphi) = {} & \frac{\varPhi}{2} \sum_{i=1}^{N_{\mathrm{m}}} \left| \underline{p}_{\mathrm{a}}(\boldsymbol{x}_{\mathrm{m},i}) - \underline{p}_i^{\mathrm{ms}} \right|^2 \\ & + \alpha_{\mathrm{r}} \sum_{n=1}^{N_{\mathrm{sc}}} |a_n|^q + \beta \sum_{n=1}^{N_{\mathrm{sc}}} \varphi_n^2 - \varrho \sum_{n=1}^{N_{\mathrm{sc}}} \left[\ln\left(\frac{\pi}{2} + \varphi_n\right) + \ln\left(\frac{\pi}{2} - \varphi_n\right) \right]\,, \end{aligned} \tag{5.10}$$

where $\varPhi$ is an appropriately chosen scaling factor to ensure convergence and to avoid rounding errors for small values of pressures $\underline{p}_{\mathrm{a}}$ and $\underline{p}_i^{\mathrm{ms}}$. The factors α_{r} and β are the regularization parameters of source amplitude and phase, respectively. The last term with the parameter ϱ ensures the phase's box constraint and avoids phase-wrapping effects. If $\varPhi \neq 1$, the identified sound source amplitudes must be scaled back by $\frac{1}{\varPhi}$ to receive the correct amplitudes for the unscaled problem.

The exponent q is chosen within $(1, 2]$. If chosen close to unity, it leads to sparser sound source reconstructions. The regularization parameters α_{r} and β are chosen according to

$$\alpha_{\mathrm{r}} = \alpha_{\mathrm{r},0} 2^{-m}, \qquad \beta = \beta_0 2^{-m}\,, \tag{5.11}$$

with starting values $\alpha_{\mathrm{r},0}$ and β_0, where m is the smallest exponent such that the inequality

$$\sqrt{\sum_{i=1}^{N_{\mathrm{m}}} \left| \underline{p}_{\mathrm{a}}(\boldsymbol{x}_{\mathrm{m},i}) - \underline{p}_i^{\mathrm{ms}} \right|^2} \leq \varepsilon_{\mathrm{m}} \tag{5.12}$$

is fulfilled. Here, ε_{m} denotes the measurement error. This principle is called the *sequential discrepancy principle*, see e. g. [159].

Sound source identification results with the Inverse Scheme tended to have phase values close to $\pm\frac{\pi}{2}$.

This could be observed mainly at source points with low amplitudes because of the low sensitivity of the resulting sound pressure to changes in the sound source's phase values. Therefore, an alternative phase regularization is introduced. The new β-term is defined as

$$-\beta \sum_{n=1}^{N_{\mathrm{sc}}} \ln \left[\left(\frac{a_n + \epsilon}{\max\{|a_n|\} + \epsilon} \right)^2 \right] \varphi_n^2 \,. \tag{5.13}$$

A small value ϵ is introduced to avoid the pole for $a_n = 0$. Note that the β-term now has a negative sign. In Fig. 5.1, the Tikhonov regularization terms in (5.10) are plotted as functions of the source amplitude a_n and phase φ_n. The x-axis in the plots is the scaled source amplitude $\frac{a_n}{\max\{|a_n|\}}$ and the source phase φ_n, respectively.

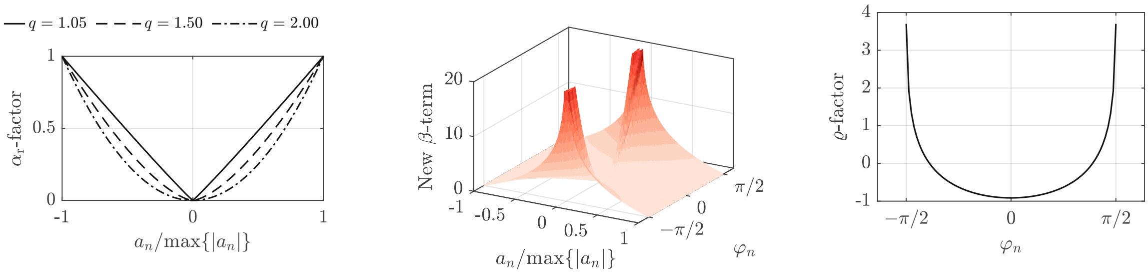

(a) Amplitude regularization for different exponents of q.

(b) New phase regularization.

(c) Regularization of phase's box constraint.

Figure 5.1: Tikhonov regularization terms of the Inverse Scheme. Plotted are the sums in (5.10) that are scaled with α_{r}, β and ϱ, respectively, as functions of scaled source amplitude and source phase.

To solve (5.9), we use a gradient method which will be computed using the adjoint approach. The application of the adjoint method will be discussed in detail in Sec. 5.1.1. A Lagrange functional is defined as

$$\mathcal{L}(a, \underline{p}_{\mathrm{a}}, \varphi, \underline{z}) = J(\underline{p}_{\mathrm{a}}, a, \varphi) + A(\underline{p}_{\mathrm{a}}, \underline{z}) + \mathrm{Re}\left\{ \sum_{n=1}^{N_{\mathrm{sc}}} a_n \mathrm{e}^{\mathrm{j}\varphi_n} \overline{\underline{w}}(\boldsymbol{x}_{\mathrm{sc},n}) \right\} , \tag{5.14}$$

with an adjoint state $\underline{z}$. Note that the source model has already been incorporated in (5.14). Due to the use of the adjoint state $\underline{z}$, we do not need a classical Lagrange multiplier λ_n, as defined in (2.114).

5.1.1 Computation of the Gradient

We define the reduced functional

$$j(a, \varphi) = J(\underline{p}_{\mathrm{a}}(a, \varphi), a, \varphi) \,, \tag{5.15}$$

where $\underline{p}_{\mathrm{a}}$ has to satisfy the constraint

$$\forall \underline{w} \in W : \;\; A(\underline{p}_{\mathrm{a}}, \underline{w}) = -\mathrm{Re}\left\{ \sum_{n=1}^{N_{\mathrm{sc}}} a_n \mathrm{e}^{\mathrm{j}\varphi_n} \overline{\underline{w}}(\boldsymbol{x}_{\mathrm{sc},n}) \right\} . \tag{5.16}$$

Due to the regularity of the constraint, a minimizer of the optimization problem has to satisfy the following first-order optimality conditions

$$0 = \frac{\partial}{\partial a_n} j(a,\varphi) = \frac{\partial}{\partial \underline{p}_{\mathrm{a}}} J(\underline{p}_{\mathrm{a}}(a,\varphi),a,\varphi)\frac{\partial}{\partial a_n}\underline{p}_{\mathrm{a}}(a,\varphi) + \frac{\partial}{\partial a_n} J(\underline{p}_{\mathrm{a}}(a,\varphi),a,\varphi) \tag{5.17}$$

$$0 = \frac{\partial}{\partial \varphi_n} j(a,\varphi) = \frac{\partial}{\partial \underline{p}_{\mathrm{a}}} J(\underline{p}_{\mathrm{a}}(a,\varphi),a,\varphi)\frac{\partial}{\partial \varphi_n}\underline{p}_{\mathrm{a}}(a,\varphi) + \frac{\partial}{\partial \varphi_n} J(\underline{p}_{\mathrm{a}}(a,\varphi),a,\varphi)\,. \tag{5.18}$$

The expressions $\partial \underline{p}_{\mathrm{a}}/\partial a_n$ and $\partial \underline{p}_{\mathrm{a}}/\partial \varphi_n$ are called sensitivities as they are the partial derivative of the solution quantity of the model with respect to the source amplitudes and phases. To directly calculate the gradient, $2N_{\mathrm{sc}}$ state equations have to be solved, which can be computationally costly since N_{sc} can be very large. In the Finite Element framework, the number of nodes within Ω_{sc} determines N_{sc}. Therefore, the number of possible source locations depends on the mesh size and the choice of the source domain Ω_{sc}. To avoid the direct calculation of the sensitivities, the adjoint approach is chosen.

The derivatives

$$\frac{\partial}{\partial a_n} j(a,\varphi) = \frac{\mathrm{d}}{\mathrm{d}a_n} J(\underline{p}_{\mathrm{a}}(a,\varphi),a,\varphi),$$

$$\frac{\partial}{\partial \varphi_n} j(a,\varphi) = \frac{\mathrm{d}}{\mathrm{d}\varphi_n} J(\underline{p}_{\mathrm{a}}(a,\varphi),a,\varphi)$$

can be expressed as

$$\begin{aligned}\frac{\mathrm{d}}{\mathrm{d}a_n} J(\underline{p}_{\mathrm{a}}(a,\varphi),a,\varphi) &= \frac{\mathrm{d}}{\mathrm{d}a_n}\Big(\mathcal{L}(\underline{p}_{\mathrm{a}}(a,\varphi),a,\varphi,\underline{z})\Big)\\ &= \frac{\partial}{\partial \underline{p}_{\mathrm{a}}}\mathcal{L}(\underline{p}_{\mathrm{a}}(a,\varphi),a,\varphi,\underline{z})\frac{\partial}{\partial a_n}\underline{p}_{\mathrm{a}}(a,\varphi) + \frac{\partial}{\partial a_n}\mathcal{L}(\underline{p}_{\mathrm{a}}(a,\varphi),a,\varphi,\underline{z})\,,\end{aligned} \tag{5.19}$$

$$\begin{aligned}\frac{\mathrm{d}}{\mathrm{d}\varphi_n} J(\underline{p}_{\mathrm{a}}(a,\varphi),a,\varphi) &= \frac{\mathrm{d}}{\mathrm{d}\varphi_n}\Big(\mathcal{L}(\underline{p}_{\mathrm{a}}(a,\varphi),a,\varphi,\underline{z})\Big)\\ &= \frac{\partial}{\partial \underline{p}_{\mathrm{a}}}\mathcal{L}(\underline{p}_{\mathrm{a}}(a,\varphi),a,\varphi,\underline{z})\frac{\partial}{\partial \varphi_n}\underline{p}_{\mathrm{a}}(a,\varphi) + \frac{\partial}{\partial \varphi_n}\mathcal{L}(\underline{p}_{\mathrm{a}}(a,\varphi),a,\varphi,\underline{z})\,,\end{aligned} \tag{5.20}$$

since $\underline{p}_{\mathrm{a}}(a,\varphi)$ satisfies the constraint (5.16).

By setting $\frac{\partial}{\partial \underline{p}_{\mathrm{a}}}\mathcal{L}$ to zero, which defines the adjoint equation, the calculation of the sensitivities can be avoided. In the following, we derive the first-order optimality conditions, with the adjoint state $\underline{z}$ and $n = 1,\dots,N_{\mathrm{sc}}$

$$\begin{aligned}0 &= \frac{\partial}{\partial a_n}\mathcal{L}(a,\varphi,\underline{p}_{\mathrm{a}},\underline{z})\\ &= \alpha_{\mathrm{r}} q |a_n|^{q-1}\mathrm{sign}(a_n) - 2\beta\frac{\varphi_n^2}{a_n+\epsilon} + \mathrm{Re}\big\{\mathrm{e}^{\mathrm{j}\varphi_n}\overline{\underline{z}}(\boldsymbol{x}_{\mathrm{sc},n})\big\}\end{aligned} \tag{5.21}$$

$$\begin{aligned}0 &= \frac{\partial}{\partial \varphi_n}\mathcal{L}(a,\varphi,\underline{p}_{\mathrm{a}},\underline{z})\\ &= -2\beta\varphi_n\ln\left(a_n^2\right) + 2\varrho\frac{\varphi_n}{\left(\frac{\pi}{2}-\varphi_n\right)\left(\frac{\pi}{2}+\varphi_n\right)} - a_n\mathrm{Im}\big\{\mathrm{e}^{\mathrm{j}\varphi_n}\overline{\underline{z}}(\boldsymbol{x}_{\mathrm{sc},n})\big\}\end{aligned} \tag{5.22}$$

$$\begin{aligned} 0 &= \frac{\partial}{\partial \underline{p}_{\mathrm{a}}} \mathcal{L}(a, \varphi, \underline{p}_{\mathrm{a}}, \underline{z})[\underline{v}] \\ &= A(\underline{v}, \underline{z}) + \Phi \sum_{i=1}^{N_{\mathrm{m}}} \mathrm{Re}\Big\{ (\underline{p}_{\mathrm{a}}(\boldsymbol{x}_{\mathrm{m},i}) - \underline{p}_i^{\mathrm{ms}}) \overline{\underline{v}}(\boldsymbol{x}_{\mathrm{m},i}) \Big\} \qquad \text{for } \underline{v} \in U \end{aligned} \tag{5.23}$$

$$\begin{aligned} 0 &= \frac{\partial}{\partial \underline{z}} \mathcal{L}(a, \varphi, \underline{p}_{\mathrm{a}}, \underline{z})[\underline{w}] \\ &= A(\underline{p}_{\mathrm{a}}, \underline{w}) + \Phi \sum_{n=1}^{N_{\mathrm{sc}}} a_n \mathrm{Re}\{ \mathrm{e}^{\mathrm{j}\varphi_n} \overline{\underline{z}}(\boldsymbol{x}_{\mathrm{sc},n}) \} \qquad \text{for } \underline{w} \in W \end{aligned} \tag{5.24}$$

(5.24) represents the derivative in the direction of $\underline{w} \in W$ with respect to the adjoint variable $\underline{z}$. Carrying out the derivative results in the scaled state equation. (5.23) is the linearized directional derivative of the Lagrange functional with respect to $\underline{p}_{\mathrm{a}}$ and defines the aforementioned adjoint equation. To derive the stated result, we approximate the derivative with respect to $\underline{p}_{\mathrm{a}}$

$$\begin{aligned} \frac{\partial}{\partial \underline{p}_{\mathrm{a}}} \mathcal{L}(a, \varphi, \underline{p}_{\mathrm{a}}, \underline{z})[\underline{v}] &\approx \mathcal{L}(\underline{p}_{\mathrm{a}} + \underline{v}) - \mathcal{L}(\underline{p}_{\mathrm{a}}) \\ &= J(\underline{p}_{\mathrm{a}} + \underline{v}, a, \varphi) - A(\underline{p}_{\mathrm{a}} + \underline{v}, \underline{z}) - J(\underline{p}_{\mathrm{a}}, a, \varphi) + A(\underline{p}_{\mathrm{a}}, \underline{z}) \,, \end{aligned} \tag{5.25}$$

where

$$J(\underline{p}_{\mathrm{a}} + \underline{v}, a, \varphi) = \frac{\Phi}{2} \sum_{i=1}^{N_{\mathrm{m}}} \left| \underline{p}_{\mathrm{a},i} + \underline{v}_i - \underline{p}_i^{\mathrm{ms}} \right|^2 + R(a, \varphi), \tag{5.26}$$

$$\begin{aligned} \underline{p}_{\mathrm{a},i} &= \underline{p}_{\mathrm{a}}(\boldsymbol{x}_{\mathrm{m},i}) \\ \underline{v}_i &= \underline{v}(\boldsymbol{x}_{\mathrm{m},i}) \,. \end{aligned}$$

Here, $R(a, \varphi)$ denotes terms in the functional J, that are not dependent on the pressure $\underline{p}_{\mathrm{a}}$, see (5.10). Expressing the pressure-dependent part of (5.26) in terms of real and imaginary parts and neglecting higher order terms of the direction $\underline{v} \in U$ amounts to

$$\begin{aligned} \frac{\Phi}{2} \left| \underline{p}_{\mathrm{a},i} + \underline{v}_i - \underline{p}_i^{\mathrm{ms}} \right|^2 &= \frac{\Phi}{2} \left| p_{\mathrm{a},i,\mathrm{Re}} + \mathrm{j} p_{\mathrm{a},i,\mathrm{Im}} + v_{i,\mathrm{Re}} + \mathrm{j} v_{i,\mathrm{Im}} - p_{i,\mathrm{Re}}^{\mathrm{ms}} - \mathrm{j} p_{i,\mathrm{Im}}^{\mathrm{ms}} \right|^2 \\ &= \frac{\Phi}{2} \big| \underbrace{(p_{\mathrm{a},i,\mathrm{Re}} - p_{i,\mathrm{Re}}^{\mathrm{ms}})}_{\widetilde{p}_{i,\mathrm{Re}}} + \mathrm{j} \underbrace{(p_{\mathrm{a},i,\mathrm{Im}} - p_{i,\mathrm{Im}}^{\mathrm{ms}})}_{\widetilde{p}_{i,\mathrm{Im}}} + v_{i,\mathrm{Re}} + \mathrm{j} v_{i,\mathrm{Im}} \big|^2 \\ &= \frac{\Phi}{2} \left[(\widetilde{p}_{i,\mathrm{Re}} + v_{i,\mathrm{Re}})^2 + (\widetilde{p}_{i,\mathrm{Im}} + v_{i,\mathrm{Im}})^2 \right] \\ &= \frac{\Phi}{2} \left[\widetilde{p}_{i,\mathrm{Re}}^2 + \widetilde{p}_{i,\mathrm{Im}}^2 + \cancelto{\approx 0}{v_{i,\mathrm{Re}}^2 + v_{i,\mathrm{Im}}^2} + 2 \widetilde{p}_{i,\mathrm{Re}} v_{i,\mathrm{Re}} + 2 \widetilde{p}_{i,\mathrm{Im}} v_{i,\mathrm{Im}} \right] \,. \end{aligned} \tag{5.27}$$

Therefore, the relation

$$J(\underline{p}_{\mathrm{a}} + \underline{v}, a, \varphi) - J(\underline{p}_{\mathrm{a}}, a, \varphi) = \Phi \left(\widetilde{p}_{i,\mathrm{Re}} v_{i,\mathrm{Re}} + \widetilde{p}_{i,\mathrm{Im}} v_{i,\mathrm{Im}} \right) \tag{5.28}$$

holds. Combining (5.28) with

$$A(\underline{p}_{\mathrm{a}} + \underline{v}, \underline{z}) - A(\underline{p}_{\mathrm{a}}, \underline{z}) = A(\underline{v}, \underline{z}) \tag{5.29}$$

and

$$\mathrm{Re}\Big\{\underline{\widetilde{p}}_i\,\underline{\overline{v}}(\boldsymbol{x}_{\mathrm{m},i})\Big\} = \widetilde{p}_{i,\mathrm{Re}} v_{i,\mathrm{Re}} + \widetilde{p}_{i,\mathrm{Im}} v_{i,\mathrm{Im}}\,, \tag{5.30}$$

results in the solution given in (5.23).

The strong form of (5.23) reads as

$$\begin{aligned} \nabla\cdot\nabla\underline{\overline{z}} + k^2\underline{\overline{z}} &= \varPhi \sum_{i=1}^{N_\mathrm{m}} \left(\underline{p}_\mathrm{a}(\boldsymbol{x}_{\mathrm{m},i}) - \underline{p}_i^\mathrm{ms}\right)\delta(\boldsymbol{x}_{\mathrm{m},i}) \qquad \text{in } \varOmega \\ \boldsymbol{n}\cdot\nabla\underline{\overline{z}} &= 0 \qquad \text{on } \partial\varOmega\,, \end{aligned} \tag{5.31}$$

which is the Helmholtz equation with the pressure differences $\underline{\widetilde{p}}_i$ as a right-hand side.

Since the adjoint equation (5.23) and (5.31) holds, calculating the gradients (5.19) and (5.20) simplify to

$$\frac{\partial}{\partial a_n} j(a,\varphi) = \frac{\partial}{\partial a_n}\mathcal{L}(\underline{p}_\mathrm{a}(a,\varphi), a, \varphi, \underline{z})\,, \tag{5.32}$$

$$\frac{\partial}{\partial \varphi_n} j(a,\varphi) = \frac{\partial}{\partial \varphi_n}\mathcal{L}(\underline{p}_\mathrm{a}(a,\varphi), a, \varphi, \underline{z})\,. \tag{5.33}$$

Hence, the computationally costly calculation of the sensitivities can be avoided by solving (5.31) in a weak sense to obtain $\underline{z}$ and subsequently calculating $\partial\mathcal{L}(a,\varphi,\underline{p}_\mathrm{a},\underline{z})/\partial a_n$ and $\partial\mathcal{L}(a,\varphi,\underline{p}_\mathrm{a},\underline{z})/\partial\varphi_n$ according to (5.21) and (5.22), respectively. Solving for the adjoint state $\underline{z}$ in the FE framework can be accomplished very efficiently since the system matrices stay the same as in the forward problem, only the right-hand side changes. Due to the use of the adjoint approach, the effort of calculating the gradient is not dependent on the number of microphones or source points.

5.1.2 Implementation of the Inverse Scheme

The Inverse Scheme is implemented in the open-source Finite Element program openCFS [160]. In the following, a pseudo code is presented to show the structure of the implementation. After calculating the gradient, an Armijo line search is used, see Sec. 2.3.1. The pseudo-code of the implementation is shown in Alg. 1, where fixed parameters are shown in Tab. 5.1.

Parameter	Symbol	Value
Measurement error	ε^ms	0.01
Initial step length	t_0	1
Armijo factor 1	β_1	0.25
Armijo factor 2	ξ	1 E−4
Maximum gradient reduction factor	tol	1 E−5
Maximum outer steps	k_max	10
Maximum gradient steps	l_max	30
Maximum line search steps	m_max	20

Table 5.1: Fixed parameters of the Inverse Scheme's implementation in openCFS.

Algorithmus 1 : Inverse Scheme

```
Input  : Regularization parameters $\alpha_r, \beta, \varrho, \Phi$, measurement data $p^{ms}$, microphone positions $\boldsymbol{x}_{m,i}$
Output : Identified source amplitudes and phases $a, \varphi$

Function res = residual(p)
    $res = \frac{\Phi}{2} \sum_{i=1}^{N_m} |p(\boldsymbol{x}_{m,i}) - p^{ms}|^2$

Function J = Tikhonov(a, φ, res)
    $J = res + \alpha_r \sum_n |a_n|^q - \beta \sum_n \ln\left[\left(\frac{a_n+\epsilon}{\max\{|a_n|\}+\epsilon}\right)^2\right] \varphi_n^2 - \varrho \sum_n \left[\ln\left(\frac{\pi}{2}+\varphi_n\right) + \ln\left(\frac{\pi}{2}-\varphi_n\right)\right]$

Function p = state(a, φ)
    solve $A(p, \underline{w}) = -\mathrm{Re}\left\{\sum_n a_n e^{j\varphi_n} \overline{\underline{w}}(\boldsymbol{x}_{sc,n})\right\}$    for p

Function z = adjoint(a, φ, p)
    solve $A(\underline{v}, z) + \Phi \sum_i \mathrm{Re}\{(p(\boldsymbol{x}_{m,i}) - p^{ms}) \overline{\underline{v}}(\boldsymbol{x}_{m,i})\}$    for z

Function d = gradient(a, φ, z)
    $da_n = \alpha_r q |a_n|^{q-1} \mathrm{sign}(a_n) - 2\beta \frac{\varphi_n^2}{a_n + \epsilon} + \mathrm{Re}\left\{e^{j\varphi_n} \overline{z}(\boldsymbol{x}_{sc,n})\right\}$
    $d\varphi_n = -2\beta\varphi_n \ln\left(a_n^2\right) + 2\varrho \frac{\varphi_n}{\left(\frac{\pi}{2}-\varphi_n\right)\left(\frac{\pi}{2}+\varphi_n\right)} - a_n \mathrm{Im}\left\{e^{j\varphi_n} \overline{z}(\boldsymbol{x}_{sc,n})\right\}$

Initialization:
$a = \varphi = p = \mathbf{0}$
res ← residual(p)
J ← Tikhonov(a, φ, res)
$k = 0$
while $res > \varepsilon^{ms}$ & $k < k_{max}$ do                              // Outer iteration
    z ← adjoint(a, φ, $p^{ms}$)
    d ← gradient(a, φ, z)    // $d = [da, d\varphi]$
    $l = 0$
    while $\|d\|_2^2 < \|d|_{k=0}\|_2^2$ tol & $l < l_{max}$ do                // Gradient steps
        $t = t_0$
        $a_{new} = a - da * t$
        $\varphi_{new} = \varphi - d\varphi * t$
        $p_{new}$ ← state($a_{new}, \varphi_{new}$)
        $res_{new}$ ← residual($p_{new}$)
        $J_{new}$ ← Tikhonov($a_{new}, \varphi_{new}, res_{new}$)
        while $J_{new} > J - \xi\beta_l t \|d\|_2^2$ & $m < m_{max}$ do        // Line search
            $t = \beta_l t$
            $a_{new} = a - da * t$
            $\varphi_{new} = \varphi - d\varphi * t$
            $p_{new}$ ← state($a_{new}, \varphi_{new}$)
            $res_{new}$ ← residual($p_{new}$)
            $J_{new}$ ← Tikhonov($a_{new}, \varphi_{new}, res_{new}$)
            $m = m + 1$
        $a = a_{new}$; $\varphi = \varphi_{new}$
        $p = p_{new}$
        $res = res_{new}$
        $J = J_{new}$
        z ← adjoint(a, φ, p)
        d ← gradient(a, φ, z)
        $l = l + 1$
    $\alpha_r = 0.5\alpha_r$,  $\beta = 0.5\beta$
    $k = k + 1$

$a = a/\Phi$   // Scaling back
p ← state(a, φ)   // Final computation of sound pressure field
```

5.2 Sound Source Identification within the Trailer with Virtual Measurements

In this section, the performance of the Inverse Scheme is tested within the stationary measurement trailer. Sound source identification results are obtained from virtual measurements and will be discussed in the following. The virtual measurements are provided from forward calculations, which were presented in Sec. 4.2. Later, in Sec. 5.3 and Chap. 6, the sound source identification with the Inverse Scheme will be applied to real measurement data. The calculations with virtual data shall serve as a proof of concept. Further, since we obtain the virtual microphone data with a forward FE simulation, it is possible to compare the sound fields of the forward simulation, carried out with the prescribed sources, and of the inverse simulation with the identified sound sources in all nodes of the computational mesh. When applying the Inverse Scheme to actual microphone data, the sound field is only known in the discrete microphone positions.

5.2.1 Virtual Measurements

A section of the computational mesh for the forward simulations is depicted in the right image in Fig. 4.5. The loudspeaker is placed in the left chamber without a tire, while in the other chamber, the measurement tire is mounted, and no loudspeaker is present. Therefore, both chambers must be included in the computational domain since there are no symmetries in the geometry and the excitation.

In the validation simulations, we defined the normal component of the membrane's surface velocity as an excitation since the results were compared to microphone measurements with an actual loudspeaker. However, since we now want to identify monopole sources with the Inverse Scheme, in the forward simulations for the virtual measurements also monopole sources are imprinted on the membrane to ensure comparability between forward and inverse simulations. The monopoles' amplitudes $a_{\mathrm{mem,fwd},n} = a_{\mathrm{mem,fwd}}$ on the membrane are assigned the same value on all nodes within Γ_{mem} – see Fig. 4.6b. The surface Γ_{p} around the membrane, called "plate", is excited with $a_{\mathrm{plate,fwd},n} = 0.5\, a_{\mathrm{mem,fwd}}$.

In the forward simulation, the sound pressure, which serves as input for the Inverse Scheme, is evaluated at the same 33 microphone positions $\boldsymbol{x}_{\mathrm{m},i}$ as in the validation simulations. In order to model uncertainties that occur in real measurements, to each microphone pressure signal $\underline{p}_i^{\mathrm{ms}}(\omega)$ a random variable $Y_i(\omega)$ is added. The signal-to-noise ratio (SNR) between the sound pressure signal and the random variables is set to $L_{\mathrm{SNR}} = 20\,\mathrm{dB}$. The added noise may account for uncertainties in the measured microphone positions, inaccuracies e. g. due to wind noise, or material parameters of the acoustic absorbers when applying the Inverse Scheme to real measurement data.

The sound pressure signals $\boldsymbol{p}_\epsilon^{\mathrm{ms}}$ with added random values $\boldsymbol{Y}(\omega)$ are computed according

$$\boldsymbol{p}_\epsilon^{\mathrm{ms}}(\omega) = \boldsymbol{p}^{\mathrm{ms}}(\omega) + \boldsymbol{Y}(\omega)\,, \tag{5.34}$$

$$\boldsymbol{Y}(\omega) = \sqrt{\frac{1}{2} 10^{(L_{\boldsymbol{p}^{\mathrm{ms}}} - L_{\mathrm{SNR}})/10}} (\boldsymbol{\gamma}_1 + \mathrm{j}\boldsymbol{\gamma}_2)\,, \tag{5.35}$$

where $\boldsymbol{\gamma}_i$ is a vector of length N_{m} with normally distributed random variables and the power level $L_{\boldsymbol{p}^{\mathrm{ms}}}$ of the microphone signals is calculated via

$$L_{\boldsymbol{p}^{\mathrm{ms}}} = 10 \log_{10} \left(\frac{1}{N_{\mathrm{m}}} \sum_{i=1}^{N_{\mathrm{m}}} |\underline{p}_i^{\mathrm{ms}}|^2 \right) . \tag{5.36}$$

In Fig. 5.2, the schematics of the Inverse Scheme with virtual measurement data is provided.

The forward computation to obtain the virtual measurements is performed on the finest mesh for all frequencies. This mesh has a mesh size of $h_{1600} = 21\,\mathrm{mm}$ which corresponds to 10 elements per

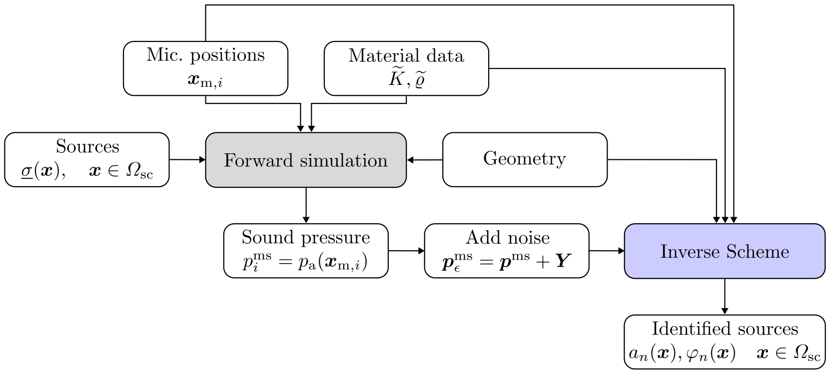

Figure 5.2: Schematics of the Inverse Scheme with virtual measurement data.

wavelength at the highest frequency of interest, $f_{\max} = 1600\,\mathrm{Hz}$, assuming an ambient temperature of approx. 20 °C.

The computations for the inverse problem are carried out on coarser meshes for frequencies $f \leq 500\,\mathrm{Hz}$ and $500\,\mathrm{Hz} < f \leq 1000\,\mathrm{Hz}$ to reduce the computational demand. The same mesh sizes as in Sec. 4.2.1 are used. Only one chamber is included in the computational domain to further decrease the number of unknowns in solving the inverse problem. Since the forward simulation is not symmetric in terms of geometry and excitation, a sound hard boundary condition at the plane dividing the two chambers, which is a symmetry boundary condition, would be wrong. Therefore, one chamber is surrounded by air and PML around the gap between the trailer's lateral walls and the floor. This means that the setup for solving the inverse problem assumes that no sound waves that are emitted to the second (empty) chamber through the gap between the two chambers are reflected back into the first chamber.

Note that since the simulations for the forward and inverse problem are not carried out on the same mesh for all frequencies, the possible source positions $\boldsymbol{x} \in \Omega_{\mathrm{sc}}$ may differ, and therefore, a direct comparison of the source amplitude and phase values of defined and identified sources is not possible.

The inverse method's computations were carried out on a server with Intel Xeon CPUs with 2.60 GHz. The simulation times for the different mesh sizes, when running the simulations on 12 cores, are shown in Tab. 5.2. These times are, of course, just approximate values, since the actual simulation time not only depends on the number of nodes but also at which point the stopping criteria in the algorithm 1 are met at the respective frequencies.

$f_{\max}$ in Hz	No. Nodes	t_{sim} in h
500	24.10 E3	≈ 0.8
1000	169.50 E3	≈ 8
1600	661.00 E3	≈ 60

Table 5.2: Approximate simulation times t_{sim} of the Inverse Scheme for the different mesh sizes depending on the maximum frequency $f_{\max}$, when running on 12 Intel Xeon CPUs with 2.60 GHz.

The source domain $\Omega_{\mathrm{sc}} = \Gamma_{\mathrm{sc}}$, where potential sources are located, is the loudspeaker's membrane, the plate, and the housing: $\Gamma_{\mathrm{sc}} = \Gamma_{\mathrm{mem}} \bigcup \Gamma_{\mathrm{p}} \bigcup \Gamma_{\mathrm{h}}$, see Fig. 4.6b. The inverse problem with virtual measurements is solved for discrete frequencies $f = 200, 300, \ldots, 1600\,\mathrm{Hz}$. The same material parameters $\underline{K}_{\mathrm{eff}}$ and $\underline{\rho}_{\mathrm{eff}}$ are assigned to the acoustic absorber region in the inverse as in the forward simulation. The material properties of the fitting in Sec. 4.2.3 are used, as the identification with virtual microphone measurements shall be as close as possible to the measurement setup where actual microphone measurements are used to identify sound sources.

The monopole sources prescribed on Γ_{mem} and Γ_{p} for the forward computation, at an exemplary frequency $f = 200\,\mathrm{Hz}$, are depicted in Fig. 5.3a, where sound source levels L_{σ_n} and the source phases $\varphi_n = \arctan \frac{\mathrm{Im}\{\sigma\}}{\mathrm{Re}\{\sigma\}}$ are plotted. The sound source level computes – analogously to the sound pressure level – as

$$L_\sigma = 20 \log_{10} \frac{|\sigma|}{\sigma_0}, \qquad \sigma_0 = 20\,\mu\mathrm{N/m}\,. \tag{5.37}$$

As it can be seen in Fig. 5.3, the difference of the prescribed sound source level between sources on membrane and plate is approximately 6 dB, since $a_{\mathrm{plate,fwd}} = 0.5\, a_{\mathrm{mem,fwd}}$. The source's phase is chosen the same for the membrane and plate.

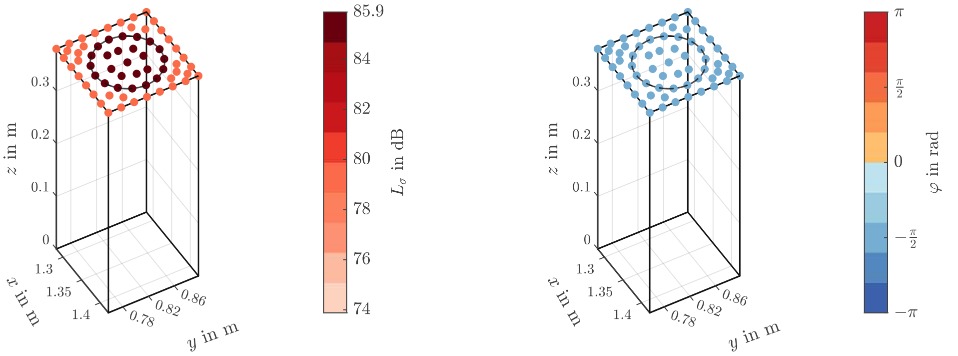

(a) Sound source level.

(b) Sound source phase.

Figure 5.3: Monopole sources prescribed on the membrane and the surrounding plate in the forward simulation to obtain virtual microphone measurements; shown exemplarily at $f = 200\,\mathrm{Hz}$.

5.2.2 Inverse Scheme – Sound Source Identification Results with Virtual Measurements

In the following, the sound sources prescribed in the forward simulation and the identified sound sources via the Inverse Scheme are compared in amplitude (Fig. 5.4) and phase (Fig. 5.5). The presented results were obtained with the following regularization parameters, which were chosen according to the findings in [83] and from experience with the new phase regularization (5.13)

$$\begin{aligned} \alpha_{\mathrm{r}} &= 10^{-6} \\ \beta &= 50 \\ \varrho &= 2 \\ q &= 1.9 \\ \varPhi &= \frac{8}{\max\{|\underline{p}_i^{\mathrm{ms}}|\}}\,. \end{aligned} \tag{5.38}$$

Since in the forward simulation, all amplitude values a_{plate} on the plate Γ_{p} are half the amplitude values of the sources on the membrane Γ_{mem}, the graphic representation of the forward amplitude in the left column of Fig. 5.4 is the same for all frequencies. Only the absolute values of L_σ, i. e. the ranges of the color bars, change. The prescribed amplitude and phase values of the forward simulation are chosen the same as in the validation simulations in Sec. 4.2, even though we prescribe monopole sources in each node here, whereas in the validation simulations the normal component of the acoustic particle velocity on each element was defined. Therefore, the resulting sound pressure levels at the microphone positions may be in an unrealistic range.

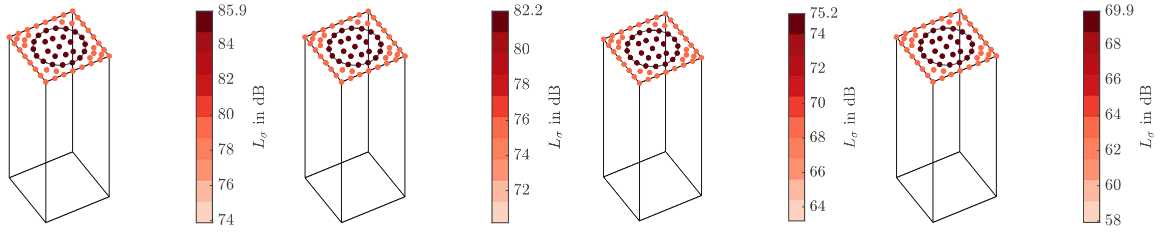

(a) Forward Simulation, $f = 200\,\text{Hz}$.

(b) Forward Simulation, $f = 300\,\text{Hz}$.

(c) Forward Simulation, $f = 600\,\text{Hz}$.

(d) Forward Simulation, $f = 1000\,\text{Hz}$.

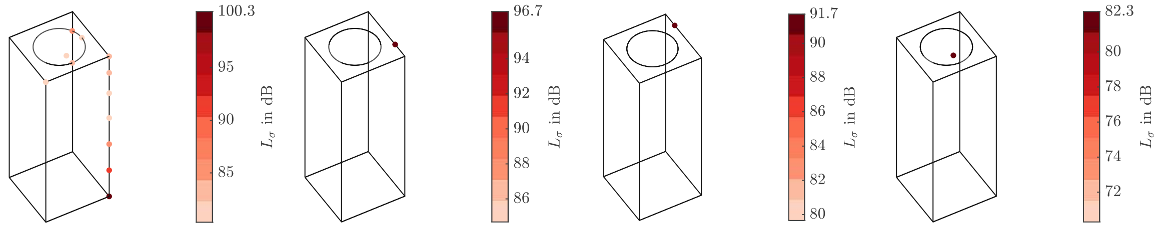

(e) Inverse Simulation, $f = 200\,\text{Hz}$.

(f) Inverse Simulation, $f = 300\,\text{Hz}$.

(g) Inverse Simulation, $f = 600\,\text{Hz}$.

(h) Inverse Simulation, $f = 1000\,\text{Hz}$.

Figure 5.4: Amplitude results of sound source identification gathered from the Inverse Scheme, with virtual measurement input data. Forward simulations are depicted in the upper row, and inverse results are in the lower row.

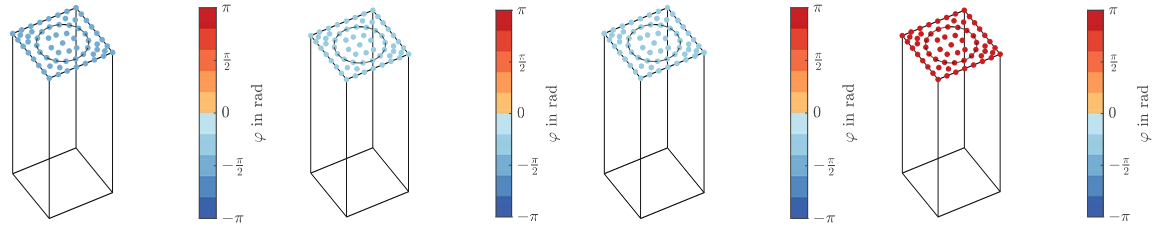

(a) Forward Simulation, $f = 200\,\text{Hz}$.

(b) Forward Simulation, $f = 300\,\text{Hz}$.

(c) Forward Simulation, $f = 600\,\text{Hz}$.

(d) Forward Simulation, $f = 1000\,\text{Hz}$.

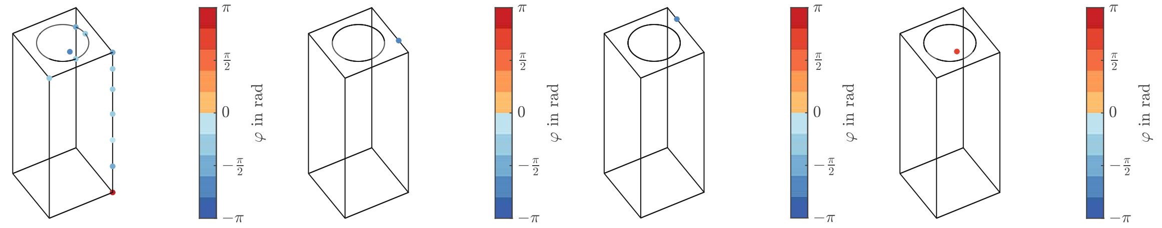

(e) Inverse Simulation, $f = 200\,\text{Hz}$.

(f) Inverse Simulation, $f = 300\,\text{Hz}$.

(g) Inverse Simulation, $f = 600\,\text{Hz}$.

(h) Inverse Simulation, $f = 1000\,\text{Hz}$.

Figure 5.5: Phase results of sound source identification gathered from the Inverse Scheme, with virtual measurement input data. Forward simulations are depicted in the upper row, and inverse results are in the lower row.

The source level's dynamic range in Figs. 5.4 and 5.5 is $L_{\mathrm{dyn}} = 12\,\mathrm{dB}$, except for the lowest frequency of $f = 200\,\mathrm{Hz}$, where it is chosen $L_{\mathrm{dyn}}(f = 200\,\mathrm{Hz}) = 24\,\mathrm{dB}$. The reasons for that will be discussed later. The phase values φ_n of the identified sources are only depicted at locations where $L_\sigma \geq L_{\mathrm{dyn}}$.

From the lower row of Fig. 5.4, it can be seen that for frequencies $f > 200\,\mathrm{Hz}$ the primary sound source is identified at the top of the loudspeaker, i. e. the loudspeaker membrane, or the plate. Due to the chosen dynamic range of 12 dB, only a single dominant monopole source is visible in the Inverse Scheme's identification. This single monopole source's amplitude is higher than the amplitudes of the individual sources in the forward simulation, since it can be interpreted as the sum of sound sources in its immediate neighborhood. Due to the compactness of the source region, with its characteristic dimension being the membrane diameter $d_{\mathrm{mem}} = 100\,\mathrm{mm}$, the resulting sound pressure at the microphone positions is not sensitive enough to the exact source positions within $\Gamma_{\mathrm{mem}} \bigcup \Gamma_{\mathrm{p}}$. With (2.65), the Helmholtz number He of the membrane region takes values in the range of

$$He = \begin{cases} 0.37 & \text{for } f = 200\,\mathrm{Hz} \\ 2.93 & \text{for } f = 1600\,\mathrm{Hz}\,. \end{cases}$$

Therefore, compactness is given according to (2.66) for the lower frequencies of interest. With increasing frequency, the location of the identified dominant sound sources converges towards the midpoint of the membrane.

Also, the identified source's phase values match the phases of the forward simulation well; see Fig. 5.5.

The only frequency which stands out concerning the location of the identified dominant sound source is the lowest frequency of 200 Hz. Here, the dominant sound source is located at the bottom of the loudspeaker's housing, where $z = 0$. It is assumed that the reason for this behavior is, again, the compactness of the source at the lowest frequency. It has to be stressed that we can only minimize the difference of simulated and (virtually) measured acoustic pressures at the microphone position $\boldsymbol{x}_{\mathrm{m},i}$, since usually no a priori information about the source distribution is known in a real-life application. An optimal sound source distribution inferred from the optimization (5.9) may cause a similar sound field at $\boldsymbol{x}_{\mathrm{m},i}$ at certain frequencies as the actual source distribution of the forward simulation. However, at $f = 200\,\mathrm{Hz}$ the Inverse Scheme's result also yielded weaker sound sources on the membrane and plate surface. Since they would not have been visible with a dynamic range of 12 dB, a value of 24 dB was chosen for this frequency. These weaker identified sources are indeed located at the top of the loudspeaker. As we will see in the following two sections, even at the lowest frequency of 200 Hz, the sound fields of the original forward simulation and the simulation with identified sound sources match well.

5.2.3 Inverse Scheme – Sound Pressure Results

In the following, we examine the sound pressure calculated from the identified sources compared to the forward simulation. Firstly, the relative errors $\varepsilon_{\mathrm{rel,L2}}$ and $\varepsilon_{\mathrm{abs,L2}}$ are investigated as a function of the discrete frequencies. These errors are computed via (4.38) and (4.39), respectively. As the measured pressures are inferred from a forward simulation here, $\underline{\boldsymbol{p}}_{\mathrm{a,meas}}$ denotes the vector of virtual measurements at the microphone positions $\boldsymbol{x}_{\mathrm{m},i}$. In Fig. 5.6, the relative errors are plotted over the frequency. As one can see, the relative errors are low at all calculated frequencies and are decreasing with increasing frequency. Again, as it could be observed in the L2-error plots in Sec. 4.2.3, the relative error of the sound pressure amplitudes $\varepsilon_{\mathrm{abs,L2}}$ is lower than the relative error of the complex-valued sound pressures $\varepsilon_{\mathrm{rel,L2}}$.

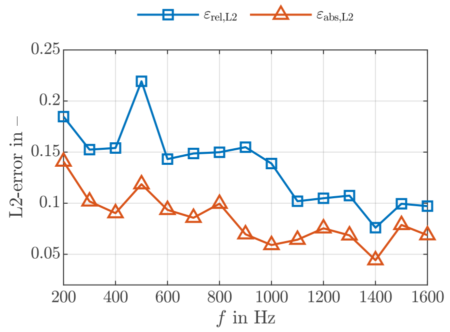

Figure 5.6: Relative L2-errors $\varepsilon_{\mathrm{rel,L2}}$ and $\varepsilon_{\mathrm{abs,L2}}$ of the acoustic pressure calculated from identified sound sources via the Inverse Scheme and the forward computation.

To take a closer look at the calculated acoustic pressure, it is plotted in each microphone position compared to the virtual measurements as a function of distance between the respective microphone to the membrane. Again, the same exemplary frequencies $f = 200, 300, 600$ and $1000\,\mathrm{Hz}$, as in the source identification results previously, are depicted in Fig. 5.7 and Fig. 5.8. The virtual measurements are plotted in blue, and the sound pressure simulation with the identified sound sources from the Inverse Scheme, are shown in amplitude (in Pa) and phase (in rad) in orange. As mentioned, the x-axis is the distance between the respective microphone position $\boldsymbol{x}_{\mathrm{m},i}$ and the membrane's center point. Additionally, the distance scaled with the wavelength at the corresponding frequency, which computes according to (4.41), is shown in a second axis. Note that the spacing between the ticks in the x-axis is equidistant and not scaled with the actual distance values to ensure readability of the plotted graph.

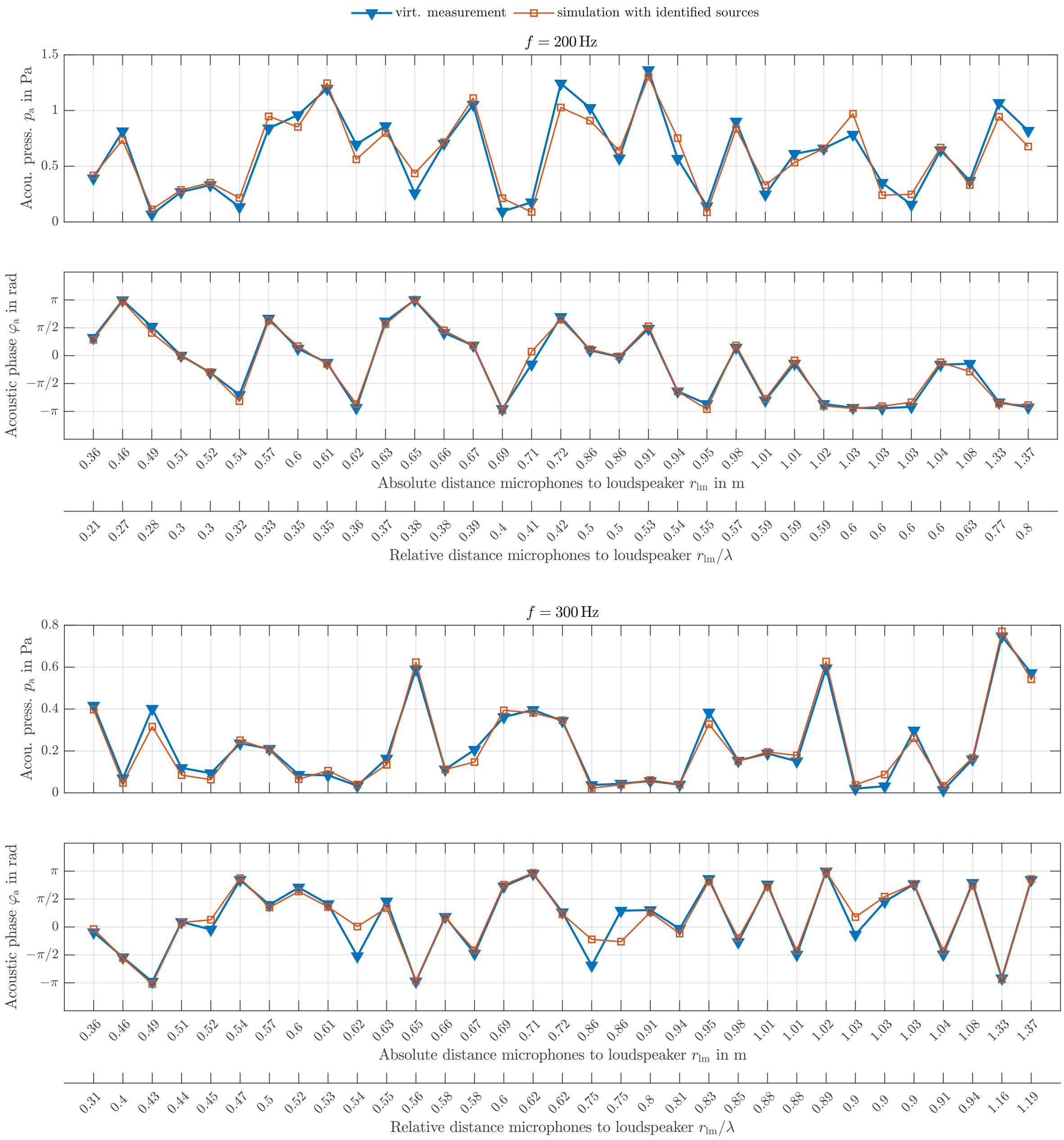

Figure 5.7: Comparison of virtual measurement and the simulated sound pressures at the microphone positions for $f = 200\,\mathrm{Hz}$ and $f = 300\,\mathrm{Hz}$.

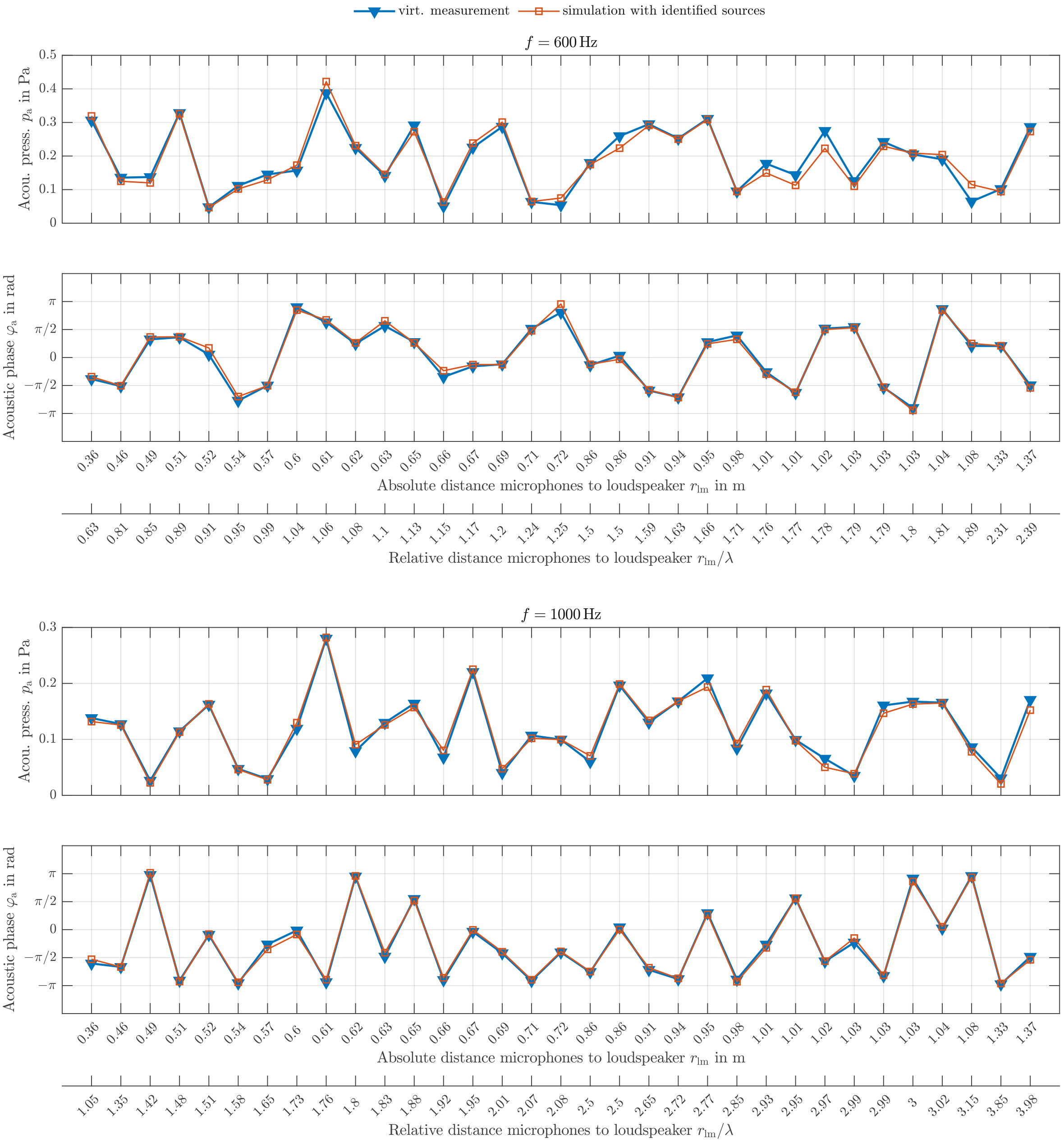

Figure 5.8: Comparison of virtual measurement and the simulated sound pressures at the microphone positions for $f = 600\,\mathrm{Hz}$ and $f = 1000\,\mathrm{Hz}$.

The figures show a very good agreement between the two sound pressures. This is also the case for the lowest frequency of 200 Hz, where the source identification did not perform as well as at higher frequencies and a monopole source was wrongly localized at the bottom of the loudspeaker's housing. The error in dB averaged over all frequencies, which computes via (4.43) is

$$L_{\mathrm{err}} = 1.76\,\mathrm{dB}\,.$$

Comparing this calculated error level value and the relative error plot in Fig. 5.6 with the results in Fig. 4.12a from Sec. 4.2.3, where the simulated sound pressure of the material property optimization was shown, the following can be concluded: The overall match of the sound pressures of Inverse Scheme's result is significantly better than those of the genetic optimization. However, one has to consider that in case of the Inverse Scheme, virtual measurements were used as sound pressure measurements. In contrast, in the validation measurements for the material properties, actual microphone data was used. Despite the differences in these two optimizations, the cost function is, in both cases, the difference between the measured and simulated acoustic pressure at the same microphone positions. This fact leads to the conclusion that the sensitivity of the sound pressure at the microphone positions to changes in the sound source amplitudes and phases and to its positions is higher than to changes in the material parameters of the acoustic absorbers on the vehicle trailer's walls. Secondly, the gradient-based optimization in the Inverse Scheme is assumed to perform better than the gradient-free optimization used in Sec. 4.2.3.

Later, sound source localization results with actual microphone data will be provided, which allows a better comparability of the optimization in the Inverse Scheme and the gradient-free optimization for the parameter fitting.

Up until now, the microphone data serving as input for the Inverse Scheme was gathered from FE simulations of the forward problem. Therefore, the (virtual) measurements can not only be compared to the sound pressure at the microphone positions but in the whole computational domain. This allows us to compare the sound pressure field from the original forward simulations and the sound pressure simulations with identified sources in arbitrary points. In the latter forward simulation,s the sound sources identified via the Inverse Scheme were prescribed. In Fig. 5.9, the sound pressure field is depicted in a section of the air domain of the measurement trailer model. The sections are in planes parallel to the xz- and yz-planes through the center point of the loudspeaker membrane.

In the left column in Fig. 5.9, the sound pressure level $L_{p_{\mathrm{a}}}$ resulting from the forward simulation is depicted. In the right column, we see the sound pressure level, which results from the FE simulation with the identified sound sources from the Inverse Scheme. Again, two exemplary frequencies are shown: $f = 200\,\mathrm{Hz}$ and $f = 1000\,\mathrm{Hz}$. From the graphical representation in Fig. 5.9a, we can see that even for the lowest frequency of 200 Hz, where the location of the identified dominant monopole sources deviated from the actual positions, the sound pressure field resulting from the identified sources is very similar to the one of the forward simulation.

From the various results shown above, it is concluded that the sound source identification with the Inverse Scheme yields satisfying results within the measurement trailer. Therefore, the next step is to apply the Inverse Scheme to source localization problems with actual microphone data. For this purpose, the microphone measurements from the validation measurements are re-used. We will compare the Inverse Scheme's results to the results from other well-known sound source localization algorithms, such as Conventional Beamforming.

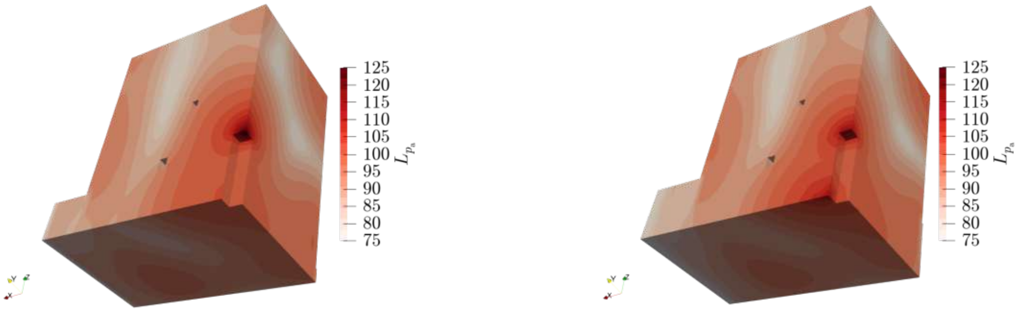

(a) Forward simulation, $f = 200\,\mathrm{Hz}$.

(b) Inverse simulation, $f = 200\,\mathrm{Hz}$.

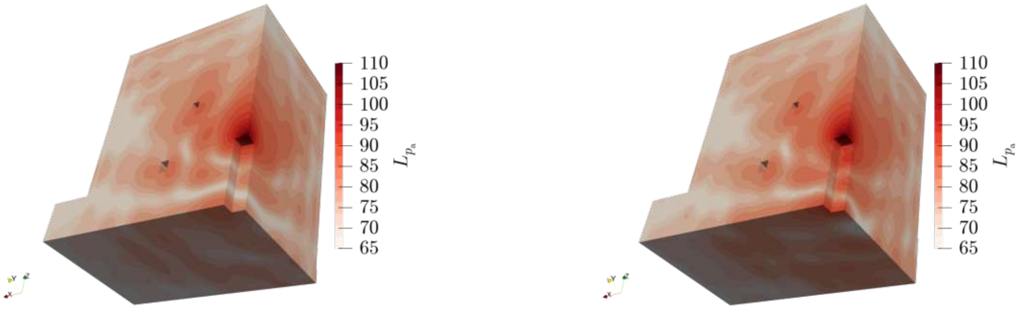

(c) Forward simulation, $f = 1000\,\mathrm{Hz}$.

(d) Inverse simulation, $f = 1000\,\mathrm{Hz}$.

Figure 5.9: Sound pressure field in a section of the computational domain of the measurement trailer for different frequencies. The forward simulation is shown in the left column and simulations with sound sources identified with the Inverse Scheme in the right column.

5.3 Sound Source Identification within the Trailer – Stationary Measurements

In this section, the performance of the Inverse Scheme is compared to conventional methods for sound source localization, namely Conventional Beamforming, Functional Beamforming, and the deconvolution method CLEAN-SC. Details on the fundamentals of these well-established methods are covered in Chap. 3.

In this section, the stationary trailer is considered. As in case of the validation measurements, the stationary trailer is excited with a loudspeaker with sinusoidal signals of discrete frequencies. Subsequently, sound sources at the loudspeaker's membrane and its housing shall be identified. Therefore, in contrast to the previous section, actual sound source measurements serves as input for the Inverse Scheme and beamforming-based algorithms. The schematics of both methods are depicted in Fig. 5.10.

Except for the sound pressure measurement data, all other inputs for the Inverse Scheme remain the same as in case of using virtual measurement data. This means, specifically, that the microphone positions are the ones depicted in Fig. 4.11. Further, the optimal acoustic absorber's material properties $\underline{K}_{\text{eff}}$ and $\underline{\rho}_{\text{eff}}$ obtained from the second optimization – where the real and imaginary parts of the effective compression modulus and effective density were fitted to microphone measurements within the measurement trailer – are prescribed in the porous absorber region of the Finite Element model. The computational mesh's element size is chosen adaptively depending on the frequency according to Tab. 4.4.

As the acoustic excitation was achieved with a loudspeaker, whose membrane is a vibrating surface,

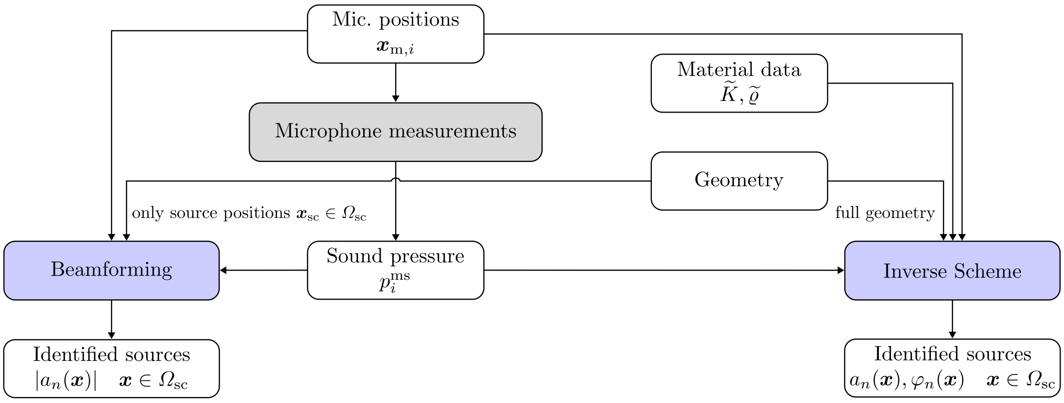

Figure 5.10: Schematics of the Inverse Scheme and beamforming-based algorithms (short *Beamforming*) with actual microphone measurement data.

the obvious approach would be to identify the normal component of the surface velocity in each finite element of the computational mesh within $\partial\Omega_{\mathrm{sc}}$. However, sound sources are again modeled as monopoles. This approach seems justified since the radiation pattern of a small oscillating surface that is small compared to the wavelength, evaluated at a distance that is large compared to the characteristic length of the surface, does not differ significantly from that of a monopole source. In the Finite Element method, the characteristic length of the oscillating surfaces is the mesh size h, which is at least smaller by a factor $\frac{1}{10}$ than the wavelength λ. Therefore, it is assumed that monopole sound sources may approximate the source distribution of vibrating surfaces well enough. Further, this has the advantage that the results of the Inverse Scheme can be compared directly with the beamforming results, where usually monopole sources are assumed.

5.3.1 Sound Source Identification Results with Microphone Measurements

The Inverse Scheme's sound source identification results were obtained with the exact regularization and optimization parameters as in the virtual measurements, which are listed in (5.38) and Tab. 5.1. The region Ω_{sc} of possible source positions is – as in case of virtual measurements – the loudspeaker's membrane, the plate around the membrane, and the loudspeaker's housing, $\Omega_{\mathrm{sc}} = \Gamma_{\mathrm{mem}} \bigcup \Gamma_{\mathrm{p}} \bigcup \Gamma_{\mathrm{h}}$, i. e. all surfaces depicted in Fig. 4.6b.

The source maps of the Inverse Scheme are presented in Fig. 5.11. Source points that are depicted as circles are located at the back-facing surfaces of the loudspeaker's housing, i. e. the surfaces parallel to the xz- and yz-plane through the point $(x, y) = (1.24, 0.9)\,\mathrm{m}$ – see Fig. 5.3. The identified source amplitudes are plotted in the upper row, and the sources' phases in the lower row. The same frequencies as in the previous section are chosen, and the dynamic range is set to 12 dB for all frequencies, except at $f = 200\,\mathrm{Hz}$. The reasons for that will be explained later. Note that there are no forward simulations available to which the sound source localization results may be compared in case of actual microphone measurements. However, it is safe to assume that the dominant sound sources are located at the membrane surface Γ_{mem} at the top of the loudspeaker.

The plots in Fig. 5.11 show that for frequencies $f > 200\,\mathrm{Hz}$, the dominant sound sources are always identified at the top of the loudspeaker, i. e. the membrane or plate surface, where the dominant sound sources of a loudspeaker are expected.

Only at the lowest frequency of 200 Hz, the dominant sound source is again localized at the bottom of the loudspeaker's housing, as with the virtual measurements. While sound sources are identified at the top of the loudspeaker, their amplitudes are lower than the amplitude of those at the bottom by approx. 15 dB. This is the same behavior as was the case with the virtual measurements, where the dominant sound source at 200 Hz was located at $z = 0$ as well. This leads to the assumption that at

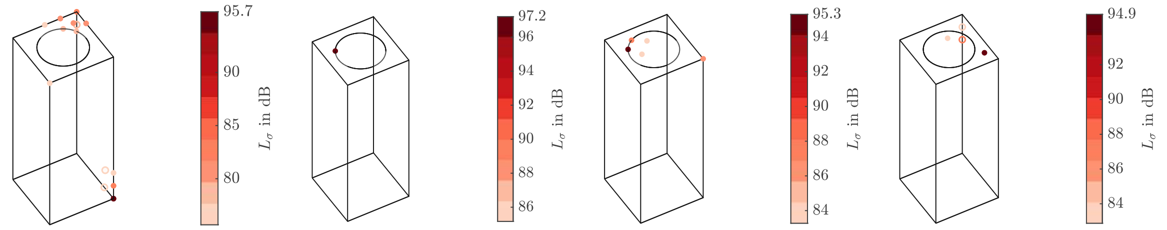

(a) Source amplitudes, $f = 200\,\mathrm{Hz}$.

(b) Source amplitudes, $f = 300\,\mathrm{Hz}$.

(c) Source amplitudes, $f = 600\,\mathrm{Hz}$.

(d) Source amplitudes, $f = 1000\,\mathrm{Hz}$.

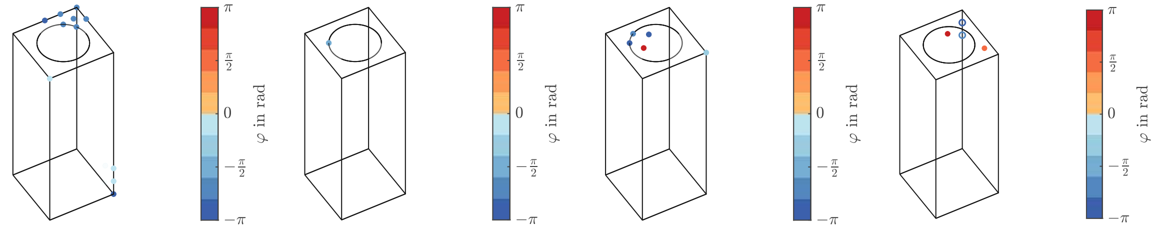

(e) Source phases, $f = 200\,\mathrm{Hz}$.

(f) Source phases, $f = 300\,\mathrm{Hz}$.

(g) Source phases, $f = 600\,\mathrm{Hz}$.

(h) Source phases, $f = 1000\,\mathrm{Hz}$.

Figure 5.11: Amplitude and phase results of sound source identification within the measurement trailer gathered from the Inverse Scheme for actual microphone measurement data of loudspeaker excitation.

this specific frequency, the sound field at the used microphone positions is not unique in terms of the exact location of the sound sources within Ω_{sc}. As stated in the previous section, the source region can be assumed to be compact at lower frequencies, where the corresponding wavelength is large compared to the loudspeaker's characteristic length.

The results at higher frequencies are very satisfying. Bear in mind that when using actual microphone measurement data as input for the Inverse Scheme, the boundary conditions, i. e. the chosen material properties in the model's acoustic absorber region, and all sound hard scatterers within the measurement trailer, which were geometrically simplified, greatly influence the identified sound sources. This does not apply to the virtual measurements, where the same geometry and material properties were used for the forward simulation and the FE simulations of the Inverse Scheme.

In the next step, the sound sources are localized using beamforming-based algorithms – Conventional Beamforming (ConvBF), Functional Beamforming (FunctBF), and CLEAN-SC – to compare these results to the Inverse Scheme's results. Concerning the sound pressure signals, the beamforming-based algorithms receive the same input as the Inverse Scheme: microphone positions and the Fourier transforms of the acoustic pressure at the considered frequency. In contrast to the Inverse Scheme, the beamforming algorithms do not consider the entire geometry of the measurement setup, as free field radiation from the scanning points to the receiving points is assumed. Therefore, scatterers and the acoustic absorbers are not modeled, and only the potential source positions $\boldsymbol{x}_{\mathrm{sc}} \in \Omega_{\mathrm{sc}}$ are taken into account concerning the measurement setup's geometry. From the microphone positions $\boldsymbol{x}_{\mathrm{m},i}$ and $\boldsymbol{x}_{\mathrm{sc}}$, the steering vectors can be computed via (3.9) and (2.54).

Another significant difference compared to the Inverse Scheme is that it is impossible to identify the sound sources' phases with beamforming algorithms since the relation between the searched for source strength $\sigma(\boldsymbol{x}_{\mathrm{sc}})$ and the beamforming result $a_{\mathrm{s}}(\boldsymbol{x}_{\mathrm{sc}})$ is given by (see Sec. 3.1.2)

$$a_{\mathrm{s}} = |\underline{\sigma}|^2 \,. \tag{5.39}$$

In Fig. 5.12, plots of sound source localization results from Conventional Beamforming (ConvBF), Functional Beamforming (FunctBF), and CLEAN-SC are shown in comparison to the previously presented Inverse Scheme's sound source identification results. In the plots of ConvBF and FunctBF in the left and center columns, respectively, the sources located at the back-facing surfaces of the loudspeaker housing have been deleted in order to increase the readability. This is necessary because of the main lobe's large width.

As it can be seen when comparing the center column of Fig. 5.12 with its left column, the main lobe width could be decreased when using the advanced algorithm Functional Beamforming. While ConvBF does not yield satisfying sound source localization results at the lower frequencies of 200, 300, and 600 Hz, with FunctBF it is noticeable at 300 and 600 Hz that the primary sound sources are located at the top. At $f = 1000\,\mathrm{Hz}$ with both ConvBF and FunctBF the dominant sound sources are identifiable at the top part of the loudspeaker.

With the deconvolution algorithm CLEAN-SC at all shown frequencies only one source point lies within the chosen dynamic range. At the lowest frequency of $f = 200\,\mathrm{Hz}$, similarly to the results obtained with the Inverse Scheme, the dominant sound source is identified at the bottom of the loudspeaker housing. With increasing frequency, the position of the identified sound source converges towards the membrane. Comparing the performance of CLEAN-SC with the Inverse Scheme shows that for frequencies $f \geq 600\,\mathrm{Hz}$ their results are very similar to each other concerning the local distribution of the identified monopole sources. Below 600 Hz, the Inverse Scheme performs better. Given the drastically higher computation time of the Inverse Scheme compared to CLEAN-SC, this leads to the recommendation of using a hybrid approach when one is solely interested in the locations of dominant sound sources. Since at lower frequencies, the Inverse Scheme outperforms the potent deconvolution algorithm CLEAN-SC and the computational times of the Inverse Scheme are relatively low when using a coarse mesh, see Tab. 5.2, it is advisable to use the Inverse Scheme. At frequencies above a specific cut-off frequency of approx. 500 Hz in this example, because of the low computational demand of CLEAN-SC and its similar performance to the Inverse Scheme's localization results, it is advisable to use CLEAN-SC. However, this recommendation is only valid if one is only interested in the locations and amplitudes of the dominant sound sources. If a good approximation of the present sound field is of interest or the source phases shall be determined, using the Inverse Scheme is necessary.

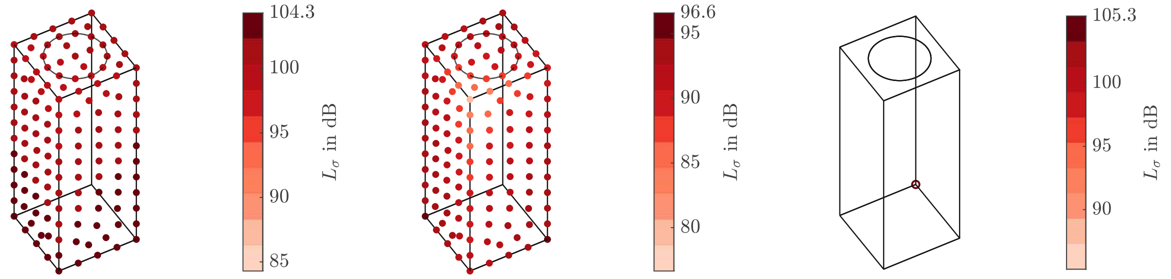

(a) ConvBF, $f = 200\,\mathrm{Hz}$.

(b) FunctBF, $f = 200\,\mathrm{Hz}$.

(c) CLEAN-SC, $f = 200\,\mathrm{Hz}$.

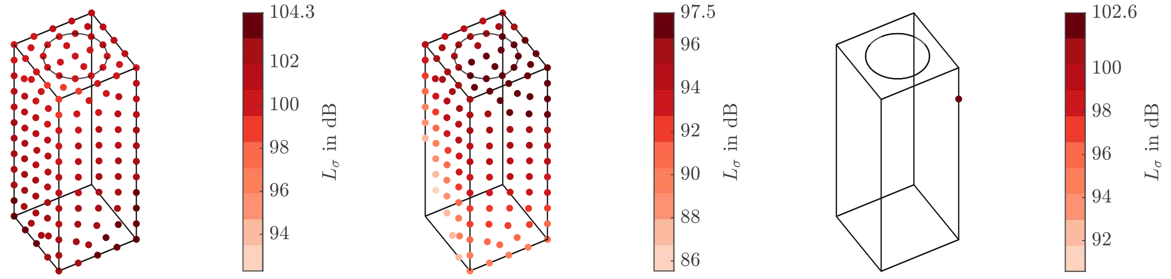

(d) ConvBF, $f = 300\,\mathrm{Hz}$.

(e) FunctBF, $f = 300\,\mathrm{Hz}$.

(f) CLEAN-SC, $f = 300\,\mathrm{Hz}$.

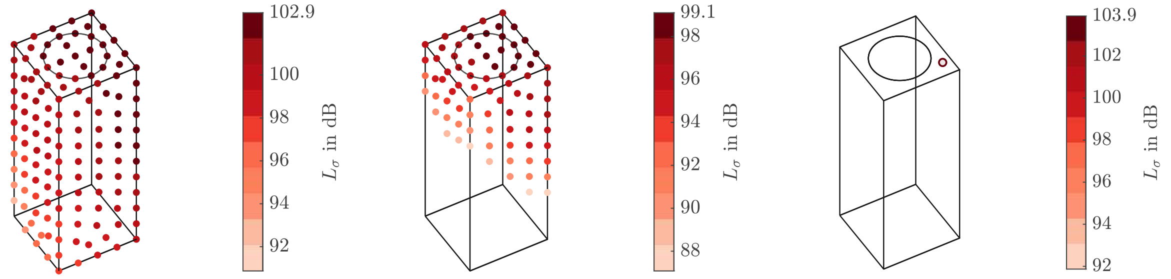

(g) ConvBF, $f = 600\,\mathrm{Hz}$.

(h) FunctBF, $f = 600\,\mathrm{Hz}$.

(i) CLEAN-SC, $f = 600\,\mathrm{Hz}$.

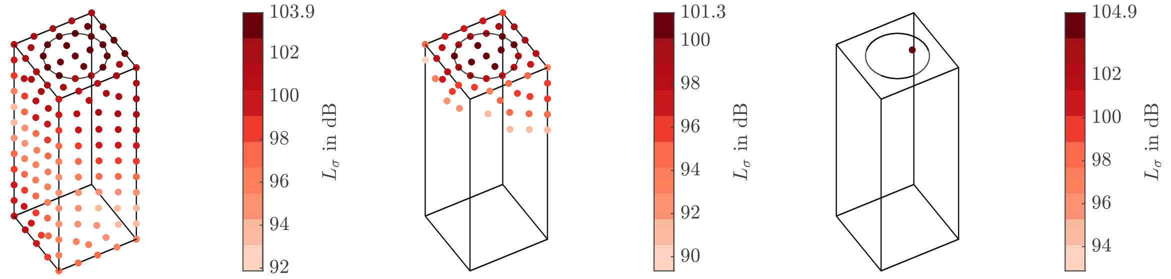

(j) ConvBF, $f = 1000\,\mathrm{Hz}$.

(k) FunctBF, $f = 1000\,\mathrm{Hz}$.

(l) CLEAN-SC, $f = 1000\,\mathrm{Hz}$.

Figure 5.12: Amplitude results from beamforming-based algorithms Conventional Beamforming (ConvBF), Functional Beamforming (FunctBF), and the deconvolution algorithm CLEAN-SC; microphone data was recorded within the stationary measurement trailer during loudspeaker excitation.

5.3.2 Inverse Scheme – Sound Pressure Results

In this section, we look at the sound pressure at the microphone positions calculated with the identified sources via the Inverse Scheme in comparison to the measured sound pressure signals. Firstly, the relative L2-errors $\varepsilon_{\mathrm{rel,L2}}$ and $\varepsilon_{\mathrm{abs,L2}}$ are considered, which compute via (4.38) and (4.39), respectively. The results, as a function of the discrete frequencies at which the sound source identification was performed, are depicted in Fig. 5.13. Again, as was the case with the virtual measurements in the previous section, the relative error of amplitudes, $\varepsilon_{\mathrm{abs,L2}}$, is lower by a factor of approx. 0.6 to 0.8 as the relative error $\varepsilon_{\mathrm{rel,L2}}$ of complex sound pressure differences. This fact indicates inaccuracies in the simulated sound pressure's phases. The lowest frequency of 200 Hz shows more significant relative errors than the other frequencies. At this frequency, the sound source identification result did not yield a satisfactory result. The relative errors decrease with increasing frequency, with two outliers at $f = 700$ and 900 Hz, at which the L2-errors are slightly higher. In general, the relative L2-errors are larger than in case of the virtual measurements. However, they are significantly lower than in the forward simulation where the material properties $\underline{K}_{\mathrm{eff}}$ and $\underline{\rho}_{\mathrm{eff}}$ were fitted to the validation measurements. This fact will be discussed in further detail later, when the sound pressure at the microphone positions will be shown.

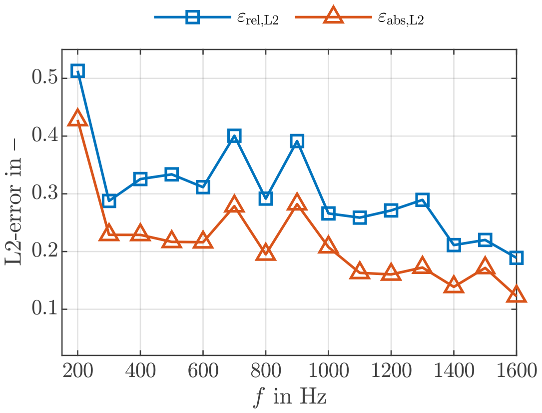

Figure 5.13: Relative L2-errors $\varepsilon_{\mathrm{rel,L2}}$ and $\varepsilon_{\mathrm{abs,L2}}$ of the acoustic pressure calculated from identified sound sources via the Inverse Scheme and the forward computation.

In order to further analyze the source identification results at the different frequencies, the sound pressure is plotted as a function of the distance r_{lm}, which is the distance between the microphone position and the midpoint of the loudspeaker membrane. Additionally, the relative distance r_{lm}/λ scaled with the wavelength at the corresponding frequency, is plotted as a second abscissa.

As it could be seen from the relative L2-errors, there are deviations between the simulated and measured acoustic pressures at 200 Hz, especially for $r_{\mathrm{lm}} \geq 0.59\lambda$. However, the simulated acoustic pressure's phase matches the measured phase very well at all microphone points. This can also be seen from Fig. 5.13, where – while the overall error values at 200 Hz are high compared to other frequencies – the relative L2-error $\varepsilon_{\mathrm{abs,L2}}$ of pressure amplitudes is close to the relative error values $\varepsilon_{\mathrm{rel,L2}}$ of the complex values.

For frequencies $f \geq 300$ Hz, the simulated and measured pressures match well in amplitude and phase. The deviation of phases at $r_{\mathrm{lm}} = 0.67$ m at $f = 600$ Hz is a phase wrapping effect at $\varphi_{\mathrm{a}} \approx \pm\pi$.

As already mentioned, the simulated acoustic pressure matches the measured pressure better in case of the Inverse Scheme, where the optimization parameters are the searched for sound source amplitudes and phases within Ω_{sc}, than in case of fitting the acoustic absorber's material parameters, where the optimization parameters were the real and imaginary parts of compression modulus $\underline{K}_{\mathrm{eff}}$

and $\underline{\rho}_{\text{eff}}$ within Ω_{abs}. The cost function is defined in both cases as the sound pressure difference

$$\sum_{i=1}^{N_\text{m}} |\underline{p}_\text{a}(\boldsymbol{x}_{\text{m},i}) - \underline{p}_i^{\text{ms}}|^2 \,,$$

see (4.35) and (5.10). Again it has to be stressed that the measurement is in both cases the same – the acoustic pressure at the microphone positions while the stationary measurement trailer is excited via the loudspeaker at the mentioned discrete frequencies. However, in case of the Inverse Scheme we regularize by means of Tikhonov, and the constrained optimization problem is solved via a gradient-based optimization. In contrast, the material property fitting is achieved via an unconstrained genetic optimization.

This fact leads to the conclusion that the optimization via a gradient-based approach is more potent than the genetic optimization. Further, the sensitivity of the sound pressure at the microphone positions $\boldsymbol{x}_{\text{m},i}$ is higher to changes in the source distribution within Ω_{sc} than it is to changes in the complex material properties within Ω_{abs}. Nevertheless, the satisfying sound source identification results via the Inverse Scheme suggest that the results of the material fitting is sufficiently accurate.

To conclude the sound source identification within the stationary trailer, the sound pressure field within the trailer is plotted in the whole computational domain, which is computed via a forward simulation with the results from the Inverse Scheme. Two exemplary frequencies are depicted in Fig. 5.16: 200 Hz and 600 Hz, which are frequencies that correspond to the highest relative L2-error of $\varepsilon_{\text{rel,L2}}(f = 200\,\text{Hz}) \approx 51\,\%$ and a relative error in the medium range of $\varepsilon_{\text{rel,L2}}(f = 600\,\text{Hz}) \approx 31\,\%$.

In Fig. 5.16a, the wrongly identified sound source at the bottom of the loudspeaker's housing causes high sound pressure levels in its vicinity. However, also near the membrane, high sound pressure levels arise from the identified sound sources near the membrane.

At $f = 600\,\text{Hz}$ one can see acoustic modes within the trailer. This indicates that the acoustic absorber cannot fully dampen the acoustic waves radiated from the loudspeaker. Further, although the dominant sound source is located at the top of the loudspeaker, regions of high sound pressure levels occur at the housing.

Since – as mentioned – there is no forward simulation available in case of microphone measurements, it is not possible to compare the simulated sound pressure field in each node of the computational mesh to the actual value. However, since the simulated sound pressure matches the measured one well at the microphone positions and these positions are evenly distributed across the measurement trailer, it is to be expected that the sound pressure field is reconstructed well in the whole chamber.

To sum up, the sound source localization with the Inverse Scheme and, at higher frequencies, also the beamforming-based algorithm CLEAN-SC yields satisfying results. Therefore, the sound source identification algorithms may be applied to measurements with the moving trailer in the next step, where not a loudspeaker but the tire-pavement interactions of the rolling tire are the sound sources to be identified.

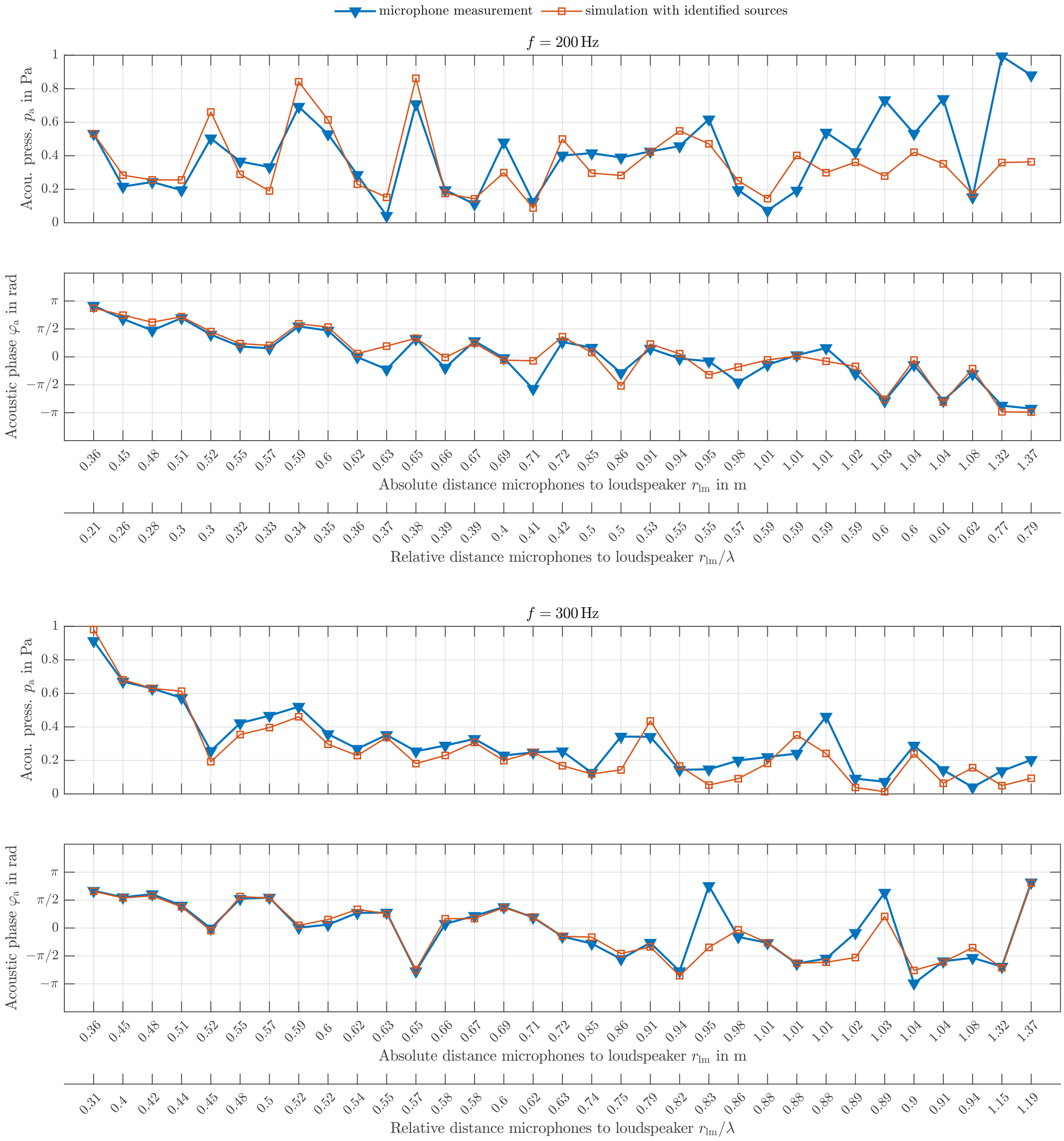

Figure 5.14: Comparison of microphone measurement and the simulated sound pressures at the microphone positions for $f = 200\,\mathrm{Hz}$ and $f = 300\,\mathrm{Hz}$.

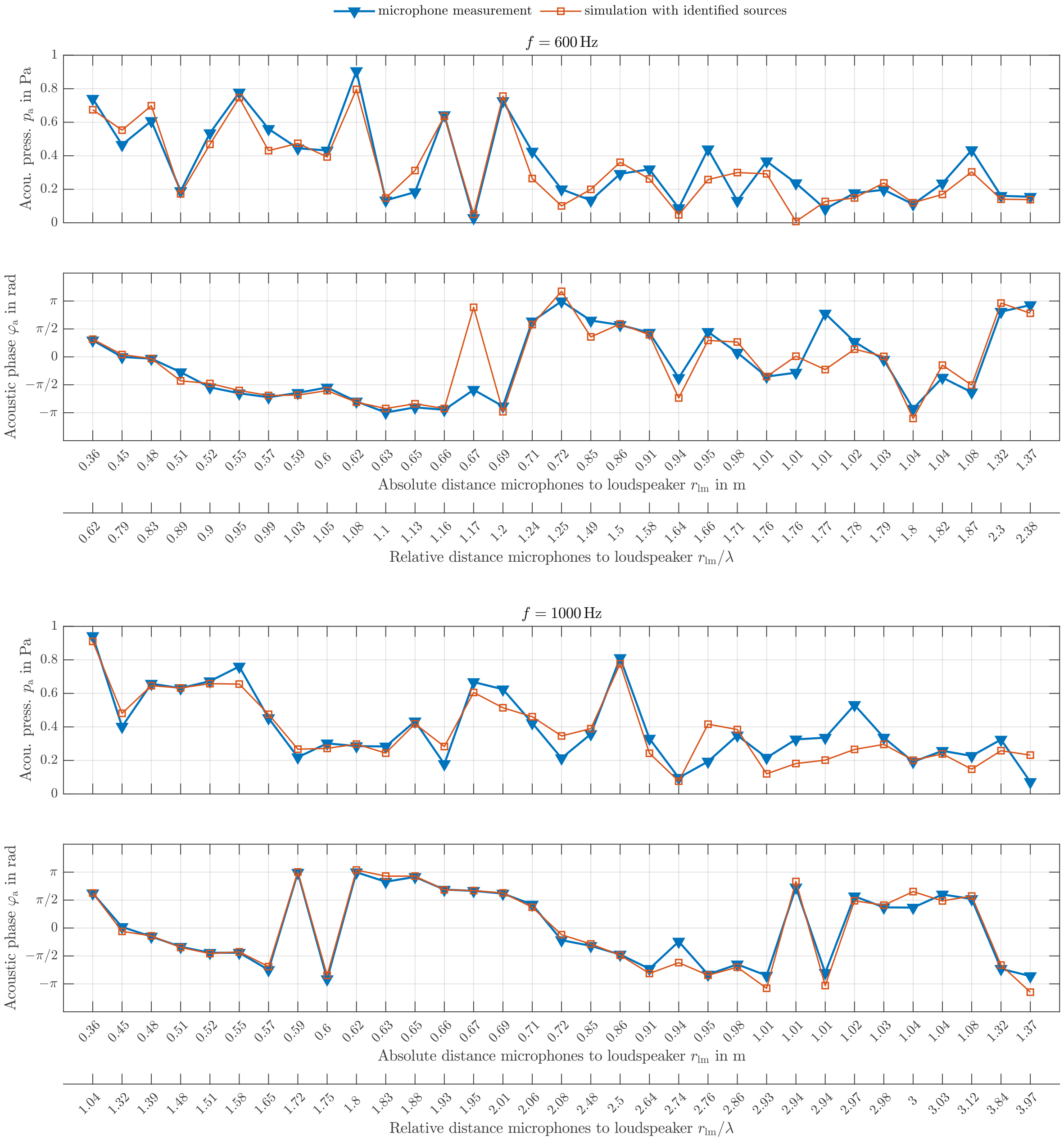

Figure 5.15: Comparison of microphone measurement and the simulated sound pressures at the microphone positions for $f = 600\,\mathrm{Hz}$ and $f = 1000\,\mathrm{Hz}$.

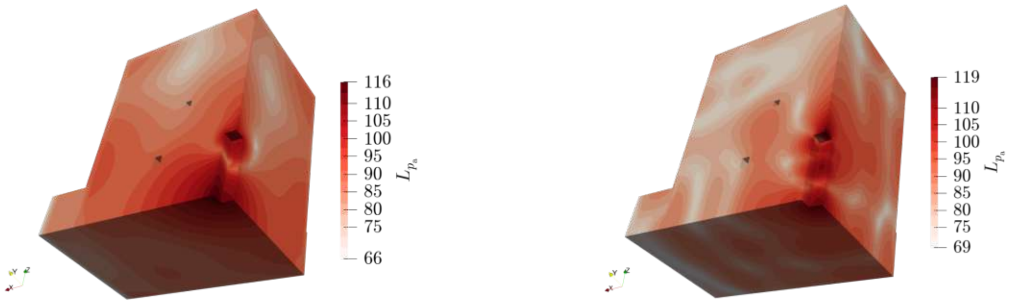

(a) $f = 200\,\mathrm{Hz}$.

(b) $f = 600\,\mathrm{Hz}$.

Figure 5.16: Sound pressure level within the computational domain, calculated from identified sources via the Inverse Scheme.

CHAPTER 6

Application of the Inverse Scheme for Sound Sources at the Rolling Tire

In this chapter, the Inverse Scheme and beamforming-based algorithms are applied to determine the dominant sound sources during the tire-pavement interaction. For this purpose, a measurement trailer is towed across different pavements. At the same time, the emitted sound is measured with the microphones positioned at similar locations within the trailer as in the stationary case described in the preceding chapter. This chapter discusses the trailer and the used sensors, covers the process of signal recording and processing, and subsequently, the application of the sound source algorithms.

6.1 Measurement Trailers

Different types of measurement trailers in Europe are mainly used for standard measurements according to ISO 11819-2 [37]. Usually, the microphones and the test tires are mounted inside a trailer with an enclosure. The trailers are equipped with sound-absorbing materials on the inside in order to limit the influence of the trailer's enclosure on the measured sound at the tire. In order to gauge if the enclosure's influence on the measured sound pressure is below certain limits, a measurement procedure is defined in [37]. This procedure requires an artificial sound source – *tire mock-up* – placed inside the stationary trailer while a white or pink noise signal is applied to the sound source. Subsequently, the sound pressure is measured at the CPX positions as shown in Fig. 1.2. The measurement is repeated with the tire mock-up and microphones only, without the trailer present. The absolute deviations between the two measured third-octave band spectra must be less or equal to 3 dB.

Besides the described most common form of trailers, alternative designs exist, such as open trailers without the protective enclosure, which eliminates the problem of unwanted reflections from the trailer's walls. In some cases the microphones are mounted outside of one of the vehicle's own tires. In the latter case, the standardized test tire has to have the appropriate dimensions for the test vehicle. An overview on different trailers can be found in [3, 161] or in reports on the Round Robin tests, which are organized regularly by a Dutch non-profit organization with international participants [162].

In addition to the trailers designed for standard measurements, there also exist trailers for research purposes with additional features, e. g. the possibility to measure the rolling resistance of the test tire [163] or with adjustable tire loads, see e. g. [164]. The trailer "SlipSonic" [3, 165] allows for an adjustable longitudinal slip of the measurement tire to investigate the sound emission of a tire with torque applied.

6.1.1 Used Trailer

In this thesis, the measurement trailer "AT^3 Acoustic Tyre Test Trailer" was used for recording the microphone data, which will be used for the different sound source localization methods to identify the dominant sound sources of the tire-pavement interactions. The trailer was already briefly presented in Sec. 4.2. It was built specifically for the AIT (Austrian Institute of Technology GmbH) to investigate the acoustics of the interactions between tires and different road surfaces. In contrast to classical trailers for measurements according to ISO 11819-2 [37] (Close Proximity Method) and RVS 11.06.64 [42], see Sec. 1.3.3, it provides enough space for additional microphones and other sensors. It has two separate chambers with one measurement tire in each chamber. The trailer's outer width of 2.5 m equals approximately the maximum width of trailers allowed on Austrian roads of 2.6 m. The internal dimensions of one chamber are approximately 1.2 m × 2.4 m × 1.4 m (width × length × height), which is considerably larger than other trailers designed for standard measurements. Its weight is approx. 750 kg, which means the trailer can be registered as a light trailer in Austria.

The test tires used are Standard Reference Test Tires (SRTT), standardized in [39], of type P1, which are the normed tires for passenger cars. The dimensions of the tire are P225/60R16, where the meaning of the string of letters and numbers can be taken from Tab. 6.1.

Symbol	Meaning
P	Tire for passenger cars
225	Nominal width w_t in mm
60	Aspect ratio r_hw (ratio of height to width) in percent
R	Radial tire
16	Rim diameter d_r in inches (16 in ≈ 406 mm)

Table 6.1: Meaning of tire designations.

Therefore, the total diameter d_t of the SRTT is calculated to $d_\mathrm{t} = 2w_\mathrm{t}r_\mathrm{hw}/100 + d_\mathrm{r} = 676\,\mathrm{mm}$. The measurement trailer consists of two separate mirror-symmetric chambers with one test tire each, which is mounted on a swing arm, depicted in yellow in the sketch in Fig. 6.1. The tires' track gauge is chosen such that the tires are running in the roads' lane grooves, which arise from the wear. The trailer is designed such that the tires' flanges are facing inwards. This means that the tire running in the left lane groove would be mounted on the right side of a vehicle and vice versa. Therefore, most microphones, depicted as gray circles in Fig. 6.1 are on the virtual outside of the vehicle tires.

The trailer's enclosure, see photo in Fig. 4.4a, can be adjusted in its height within limits. This is achieved with a pneumatic spring. The trailer can be lowered to the measurement position, where the gap between the trailer's enclosure and the pavement is approximately 80 mm. Due to the adjustable height and the trailer's suspension, in the lowest position, there is still a small relative movement possible between the enclosure and the swing arms. Since the microphones will be mounted on mounting rails – depicted in light blue in Fig. 6.1 – connected to the enclosure, the microphone positions may move relative to the tire during the measurement run. Therefore, an acceleration and a distance sensor are mounted within the trailer to determine whether the relative motion between microphones and the tire is within acceptable bounds.

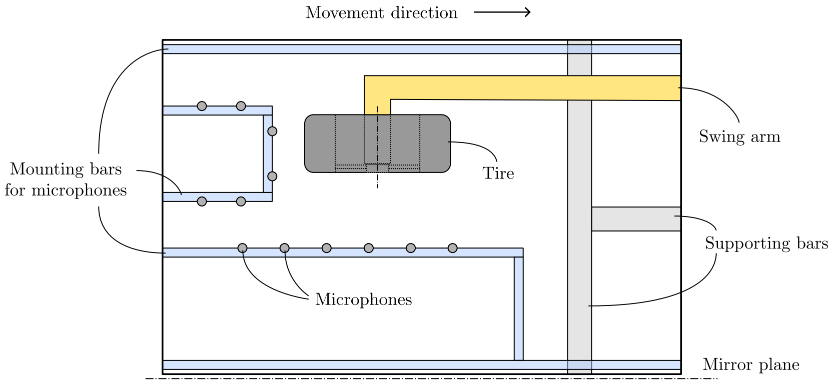

Figure 6.1: Sketch of the trailer's left chamber with main components, not drawn to scale.

6.2 Used Sensors

This section lists and describes the sensors including the 37 microphones that were used during the measurement runs. In addition to the sensors listed below, the trailer's left chamber was monitored via a live video feed during the measurement runs. From this video feed, it could already be observed during the measurements that the trailer exhibited a high running smoothness, resulting in a small amplitude of the relative displacement between the tire and microphones.

6.2.1 Microphones

The used microphones are electret microphones, an alternative type of condenser microphones with a thin dielectric foil between the electrodes [166]. Traditional condenser microphones are state-of-the-art in measurement technology when high-quality microphones with a flat frequency response are needed. However, they can be costly, and require a rather high DC bias, usually in the order of 200 V for measurement microphones. Since methods for sound source localization need a high number of microphones, for the measurements in this thesis the much cheaper electret microphones were used. They consist of a capsule of type KE 4-244-2 by Sennheiser [167] and a self-built preamplifier. Apart from the lower costs, they also lack the necessity of DC bias. In addition to electret microphones, in the last two decades, MEMS microphones have become cheap and reliable for medium-quality applications. Some MEMS microphones have integrated AD-converters. However, the time-synchronous recording of many microphones can be challenging.

The pre-amplified electret microphones' signals are amplified with a 64-channel microphone amplifier with an integrated band-pass filter with cut-off frequencies of 50 Hz and 20 kHz. For analog/digital (A/D) conversion of the microphone signals, two M-32 AD by RME [168] are used, which are A/D converters with 32 microphone channels each. The two A/D converters are synchronized via optical fiber with the MADI (Multichannel Audio Digital Interface) standard, where one of the two M-32 AD serves as a master clock. Thereby, a sampling rate of 48 kHz at a bit depth of 24 bits per sample can be achieved. The microphone data is transferred to a measurement laptop via a MADIface XT by RME [169]. It receives the digital signal from the A/D converter via optical fiber and transmits it to the PC via a USB 3.0 standard cable.

The microphones are calibrated with a Brüel & Kjær Sound Calibrator Type 4231 [156], which is a portable sound source that emits a sinusoidal test tone of a defined sound pressure of $p_{\mathrm{ref,rms}} = 1\,\mathrm{Pa} \approx 94\,\mathrm{dB}$ at a frequency of $f = 1000\,\mathrm{Hz}$ and a feedback loop with a built-in reference condenser microphone. Here, the suffix $\square_{\mathrm{rms}}$ stands for root mean square, which computes as

$$p_{\mathrm{a,rms}} = \sqrt{\frac{1}{T}\int\limits_0^T p_{\mathrm{a}}^2(t)\,\mathrm{d}t}\,. \tag{6.1}$$

From the measured microphone output voltage $U_{p_{\mathrm{a}},\mathrm{rms}}$, which is proportional to the acoustic pressure p_{a}, and the knowledge of the RMS value of the reference signal, the microphone's sensitivity $S_{\mathrm{mic,1000\,Hz}}$ at 1000 Hz, including the measurement chain, is calculated via

$$S_{\mathrm{mic,1000\,Hz}} = \frac{U_{p_{\mathrm{a}},\mathrm{rms}}}{p_{\mathrm{ref,rms}}} = \frac{U_{p_{\mathrm{a}},\mathrm{rms}}}{1\,\mathrm{Pa}}\,. \tag{6.2}$$

As the calibration only takes place at 1 kHz, the frequency dependency of the microphone's sensitivity is neglected. In [83], the frequency responses of the used electret microphones were measured compared to a reference microphone, a half-inch free-field microphone by Brüel & Kjær, Type 4190-L-001 [170]. The findings confirmed the flat frequency response in the frequency range of interest in this thesis.

Microphone Positions

The microphones are mounted to the bars inside the trailer. Instead of the clamp holders used in the stationary measurements, the microphones are mounted to the bars with pipe clamps. They are equipped with a sound insulation inlay. Hereby, the impact of vibrations stemming from the moving measurement trailer on the microphones' membranes shall be reduced. The slightly different mounting method results in marginally different microphone positions compared to the stationary measurements. Further, four more microphones were added, resulting in 37 microphones inside the trailer. Two of the added microphone positions are the two mandatory positions of the CPX method, see Fig. 1.2.

6.2.2 Position Sensor

In order to measure the relative displacement s_{rel} between the microphone mounting bars and the swing arm, the laser displacement sensor LK-G152 by Keyence was used [171]. With this sensor, the displacement of an object within the focus range of ±40 mm can be measured at a maximum rate of 50 kHz. The reference distance for diffused reflection amounts to 150 mm. Therefore, this sensor is suitable to measure the relative displacement between the tire and the trailer's enclosure since its maximum amplitude during the measurement run – compared to the relative reference deviation when the trailer is stationary – is expected to be below 40 mm, if the trailer is set to the lowest possible position with the pneumatic spring. In this position, the trailer's enclosure rests on rubber buffers with high hardness.

6.2.3 Acceleration Sensor

For additional information about the measurement trailer's running smoothness, a MEMS acceleration sensor is placed on one of the microphone mounting bars. A 3D accelerometer type ADXL335 by Analog Devices [172] was used, but only the direction normal to the pavement and in the lateral direction was recorded. The sensor's sensitivity S_{acc} amounts to

$$S_{\mathrm{acc}} = 300\,\frac{\mathrm{mV}}{g} \approx \frac{300\,\mathrm{mV}}{9.81\,\mathrm{m/s^2}} \approx 30.58\,\mathrm{mVs^2m^{-1}}\,.$$

Moreover, the sensor's upper frequency limit is 500 Hz. This frequency limit is considered as sufficiently high since the deflection's amplitude $|\underline{s}(\omega)|$ is related to the acceleration's amplitude $|\underline{a}(\omega)|$ via

$$|\underline{s}| = \frac{1}{\omega^2} |\underline{a}| \,.$$

Therefore, with increasing frequency, the displacement amplitudes are decreasing and, therefore, an acceleration measurement at higher frequencies becomes irrelevant. The sensor's measurement range is $\pm 3\,g \approx 29.40\,\mathrm{m/s^2}$.

6.2.4 Rotational Frequency Sensor

In order to determine the measurement trailer's speed, the rotational frequency $f_\mathrm{R} = \frac{\omega_\mathrm{R}}{2\pi}$ of the measurement tire SRTT in the trailer is determined. From the rotational frequency, the trailer's speed v_t can readily be calculated via

$$v_\mathrm{t} = \omega_\mathrm{R} \frac{d_\mathrm{t}}{2} = \pi f_\mathrm{R} d_\mathrm{t} \,. \tag{6.3}$$

An eddy current probe of type IC12-02 by WayCon [173], with which the distance to electrically conductive materials can be measured, was used to determine the distance of the rear side of the rim from the sensor. The sensor is positioned on the swing arm so that the five wheel bolts pass the sensor during the tire rotation. Since the sensors have a measurement range of 0–2 mm, the eddy current probe has to be placed close to the head of the wheel bolt. Thereby, the measured signal exhibits five significant peaks per revolution of the tire – whenever a screw head passes the sensor. When there is no screw in front of the sensor, the distance to the nearest conductive material is the rim, whose distance is outside the sensor's measurement range.

6.3 Sections of Measurements

The measurement data was gathered with the measurement trailer on Austrian highways in August 2022. In the following sections of this thesis, the measurement sections are presented. Further, the criteria to choose the specific measuring segments and frequencies at which the sound source localization algorithms are applied are discussed.

In order to cover different pavements, measurements were performed on asphalt, concrete, and concrete with grinding. The latter is a traditional concrete pavement with longitudinal grooves cut into its surface. This technique is used to reduce the noise due to the tire-pavement interactions by adding voids to the concrete surface. Thereby, the disadvantages of the otherwise mostly sealed concrete pavement's surface compared to asphalt pavements shall be compensated. The method is expected to reduce noise due to the air-pumping effect, described in Sec. 1.3.1, and increase the pavement's evenness, thereby reducing vibration effects.

To decide which measurement data is used to apply the sound source localization methods, the quality of the sound pressure measurements is the main criterion. Due to the high noise level, caused by wind noise, vibrations of the microphone mounting bars, and the increasing sound pressure with increasing trailer speeds, overdrives (clipping) of the audio signals occurred. It could be observed that overloads occurred primarily at the A/D converters. Therefore, only sound pressure data at lower vehicle speeds of 50 km/h to 80 km/h could be evaluated. The microphone data from untreated concrete surfaces showed a higher likelihood of overdriving. In order to determine if a microphone signal shows overdriving, the following method is used:

1. Calculate the maximum and minimum value of each microphone's time signal.
2. Determine all locations in the signal, where one or more microphone channels show at least two consecutive data samples where the maximum or minimum value is reached.

3. Determine the maximum length between the previously determined locations.
4. All microphone signal data outside of this period are omitted.

The procedure is illustrated in Fig. 6.2, where the time signals of two microphone channels are depicted. At $t \approx 7530\,\mathrm{ms}$ and $t \approx 8807\,\mathrm{ms}$ one of the two plotted signals reaches its respective maximum value in four and five consecutive data samples, respectively. Therefore, the areas marked in gray are omitted. The resulting valid microphone signals have a length of $T_{\mathrm{meas}} \approx 1.28\,\mathrm{s}$.

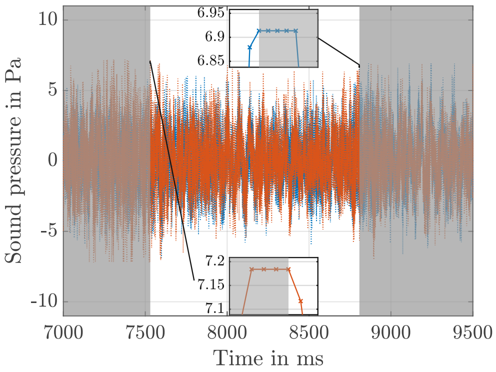

Figure 6.2: To avoid overdriving in microphone signals, all data marked in grey is omitted since the corresponding maximum time signal values are reached at the marked positions.

A list of potential measurements is obtained by evaluating the maximum lengths of the valid time spans for all measurement runs. Depending on the valid signals' lengths, after applying the Fourier transform to each signal, the corresponding frequency resolutions differ for each signal. The frequency resolution Δf can be calculated from the measurement time T_{meas} by

$$\Delta f = \frac{1}{T_{\mathrm{meas}}} = \frac{f_{\mathrm{S}}}{N_{\mathrm{s}}}\,, \tag{6.4}$$

where $f_{\mathrm{S}} = 48\,\mathrm{kHz}$ denotes the sampling frequency of the microphone signals, and N_{s} is the number of samples.

6.3.1 Locations and Pavements

From the evaluated valid periods of each measurement, the following sound pressure measurements were chosen for being processed by sound source localization algorithms:

Meas. No.	Speed in km/h	Pavement Type	Highway	Valid length in s
1	78	Asphalt SMA-S1	S05	1.2
2	68	Asphalt SMA-S1	S05	7.7
3	59	Asphalt SMA-S3	A21	20
4	50	Asphalt SMA-S3	A21	12.3
5	59	Concrete with grinding	A02	10.9

Table 6.2: Measurements chosen for sound source identification algorithms.

Measurements 1 to 4 were recorded on an asphalt pavement, and measurement 5 on a concrete pavement. Here, the name "SMA" is short for *Stone Matrix Asphalt* or *Stone Mastic Asphalt*, which is an asphalt developed to increase the pavements working lifetime combined with good sound absorption capabilities [174]. The name “SMA-S1” stands for a dense asphalt, and “SMA-S3” is an open-graded asphalt with usually better sound absorption properties because of its higher porosity.

The measurements were recorded in August 2022, with air temperatures inside of the trailer varying between 28 °C and 34 °C.

6.3.2 Evaluation of Sensor Data

This section deals with the interpretation of the gathered measurement signals. As mentioned in the previous section, the most crucial criterion is that the sound pressure signals are free of overdriving. The other sensor signals are evaluated in the resulting period to determine the relative displacement between microphone bars and the tire swing. Further, the trailer’s speed is calculated from the rotational frequency of the measurement tire.

Position Sensor

As shown from the plots in Fig. 6.3, the relative deviation s_{rel} between the microphone mounting bars and the trailer’s swing arm is relatively small. Note that the zero level of the sensor was determined at the stationary trailer on a level ground. Due to tilted and inclined pavements, the measured deflections may have a different mean position during the measurement runs.

Within the valid periods, the maximum peak-to-peak $s_{\text{rel,pp}}$ value of s_{rel} is below 10 mm for all measurement numbers. Since the maximum frequency of interest is 1600 Hz the corresponding minimal wavelength of interest is $\lambda \approx 219\,\text{mm}$ for the mean temperature during the measurements. This equals more than $20 s_{\text{rel,pp}}$, and therefore, this deviation of the nominal microphone positions is negligible. Thus, no further restrictions concerning the evaluable microphone signal lengths arise from the deflection measurements.

However, the relative deflections show that the valid periods, evaluated from the microphone signals, often correspond to minimal values of the relative deviation s_{rel} during the measurements. This can be seen especially in the plot of measurement 1, where distinctive peaks in the deflection signal occur at the end and beginning of the invalid time periods, respectively. Invalid periods where overdriving occurs are again marked in gray.

The relative deviation s_{rel} of measurement 5 in Fig. 6.3 exhibits periodic peaks with a spacing of approx. 336 ms. With the speed during measurement 5 of $59\,\text{km/h} \approx 16.4\,\text{m/s}$, this corresponds to a spacial distance of approx. 5.5 m between two peaks. At the measurement location, this equals exactly the distance of two joint gaps between the concrete blocks.

Rotational Frequency Sensor

In the following, the evaluation of the tire’s rotational frequency sensor is addressed. In Fig. 6.4a, the eddy current probe’s signal is plotted. As previously mentioned, when a wheel bolt’s head passes the sensor, a conductive material is within the sensor’s measurement range. This manifests as peaks in the signal, marked as triangles in Fig. 6.4a. Note that the depicted signal has been mirrored vertically and shifted, such that the points in time, where the wheel bolts pass in front of the sensor, manifest as positive peaks and can therefore easily be detected by Matlab’s `findpeaks` algorithm. Values close to zero indicate that the sensor is out of range. Since each bolt causes two peaks in the signal – it is assumed that the cause for that is the screw’s hexagon socket – only every other peak is taken into account. Those peaks are marked with a red ’x’. Since we only want to obtain information about the rotational frequency of the tire, the absolute values of the displacement data are not of interest and are, therefore, not evaluated. From the time $\Delta t_{\text{tire,rot}}$ between the peaks marked with ’x’ in Fig. 6.4a, the tire’s rotational frequency $f_{\text{tire,rot}}$ can be obtained via

$$f_{\text{tire,rot}} = \frac{1}{N_{\text{screw}}} \frac{1}{\Delta t_{\text{tire,rot}}} , \tag{6.5}$$

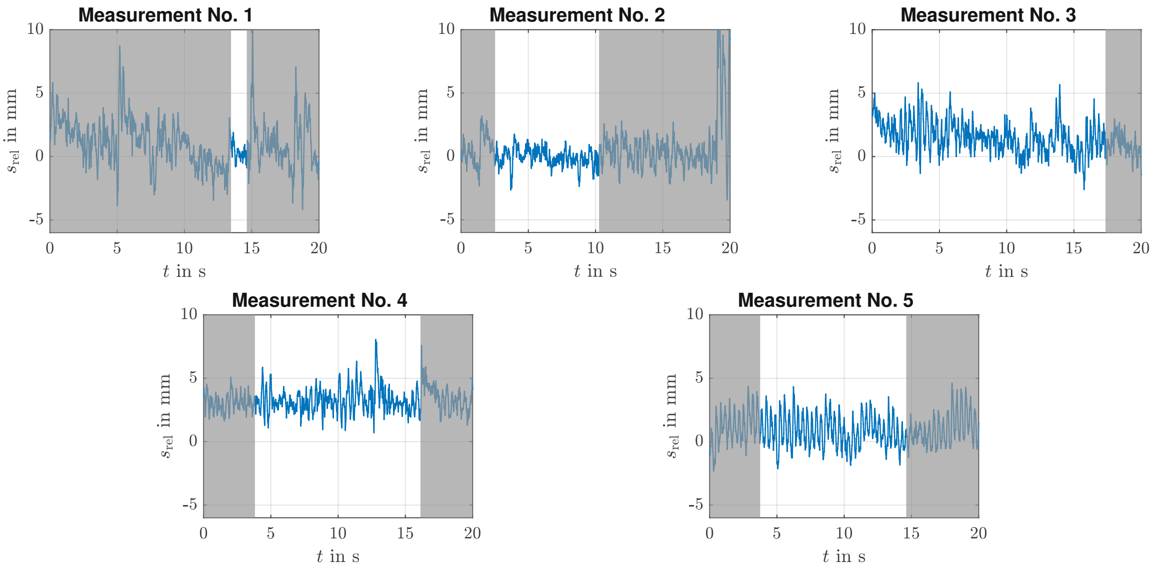

Figure 6.3: Evaluation of the positional sensor signal: relative deflection s_{rel} between the microphone mounting bars and the trailer's swing arm. Time periods where the microphone signals are overdriven are marked in gray.

with the numbers of screws $N_{\mathrm{screw}} = 5$. Therefore, during one revolution of the tire, four independent values of $f_{\mathrm{tire,rot}}$ can be determined.

With (6.3), the trailer's speed during the measurements is calculated. In Fig. 6.4b, the speeds are depicted as a function of time, where only valid periods are considered. Therefore, the signals' lengths differ according to Tab. 6.2. Figure 6.4b indicates, that the trailer's speed is almost constant during the measurement time.

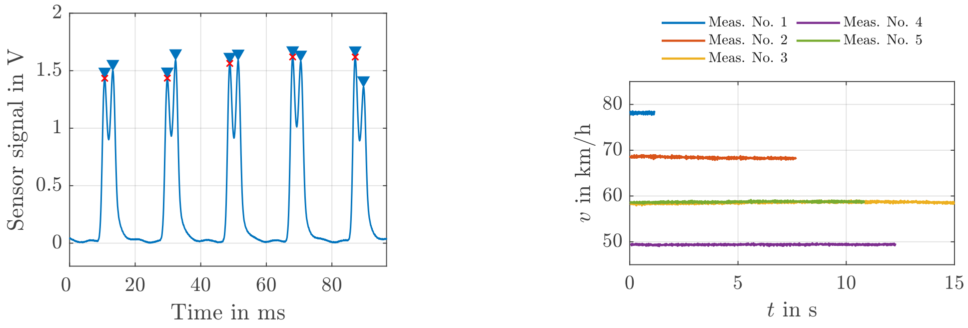

(a) Mirrored and shifted signal of the eddy current sensor. Detected peaks are marked with a triangle, values for the evaluation of the rotational frequency are marked with a red 'x'.

(b) Trailer's speed v, calculated from the rotational frequency $f_{\mathrm{tire,rot}}$.

Figure 6.4: Evaluation of the eddy current sensor to obtain the tire's rotational frequency.

The evaluation of the acceleration sensor did not yield relevant information concerning the validity of the microphone measurements and is therefore not shown here.

Sound Pressure Signals

The recorded microphone signals shall be investigated before performing sound source identification on the rolling tire. Thereby, suitable frequencies for the sound source localization can be chosen. Localizing sound sources with beamforming-based algorithms is often done for multiple frequencies within a frequency band, e. g. a third-octave band. Since compared to beamforming-based algorithms, the Inverse Scheme is computationally demanding, see Tab. 5.2, a broadband analysis is not feasible. Therefore, sound source identification results are only obtained for discrete frequencies. In order to ensure a high signal-to-noise ratio, tonal components within the recorded signals are chosen for these frequencies.

In Fig. 6.5, the sound pressure spectra averaged over all microphones are plotted in the relevant frequency range for the five measurements listed in Tab. 6.2. In addition to the averaging over all microphones, a temporal averaging was applied: the FFT was performed using a block size of $N_\mathrm{b} = 12000$, a Hann window, and an overlap of $50\,\%$ between the blocks. Therefore, the resulting frequency resolution $\Delta f = \frac{f_\mathrm{S}}{N_\mathrm{b}} = 4\,\mathrm{Hz}$, with the sampling frequency $f_\mathrm{S} = 48\,\mathrm{kHz}$. Since the valid measurement times differ in each measurement run, see Tab. 6.2, and the block size is held constant, the resulting numbers of averages differ for each measurement.

Note that the averaging of the Fourier transforms of the sound pressure spectra is only performed for the sake of readability of the plots. The Fourier transforms of each microphone without averaging serve as input data for the Inverse Scheme and other sound source localization algorithms.

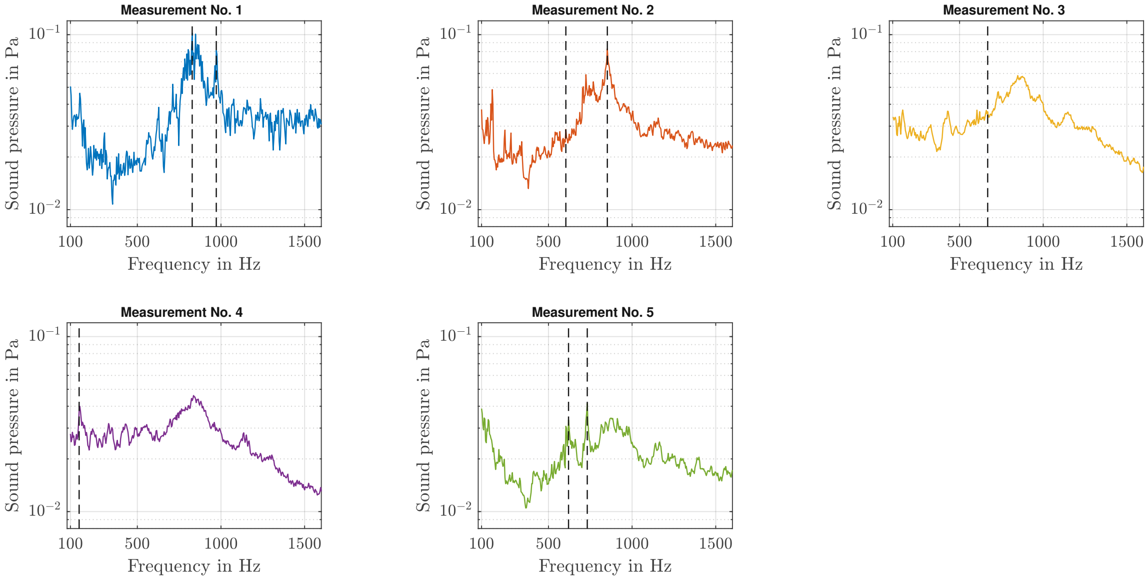

Figure 6.5: Mean sound pressure spectra averaged over all microphone positions during measurements 1–5. Tonal components chosen for sound source localization are marked with a vertical dashed line.

In Fig. 6.6, the third-octave bands of the sound pressure levels, again averaged over all microphone positions, of measurements 1 until 5 are plotted. Note, that the center frequencies are calculated according to [175], and therefore differ slightly from the commonly known values.

From the plots, it can be concluded that the dominant frequency range of the sound sources during the tire-pavement interaction lies between 700 Hz and 1000 Hz, which is consistent with the literature, see e. g. [3]. The two dominant third-octave bands for all pavements are $f_\mathrm{c} \approx 800\,\mathrm{Hz}$ and $f_\mathrm{c} = 1000\,\mathrm{Hz}$. In the spectra depicted in Fig. 6.5, it can be seen that additional tonal components occur at frequencies outside of the dominant range, which will later be chosen for the application of the sound source

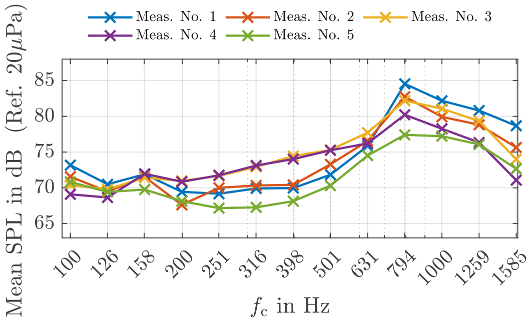

Figure 6.6: Third-octave band sound pressure levels of measurement 1–5 in the relevant frequency bands with center frequencies $f_\mathrm{c} < 1600\,\mathrm{Hz}$.

identification algorithms. Especially measurement 5, which was gathered on a concrete pavement with grinding, shows distinctive tonal components at approximately 620 Hz and 730 Hz, below the dominant third-octave center frequency.

The overall A-weighted sound pressure levels can be found in Tab. 6.3. A comparison of measurements 3 and 4, which were recorded immediately following each other on the same asphalt pavement, show the speed dependency of the tire noise levels, as stated in Sec. 1.2. The sound pressure level difference ΔL_p between the two speeds v_3, and v_4 is $\Delta L_p \approx 2.2\,\mathrm{dB}$, which is an excellent agreement with the speed dependency of tire-pavement noise according to the literature review in Sec. 1.2. There, the dependency factor is stated as $A \log(v/v_\mathrm{ref})$, with $A \approx 30$. The norm of the CPX method [37] defines speed coefficients for correcting the measured sound pressure for deviations from the reference speed of $A = 25$ for porous pavements in new conditions and $A = 30$ for dense asphalt pavements.

The calculated speed proportionality factor A_calc reads as

$$A_\mathrm{calc}(v_3, v_4) = \frac{\Delta L_p}{\log \frac{v_3}{v_4}} \approx 30.6\,.$$

The speed factor of measurements 1 and 2 is in the same scale, with $A_\mathrm{calc}(v_1, v_2) \approx 32.7$. Measurements 1 and 2 cannot be directly compared to 3 and 4 since they were recorded on different types of asphalt pavements. The fact that the asphalt pavement SMA-S3 has a lower speed proportionality factor than the more dense asphalt SMA-S1 is expected due to the higher porosity of SMA-S3. This means that higher speeds lead to a lower sound pressure increase in case of the open-graded asphalt.

Meas. No.	Pavement	Speed in km/h	SPL in dBA
1	Asphalt SMA-S1	78	92.0
2	Asphalt SMA-S1	68	90.1
3	Asphalt SMA-S3	59	89.9
4	Asphalt SMA-S3	50	87.7
5	Concrete with grinding	59	87.3

Table 6.3: Overall sound pressure levels of chosen measurements.

6.4 Sound Source Identification Results

In the previous sections, the valid measurement sections could be established, and the measured signals were discussed in detail. Therefore, we now identify the sound sources via the Inverse Scheme and compare the results obtained with beamforming-based algorithms.

6.4.1 Results – Inverse Scheme

The source region Ω_{sc}, where the dominant sound sources are expected to be located, is defined as the surfaces of the measurement tire. The tire is modeled as a sound-hard cylinder with the diameter and the width of the SRTT. Therefore, the actual tire geometry is simplified. The computational mesh is similar to the one used for solving the inverse problem for the stationary trailer, where sources on a loudspeaker were identified. However, since a measurement tire is now mounted in both chambers of the trailer, the computational mesh has a symmetry plane in the middle of the wall dividing the two chambers. Therefore, a sound-hard boundary condition is imposed there.

Further, to model that the tire deforms under load due to its elasticity, the distance between the wheel axle and the pavement is slightly less than the tire's radius. Therefore, the tire's lowest part is intersected with the pavement plane and the tire contact patch is modeled as a rectangle. All other parameters, including the material parameters of the acoustic absorber region, remain the same as in the previous sound source identifications with the Inverse Scheme, see Sec. 5.3. The Inverse Scheme's results were obtained with the regularization parameters in (5.38).

In the following, the identified sound sources are depicted as a sound source level, which calculates via (5.37). The dynamic range is chosen 12 dB and 20 dB for Fig. 6.7 and Fig. 6.8, respectively. All sources with a source level below this dynamic range are omitted. Owing to space limitations, only results of selected frequencies can be presented here. Since – as mentioned – the SNR is expected to be highest at frequencies of tonal components in the microphone signals, the localization algorithms are applied at those frequencies. The chosen frequencies of the respective measurements are marked with a vertical dashed line in Fig. 6.5.

In the result plots, the trailer's left tire is depicted in side view, with the tire turning clockwise. Identified sound sources at the tire's left side wall and the rear-facing trailing edge are shown as a small circle; all sources on surfaces facing the front – i. e. the right side wall and the front-facing leading edge – are depicted as solid circles.

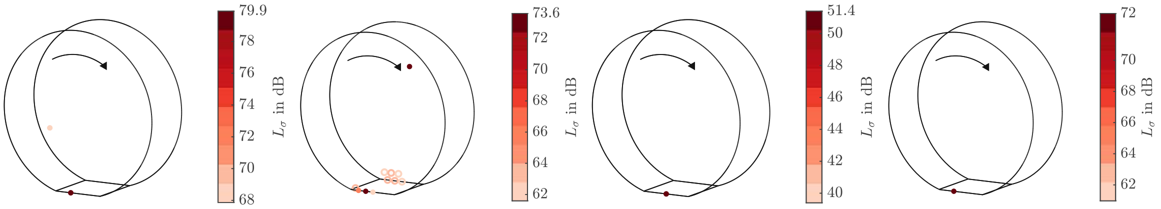

(a) Meas. No. 1, $f = 827\,\text{Hz}$.

(b) Meas. No. 1, $f = 974\,\text{Hz}$.

(c) Meas. No. 2, $f = 604\,\text{Hz}$.

(d) Meas. No. 2, $f = 851\,\text{Hz}$.

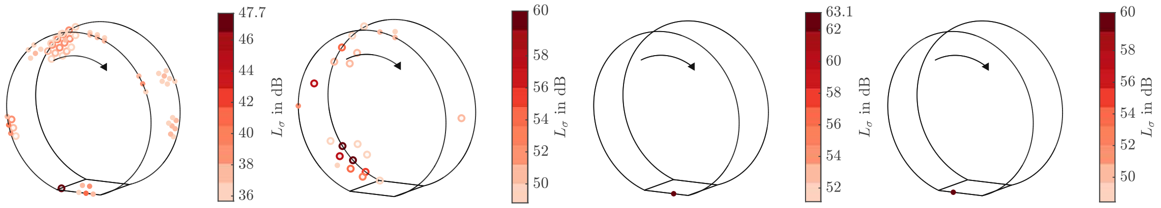

(e) Meas. No. 3, $f = 667\,\text{Hz}$.

(f) Meas. No. 4, $f = 153\,\text{Hz}$.

(g) Meas. No. 5, $f = 622\,\text{Hz}$.

(h) Meas. No. 5, $f = 732\,\text{Hz}$.

Figure 6.7: Sound source identification results via the Inverse Scheme; with a dynamic range of 12 dB.

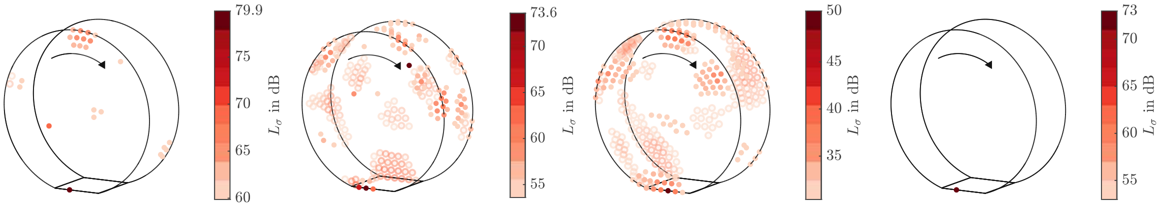

(a) Meas. No. 1, $f = 827\,\text{Hz}$.

(b) Meas. No. 1, $f = 974\,\text{Hz}$.

(c) Meas. No. 2, $f = 604\,\text{Hz}$.

(d) Meas. No. 2, $f = 851\,\text{Hz}$.

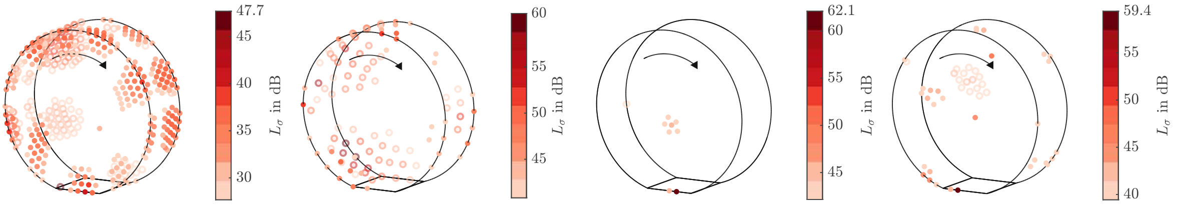

(e) Meas. No. 3, $f = 667\,\text{Hz}$.

(f) Meas. No. 4, $f = 153\,\text{Hz}$.

(g) Meas. No. 5, $f = 622\,\text{Hz}$.

(h) Meas. No. 5, $f = 732\,\text{Hz}$.

Figure 6.8: Sound source identification results via the Inverse Scheme; with a dynamic range of 20 dB.

As shown in the plots in Fig. 6.7, the most dominant sound source in each evaluated frequency of the corresponding measurement is always identified near the contact zone between the tire and pavement. If weaker sound sources within the dynamic range of 12 dB are identified, they are mainly located around the tire's circumference – see identification results in Fig. 6.7e. This indicates strong sidewall and tire belt vibrations at these frequencies.

The only exception to this pattern is the identification result shown in Fig. 6.7f, which is the lowest depicted frequency at $f = 153\,\mathrm{Hz}$. At this frequency, the dominant sound source is located at the tire's trailing edge, with other dominant sound sources located along the trailing edge to the top of the tire. In the literature, the low frequency range is associated with tire vibrations, which lies in good agreement with the result at this lowest frequency, where the sources are more distributed over the whole tire than at higher frequencies. However, as stated in the previous results, one has to consider the compactness of the source at low frequencies and, subsequently the low sensitivity of the sound pressure to the exact source locations.

The plots in Fig. 6.8 also reveal weaker identified sources. Thereby, e. g. a cluster of monopole sources with lower amplitudes becomes visible at the top of the tire in Fig. 6.8a, and further sources are depicted along the tire's circumference in Fig. 6.8e.

6.4.2 Results – Beamforming-Based Algorithms

In order to compare the Inverse Scheme's performance with commonly known algorithms, the results are – as in the section before – validated with beamforming-based algorithms. Again, the beamforming-based algorithms are Conventional Beamforming (*ConvBF*), Functional Beamforming (*FunctBF*), and CLEAN-SC.

To obtain the beamforming results, the same sound pressure data in the frequency domain as in the Inverse Scheme are used, along with the same microphone and potential source locations. From these positions, the steering vectors are calculated according to (3.9), which use the free-field Green's function (2.56) for monopoles. Note that besides the aforementioned information, namely Fourier-transforms of the sound pressure data and microphone and potential source positions, no additional information are passed to the beamforming algorithms. Therefore, no information concerning boundary conditions of the actual measurement setup, such as the porous acoustic absorbers or the sound-hard obstacles within the computational domain, including the tire itself, are known to the beamforming-based methods. This fact might be seen as if the beamforming-based algorithms are put at a disadvantage. However, in [83] the beamforming steering vectors were determined with numerically calculated Green's functions via the FE method, considering the actual boundary conditions. But the numerically calculated transfer functions did not significantly improve the source maps compared to the analytically calculated steering vectors. Therefore, in this thesis, only the standard approach according to (3.9) was chosen.

The results of the three mentioned algorithms, calculated at the same frequencies and measurements as the previously shown Inverse Scheme's results, are depicted in Fig. 6.9, Fig. 6.10 and Fig. 6.11, respectively. Here, only figures with a dynamic range of 20 dB are plotted.

From Fig. 6.11, one can see that the very fast and basic algorithm ConvBF yields qualitatively good results for some frequencies regarding the primary sound source being at the contact zone between tire and pavement. This is especially the case for the higher of the depicted frequencies. At the lowest frequency of $f = 153\,\mathrm{Hz}$ the location of the dominant sound source cannot be established due to the large width of the main-lobe. At all other shown frequencies, relatively high side-lobe levels are visible, which makes it difficult to interpret whether there are sources present additionally to the dominant ones located in the lowest region of the tire.

The algorithm FunctBF yields better results concerning the side-lobe level, see Fig. 6.10. Comparing Fig. 6.8f and Fig. 6.10f, one can see that both algorithms locate the dominant sound sources along the tire's trailing edge. The main sound sources are again located near the tire's contact patch at all other measurements. However, no sources along the tire's circumference are identified, as it was the case with the Inverse Scheme.

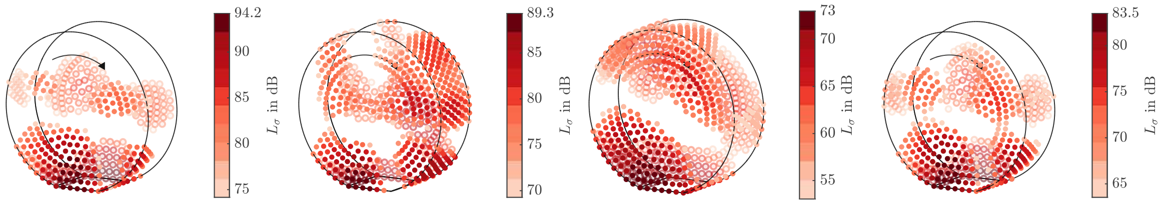

(a) Meas. No. 1, $f = 827\,\mathrm{Hz}$.

(b) Meas. No. 1, $f = 974\,\mathrm{Hz}$.

(c) Meas. No. 2, $f = 604\,\mathrm{Hz}$.

(d) Meas. No. 2, $f = 851\,\mathrm{Hz}$.

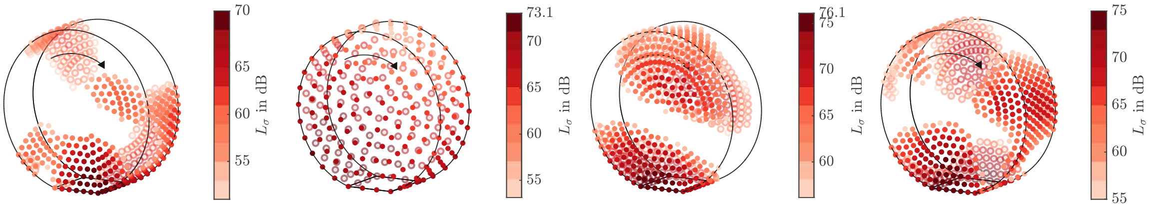

(e) Meas. No. 3, $f = 667\,\mathrm{Hz}$.

(f) Meas. No. 4, $f = 153\,\mathrm{Hz}$.

(g) Meas. No. 5, $f = 622\,\mathrm{Hz}$.

(h) Meas. No. 5, $f = 732\,\mathrm{Hz}$.

Figure 6.9: Sound source identification results via Conventional Beamforming.

The de-convolution algorithm CLEAN-SC, which calculates its *clean* source maps from the "*dirty*" ConvBF maps, yields sparse source distributions at all frequencies. Only one monopole source is present at all frequencies, which is always located near the tire-pavement contact zone. This means that there is only one source within the dynamic range of 20 dB present, although it could be possible that other sound sources with high amplitudes are omitted by the algorithm. This may be the case since CLEAN-SC eliminates the side-lobes of the dirty map by exploiting the fact that they are coherent with the main lobe, see Sec. 3.2.2. Therefore, sources coherent to the dominant sound source may be omitted by CLEAN-SC.

The results obtained via CLEAN-SC resemble the plots of the Inverse Scheme's results with the dynamic range set to 12 dB, where also mainly one sound source near the contact patch was identified as the dominant sound source. However, as Fig. 6.8 shows, in contrast to CLEAN-SC, the Inverse Scheme identifies more sound sources on the tire's surface with source levels $L_\sigma < L_\sigma - 12\,\mathrm{dB}$. As we will see in the next section, these weaker sound sources are essential for accurately reconstructing the sound pressure at the microphone positions.

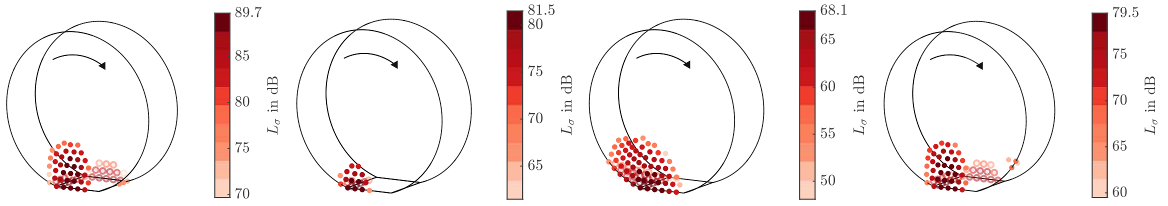

(a) Meas. No. 1, $f = 827\,\text{Hz}$.

(b) Meas. No. 1, $f = 974\,\text{Hz}$.

(c) Meas. No. 2, $f = 604\,\text{Hz}$.

(d) Meas. No. 2, $f = 851\,\text{Hz}$.

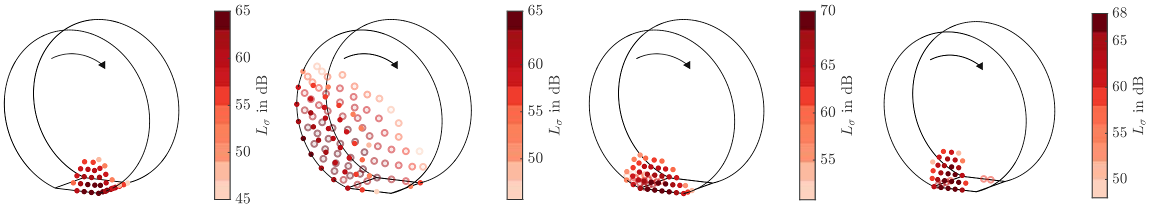

(e) Meas. No. 3, $f = 667\,\text{Hz}$.

(f) Meas. No. 4, $f = 153\,\text{Hz}$.

(g) Meas. No. 5, $f = 622\,\text{Hz}$.

(h) Meas. No. 5, $f = 732\,\text{Hz}$.

Figure 6.10: Sound source identification results via Functional Beamforming.

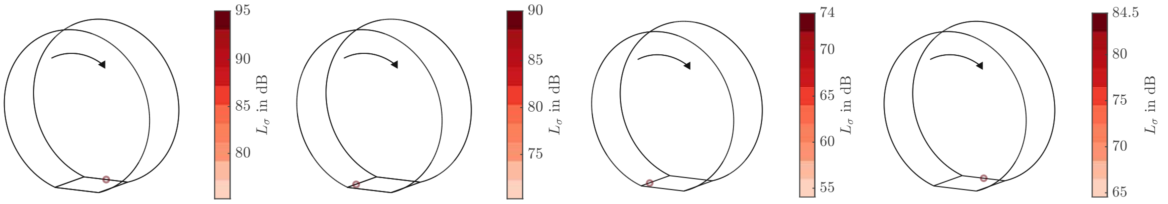

(a) Meas. No. 1, $f = 827\,\text{Hz}$.

(b) Meas. No. 1, $f = 974\,\text{Hz}$.

(c) Meas. No. 2, $f = 604\,\text{Hz}$.

(d) Meas. No. 2, $f = 851\,\text{Hz}$.

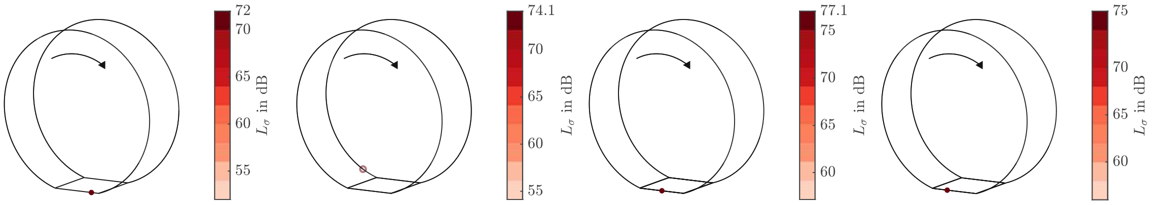

(e) Meas. No. 3, $f = 667\,\text{Hz}$.

(f) Meas. No. 4, $f = 153\,\text{Hz}$.

(g) Meas. No. 5, $f = 622\,\text{Hz}$.

(h) Meas. No. 5, $f = 732\,\text{Hz}$.

Figure 6.11: Sound source identification results via CLEAN-SC.

6.5 Sound Pressure Field Results

The sound pressures at the microphone positions may be calculated from the identified sound sources via FE simulations and will be compared to the measurements. This forward computation will be performed using the sources identified from the Inverse Scheme and those determined by the deconvolution algorithm CLEAN-SC. However, since beamforming-based algorithms can only reconstruct the source amplitudes, the phases of the CLEAN-SC sources are set to zero. Therefore, comparing the calculated sound pressure phases to the measured phases is only possible to a limited extent. Since in all presented sound source identifications, CLEAN-SC identifies a single sound source only, and due to the linearity of the acoustic wave equation, the assumption of setting the source phase to zero results in a potential constant phase offset, which is the same for all microphone positions.

6.5.1 Comparison Forward Simulation with Measurement

In the following figures, Fig. 6.12 until Fig. 6.16, the acoustic pressure simulated via the forward model of the trailer, which was established in Chap. 4, is compared to the microphone measurements at one frequency of the respective measurements. As excitation, three different source distributions are computed at each frequency:

- All sources identified via the Inverse Scheme (solid orange lines)
- Sources identified via the Inverse Scheme, which are visible when the dynamic range is set to 12 dB (solid yellow lines)
- Sources identified with the CLEAN-SC (dashed purple lines).

The measurements are depicted as a solid blue line. The acoustic pressure at the microphone positions is plotted as a function of r_{tm}, which is the distance between the center point of the tire contact patch and the respective microphone position. Again, to ensure readability, the spacing of the x-axis ticks is equidistant and, therefore, not proportional to the distance r_{tm}.

In all cases, the acoustic pressure simulation with all sources identified via the Inverse Scheme matches the microphone signals best. If only the dominant sources, with a source level of max. 12 dB lower than the source with the highest amplitude are taken into account, the simulated pressure is too low for most of the presented results. The only exception to this is the lowest frequency of $f = 153\,\mathrm{Hz}$, where the sound pressure calculated with only the sources within 12 dB dynamic range is higher than in case of taking all monopole sources into account, see Fig. 6.15. This can be explained by the fact that most identified sources have opposite phases, leading to an *acoustic* or *hydrodynamic short-circuit*. This is a phenomenon which occurs when two sound sources with opposite phases cancel any sound radiation due to air flowing from one to the other source point. If some sound sources are omitted, and the cancellation is thereby partially prevented, the sound radiation can be more effective with fewer acoustic monopoles.

The acoustic pressure's phase calculated with all sources within the 12 dB range matches the measured phase well, although the deviation is more significant than when simulating with all identified sources.

If the acoustic pressure is calculated with the CLEAN-SC sources, the simulated acoustic pressures' amplitudes do not match the measured values well. In particular, the agreement is worse than in case of the 12 dB-sources inferred from the Inverse Scheme, although the plots of the identified source maps of the two algorithms are often similar to each other, see e. g. Fig. 6.7g and Fig. 6.11g. Again, it has to be stressed that the acoustic pressure phases calculated with the sources identified via CLEAN-SC may differ by a constant offset over all microphones since the source phases are assumed to be zero in the forward computation. However, the calculated deviations of the pressures' phases are not constant over the microphone positions for all frequencies. The best agreement of the acoustic phases for the CLEAN-SC sources is found at the lowest of the presented frequencies, where $f = 153\,\mathrm{Hz}$, see

Fig. 6.15. Note that the y-axis is scaled logarithmically to increase the readability since the sound pressures calculated from the CLEAN-SC sources partially have very high amplitudes.

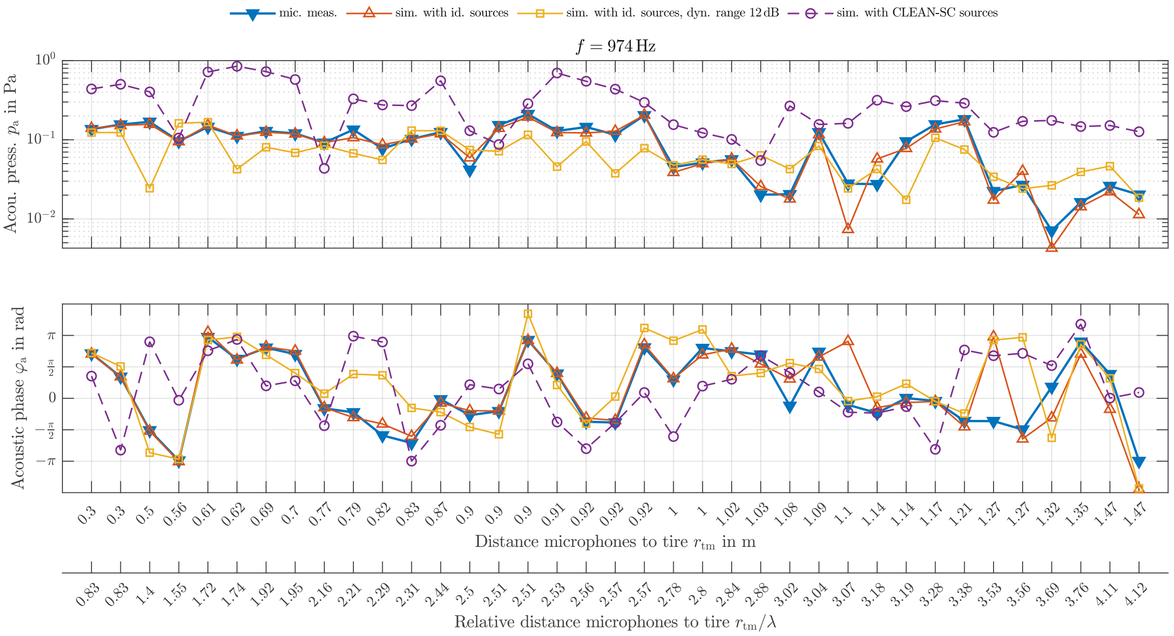

Figure 6.12: Comparison of simulated acoustic pressures to microphone measurements for measurement 1.

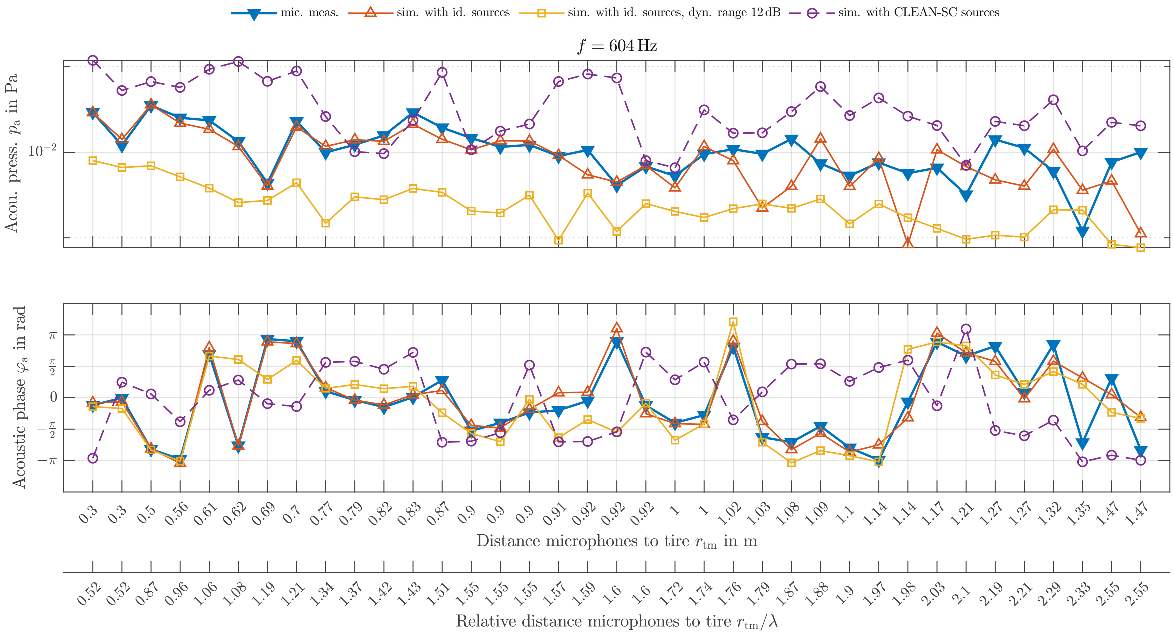

Figure 6.13: Comparison of simulated acoustic pressures to microphone measurements for measurement 2.

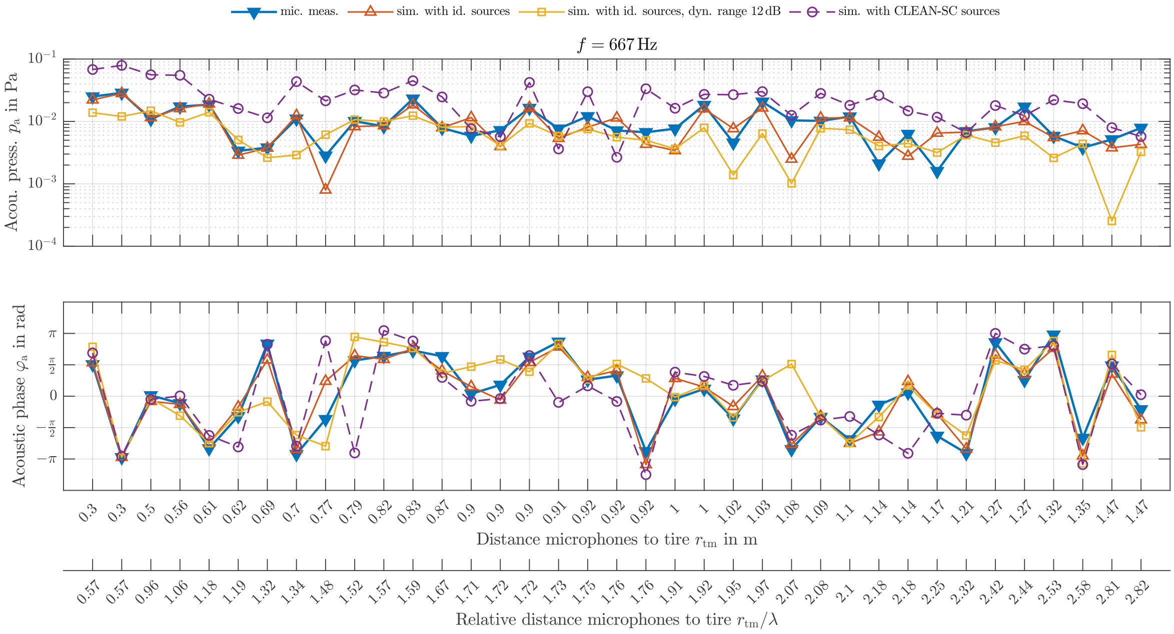

Figure 6.14: Comparison of simulated acoustic pressures to microphone measurements for measurement 3.

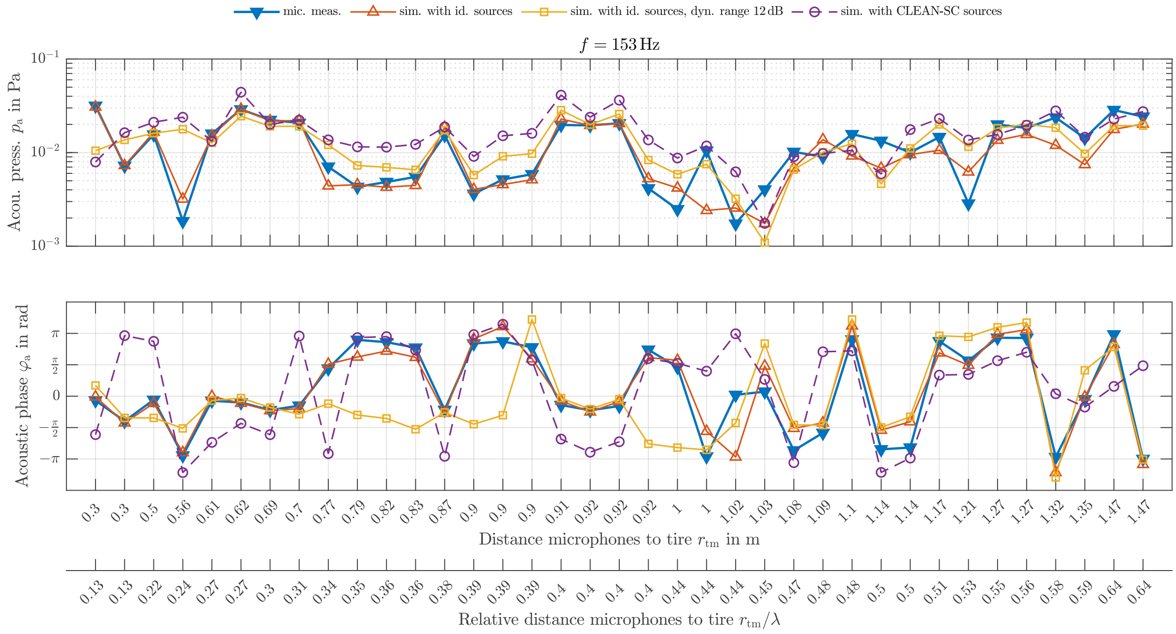

Figure 6.15: Comparison of simulated acoustic pressures to microphone measurements for measurement 4.

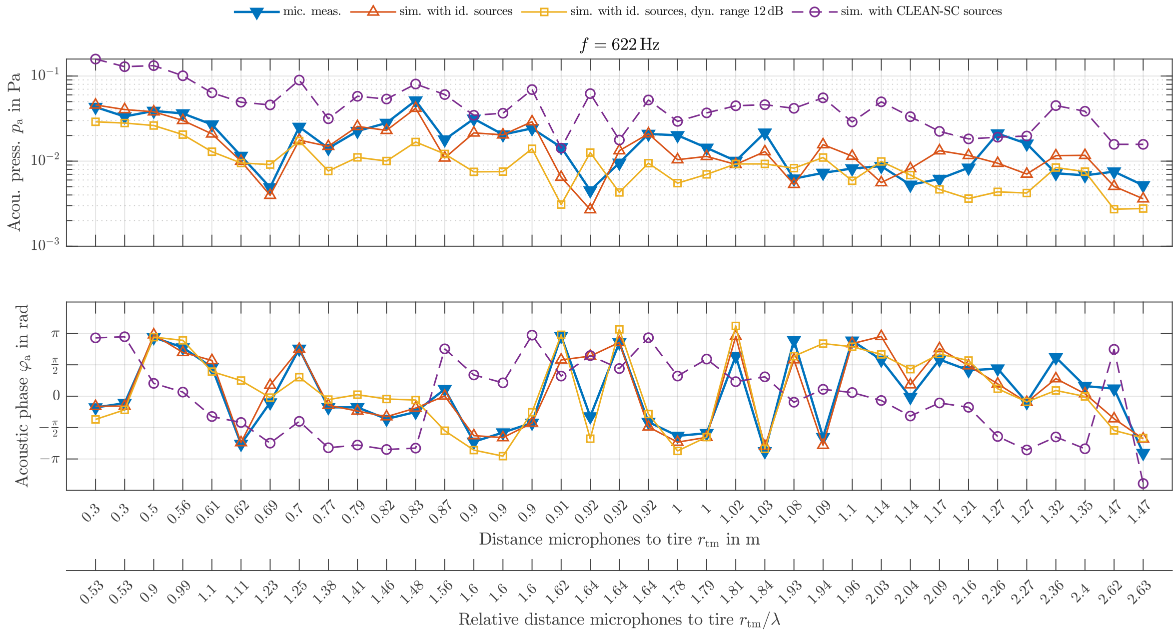

Figure 6.16: Comparison of simulated acoustic pressures to microphone measurements for measurement 5.

In Tab. 6.4, the relative L2-error, calculated according to (4.38), of the simulated acoustic pressures at the microphone positions, is listed. For each frequency, the aforementioned three different forward computations are taken into account. This table demonstrates that the Inverse Scheme is superior to beamforming-based algorithms. However, they perform well when only the location of the most dominant sound source is of interest, and no forward computation of the sound pressure field is required.

Meas. No.	f in Hz	$\varepsilon_{\mathrm{rel,inv}}$	$\varepsilon_{\mathrm{rel,inv,12\,dB}}$	$\varepsilon_{\mathrm{rel,CLEAN-SC}}$
1	827	0.24	0.77	1.20
1	974	0.22	0.84	3.50
2	604	0.40	0.86	4.13
2	851	0.25	0.77	1.33
3	667	0.36	0.69	1.93
4	153	0.43	0.74	1.67
5	622	0.37	0.74	3.54
5	732	0.34	0.78	3.40

Table 6.4: Relative L2-errors of the simulated acoustic pressures for all presented frequencies and measurement numbers if the forward computation is performed with all sources identified via the Inverse Scheme ($\varepsilon_{\mathrm{rel,inv}}$), with identified sources via the Inverse Scheme within the 12 dB-range ($\varepsilon_{\mathrm{rel,inv,12\,dB}}$) and with the sources identified via CLEAN-SC ($\varepsilon_{\mathrm{rel,CLEAN-SC}}$).

The relative errors of the forward computations via the Inverse Scheme sources are lowest for all frequencies, while the relative errors of the CLEAN-SC sources are always highest. While the values of $\varepsilon_{\mathrm{rel,inv}}$ are in the range of 0.22 to 0.40, the values of $\varepsilon_{\mathrm{rel,inv,12\,dB}}$ are larger by a factor of approx. 1.7 ($f = 153\,\mathrm{Hz}$) to 3.8 ($f = 974\,\mathrm{Hz}$), which corresponds to the lowest and highest frequency, respectively. The error values of $\varepsilon_{\mathrm{rel,CLEAN-SC}}$ are higher than that of the Inverse Scheme by a factor of approx. 3.9 to 15.9. Again, the lowest factor corresponds to the lowest frequency, and the highest factor to the highest frequency. Although these frequencies are taken from different measurement runs, and therefore, the comparison has to be treated with caution, this fact demonstrates once more that the sound pressures' sensitivity to the source distribution – including weaker sources – increases with increasing frequency.

The overall value of the relative error $\varepsilon_{\mathrm{rel,inv}}$ decreases with increasing frequency. This substantiates the assertion that the sensitivity of the acoustic pressure to the exact locations and amplitudes as well as phases of the sources is higher at high frequencies, and thus, the measured acoustic pressure can be matched better by the Inverse Scheme with sources within the finite source domain of the tire's surface at higher frequencies. The relative error of the CLEAN-SC forward computations does not show the same dependency on frequency as the computations with sources from the Inverse Scheme.

6.5.2 Reconstruction of Sound Pressure at CPX Positions

To conclude the analysis of the sound source identification results and the subsequent calculation of the sound pressures at the microphone positions, it is investigated how the sound pressure from a forward simulation matches the measured sound pressure if the measurements at those positions are excluded from the input to the Inverse Scheme. In other words, some microphone measurements are excluded during the sound source identification process. Subsequently, with the resulting identified sound sources, a forward simulation is performed, and the simulated sound pressure at the excluded position is compared to the measured sound pressure. This procedure is analog to comparing the sound pressure fields in the whole computational domain in case of virtual measurements – see Fig. 5.9 –, with the difference that the sound pressure in a real-world scenario is only known at the microphone positions.

The positions excluded from the algorithm are the two mandatory microphone positions defined in the standard for CPX measurements [37], see Fig. 1.2. We investigate how well the calculated sound field matches the existing in the near field. The CPX positions are chosen as they are of great interest in the practical application when pavements are characterized.

Due to the reduced number of microphones and the therefore different input data for the Inverse Scheme and other algorithms, the sound source identification results will change. By comparing these source maps to the original results, the impact of providing sound pressure measurements in immediate proximity to the localization algorithm may be determined.

The results of the sound source identification via the Inverse Scheme and the simulated acoustic pressure are shown for three different frequencies. In Fig. 6.17, the highest frequency of $f = 974\,\text{Hz}$ is depicted, Fig. 6.18 shows measurement 3 with a frequency of $f = 667\,\text{Hz}$ and results of the lowest frequency at $f = 153\,\text{Hz}$ can be taken from Fig. 6.19.

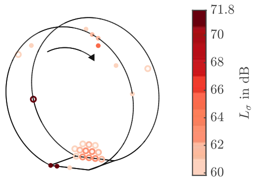

(a) Inv. res., 12 dB.

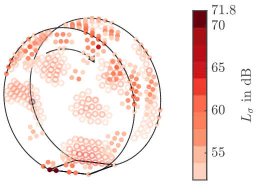

(b) Inv. res., 20 dB.

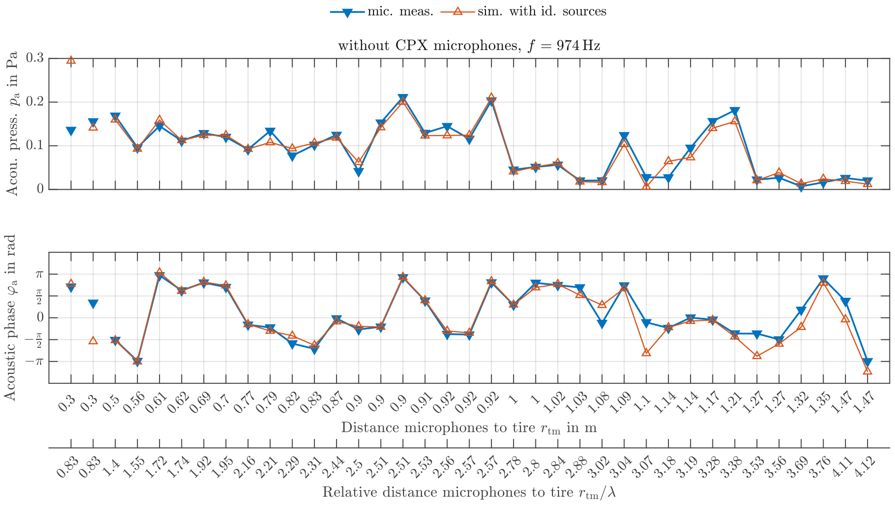

(c) Comparison of simulated acoustic pressures to microphone measurements.

Figure 6.17: Sound source identification results and simulated sound pressures at microphone positions without CPX microphone positions, $f = 974\,\text{Hz}$, measurement 1.

As can be seen by comparing the sound source identification results at 974 Hz obtained without the microphones at the CPX positions in Fig. 6.17a, and Fig. 6.17b to the original result in Fig. 6.7b and Fig. 6.8b, respectively, the SNR is lower, if the sound pressure signals from the CPX microphones are not taken into account. While the positions of the dominant sound source near the tire contact patch and the weaker sources along the tire's circumference remain mostly the same as in case of the result using all microphones, the amplitude of the dominant sound source decreases by approx 2 dB.

The CPX positions have the same distance to the center of the tire contact patch of 0.3 m. The first data point in Fig. 6.17c corresponds to the rear CPX position, and the second data point to the front CPX position. These two data points are not connected to the other points, indicating that they were not included in the input data.

The simulated sound pressure amplitude at the rear CPX position is overestimated by the simulation since sources identified at the tire's trailing edge have a slightly higher amplitude than in the result of the original configuration. However, the front CPX position's sound pressure amplitude is reconstructed well. The phase of the simulated sound pressure matches the measured phase better at the rear position.

The sound pressure amplitudes and phases at the other microphone positions, which were taken into account during the optimization of the Inverse Scheme, are matched very well by the forward simulation, and therefore, the amplitude and phase values are very similar to the ones from the original configuration with all microphones.

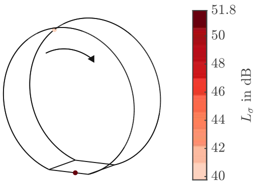

(a) Inv. res., 12 dB.

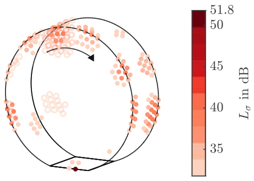

(b) Inv. res., 20 dB.

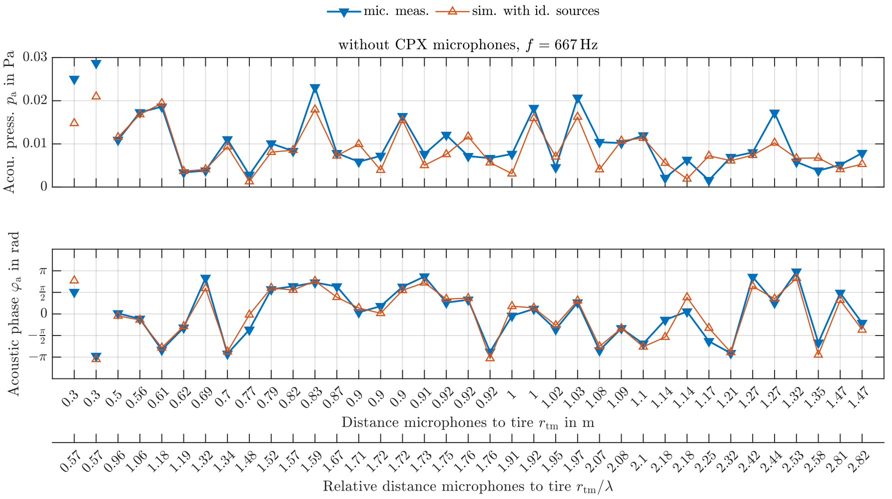

(c) Comparison of simulated acoustic pressures to microphone measurements for measurement 2, without CPX microphones.

Figure 6.18: Sound source identification results and simulated sound pressures at microphone positions without CPX microphone positions, $f = 667$ Hz, measurement 3.

The same considerations hold for the frequency of $f = 667$ Hz, – the simulated sound pressure amplitudes and phases match the measurement very well at positions with $r_{tm} \geq 0.5$ m. While the simulation slightly overestimates the sound pressure amplitudes at both CPX positions, the simulated phases match the measured phases well, see Fig. 6.18.

At the lowest frequency of $f = 153$ Hz, the matching between simulated and measured acoustic pressures at the CPX positions is the best of the presented frequencies in both amplitudes and phases. The source maps in Fig. 6.19a and Fig. 6.19b are very similar to the ones obtained with all microphones, see Fig. 6.7f and Fig. 6.8f. However, the SNR again decreased because of the reduced number of microphones.

The presented figures show that the sound pressures are still reproduced fairly well at locations in the immediate near field, even without microphone measurements entering the optimization at those positions. However, the deviations are considerably larger at those positions than if the respective microphone data are considered by the Inverse Scheme. This demonstrates the importance of positioning microphones in the immediate near-field if the accurate reconstruction of the sound pressure close to the dominant sound sources is of interest. Further, taking the sound pressure measurements at the CPX positions into account proved to be essential for the SNR of the source map. However, the overall positions of the identified sound sources did not change if the CPX measurements were omitted.

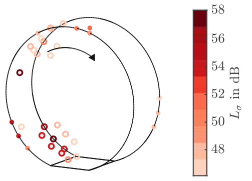

(a) Inv. res., 12 dB.

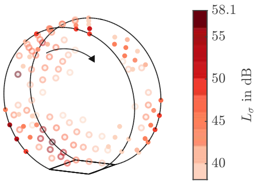

(b) Inv. res., 20 dB.

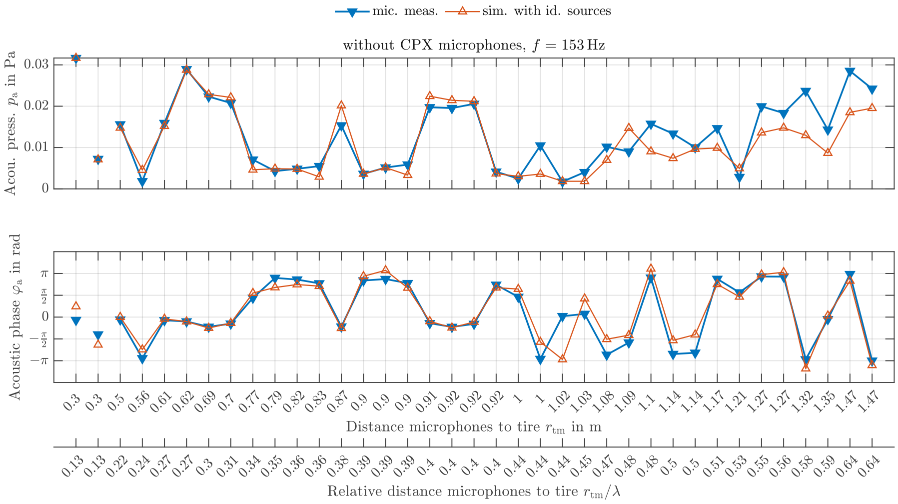

(c) Comparison of simulated acoustic pressures to microphone measurements for measurement 4, without CPX microphones.

Figure 6.19: Sound source identification results and simulated sound pressures at microphone positions without CPX microphone positions, $f = 135$ Hz, measurement 4.

Relative errors

In Tab. 6.5, the relative errors calculated according to (4.38) are listed for the Inverse Scheme without the CPX microphones in comparison to the values calculated before, where all microphones are taken into account. In doing so, we see that the relative errors of the calculated sound pressures take nearly the same value in both cases. For most frequencies $\varepsilon_{\mathrm{rel,inv}}$ is slightly higher if the CPX microphone signals are omitted.

Note that in the first case, the summation in (4.40) is carried out over the remaining 35 microphones only, and therefore, the CPX microphones are not considered in the relative L2-error. Otherwise, the error would not be comparable to the previously calculated error values.

Meas. No.	f in Hz	$\varepsilon_{\mathrm{rel,inv}}$	
		without CPX mics.	with CPX mics.
1	827	0.28	0.24
1	974	0.22	0.22
2	604	0.42	0.40
2	851	0.24	0.25
3	667	0.39	0.36
4	153	0.44	0.43
5	622	0.37	0.37
5	732	0.34	0.34

Table 6.5: Comparison of the relative L2-errors of the simulated sound pressures via the Inverse Scheme, if the measurements at the CPX positions in the acoustic near-field are considered or if they are omitted.

CHAPTER 7

Summary and Outlook

This thesis' objective was to apply an inverse method – called *Inverse Scheme* – for identifying the dominant sound sources on a rolling tire due to tire-pavement interactions. The Inverse Scheme obtains the sound sources within a predefined source region via an optimization. This optimization minimizes the differences between the sound pressures measured with a microphone array and Finite Element (FE) simulations at the respective positions. The sound source localization was preformed in the frequency range of interest between 150 Hz and 1600 Hz. The dominant sound sources of the tire noise lie in this frequency range. Subsequently, the sound field around the tire was calculated by means of the Finite Element Method.

Using a measurement trailer, the sound emitted by a rolling test tire was recorded. The trailer has a protective enclosure equipped with a porous acoustic absorber for sound insulation and to absorb the sound radiated from the tire. In the first step a suitable FE model of this given measurement setup had to be established. In doing so, one challenging task was to model the sound absorption in the acoustic absorbers within the FE framework. This includes obtaining the absorbers' correct material parameters. Based on Biot's theory, the region was modeled as an equivalent fluid. Its material properties were calculated using the Johnson-Champoux-Allard-Lafarge model. Its parameters were obtained via a genetic optimization, fitting the material's calculated reflection coefficient to impedance tube measurements.

The obtained material properties were validated via microphone measurements while the stationary trailer was excited with a loudspeaker. In order to model the loudspeaker as an acoustic source, its membrane deflection was determined as a function of frequency and of the electric current through the loudspeaker using a laser scanning vibrometer. Further, the material properties were optimized in a second step, where the acoustic pressure simulated with the FE method was fitted to the microphone measurements.

As a preliminary step to the source identification at the rolling tire, the Inverse Scheme's performance was investigated using the stationary measurements. The inverse method's source identification results were compared to results of established, beamforming-based sound source localization algorithms. Thereby, it could be demonstrated, that the Inverse Scheme is superior to the beamforming-based methods regarding the ability to localize source in the low frequency regime. Additionally, computations of the sound field with the identified sound sources obtained via the Inverse Scheme showed a better agreement with the microphone measurements.

The application of the Inverse Scheme to actual measurement data, recorded during measurement runs with the measurement trailer on Austrian highways, concludes this thesis. For this purpose, the measurement trailer was equipped with 37 microphones positioned in a three-dimensional array inside the trailer. These include those two microphone positions in the tire's near-field that are mandatory in the Close-Proximity (CPX) method, a standardized method used to characterize pavements. A method for determining whether a measurement run may be used for the sound source localization was established, using sensors to evaluate the trailer's running smoothness and the rotational frequency of the tire. The Inverse Scheme and established sound source localization algorithms were applied to different frequencies of five measurement runs, including various types of asphalt pavements and a concrete pavement.

The Inverse Scheme and the beamforming-based de-convolution algorithm CLEAN-SC identified the dominant sound source during the tire-pavement interaction near the tire contact patch for most of the evaluated frequencies, which is in accordance with the literature review presented in the first chapter. However, the Inverse Scheme could identify additional weaker sources along the tire's circumference. The basic algorithms Conventional Beamforming and the advanced Functional Beamforming could localize the dominant sound sources' exact positions only at higher frequencies. However, weaker sound sources at the tire could not be identified by these simpler methods.

Further, the sound pressure field around the tire was calculated by solving the forward problem via the FE method, prescribing the identified sound sources in the FE model. It could be shown that the sound field calculated from sources obtained via the inverse method matched the microphone measurements better than sound sources inferred with the alternative methods. It was also investigated how well the sound pressure can be reconstructed in the near-field of the tire at locations other than the microphone positions. In doing so, the sound pressure measurements at the CPX positions were omitted for the identification via the Inverse Scheme, and the sound pressure at the respective positions therefore did not enter the optimization. It could be shown that, especially at low frequencies, the reconstruction of the sound pressure in the near field – again obtained via solving the forward problem with the identified sound sources prescribed – matched the microphone measurements well. However, at higher frequencies, the simulated pressure deviated from the measurements. Further, it could be observed that taking microphone measurements at the CPX positions into account for the sound source localization yielded source maps with a higher signal-to-noise ratio. These facts indicate the importance of choosing the microphone positions carefully, both for the identification results and the simulated sound pressures in the near-field.

Therefore, future works should focus on the influence the chosen microphone positions have on the identified sound source locations and amplitudes. Further, since it could be observed that the Inverse Scheme's gradient-based optimization performed better concerning the matching of measured and calculated sound pressures than the genetic-based optimization used for the material parameter identification, it should be investigated how the fitting of the material parameters could be improved by using gradient-based algorithms.

Bibliography

[1] World Health Organization. *Environmental Noise. In: Compendium of WHO and Other UN Guidance on Health and Environment, 2022 Update*. Geneva, 2022. URL: `https://cdn.who.int/media/docs/default-source/who-compendium-on-health-and-environment/who_compendium_noise_01042022.pdf?sfvrsn=bc371498_3` (visited on 04/21/2023).

[2] European Environment Agency (EEA). *Environmental Noise in Europe – 2020*. 2020. URL: `https://www.eea.europa.eu/publications/environmental-noise-in-europe` (visited on 04/21/2023).

[3] Ulf Sandberg and Jerzy A. Ejsmont. *Tyre/Road Noise: Reference Book*. eng. 1. ed. Kisa, Sweden: INFORMEX Ejsmont & Sandberg Handelsbolag, 2002. ISBN: 9789163126109.

[4] Paul R. Donavan and Richard Schumacher. "Exterior Noise of Vehicles – Traffic Noise Prediction and Control". en. In: *Handbook of Noise and Vibration Control*. Ed. by Malcolm J. Crocker. Hoboken, NJ, USA: John Wiley & Sons, Inc., Sept. 2007, pp. 1427–1437. ISBN: 9780470209707. DOI: `10.1002/9780470209707.ch120`.

[5] Rebecca Bernhard Robert; McDaniel. "Basics of Noise Generation for Pavement Engineers". In: *Transportation Research Record Journal of the Transportation Research Board* 1941 (Jan. 2005). DOI: `10.3141/1941-21`.

[6] Robert Otto Rasmussen et al. *The Little Book of Quieter Pavements. FHWA-IF-08-004*. Tech. rep. 2007. URL: `https://rosap.ntl.bts.gov/view/dot/41905` (visited on 04/21/2023).

[7] Sara Gasparoni et al. "Impact of Low-Noise Tyres on Electric Vehicle Noise Emission". In: *IFSTTAR – Institut Français de Sciences et Technologies des Transports, de l'Aménagement et des Réseaux.* (2015).

[8] Tan Li. "Literature Review of Tire-Pavement Interaction Noise and Reduction Approaches". In: *Journal of Vibroengineering* 20 (Sept. 2018), pp. 2424–2452. DOI: `10.21595/jve.2018.19935`.

[9] M.E. Braun et al. "Noise Source Characteristics in the ISO 362 Vehicle Pass-by Noise Test: Literature Review". In: *Applied Acoustics* 74 (11 Nov. 2013). DOI: `10.1016/j.apacoust.2013.04.005`.

[10] M. Heckl. "Tyre Noise Generation". en. In: *Wear* 113.1 (Dec. 1986), pp. 157–170. DOI: `10.1016/0043-1648(86)90065-7`.

[11] Tyler Dare and Robert Bernhard. "Accelerometer Measurements of Tire Tread Vibrations and Implications to Wheel-Slap Noise". en. In: *Tire Science and Technology* 41.2 (Apr. 2013), pp. 109–126. DOI: `10.2346/tire.13.410202`.

[12] Tan Li. "Influencing Parameters on Tire-Pavement Interaction Noise: Review, Experiments, and Design Considerations". In: *Designs* 2.4 (2018). DOI: `10.3390/designs2040038`.

[13] William A. Leasure and Erich K. Bender. "Tire-Road Interaction Noise". en. In: *The Journal of the Acoustical Society of America* 58.1 (July 1975), pp. 39–50. ISSN: 0001-4966. DOI: `10.1121/1.380662`.

[14] Robert C. Chanaud. "Experimental Study of Aerodynamic Sound from a Rotating Disk". en. In: *The Journal of the Acoustical Society of America* 45.2 (Feb. 1969), pp. 392–397. DOI: `10.1121/1.1911386`.

[15] Richard J. Ruhala and Courtney B. Burroughs. "Identification of Sources of Tire/Pavement Interaction Noise". en. In: *The Journal of the Acoustical Society of America* 103.5 (May 1998), p. 2919. ISSN: 0001-4966. DOI: `10.1121/1.422109`.

[16] R. E. Hayden. "Roadside Noise from the Interaction of a Rolling Tire with the Road Surface". en. In: *Proceedings of the Purdue Noise Control Conference* (July 1971), pp. 59–64.

[17] JF Hamet, C Deffayet, and MA Pallas. "Air Pumping Phenomena in Road Cavities". In: *Proceedings of the International Tire/Road Noise Conference*. 1990.

[18] Thomas Beckenbauer and Deutschland, eds. *Einfluss der Fahrbahntextur auf das Reifen-Fahrbahn-Geräusch [Influence of Pavement Texture on Tire/Road Noise]*. ger. Forschung Strassenbau und Strassenverkehrstechnik 847. Bonn: Bundesministerium für Verkehr, Bau- und Wohnungswesen, Abteilung Straßenbau, Straßenverkehr, 2002. ISBN: 9783934458796.

[19] Thomas Beckenbauer et al. "Tyre/Road Noise Prediction: A Comparison Between the SPERoN and HyRoNE Models - Part 1". en. In: *The Journal of the Acoustical Society of America* 123.5 (May 2008), pp. 3388–3388. ISSN: 0001-4966. DOI: `10.1121/1.2934048`.

[20] Philippe Klein et al. "Tyre/Road Noise Prediction: A Comparison Between the SPERoN and HyRoNE Models - Part 2". en. In: *The Journal of the Acoustical Society of America* 123.5 (May 2008), pp. 3389–3389. ISSN: 0001-4966. DOI: `10.1121/1.2934049`.

[21] Sungtae Kim et al. "Prediction Method for Tire Air-Pumping Noise Using a Hybrid Technique". en. In: *The Journal of the Acoustical Society of America* 119.6 (June 2006), pp. 3799–3812. ISSN: 0001-4966. DOI: `10.1121/1.2200140`.

[22] M. J. Gagen. "Novel Acoustic Sources From Squeezed Cavities in Car Tires". In: *The Journal of the Acoustical Society of America* 106.2 (1999), pp. 794–801. DOI: `10.1121/1.427096`.

[23] M. J. Gagen. "Nonlinear Acoustic Sources in Squeezed Car Tyre Cavities". In: *Noise & Vibration Worldwide* 31.4 (2000), pp. 9–19. DOI: `10.1260/0957456001497481`.

[24] Prashanta Gautam and Abhilash J. Chandy. "A Three-Dimensional Numerical Investigation of Air Pumping Noise Generation in Tires". en. In: *Journal of Vibration and Acoustics* 138.6 (Dec. 2016), p. 061005. ISSN: 1048-9002, 1528-8927. DOI: `10.1115/1.4034100`.

[25] Marianne Bou Leba Bassil, Julien Cesbron, and Philippe Klein. "Tyre/Road Noise: A Piston Approach for CFD Modeling of Air Volume Variation in a Cylindrical Road Cavity". In: *Journal of Sound and Vibration* 469 (2020), p. 115140. DOI: `https://doi.org/10.1016/j.jsv.2019.115140`.

[26] Frédéric Conte and Philippe Jean. "CFD Modelling of Air Compression and Release in Road Cavities During Tyre Road Interaction". In: *Proc. Euronoise*. Vol. 30. 2006.

[27] Frédéric Conte and Philippe Klein. "3D CFD Modelling of Air Pumping Noise From Road Cavities With Constant Volume". In: *Internoise 2013: 42nd International Congress and Exposition on Noise Control Engineering*. 2013.

[28] R.A.G. Graf et al. “On the Horn Effect of a Tyre/Road Interface, Part I: Experiment and Computation”. In: *Journal of Sound and Vibration* 256 (3 Sept. 2002). DOI: `10.1006/jsvi.2001.4238`.

[29] Wolfgang Kropp et al. “On the Sound Radiation of a Rolling Tyre”. In: *Journal of Sound and Vibration* 331.8 (2012), pp. 1789–1805. ISSN: 0022-460X. DOI: `https://doi.org/10.1016/j.jsv.2011.11.031`.

[30] Carsten Hoever. *The Simulation of Car and Truck Tyre Vibrations, Rolling Resistance and Rolling Noise*. Chalmers Tekniska Hogskola (Sweden), 2014.

[31] Maik Brinkmeier et al. “A Finite Element Approach for the Simulation of Tire Rolling Noise”. en. In: *Journal of Sound and Vibration* 309.1-2 (Jan. 2008), pp. 20–39. ISSN: 0022460X. DOI: `10.1016/j.jsv.2006.11.040`.

[32] Jan Biermann et al. “Computational Model to Investigate the Sound Radiation from Rolling Tires”. en. In: *Tire Science and Technology* 35.3 (Sept. 2007), pp. 209–225. ISSN: 1945-5852, 0090-8657. DOI: `10.2346/1.2768608`.

[33] Julia Winroth et al. “Investigating Generation Mechanisms of Tyre/Road Noise by Speed Exponent Analysis”. In: *Applied Acoustics* 115 (2017), pp. 101–108. ISSN: 0003-682X. DOI: `https://doi.org/10.1016/j.apacoust.2016.08.027`.

[34] DIN EN ISO 11819-1:2021. *Acoustics – Measurement of the Influence of Road Surfaces on Traffic Noise - Part 1: Statistical Pass-By Method*. 2021. DOI: `10.31030/2575051`.

[35] DIN ISO 362-1. *Measurement of Noise Emitted by Accelerating Road Vehicles – Engineering Method – Part 1*. 2016.

[36] ISO 10844:2014. *Acoustics – Specification of Test Tracks for Measuring Noise Emitted by Road Vehicles and Their Tyres*. 2014.

[37] ISO 11819-2:2017. *Acoustics – Measurement of the Influence of Road Surfaces on Traffic Noise – Part 2: The Close-Proximity Method*. DOI: `10.31030/2575051`.

[38] National Highway Traffic Safety Administration (NHTSA). *Standard Reference Test Tire*. URL: `https://www.federalregister.gov/documents/2021/08/05/2021-15361/standard-reference-test-tire` (visited on 12/20/2022).

[39] ISO/TS 11819-3:2021. *Acoustics – Measurement of the Influence of Road Surfaces on Traffic Noise – Part 3: Reference Tyres*.

[40] Rasmus Stahlfest Holck SKOV. “Analysis and Comparison of Methods, CPX and SPB, for Measuring Noise Properties of Road Surfaces”. In: *Internoise 2016: 45th International Congress and Exposition of Noise Control Engineering*. 2016.

[41] Manfred Haider et al. *Rollgeräuschmessung auf Straßenoberflächen – Evaluierung und Aktualisierung ROSALIA [Measurement of Tire/Road Noise on Road Surfaces – Evaluation and Update ROSALIA]*. Tech. rep. 2022. URL: `https://projekte.ffg.at/anhang/63b59ca97c41f_ROSALIA_Ergebnisbericht.pdf` (visited on 07/04/2023).

[42] RVS 11.06.64. *RVS 11.06.64 Rollgeräuschmessungen [Measurement of Tire/Road Noise]*.

[43] Stefan Gombots et al. “Tire-Road Noise Measurements at the Test Rig of BASt”. In: *Tagungsband DAGA 2018*. 2018, pp. 1137–1140.

[44] AASHTO TP 76-13. *Measurement of Tire/Pavement Noise Using the On-Board Sound Intensity (OBSI) Method*. American Association of State Highway and Transportation Officials (AASHTO), 2015.

[45] Jens Oddershede et al. “CPX – OBSI Relation in Tyre/Road Noise Measurement Results”. In: *Internoise 2013: 42nd International Congress and Exposition on Noise Control Engineering*. 2013.

[46] *Vehicle-Pavement Interaction Facility (PFF).* `https://www.bast.de/EN/Traffic_Engineering/Technology/PFF.html`. (Visited on 12/20/2022).

[47] Allan D. Pierce. *Acoustics: An Introduction to its Physical Principles and Applications.* eng. Third edition. Cham: ASA Press, Springer, 1989. ISBN: 9783030112134.

[48] Manfred Kaltenbacher. *Computational Acoustics.* eng. 1st ed. 2018. CISM International Centre for Mechanical Sciences, Courses and Lectures 579. Cham: Springer International Publishing Imprint: Springer, 2018. DOI: `10.1007/978-3-319-59038-7`.

[49] F. Durst. *Grundlagen der Strömungsmechanik: Eine Einführung in die Theorie der Strömung von Fluiden.* Springer Berlin Heidelberg, 2007. ISBN: 9783540313243.

[50] M. S. Howe. *Theory of Vortex Sound.* Cambridge Texts in Applied Mathematics. New York: Cambridge University Press, 2003. ISBN: 9780521812818.

[51] A. P. Dowling and J. E. Efowcs Williams. *Sound and Sources of Sound.* Ellis Horwood Series in Engineering Science. Chichester New York: E. Horwood ; Halsted Press, 1983.

[52] R. J. Beerends et al. *Fourier and Laplace Transforms.* Cambridge University Press, 2003. ISBN: 9780511673122.

[53] A. Hirschberg and S.W. Rienstra. *An Introduction to Acoustics.* IWDE-Report. 2017. URL: `https://www.win.tue.nl/~sjoerdr/papers/boek.pdf` (visited on 04/21/2023).

[54] Daniel Russell, Joseph Titlow, and Ya-Juan Bemmen. "Acoustic Monopoles, Dipoles, and Quadrupoles: An Experiment Revisited". In: *American Journal of Physics* 67 (Aug. 1999), pp. 660–664. DOI: `10.1119/1.19349`.

[55] Reinhard Lerch, Gerhard M. Sessler, and Dietrich Wolf. *Technische Akustik: Grundlagen und Anwendungen [Technical Acoustics: Fundamentals and Applications].* Berlin Heidelberg: Springer, 2009. ISBN: 9783540234302.

[56] Thomas Rossing. *Springer Handbook of Acoustics.* Springer Handbooks. Springer, 2007. ISBN: 9780387304465.

[57] Petre Stoica and Randolph L. Moses. *Spectral Analysis of Signals.* Upper Saddle River, N.J: Pearson/Prentice Hall, 2005. ISBN: 9780131139565.

[58] Earl George Williams. *Fourier Acoustics: Sound Radiation and Nearfield Acoustical Holography.* eng. San Diego, Calif: Academic Press, 1999. ISBN: 9780127539607.

[59] Heinrich Kuttruff. *Acoustics: An Introduction.* Taylor & Francis, 2006. ISBN: 9780415386807.

[60] Michael Möser. *Technische Akustik [Technical Acoustics].* de. Berlin, Heidelberg: Springer Berlin Heidelberg, 2015. ISBN: 9783662477038. DOI: `10.1007/978-3-662-47704-5`. URL: `http://link.springer.com/10.1007/978-3-662-47704-5` (visited on 04/21/2023).

[61] ASTM E2611-09. *Standard Test Method for Measurement of Normal Incidence Sound Transmission of Acoustical Materials Based on the Transfer Matrix Method.* West Conshohocken, PA: ASTM International, 2009.

[62] J. Y. Chung and D. A. Blaser. "Transfer Function Method of Measuring In-duct Acoustic Properties. II. Experiment". en. In: *The Journal of the Acoustical Society of America* 68.3 (Sept. 1980), pp. 914–921. ISSN: 0001-4966. DOI: `10.1121/1.384779`.

[63] Albert London. "The Determination of Reverberant Sound Absorption Coefficients from Acoustic Impedance Measurements". en. In: *The Journal of the Acoustical Society of America* 22.2 (Mar. 1950), pp. 263–269. ISSN: 0001-4966. DOI: `10.1121/1.1906600`.

[64] ISO 10534-2:1998. *Acoustics – Determination of Sound Absorption Coefficient and Impedance in Impedance Tubes – Part 2: Transfer-Function Method.* Genève, Switzerland: International Organization for Standardization, 1998.

[65] Brüel & Kjær. *Standing Wave Apparatus Type 4002: Instruction Manual.* 1979.

[66] S.W. Rienstra. *Fundamentals of Duct Acoustics.* Technische Universiteit Eindhoven, 2015. URL: `https://www.win.tue.nl/~sjoerdr/papers/VKI_Rienstra.pdf` (visited on 04/21/2023).

[67] J. Stuart Bolton, Taewook Yoo, and Oliviero Olivieri. "Measurement of Normal Incidence Transmission Loss and Other Acoustical Properties of Materials Placed in a Standing Wave Tube". In: *Technical Review* No. 1 (2007).

[68] Hans Bodén and Mats Åbom. "Influence of Errors on the Two-Microphone Method for Measuring Acoustic Properties in Ducts". In: *The Journal of the Acoustical Society of America* 79 (2 Feb. 1986). DOI: `10.1121/1.393542`.

[69] C. W. Groetsch Charles W. Groetsch. *Inverse Problems in the Mathematical Sciences (Theory & Practice of Applied Geophysics).* Informatica International, Inc., 1993. ISBN: 3528065451.

[70] Michel Kern. *Numerical Methods for Inverse Problems.* 1st ed. Wiley-ISTE, 2016. ISBN: 1848218184.

[71] Jacques Hadamard. *Sur Les Problémes aux Dérivées Partielles et leur Signification Physique.* Princeton University Bulletin Vol. XIII. Princeton University, 1902.

[72] Andreas Rieder. *Keine Probleme Mit Inversen Problemen: Eine Einführung in Ihre Stabile Lösung.* 1st ed. Vieweg+Teubner Verlag, 2003. ISBN: 9783528031985.

[73] Barbara Kaltenbacher. *Lecture Notes on Parameter Identification in Differential Equations.* 2016.

[74] Jorge Nocedal and Stephen J. Wright. *Numerical Optimization.* 2nd ed. Springer Series in Operations Research. New York: Springer, 2006. ISBN: 9780387303031.

[75] Daniel N Snyman Jan A.; Wilke. *Practical Mathematical Optimization: Basic Optimization Theory and Gradient-Based Algorithms.* 2nd ed. 2018. Springer Optimization and Its Applications 133. Springer, 2018. ISBN: 9783319775869.

[76] Bruce D. Craven and B. D. Craven. *Control and Optimization.* 1. Ed. Chapman & Hall Mathematics Series. London: Chapman & Hall, 1995. ISBN: 9780412558900.

[77] Dimitri P. Bertsekas. *Nonlinear Programming.* 2nd. Athena Scientific, 1999. ISBN: 9781886529007.

[78] Jeffrey Larson, Matt Menickelly, and Stefan M. Wild. "Derivative-Free Optimization Methods". en. In: *Acta Numerica* 28 (May 2019), pp. 287–404. ISSN: 0962-4929, 1474-0508. DOI: `10.1017/S0962492919000060`.

[79] Melanie Mitchell. *Introduction to Genetic Algorithms.* Third Printing. Complex Adaptive Systems. The MIT Press, 1998. ISBN: 9780262631853.

[80] Tim A. Wheeler Mykel J. Kochenderfer. *Algorithms for Optimization.* 1st Edition. The MIT Press, 2019. ISBN: 9780262039420.

[81] Dan E. Dudgeon Don H. Johnson. *Array Signal Processing: Concepts and Techniques.* 1st ed. Prentice Hall, 1993. ISBN: 9780130485137.

[82] Ulf Michel and Michael Möser. "Akustische Antennen". In: *Messtechnik der Akustik.* Ed. by Michael Möser. Berlin, Heidelberg: Springer, 2010, pp. 365–425. ISBN: 978-3-540-68087-1. DOI: `10.1007/978-3-540-68087-1_6`.

[83] Stefan Gombots. "Acoustic Source Localization at Low Frequencies Using Microphone Arrays". PhD thesis. TU Wien, Austria, 2020.

[84] Ennes Herold Gert; Sarradj. "Performance Analysis of Microphone Array Methods". In: *Journal of Sound and Vibration* 401 (Aug. 2017). DOI: `10.1016/j.jsv.2017.04.030`.

[85] P. Welch. "The Use of Fast Fourier Transform for the Estimation of Power Spectra: A Method Based on Time Averaging Over Short, Modified Periodograms". In: *IEEE Transactions on Audio and Acoustics* 15.2 (1967), pp. 70–73. DOI: `10.1109/TAU.1967.1161901`.

[86] Ennes Sarradj. “Three-Dimensional Acoustic Source Mapping with Different Beamforming Steering Vector Formulations”. en. In: *Advances in Acoustics and Vibration* 2012 (June 2012), pp. 1–12. DOI: `10.1155/2012/292695`.

[87] Jeoffrey Fischer and Con Doolan. “Beamforming in a Reverberant Environment Using Numerical and Experimental Steering Vector Formulations”. In: *Mechanical Systems and Signal Processing* 91 (Jan. 2017), pp. 10–22. DOI: `10.1016/j.ymssp.2016.12.025`.

[88] Pieter Sijtsma and Hermann Holthusen. “Corrections for Mirror Sources in Phased Array Processing Techniques”. en. In: *9th AIAA/CEAS Aeroacoustics Conference and Exhibit*. Hilton Head, South Carolina: American Institute of Aeronautics and Astronautics, May 2003. ISBN: 9781624101021. DOI: `10.2514/6.2003-3196`.

[89] Robert P. Dougherty. “Beamforming In Acoustic Testing”. In: *Aeroacoustic Measurements*. Ed. by Thomas J. Mueller. 1st ed. Experimental Fluid Mechanics. Springer, 2002. ISBN: 9783642075148.

[90] Robert Dougherty, Rakesh Ramachandran, and Ganesh Raman. “Deconvolution of Sources in Aeroacoustic Images From Phased Microphone Arrays Using Linear Programming”. In: *International Journal of Aeroacoustics* 12 (7-8 Dec. 2013). DOI: `10.1260/1475-472X.12.7-8.699`.

[91] C.M. Sparrow. “On Spectroscopic Resolving Power”. In: *The Astrophysical Journal* 44 (Sept. 1916), p. 76. DOI: `10.1086/142271`.

[92] Ennes Sarradj. “A Fast Signal Subspace Approach for the Determination of Absolute Levels From Phased Microphone Array Measurements”. en. In: *Journal of Sound and Vibration* 329.9 (Apr. 2010), pp. 1553–1569. ISSN: 0022460X. DOI: `10.1016/j.jsv.2009.11.009`.

[93] Robert P. Dougherty. “Functional Beamforming for Aeroacoustic Source Distributions”. In: *20th AIAA/CEAS Aeroacoustics Conference*. American Institute of Aeronautics and Astronautics, June 2014. ISBN: 9781624102851. DOI: `10.2514/6.2014-3066`.

[94] Robert P. Dougherty. “Functional Beamforming”. In: *Proceedings the 5th Berlin Beamforming Conference, 19–20 February 2014*. GFaI, Gesellschaft zur Förderung angewandter Informatik e.V., Berlin, Feb. 2014. ISBN: 9783942709125.

[95] Klaus Ehrenfried and Lars Koop. “Comparison of Iterative Deconvolution Algorithms for the Mapping of Acoustic Sources”. In: *AIAA Journal* 45.7 (2007), pp. 1584–1595. DOI: `10.2514/1.26320`.

[96] Zhigang Chu and Yang Yang. “Comparison of Deconvolution Methods for the Visualization of Acoustic Sources Based on Cross-Spectral Imaging Function Beamforming”. en. In: *Mechanical Systems and Signal Processing* 48.1-2 (Oct. 2014), pp. 404–422. ISSN: 08883270. DOI: `10.1016/j.ymssp.2014.03.012`.

[97] Thomas Padois and Alain Berry. “Two and Three-Dimensional Sound Source Localization with Beamforming and Several Deconvolution Techniques”. en. In: *Acta Acustica united with Acustica* 103.3 (May 2017), pp. 392–400. ISSN: 1610-1928. DOI: `10.3813/AAA.919069`.

[98] Q Leclére et al. “A Unified Formalism for Acoustic Imaging Based on Microphone Array Measurements”. In: *International Journal of Aeroacoustics* 16 (4-5 July 2017). DOI: `10.1177/1475472X17718883`.

[99] Thomas Brooks and William Humphreys. “Extension of DAMAS Phased Array Processing for Spatial Coherence Determination (DAMAS-C)”. en. In: *12th AIAA/CEAS Aeroacoustics Conference (27th AIAA Aeroacoustics Conference)*. Cambridge, Massachusetts: American Institute of Aeronautics and Astronautics, May 2006. ISBN: 9781624100215. DOI: `10.2514/6.2006-2654`.

[100] Patricio Ravetta, Ricardo Burdisso, and Wing Ng. "Noise Source Localization and Optimization of Phased Array Results (LORE)". en. In: *12th AIAA/CEAS Aeroacoustics Conference (27th AIAA Aeroacoustics Conference)*. Cambridge, Massachusetts: American Institute of Aeronautics and Astronautics, May 2006. ISBN: 9781624100215. DOI: `10.2514/6.2006-2713`.

[101] Thomas Brooks and William Humphreys. "A Deconvolution Approach for the Mapping of Acoustic Sources (DAMAS) Determined from Phased Microphone Arrays". In: *10th AIAA/CEAS Aeroacoustics Conference*. DOI: `10.2514/6.2004-2954`.

[102] Thomas F. Brooks and William M. Humphreys. "A Deconvolution Approach for the Mapping of Acoustic Sources (DAMAS) Determined From Phased Microphone Arrays". In: *Journal of Sound and Vibration* 294.4 (2006), pp. 856–879. ISSN: 0022-460X. DOI: `https://doi.org/10.1016/j.jsv.2005.12.046`.

[103] Robert Dougherty. "Extensions of DAMAS and Benefits and Limitations of Deconvolution in Beamforming". en. In: *11th AIAA/CEAS Aeroacoustics Conference*. Monterey, California: American Institute of Aeronautics and Astronautics, May 2005. ISBN: 9781624100529. DOI: `10.2514/6.2005-2961`. URL: `https://arc.aiaa.org/doi/10.2514/6.2005-2961` (visited on 04/21/2023).

[104] Tarik Yardibi et al. "Sparsity Constrained Deconvolution Approaches for Acoustic Source Mapping". In: *The Journal of the Acoustical Society of America* 123 (5 May 2008). DOI: `10.1121/1.2896754`.

[105] Pieter Sijtsma. "CLEAN Based on Spatial Source Coherence". In: *International Journal of Aeroacoustics* 6.4 (2007), pp. 357–374. DOI: `10.1260/147547207783359459`.

[106] J. A. Högbom. "Aperture Synthesis with a Non-Regular Distribution of Interferometer Baselines". In: *Astronomy and Astrophysics Supplement Series* 15 (June 1974), p. 417.

[107] Paul R. Donavan and Oswald L. *Quantification of Noise Mechanisms of Blank, Rib, and Cross-Bar Tread Bias-Ply Truck Tires*. Tech. rep. General Motors Research Laboratories, July 1981.

[108] L. J. Oswald and P. R. Donavan. "Acoustic Intensity Measurements in Low Much Number Flows With Moderate Turbulence Levels". en. In: *The Journal of the Acoustical Society of America* 67.S1 (Apr. 1980), S71–S71. ISSN: 0001-4966. DOI: `10.1121/1.2018365`.

[109] Yasuo Oshino and Hideki Tachibana. "Noise Source Identification on Rolling Tires by Sound Intensity Measurement." en. In: *Journal of the Acoustical Society of Japan (E)* 12.2 (1991), pp. 87–92. ISSN: 0388-2861, 2185-3509. DOI: `10.1250/ast.12.87`.

[110] Stijn Vercammen et al. "Comparison of Two Measurement Methods for Exterior Noise Radiation Characterization of a Loaded Rotating Tyre". In: *SAE Technical Paper Series* 1 (June 2015). DOI: `10.4271/2015-01-2197`.

[111] Rolf Steiner and Jorgen Hald. "Near-field Acoustical Holography without the Errors and Limitations Caused by the Use of Spatial DFT". In: *The International Journal of Acoustics and Vibration* 6.2 (2001). ISSN: 24151408. DOI: `10.20855/ijav.2001.6.278`.

[112] Sean F. Wu. "On Reconstruction of Acoustic Pressure Fields Using the Helmholtz Equation Least Squares Method". en. In: *The Journal of the Acoustical Society of America* 107.5 (May 2000), pp. 2511–2522. ISSN: 0001-4966. DOI: `10.1121/1.428639`.

[113] Zhaoxi Wang and Sean F. Wu. "Helmholtz Equation – Least-Squares Method for Reconstructing the Acoustic Pressure Field". en. In: *The Journal of the Acoustical Society of America* 102.4 (Oct. 1997), pp. 2020–2032. DOI: `10.1121/1.419691`.

[114] Susan Dumbacher et al. "Source Identification Using Acoustic Array Techniques". In: May 1995, p. 951360. DOI: `10.4271/951360`.

[115] Ernst-Ulrich Saemann and Jørgen Hald. "Transient Tyre Noise Measurements Using Time Domain Acoustical Holography". In: May 1997, pp. 1423–1430. DOI: `10.4271/972050`.

[116] Per Rasmussen and Svend Gade. *Tyre Noise Measurement on a Moving Vehicle*. Tech. rep. Brüel & Kjær, 1996.

[117] Ennes Sarradj, Christoph Fritzsche, and Thomas Geyer. "Silent Owl Flight: Bird Flyover Noise Measurements". en. In: *AIAA Journal* 49.4 (Apr. 2011), pp. 769–779. DOI: `10.2514/1.J050703`.

[118] José A. Ballesteros et al. "Noise Source Identification With Beamforming in the Pass-by of a Car". en. In: *Applied Acoustics* 93 (June 2015), pp. 106–119. ISSN: 0003682X. DOI: `10.1016/j.apacoust.2015.01.019`.

[119] William D'Andrea Fonseca and Samir N. Y. Gerges. "Development of a Low Cost System for Pass-by Noise Beamforming Measurements". In: *Proceedings of 20th International Congress on Acoustics, ICA 2010*. 2010.

[120] Paulo Alexandre Galarce Zavala et al. "Heavy Vehicles Pass-by Noise Beamforming using Generalized Inverse Method and an Optimized Array". In: Oct. 2013. DOI: `10.4271/2013-36-0469`.

[121] Hyu-Sang Kwon and Yang-Hann Kim. "Moving Frame Technique for Planar Acoustic Holography". en. In: *The Journal of the Acoustical Society of America* 103.4 (Apr. 1998), pp. 1734–1741. ISSN: 0001-4966. DOI: `10.1121/1.421375`.

[122] Soon-Hong Park and Yang-Hann Kim. "An Improved Moving Frame Acoustic Holography for Coherent Bandlimited Noise". en. In: *The Journal of the Acoustical Society of America* 104.6 (Dec. 1998), pp. 3179–3189. ISSN: 0001-4966. DOI: `10.1121/1.423958`.

[123] Philip Morgan, S Phillips, and G.R Watts. "The Localisation, Quantification and Propagation of Noise From a Rolling Tyre". In: *Project Report* (July 2006).

[124] Tan Li. "A State-of-the-Art Review of Measurement Techniques on Tire–pavement Interaction Noise". en. In: *Measurement* 128 (Nov. 2018), pp. 325–351. ISSN: 02632241. DOI: `10.1016/j.measurement.2018.06.056`.

[125] M. Batel et al. "Noise Source Location Techniques – Simple to Advanced Applications". In: *Sound and Vibration* 37 (Mar. 2003), pp. 24–36.

[126] M.A. Biot. "Theory of Propagation of Elastic Waves in a Fluid-Saturated Porous Solid. I. Low Frequency Range". In: *Journal of the Acoustical Society of America* 28 (Mar. 1956), pp. 168–178. DOI: `10.1121/1.1908239`.

[127] M.A. Biot. "Theory of Propagation of Elastic Waves in a Fluid-Saturated Porous Solid. II. Higher Frequency Range". In: *Journal of the Acoustical Society of America* 28 (Mar. 1956), pp. 179–191. DOI: `10.1121/1.1908241`.

[128] Jean Allard and Noureddine Atalla. *Propagation of Sound in Porous Media: Modelling Sound Absorbing Materials*. 2nd ed. Wiley, 2009. ISBN: 0470746610.

[129] François-Xavier Bécot and Luc Jaouen. "An Alternative Biot's Formulation for Dissipative Porous Media With Skeleton Deformation". en. In: *The Journal of the Acoustical Society of America* 134.6 (Dec. 2013), pp. 4801–4807. DOI: `10.1121/1.4826175`.

[130] Leo L. Beranek. "Acoustical Properties of Homogeneous, Isotropic Rigid Tiles and Flexible Blankets". In: *The Journal of the Acoustical Society of America* 19.4 (June 1947), pp. 556–568. DOI: `10.1121/1.1916521`.

[131] K.U. Ingard. *Notes on Sound Absorption Technology*. Noise Control Foundation, 1994. ISBN: 9780931784286.

[132] Srinivas Katragadda, Heng-Yi Lai, and J. Stuart Bolton. "A Model for Sound Absorption by and Sound Transmission Through Limp Fibrous Layers". en. In: *The Journal of the Acoustical Society of America* 98.5 (Nov. 1995), pp. 2977–2977. ISSN: 0001-4966. DOI: `10.1121/1.413937`.

[133] Raymond Panneton. “Comments on the Limp Frame Equivalent Fluid Model for Porous Media”. en. In: *The Journal of the Acoustical Society of America* 122.6 (Dec. 2007), EL217–EL222. ISSN: 0001-4966. DOI: `10.1121/1.2800895`. URL: `https://pubs.aip.org/asa/jasa/article/122/6/EL217-EL222/917668` (visited on 05/04/2023).

[134] Noé Jiménez, Olga Umnova, and Jean-Philippe Groby. *Acoustic Waves in Periodic Structures, Metamaterials, and Porous Media: From Fundamentals to Industrial Applications.* 1st ed. Topics in Applied Physics. Springer, 2021. ISBN: 9783030843007.

[135] Luc Jaouen. *APMR: Acoustical Porous Material Recipes.* 2023. URL: `https://apmr.matelys.com/PropagationModels/MotionlessSkeleton/JohnsonChampouxAllardLafargeModel.html` (visited on 12/21/2022).

[136] Sebastian Floss. “Mitigation of Sound by Micro-Perforated Absorbers in Different Types of Sound Fields – Design and Evaluation”. PhD thesis. TU Wien, Austria, 2022.

[137] C. Zwikker and Cornelis Willem Kosten. *Sound Absorbing Materials.* Elsevier Pub. Co., 1949. ISBN: 9780444406613.

[138] Yvan Champoux. “Air-Based System for the Measurement of Porosity”. In: *The Journal of the Acoustical Society of America2* 89 (2 Feb. 1991). DOI: `10.1121/1.1894653`.

[139] *EN ISO 9053-1:2019-03, Acoustics – Determination of Airflow Resistance – Part 1: Static Airflow Method (ISO 9053-1:2018); German Version.* Tech. rep. Beuth Verlag GmbH. DOI: `10.31030/2874934`.

[140] Yvan Champoux and Jean-F. Allard. “Dynamic Tortuosity and Bulk Modulus in Air-Saturated Porous Media”. In: *Journal of Applied Physics* 70 (4 Aug. 1991). DOI: `10.1063/1.349482`.

[141] David Linton Johnson, Joel Koplik, and Roger Dashen. “Theory of Dynamic Permeability and Tortuosity in Fluid-Saturated Porous Media”. In: *Journal of Fluid Mechanics* 176 (Mar. 1987), pp. 379–402. DOI: `10.1017/S0022112087000727`.

[142] Yasushi Miki. “Acoustical Properties of Porous Materials – Modifications of Delany-Bazley Models”. In: *Journal of the Acoustical Society of Japan* 11.1 (1990), pp. 19–24. DOI: `10.1250/ast.11.19`.

[143] M.E. Delany and E.N. Bazley. “Acoustical Properties of Fibrous Absorbent Materials”. In: *Applied Acoustics* 3.2 (1970), pp. 105–116. DOI: `https://doi.org/10.1016/0003-682X(70)90031-9`.

[144] Takeshi Komatsu. “Improvement of the Delany-Bazley and Miki Models for Fibrous Sound-Absorbing Materials”. en. In: *Acoustical Science and Technology* 29.2 (2008), pp. 121–129. DOI: `10.1250/ast.29.121`.

[145] K. Attenborough. “Acoustical Impedance Models for Outdoor Ground Surfaces”. In: *Journal of Sound and Vibration* 99 (4 Apr. 1985). DOI: `10.1016/0022-460x(85)90538-3`.

[146] Denis Lafarge et al. “Dynamic Compressibility of Air in Porous Structures at Audible Frequencies”. In: *The Journal of the Acoustical Society of America* 102.4 (Oct. 1997), pp. 1995–2006. DOI: `10.1121/1.419690`.

[147] Steven R. Pride, Frank Dale Morgan, and Anthony F. Gangi. “Drag Forces of Porous-Medium Acoustics”. In: *Phys. Rev. B* 47 (9 Mar. 1993), pp. 4964–4978. DOI: `10.1103/PhysRevB.47.4964`.

[148] D. Keith Wilson. “Relaxation-matched Modeling of Propagation Through Porous Media, Including Fractal Pore Structure”. In: *The Journal of the Acoustical Society of America* 94.2 (Aug. 1993), pp. 1136–1145. DOI: `10.1121/1.406961`.

[149] Panasorb. *Akustik Planer Schaumstoff 100x50x5cm Anthrazit mit Verhautung Klebend [Acoustic Flat Foam 100x50x5cm Anthracite with Skin Adhesive].* 2023. URL: `https://www.panasorb.eu/store-pdf-info.php?pID=399` (visited on 02/12/2023).

[150] The MathWorks Inc. *Global Optimization Toolbox: Genetic Algorithm*. Natick, Massachusetts, United States, 2022. URL: `https://www.mathworks.com/help/gads/ga.html` (visited on 04/21/2023).

[151] M. Kaltenbacher. *Numerical Simulation of Mechatronic Sensors and Actuators: Finite Elements for Computational Multiphysics*. 3rd ed. Springer, 2015.

[152] A. Bermúdez et al. “An Optimal Perfectly Matched Layer With Unbounded Absorbing Function for Time-Harmonic Acoustic Scattering Problems”. en. In: *Journal of Computational Physics* 223.2 (May 2007), pp. 469–488. DOI: `10.1016/j.jcp.2006.09.018`. (Visited on 03/21/2023).

[153] Robert Clayton and Björn Engquist. “Absorbing Boundary Conditions for Acoustic and Elastic Wave Equations”. en. In: *Bulletin of the Seismological Society of America* 67.6 (Dec. 1977), pp. 1529–1540. DOI: `10.1785/BSSA0670061529`.

[154] Lorraine G. Olson and Klaus-Jürgen Bathe. “An Infinite Element for Analysis of Transient Fluid—Structure Interactions”. en. In: *Engineering Computations* 2.4 (Apr. 1985), pp. 319–329. DOI: `10.1108/eb023631`.

[155] Visaton. *Data sheet FR10*. 2023. URL: `https://www.visaton.de/sites/default/files/dd_product/FR_10_0.pdf` (visited on 03/22/2023).

[156] Brüel & Kjær. *Data Sheet Sound Calibrator Type 4231*. URL: `https://www.bksv.com/-/media/literature/Product-Data/bp1311.ashx` (visited on 04/21/2023).

[157] Manfred Kaltenbacher, Barbara Kaltenbacher, and Stefan Gombots. “Inverse Scheme for Acoustic Source Localization using Microphone Measurements and Finite Element Simulations”. In: *Acta Acustica* 104 (2018), pp. 647–656.

[158] Jonathan Nowak et al. “Inverse Scheme for Sound Localization”. In: *Tagungsband DAGA 2020*. 2020, pp. 635–638.

[159] Stephan W. Anzengruber, Bernd Hofmann, and Peter Mathé. “Regularization Properties of the Sequential Discrepancy Principle for Tikhonov Regularization in Banach Spaces”. en. In: *Applicable Analysis* 93.7 (July 2014), pp. 1382–1400. ISSN: 0003-6811, 1563-504X. DOI: `10.1080/00036811.2013.833326`.

[160] Verein zur Förderung der Software openCFS [Association for the Promotion of the Software openCFS]. *openCFS*. 2021. URL: `https://opencfs.org/` (visited on 08/24/2021).

[161] Ulf Sandberg. “Noise Trailers of the World – Tools for Tire/ Road Noise Measurements with the Close-Proximity Method”. In: *Proceedings of the 1998 National Conference on Noise Control Engineering (NOISE-CON 98)*. 1998. URL: `https://www.diva-portal.org/smash/get/diva2:672828/FULLTEXT01.pdf` (visited on 04/21/2023).

[162] Infrastructure Technology Platform for Transport and Public Space in the Netherlands. *CROW*. 2023. URL: `https://crowplatform.com/` (visited on 04/30/2023).

[163] Beata Świeczko-Żurek et al. “Rolling Resistance and Tyre/Road Noise on Rubberised Asphalt Pavement in Poland”. en. In: *Road Materials and Pavement Design* 18.1 (Jan. 2017), pp. 151–167. ISSN: 1468-0629, 2164-7402. DOI: `10.1080/14680629.2016.1159245`.

[164] Irvin D. Wilken, Robert Hickling, and Harold V. Wiknich. “A Single-Wheel Trailer for Tire Noise Research”. In: vol. 83. SAE International, 1974, pp. 526–536.

[165] Ryszard Woźniak. “Hałas Opon W Warunkach Występowania Znacznych Sił Stycznych W Strefie Styku Opony Z Jezdnią. [Tire Noise Under Conditions of Significant Contact Forces in the Tire-Pavement Contact Zone]”. Politechnika Gdańska, 2002.

[166] G. M. Sessler and J. E. West. “Self-Biased Condenser Microphone with High Capacitance”. en. In: *The Journal of the Acoustical Society of America* 34.11 (Nov. 1962), pp. 1787–1788. DOI: `10.1121/1.1909130`.

[167] Sennheiser. *Data Sheet KE 4-211-2*. URL: `https://www.distrelec.de/Web/Downloads/01/00/03010100.pdf` (visited on 04/21/2023).

[168] RME. *Data Sheet RME M-32 AD*. URL: `https://archiv.rme-audio.de/download/sheets/m32ad_m16ad_e.pdf` (visited on 04/21/2023).

[169] RME. *Data Sheet MADIface XT*. URL: `https://archiv.rme-audio.de/download/sheets/madiface_xt_e.pdf` (visited on 04/21/2023).

[170] Brüel & Kjær. *Data Sheet Free-Field Microphone Type 4190*. URL: `https://www.bksv.com/-/media/literature/Product-Data/bp2211.ashx` (visited on 04/21/2023).

[171] Keyence. *Data Sheet Laser Displacement Sensor LK-G152*. URL: `https://www.keyence.eu/products/measure/laser-1d/lk-g3000/models/lk-g152/` (visited on 04/21/2023).

[172] Analog Devices. *Data Sheet 2D Accelerometer ADXL335*. URL: `https://www.analog.com/media/en/technical-documentation/data-sheets/ADXL335.pdf` (visited on 04/21/2023).

[173] WayCon Engineering. *Data Sheet Eddy Current Probe IC12-02*.

[174] Krzysztof Blazejowski. *Stone Matrix Asphalt: Theory and Practice*. 1st. CRC Press, 2016. ISBN: 9781439819722.

[175] *Electroacoustics – Octave-Band and Fractional-Octave-Band Filters - Part 1: Specifications (IEC 61260-1:2014); German Version EN 61260-1:2014*. Tech. rep. Beuth Verlag GmbH. DOI: `10.31030/2231136`.